NORTHWESTERN UNIVERSITY

Design Driven Mulit-scale Mechanical Property Characterization of Polymer Composites

A DISSERTATION

SUBMITTED TO THE GRADUATE SCHOOL IN PARTIAL FULFILLMENT OF THE REQUIREMENTS

for the degree of

DOCTOR OF PHILOSOPHY

Field of Materials Science and Engineering

by

Matthew D. Eaton

EVANSTON, ILLINOIS

September, 2020

Abstract

There is no group of materials as diverse, complex, and ubiquitous as polymers. From plastic bags, to rubber tires, electronics, food packaging, water filtration and even aerospace applications, the penetration of polymer materials into all aspects of life make them very important materials throughout all engineering fields. However, this breadth of application means that many different variables can affect the properties of polymer materials, such as the chemical and physical structure of the polymer, the addition of any filler material or additive, or the effect of external stimuli like temperature, strain rate, and humidity. Thus, the development of new polymer materials can be an expensive and time consuming task. Computational simulations can be used to help predict properties and test a range of polymer formulations, but efficient models require robust experimental data to verify the accuracy of the models used. Smart experimental design is therefore imperative to efficiently develop new polymer materials.

This thesis takes a design-driven approach to polymer materials characterization to establish and develop experimental methods to connect local properties and morphology to bulk mechanical behavior and bridging the gap between experiments and computational models. Given the breadth of polymer materials, three polymer systems will be explored in more detail, crosslinked rubber blends and nanocomposites, epoxies for fiber reinforced composite matrices, and thermoplastic starch. Each of these polymer material systems had unique motivations and characterization challenges, and so the experimental approaches had to be tailored for each system for efficient materials design and development.

In rubber nanocomposites, chemical and physical interactions between fillers and rubber can result in interphase regions that have properties distinct from the constituent materials, which can complicate predictive models. Therefore, a novel atomic force microscopy (AFM) viscoelastic property characterization technique is developed and validated through comparison to bulk dynamic mechanical analysis (DMA). It is applied to multi-phase systems such as crosslinked rubber blends carbon black-rubber composites, and shows great potential for better understanding the time and temperature dependence of these local properties. Additionally, finite element simulations are paired with AFM indentation experiments for rubber composite systems to better understand the effect of indentation artifacts that can lead to artificial increases in modulus near a rigid particle. Pairing the results from FEA simulation and AFM experimentation leads to better interpretation of experimental data and initial results show potential for improved predictive computational viscoelastic rubber composite models.

For fiber-reinforced epoxy composite systems, applications for extreme, cryogenic temperature conditions

are complicated by the thermal expansion differences between fibers and polymer matrices, resulting in large thermal stresses and microcracking, and therefore matrix materials with strong fracture toughness are desired to prevent catastrophic failure. This lead to the investigation of a set of model epoxy systems with nanoscale heterogeneity, that has previously been reported to have interesting ballistic properties. In this thesis, the temperature dependent mechanical and fracture properties of the model epoxy system are further characterized using a custom set-up force-displacement analyzer attached to a temperature control chamber and performing Vicker's indentation hardness and single edge notched bend (SENB) toughness tests. Distinct correlations between temperature dependent mechanical and fracture behavior, fracture surface morphology, and nanoscale heterogeneity are made. Additionally, these model epoxy systems are further investigation by fabricating and testing semi interpenetrating polymer networks (IPNs) of the epoxy with thermoplastic poly(methylmethacrylate), which initial data shows the potential for improved mechanical properties over a wider temperature range.

Finally, due to their low cost, abundance and biodegradability, thermoplastic starch (TPS) materials have emerged as potential replacements for petrochemical-based single use plastics. However, these materials are very sensitive to atmospheric humidity, and current methods characterizing the effect of water content on TPS materials are labor intensive and time consuming. This thesis will present a non-destructive, efficient method to measure the full range of humidity dependence of viscoelastic mechanical properties and moisture absorption of thermoplastic starch (TPS) films using a quartz crystal microbalance (QCM). It will also be used to evaluate the effect of different plasticizers on TPS properties, and lays the groundwork for future investigations into efficient TPS materials development.

From the demonstration of a diverse set of design driven mechanical property characterization approaches on multiple polymer systems, the work presented in this thesis can improve materials design and optimization in polymer materials development.

Acknowledgements

The last five years at Northwestern University have been an incredible experience, and I could not imagine a better place by my academic, educational and professional development. The work I've done and the experience I had would be nothing without the help, guidance, and support from my colleagues, mentors, friends, and family, and I am beyond grateful to you all.

To **Dr. Ken Shull**, my primary adviser for the last 2.5 years, thank you for being a great mentor, and accepting me into the group halfway through my grad school tenure. You always encourage me and challenged me to do better, even if it involved making significant changes to publication drafts and data analysis. Your wisdom and guidance was always appreciated, and I am a better researcher for it. I could always count of swinging by your office for whenever I needed to ask you a question, show you research data, or discuss a publication. You always gave me the flexibility to follow whatever crazy research idea I had, and encouraged and supported my decision to conduct research in Spain. I'll always remember my time being a TA for your class was one of my favorite experiences in graduate school.

To **Dr. Cate Brinson**, my primary adviser for my first 2.5 years of graduate school. You are incredibly intelligent and hard working, and I admire your successes in every area of academia. You encouraged me to work and learn independently, and gave excellent feedback in terms of writing papers, proposal, and research. Without your help, I don't think I would have received the NDSEG fellowship! Even after moving to Duke, you still remained involved in my work and progress, and I always appreciated your advice and discussions on the new work I was doing. I am grateful of the opportunity I had to work with you.

To **Dr. Wes Burghardt,** thank you for being a member of my thesis committee, and giving me excellent feedback and advice. Your class was my favorite that I took at Northwestern.

To **Dr. Christopher Soles**, thank you agreeing to join my committee on (relatively) short notice! Our collaboration in ChiMad was very beneficial to this work.

To **Dr. Ignacio Martin-Gullon**, I greatly appreciated the opportunity to spend three months in Alicante working with your group. I learned so much about research in Europe, Spain. I hope that this is just a beginning of future collaborations between UA and Northwestern.

To **David Collinson**, thanks for being a great friend, office mate, and colleague. I admire your diligence and intelligence, and I learned so much from working with you on our first couple papers and first few years in grad school. I look forward to seeing what you accomplish!

To **Dr. Qifeng Wang**, thank you for helping me learn QCM! I was always inspired by your work ethic

and intelligence.

To **Dr. Pavan Kolluru**, I owe most of my knowledge of AFM and MATLAB from working with you, and definitely learned a lot about the publication writing process from you. Thanks for the guidance in my first 2 years of graduate school.

To **Dr. Patricia Mabrouk**, my senior research adviser from Northeastern University, thank you for encouraging me to apply and attend graduate school in the first place!

I appreciate the great user facilities here at Northwestern: the NUANCE, the EPIC and the MatCI facility and all the experienced specialists involved. Especially, I would like to thank **Dr. Carla Shute** in MatCI facility and **Dr. Gajendra Shekhawat** in SPID facility for sharing their respective expertise and their tireless support. I would also like to thank **Dr. Eric Roth** from the BioCryo facility for his support and knowledge of ultra-cryomicrotomy.

To **Keith Jones** and **Ryan Fuierer**, and the rest of the Asylum/Oxford Instrument team. I learn a lot from my time in NC learning about Asylum AFM from you guys! Additionally thanks to **Roger Proksch** for taking time to discuss AFM indentation technique and Fast Force Mapping compatibility.

To **Dr. David Delgado** and **Dr. Kazi Sadman** who made office life in the Shull Group a blast.

To former members of the Shull Group, **Dr. Shawn Chen, Dr. Yaoyao Chen,** and **Dr. Ha-Kyung Kwon**, as well as members of the Brinson group: **Dr. Xiaolin Li, Dr. Richard Zhao, Dr. Min Zhang (2x), Dr. Partha Paul, and Dr. Anqi Hu**, it was a pleasure getting to work with and learn from all of you.

To current members Shull group, present: **Qihua Chen, Gwen DePolo, Anthony Silvaroli, Yuling Chen, and Tom Schmitt**, it was awesome working with you guys as well and getting to know you. Good luck with the rest of your PhD programs! (And thanks, Qihua for taking care of Monty every once in a while!)

To **Ruiqi Xiao**, I had a blast working and mentoring you. I am very proud on how fast you were able to learn all the epoxy synthesis and characterization procedures. Looking forward to where you take the project!

To **Ryan Tris**, I appreciate your help on the epoxy project during your REU program here at Northwestern. Your work was very helpful in ironing out the kinks in the synthetic and characterization techniques at the beginning of the project. Additionally you work on 3D modeling and printing was very helpful for the future of the project!

To **Matthias Agne**, who I could always count on to hang out when bored, to come over for a beer (or

two... or three), to talk, hang out, watch Hot Ones, or whatever. Most of the best memories I've had over the past few years were spent hanging out with you. Whether we were in Chicago, Pamplona, or Alicante, you always know how to have a good time, and to light up the room around you (even if you sometimes dance a little too aggressively!!). Looking forward to the work you do in Germany, and I know you will visit us in Spain!

To the "Taddifers," a.k.a. **Thaddeus Reese** and **Jennifer DiStefano,** with whom the last couple years Edurne and I developed a great friendship. Whether we were solving mystery cases, eating brunch in our front yard, or just hanging out drinking "Sex On The Beach" cocktails, we would always have a great time. And thanks for always being super excited to look after Franklin!!!

To all the other friends I made at Northwestern over the past 5 years, including but not limited to **Drew Wolek, Jann Grovogui, Megan Hill, Kazuki Imasato, Alex Lupo, Nate Bradshaw, Nate Coocher, Alli DiCorato, Ridvan Kahraman, David Lam, Chris Mizzi, Shane Patel, Rohit Ramanathan, Max Wood, Max Dylla, Nando Reyes, Cesar Villa, James Male, Jaye Harada**, and everyone else who made time here at Northwestern more than just about work and research, but also about enjoying life and having fun!

To **Daniel Domene-López**, **José Javier Delgado-Marin**, and **Dra. Mercedes García-Montalbán**. I could not imagine a better group of people to work with when I was in Alicante. You all welcomed me into the group with open arms, and I always looked forward to coming to the office. I learned so much from my time there, and I hope we see each other again soon!

To my parents, **David and Jeannine Eaton**, for their unconditional love and support throughout my life, education, and career. I would not be where I am today without them.

And last, but certainly not least, to my loving, amazing, beautiful, fantastic, and wonderful wife and life partner, **Edurne Vega Ezquieta**. You are my rock, my support, and my solid foundation. In these crazy 5 years of graduate school, you were the one thing I could count on to always be there. When I had writers block, you inspired me. When my experiments wouldn't work, you would cheer me up. When I got discouraged, you would always encourage me. You put up with me and supported me, and I am the luckiest man on earth to have you in my life. I am so excited for what our future holds. I love you. Siempre y para siempre.

I would like to acknowledge support from the the Department of Defense (DoD) through the National Defense Science and Engineering Graduate (NDSEG) program, as well as support from the Richter Trust Funds.

Additionally, I would like to acknowledge support from **Dr. Craig Burkhart, Dr. Brian Korth,** and Goodyear Tire Company for their financial and technical support for the rubber composite project (PO#4510883960). Additional funding for the rubber composite projects was supported from NIST (70NANB14H012), NSF (BCS-1734981), and AFOSR (FA9550-18-1-0381).

Epoxy and Thermoplastic starch work was supported by the National Science Foundation (NSF) (No. DMR-1710491) and by Financial Assistance Award No. 70NANB19H005 from the U.S. Department of Commerce, National Institute of Standards and Technology as part of the Center for Hierarchical Materials Design (CHiMaD).

Additionally, the work made use of the MatCI Facility which receives support from the MRSEC Program (NSF DMR-1121262) of the Materials Research Center at Northwestern University. Also, this work made use of the IMSERC at Northwestern University, which has received support from the Soft and Hybrid Nanotechnology Experimental (SHyNE) Resource (NSF NNCI-1542205); the State of Illinois and the International Institute for Nanotechnology (IIN).

This work was performed, in part, at the Duke University Shared Materials Instrumentation Facility (SMIF), a member of the North Carolina Research Triangle Nanotechnology Network (RTNN), which is supported by the National Science Foundation (Grant ECCS-1542015) as part of the National Nanotechnology Coordinated Infrastructure (NNCI).

Table of Contents

List of Figures

List of Tables

Chapter 1

Introduction

Polymer systems have become widespread throughout all engineering fields due to their lightweight, design flexibility, diversity, and ease of processing [11]. Applications of polymers have been limited due to their relatively low mechanical strength compared to metals and ceramics, but the development of polymer composites, where the polymer material is strengthened by adding reinforcing materials such as fibers or particles, has further expanded the use of polymers for more high performance applications [12]. However, the design and development of new polymer composite materials is no easy task, as there are many different fabrication variables that can effect a polymer's properties. Additionally, a polymer's mechanical properties is highly dependent on its environment, such as temperature, humidity, and timescale/testing rate, and can vary by orders of magnitude depending on testing condition. Thus, each fabrication/processing variable must be testing under all possible conditions before use, which can be a time - and money- consuming process.

The chart in figure 1.1 demonstrates the complexity that goes into designing a polymer composite system for a specific application and displays the interconnection between the processing and structure and properties of the system. Computational models of polymers and polymer composites have been developed to help improve materials design and optimization. However, computational models are only as good as the understanding of the physics and chemistry of polymers at all length-scales, and the multi-length scale complexity of polymers and polymer composites can make their bulk properties very difficult to predict, as sometimes interactions between polymers and added materials result in properties distinct from their constituents [13]. To improve these models, experimental methods that try to understand the local behavior of multi-phase polymers as it relates to the bulk material, improve the efficiency of polymer mechanical property testing, and model a wide range of polymer formulations, need to be developed.

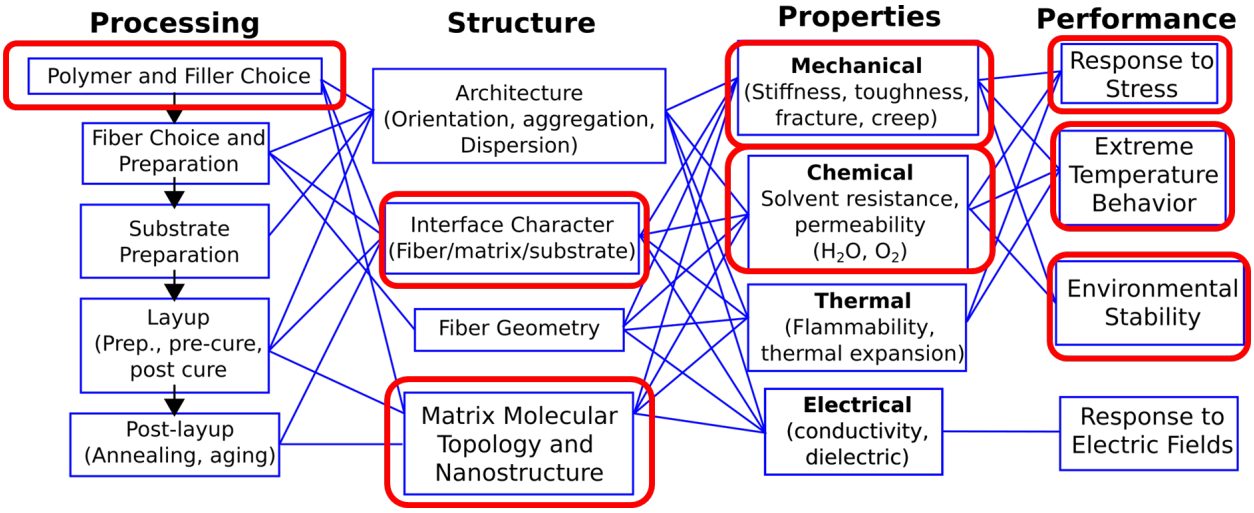

Figure 1.1: Design chart demonstrating the complexity and interconnectivity of parameters and flow in polymer composite design. The red boxes are the focus of this dissertation.

Thus, the goal of this thesis is to develop such experimental methods to contribute to the understanding of what affects the mechanical properties of several specific polymer materials in hopes to improve the design of similar polymer composite systems in the future. Of the design chart of a polymer composite (fig 1.1), only the red boxes are the focus of this dissertation, focusing mainly on the characterization polymers to be used in the matrix of a composite (chapters 3, 5, 6, 7), but there will be some discussion of the poylmer fiber/filler interactions (chapter 4, and briefly in chapter 3), and the incorporation of these results in the overall design of potential polymer composites will be the topic of the future direction of the projects (chapter 8). Three types of polymer systems will be explored in more detail: crosslinked rubbers and rubber nanocomposites (chapters 3-4), epoxies with nanoscale heterogeneity (chapters 5-6), and thermoplastic starch (chapter 7). Although each material-system investigated had unique motivations and goals, each explored at least two out of the three major over-arching themes of this dissertation:

1. Mechanical characterization technique development. The development of new or adapted experimental methods improve the resolution (chapter 3) or efficiency (Chapters 5, 6, 7) of the mechanical properties of the polymer materials in hopes to improve materials design for the applications of interest.

2. Understanding the structure-property relationships, and by extension, the link between bulk and local mechanical properties. This is an essential theme in material science and materials design, as is discussed in all chapters

3. Bridging the gap between experiments and computational simulations. As mentioned, computational

models are only as good as the understanding of the polymer physics, which is verified through experimentation (chapters 3, 5). At the same time, simulations can be used to help better understand experimental results (chapter 4). This dissertation is more experimental focused, but future direction of much of the work will be in applying what is learned from experiments to computational models (chapter 8), so the experiments are designed with this in mind.

Chapter 2 provides background information on the relevant physics and properties of polymers in general, such as the molecular basis for viscoelasticity. Additionally, important bulk and local mechanical characterization techniques that will be applied and modified in the subsequent chapters, such as dynamic mechanical analysis (DMA), instrumented indentation, and atomic force microscopy (and relevant contact mechanical models), will be discussion. These topics are necessary to lay the foundation of the novel research this thesis is based on.

Chapter 3 will describe the development of a novel and fast AFM dynamic indentation technique used to measure the local viscoelastic properties of rubber, rubber blends, and rubber composites. The results of this technique compare well with bulk DMA data and, for the multi-phase systems such as crosslinked rubber blends carbon black-rubber composites, expected local phase morphology, and shows great potential for better understanding the time and temperature dependence of these local properties. This chapter reproduces work from "AFM-based Dynamic Scanning Indentation (DSI) Method for Fast, High-resolution Spatial Mapping of Local Viscoelastic Properties in Soft Materials" published in *Macromolecules* in 2018 [4]. This work was published by myself with co-authors Dr. Pavan V. Kolluru, David W. Collinson, Dr. Xu Cheng, Dr. David E. Delgado, Dr. Kenneth R. Shull, and Dr. L. Catherine Brinson.

In chapter 4, finite element analysis is utilized to help understand possible indentation artifacts that result from the indentation of an indenter tip into a polymer matrix near a rigid substrate to simulate an AFM experiment of a rubber composite. Stress fields generated by the tip indenting near a hard surface can potentially overestimate modulus measurements near the interface. So, using the results of these simulations, actual AFM experiments of rubber composites will be further analyzed to see if this stress-field interaction effect can be deconvoluted. This chapter reproduces work from "Deconvolution of Stress Interaction Effects from Atomic Force Spectroscopy Data across Polymer−Particle Interfaces" published in *Macromolecules* in 2019 [14] published by myself with co-authors David W. Collinson, Dr. Kenneth R. Shull, and Dr. L. Catherine Brinson.

Chapters 5 and 6 explore the temperature dependent fracture and mechanical properties of a model-epoxy system whose properties are controlled by changing the chemistry of the system. One set of formulations

results in nano-scale heterogeneity in the system the leads to interesting rheological behavior. In chapter 5, the fracture toughness, fracture mechanisms, hardness, and shape memory behavior as a function of temperature of these epoxies are explored to see how this nano-scale heterogeneity affects the fracture behavior compared to similar systems without this heterogeneity. Special attention is paid to low temperature behavior (approaching -100°C), as the possibility of these epoxies for low temperature applications are of interest. This chapter reproduces work to be published in "Temperature Dependent Fracture Behavior in Model Epoxy Networks with Nanoscale Heterogeneity," submitted to *Polymer* in 2020 by myself with co-authors Dr. Kenneth R. Shull, and Dr. L. Catherine Brinson.

Chapter 6 explores the use of interpenetrating polymer networks as a means of strengthening the same epoxy systems from Chapter 5, and explores how the introduction of a second glassy polymer in the epoxy matrix affects the sample low temperature properties.

Chapter 7 presents an investigation into the use of the quartz crystal microbalance (QCM) to measure the high frequency viscoelastic mechanical properties and the absorption of water of a thermoplastic starch (TPS) systems in response to humidity. It will compare the responses of TPS made with two different plasticizers: glycerol and an ionic liquid, and the molecular basis for these differences will be discussed. Additionally, QCM will be shown to be an efficient tool to evaluate TPS films over traditional mechanical testing methods. This chapter reproduces work to be published in "Exploring the Eect of Humidity on Thermoplastic Starch Films using the Quartz Crystal Microbalance" submitted to *Carbohydrate Polymers* in 2020 by myself with co-authors Daniel Domene-López, Dr. Qifeng Wang, Dr. Mercedes G. Montalbán, Dr. Ignacio Martin-Gullon, and Dr. Kenneth R. Shull.

Finally, chapter 8 will summarize this dissertation and discuss the outlook and the future directions that can be explored to continue each project as a result of the work presented.

Chapter 2

Background: Mechanical Characterization of Polymers

2.1 Viscoelasticity in Polymers

2.1.1 Polymer Dynamics and Dynamic Mechanical Analysis

A polymer is by definition a large organic macromolecule that consists of long chains of repeated covalently bonded molecular units known as monomers. The long chains are highly disordered, resulting in a mostly amorphous structure amorphous. Some polymers, thermoplastics, consist of loosely bound network of many chains, seen in figure 2.1a, where a single polymer chain (in red) interacts with other polymer chains, bonded my mostly weak inter-polymer network interactions, such as hydrogen bonding [15], electrostatic interactions [16], or physical chain entanglements [17], that will flow when heated. Other polymers, thermosets can be crosslinked, where different polymer chains are covalently bonded leads to networks that cannot flow or melt (2.1b). The shape and chemical make of of polymer chains and the interactions with other chains leads to hierarchical structures, (2.1c) that can lead to some semi-crystalline regions within the amorphous networks [18]. As a result, the mechanical response of polymers is directly related to the ease of motion of the polymer chains, that is related to the interactions and strength of the bonds between them [19].

The molecular motions of polymers are dissipation mechanisms, meaning they can relieve applied stress or strain if given enough time to relax, resulting in a time-dependent mechanical response. Thus, the mechanical response to mechanical stress or applied strain is highly sensitive to both the temperature, which increases

molecular motions, and consequently, the timescale of applied mechanical stimulus. The molecular motions of polymers are dissipative mechanisms, meaning they can relieve applied stress or strain, resulting in a time-dependent mechanical response [19]. Figure 2.1d plots the frequency dependent modulus, or complex modulus, E^*, of a viscoelastic polymer as a function of both temperature, and frequency. Sharp drops in modulus correspond to the relaxation modes of different molecular motions of the polymer, with the shorter motions occurring at high frequency/low temperature, and larger motions at low frequency/high temperature. The most characteristic molecular motion is the α-transition, or the glass transition (T_g), relates to the largest scale molecular motion, and corresponds to largest drop in modulus, where below the polymer is in the glassy state, where it is rigid and relatively brittle, and above , it is in the "rubbery" state, where the material is softer and more compliant [19].

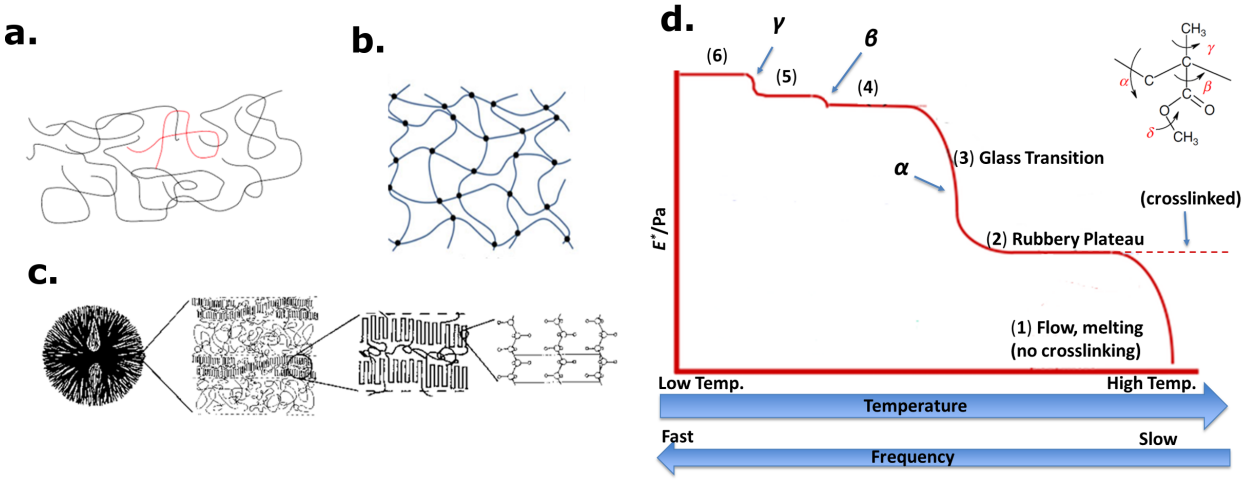

Figure 2.1: (a) Schematic an amorphous polymer. A single polymer chain is highlighted in red, and interacts with adjacent polymer chains. (**b**) Schematic of a crosslinked polymer network. (**c**) Schematic showing the hierarchical ordered structures that are present in polymer networks that result in multiple mechanical relaxation mechanisms at different length scales. Images adapted from Shull & Emery [1]. (**d**) Example of the complex modulus of a polymer as a function of both temperature and frequency, with transitions indicated in the plot of result of molecular motions of example polymer in top right corner. Adapted from PerkinElmer, Inc. [2].

The complex modulus, E^*, of a bulk polymer it typically measured through a technique called dynamic mechanical analysis (DMA). An oscillatory sinusoidal strain, $\varepsilon(t)$, is applied to a pre-strained rectangular tensile with a strain amplitude, ε_0, around at a set frequency, ω, via eq. 2.1. Due to the molecular motions, there is a phase lag, ϕ, between the applied strain wave and the stress response. As a result, the measured stress in eq. 2.2 is a superposition of a sine wave in phase with the applied strain, and a sine wave completely out of phase with the strain.

$$\varepsilon(\omega, t) = \varepsilon_0 \sin(\omega t) \tag{2.1}$$

$$\sigma(\omega, t) = \sigma_0 \sin(\omega t + \phi) = \sigma_0 \cos(\phi) \sin(\omega t) + \sigma_0 \sin(\phi) \cos(\omega t) \tag{2.2}$$

Thus, the the in-phase component of stress-strain ratio is the storage modulus, E', which is related to the elastic response of the material, where as the out-of phase component is the loss modulus, E'', which is related to the viscous response of the material, and therefore the molecular motions of the polymer that can dissipate stress. Together, they are the real and imaginary parts of the complex modulus, E^*, whose magnitude is the ratio of the stress to strain amplitudes (eq. 2.4). Additionally, the ratio of E'' to E' is related to the phase angle per 2.5

$$E' = \frac{\sigma_0}{\varepsilon_0} \cos(\phi), \; E'' = \frac{\sigma_0}{\varepsilon_0} \sin(\phi) \tag{2.3}$$

$$E^* = E' + iE'', \; |E^*| = \frac{\sigma_0}{\varepsilon_0} \tag{2.4}$$

$$\frac{E''}{E'} = \tan \phi \tag{2.5}$$

As mentioned, the complex modulus and viscoelastic phase angle, dependent on both temperature and the frequency of the test. Thus, to understand the full behavior of a polymer, it must be conducted at multiple frequencies, known as a frequency experiment [20]. Figure 2.2a shows the typical stress and strain data of a frequency sweep DMA experiment. However, most DMA instruments are limited in the range of frequencies they can probe, typically 0.1 - 10 Hz. So, typically the frequency sweep experiments are coupled with experiments done at different temperatures as well, where a much broader range of temperatures can typically be tested on these DMA instruments. Figures 2.2b and c show the results of the complex modulus vs. frequency conducted at different temperatures and the complex modulus vs. temperature at different frequencies for a sample of styrene-butadiene rubber (SBR), respectively. The frequency sweep experiments show that the slope of each frequency sweep changes slightly with each increase in temperature. If the frequency sweep data is shifted along the frequency axis (x-axis) to overlap with the slope of the data of the adjacent temperature, a master curve can be reconstructed of the viscoelastic properties (2.2d). This

is master curve construction is the result of the principle of time-temperature superposition (TTS), which dictates the temperature dependence of a polymer's mechanical properties is directly related to the frequency dependence of the property [20]. According to the TTS principle, the frequency (ω_T) at a temperature T is related to the reference frequency ω_{T_r} at the reference temperature (T_r) by the temperature dependence shift factor, a_T, per the relation in eq. 2.6.

$$\omega_{T_r} = a_T \omega_T \tag{2.6}$$

This master curve allows the prediction of mechanical properties well above or below the testing frequencies of the DMA experiment at the T_r [20, 21]. For the SBR material, the master curve of $|E^*|$ and ϕ at $T_r = -20°\text{C}$ are shown in 2.2d, but the mastercurve for any T_r can be constructed by dividing all shifted frequencies by the shift factor at the desired reference temperature. However, the development of experimental viscoelastic master curves works best when there is an appreciable gradient in the viscoelastic properties of the frequency sweep data segments obtained from any two successive temperatures. As we approach the rubbery or glassy regimes (e.g., for SBR in Figure 2.2, this is above 15± 5 °C or below -45 °C, respectively), the gradient in frequency sweep data for $|E^*|$ at each temperature decreases, leading to a reduction in the accuracy of the empirical shift factors and in turn, the master curves in these two regimes, as compared to the transition regime. Theoretically, shift factors in the transition regime and above should follow the Vogel-Fulcher-Tamman relation, given by eq. 2.7, where B and T_∞ are fitting parameters, which is derived from modeling the macroscopic motion of the bulk polymer [22, 23]. As can be seen by the plot of the shift factors in 2.2e, the empirical shift factors deviate from the VFT fit at high temperatures (which in this case are ambient temperatures), and so constructing a master curve at such temperatures would have more error in it. Thus, the use of higher rate viscoelastic measurement techniques have been explored to couple with DMA to better predict high frequency behavior [4, 24]. Once such method developed using an atomic force microscopy dynamic indentation technique is the topic of chapter 3.

$$\log(a_T) = \frac{B}{(T - T_\infty)} - \frac{B}{(T_r - T_\infty)} \tag{2.7}$$

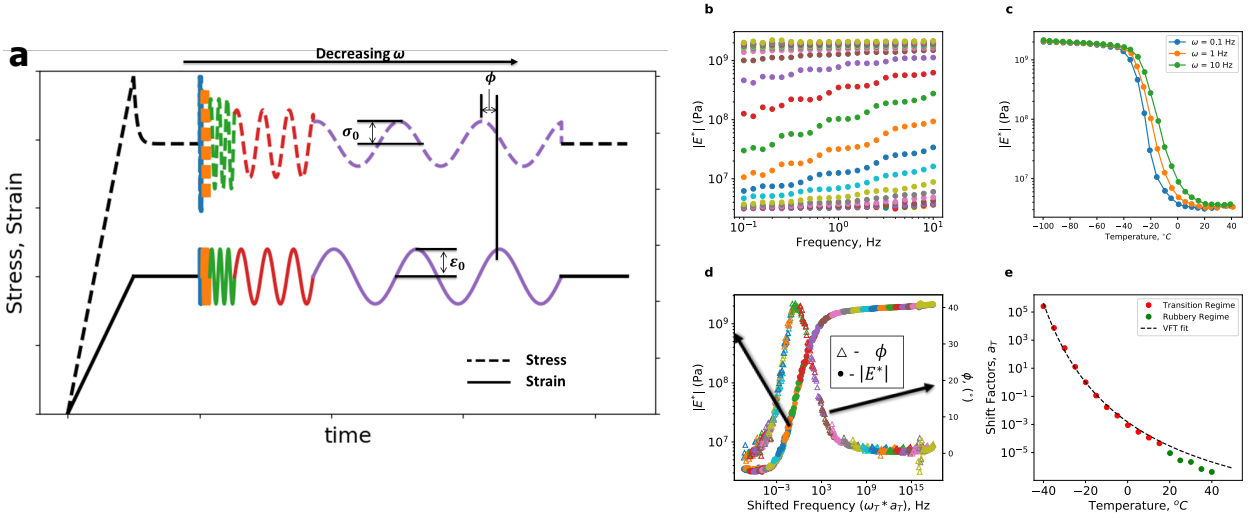

Figure 2.2: (a**).** Example plot of stress, σ, and strain, ε, vs. time for a theoretical DMA experiment in a viscoelastic material. In tension, a rectangular tensile sample is pulled to a set strain, allowed to relax, and then oscillated with an applied strain amplitude, ε_0 at set frequency, ω, and the resulting stress, σ is measured to calculate viscoelastic properties according to eqs. 2.3-2.5 [3]. (**b**) $|E^*|$ plot from DMA frequency sweep from 0.1 - 10Hz of a sample of styrene-butadiene rubber (SBR) conducted at different temperatures (each color is a different temperature, -120 to 40°C). (**c**) Same DMA data, but plotting $|E^*|$ vs. temperature for 3 different frequencies. (**d**) DMA mastercurve formed from same DMA frequency sweep data of SBR, with a reference temperature of -20°C. (**e**) Plot of shift-factors used to shift the frequencies of each temperature to form mastercurve in (**d**), with transition regime fit to VFT equation. [4].

As discussed, the changes in the frequency dependent modulus with time or temperature depend on the molecular motions of the polymer. Thus, any changes to the polymer network that facilitate (i.e. plasticizers) or inhibit (i.e. rigid fillers) the molecular motions of a polymer will change the frequency and temperature dependence of their viscoelastic mechanical properties. However, the addition of other materials to a polymer matrix tends to violate the assumptions needed for TTS and master curve construction, namely that the material is homogeneous, isotropic, amorphous, and the viscoelastic response is linear [20, 21]. As such, the ability to measure local viscoelastic mechanical properties at the lengthscales of these additives and phases or model the changes in properties in regards to the addition of secondary phases, fillers, or plasticizers is essential in the materials design of polymers and polymer composites.

2.1.2 Indentation of Viscoelastic Materials

The length-scale of the mechanisms that affect the mechanical behavior of polymer composites and polymer thin films is often on the microscale, and more recently, the nanoscale [25]. The use of techniques that

can probe at these lengths scales and accurately quantify mechanical properties are of great interest. Instrumented indentation, as its name suggests, indents a sharp tip into the surface of material that can be carefully controlled via force or displacement that can be measured continuously and simultaneously over the entire indentation cycle [26]. The resulting force-displacement curve provides a lot of information about the mechanical behavior of the material, such as hardness, elastic moduli, and plastic deformation. Force control from nN-mN and tip radii that can range from nm to mm means that a wide variety of materials can be characterized at many different length scales, from hard materials like ceramics to soft materials like polymers. Early work began in the 1970's from the research of Bulychev, Alekhin, Shorshorov, who determined that the Young's modulus of a material can be determined from the slope of a force vs. displacement indentation curve as seen in eq. 2.8 [27].

$$S = \frac{dP}{d\delta} = \frac{2}{\sqrt{\pi}} E_r \sqrt{A} \tag{2.8}$$

Where the slope of the curve is the material stiffness, S, and A is the tip-sample contact area, and E_r is the reduced modulus, defined as eq. 2.9. An example force-displacement curve of an indentation experiment in a glassy polymer is shown in figure 2.3a.

$$\frac{1}{E_r} = \frac{1 - \upsilon_s^2}{E_s} + \frac{1 - \upsilon_i^2}{E_i} \tag{2.9}$$

Where E_s and υ_s are the Young's modulus and Poisson's ratio of the sample, an E_i and υ_i are that of the indenter. Since, typically, $E_i >> E_s$, the second term can typically be ignored.

Additionally the hardness, H, of a material can be calculated from eq. 2.10. The hardness is a measure of localized deformation of a material, and is a superposition of both reversible elastic and irreversible plastic deformation. However, polymer materials tend to creep when held at a constant force, as can be seen by the displacement change at P_{max} in the example curve in figure 2.3a [28]. And so, the contact area increases with increasing hold time. Thus, the hold time must be reported when indicating hardness in polymer systems, and it must be held constant when comparing hardness data [29, 30].

$$H = \frac{P_{max}}{A} \tag{2.10}$$

Initially, the use of indentation techniques to characterize the mechanical properties of materials was revolutionized by Oliver & Pharr in their landmark 1992 article establishing a technique to accurately

quantify the elastic modulus from a nonlinear indentation curve [26]. In nanoindentation, the indenter has a well-defined pyramidal-shaped tip, such as a Berkovich (3-sided pyramid) or Vicker's indenter (4-sided pyramid). These indenters have a well defined area function, that are given by eq. 2.11, where h_c is the contact depth, shown by the schematic in fig. 2.3c, which due to the elastic deformation if the surface, is slightly less than the maximum indentation depth, h_{max}. Oliver-Pharr showed that the contact depth can be measured from the h_{max} and S via eq. 2.12, where ε is a tip geometric constant, $\varepsilon = 0.75$ for pyramid indenters. Additionally, the area of the indent using a Vicker's type indenter (which is used in chapters 5 & 6), can also be measured by optically measuring the diagonal of the residual imprint per eq. 2.13, as seen in the schematic in fig 2.3b. However, the viscoelastic nature of polymer results in a significant amount of indentation recovery of the indent, resulting in a decrease in the residual indentation depth, h_f (see fig 2.3c) , after the indenter is removed [31]. However, research has shown that the viscoelastic recovery of the indentation of polymers is concentrated in the walls of the indent bowing inward, described as a "pin-cushion" effect [32]. Thus, for Vicker's indentation of glassy polymers, recovery on the diagonals of the indent is negligible, so the hardness measurement from measuring the diagonal lengths remains fixed even as the indent recovers [30].

$$A = 26.43 h_c^2 \tag{2.11}$$

$$h_c = h_{max} - \varepsilon \frac{P_{max}}{S} \tag{2.12}$$

$$A_V = \frac{d^2}{1.8544} \tag{2.13}$$

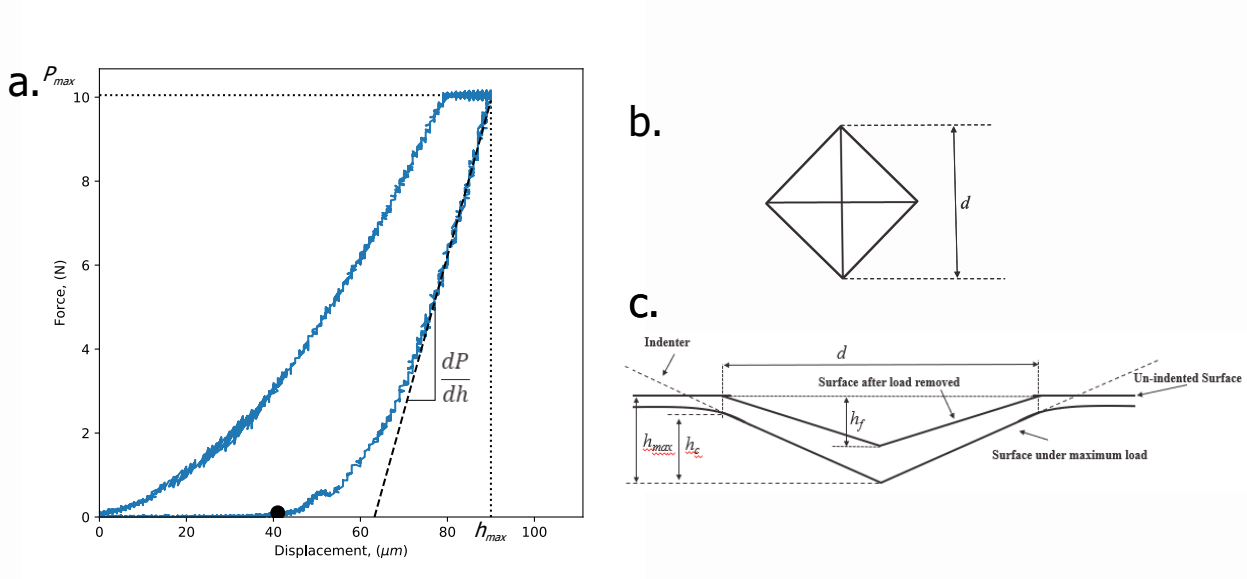

Figure 2.3: (**a**). Example force-displacement curve in an instrumented indentation experiment on an epoxy material (D400-100, see chapter 5) using a Vicker's tip. (b) Top-view Schematic of indent left behind by Vicker's indenter with diagonal, *d,* used to calculate the contact area. (**c**) Side-view schematic of Vicker's indentation experiment (adapted from [5]).

However the elastic indentation experiments of modulus and hardness are typically done with glassy polymers well below the T_g that have a very low phase angle ($< 5°$). As the T_g is approached, the speed at which an indenter pushes into a material can greatly affect the measured mechanical properties, and so dynamic indentation techniques have been developed to more accurately describe their time-dependent response [3, 33, 34]. One of the ways to do this with a nanoindenter is a technique called nano-dynamic mechanical analysis (nano-DMA). The tip is indented to a specified displacement, and then, after time given for the material to relax, to a displacement oscillation with amplitude δ_0 at a specified frequency, ω, is applied, and the resulting force response, with amplitude P_0 is recorded. This is analogous to the bulk tensile DMA experiments described in the previous section, and the resulting data collected is follows the same shape as the stress-strain data shown in 2.2a, except force and displacement are measured instead [34]. In this case, the complex modulus becomes the reduced complex modulus $|E_r^*|$, and is calculated via 2.14, and derived from eq. 2.8, where for an oscillatory indent, $S = \frac{P_0}{\delta_0}$. The viscoelastic phase angle, ϕ, is calculated similarly as in bulk tensile DMA by the phase lag, and the relations of reduced storage and loss modulus of eqns. 2.3, 2.4, and 2.5 still apply [33, 34].

$$|E_r^*| = \frac{P_0\sqrt{\pi}}{2\delta_0\sqrt{A}} \tag{2.14}$$

However, these derivations require the assumption that the contact radius remains constant, which can be true for a flat-punch indenters, but not for other tip geometries whose contact area is depth dependent [35, 36]. Although, possible ways to get around this are small oscillations (small δ_0), indenting the tip while oscillating (known as the continuous stiffness measurement (CSM)) [37], or if the material has strong adhesion to the tip [36, 37], which will be discussed in chapter 3.

2.2 Atomic Force Microscopy

Another technique to probe the mechanical properties at small length scales is Atomic force microscopy (AFM). AFM probes samples at the nanoscale using the deflection of cantilevers with tips with radii on the size of nanometers to tens of nanometers. AFM is very versatile, having many different modes of operation for different applications, such as topography, phase contrast, electrical properties, and, of course, mechanical properties [38]. Techniques that monitor the force on the cantilever and the corresponding indentation into the sample, to collect a force-displacement indentation curves (FDC) are called scanning force spectroscopy (SFS) methods. By monitoring the deflection of the cantilever properly calibrating its stiffness, FDCs can be collected from which material properties can be calculated, similarly to that of nanoindentation curves [6]. This section explores the fundamentals of AFM force spectroscopy and how to accurately measure the mechanical properties from the AFM force-displacement curves. For the majority of this AFM work conducted for this thesis, a Bruker Dimension Icon AFM was used, and will be referred to the most, although some work was done with the Asylum Cypher-ES AFM from Oxford Instruments.

2.2.1 Fundamentals of AFM Force Spectroscopy

Atomic Force Microscopy (AFM) is a technique to characterize the surface of a material through the interactions between a cantilever probe and the material surface. The cantilever is attached to a piezo, whose vertical motion, δ_p, can be controlled and monitored by the AFM [38]. When the tip meets the surface, the cantilever deflects a distance,δ_c . By monitoring this cantilever deflection with a laser reflected off the back of the cantilever, the applied force on the surface of the material, P, can be measured [39]. Figure 2.4a shows a schematic of AFM tip indenting into a sample. Most AFM's only directly measure two parameters, the voltage applied to the piezo, V_p, and signal from the laser reflected from the cantilever, V_c. To measure the mechanical properties, namely the material modulus, as shown in eq. 2.8, force, P, and displacement into the sample, δ_s, must be determined from V_c and V_p. The displacement of the piezo is calculated by

multiplying the voltage by the piezoelectric charge coefficient of the piezo, which is typically calibrated by the manufacturer. Although the piezo may need to be recalibrated once a year due to piezoelectric drift, it is not necessary to conduct before each measurement and the piezo electric displacement, δ_p, is typically output by the AFM instrument with the raw data. As seen by the schematic in figure 2.4a, δ_p is distributed through the cantilever as the sum of δ_c and δ_s (eq. 2.15).

$$\delta_p = \delta_c + \delta_s \tag{2.15}$$

The cantilever deflection, as is mentioned previously is monitored by a laser reflected off the back the cantilever, which can either detect the voltage or the current through the detector (the Bruker Dimension Icon AFM measures the voltage), to determine δ_c from this signal, a calibration on a rigid sample, usually Sapphire must be conducted [40]. The sample must be rigid enough so that the tip does not indent into the sample, so $\delta_s = 0$, and ergo, $\delta_p = \delta_c$. With this, the inverse of the slope of the signal - displacement curve on the rigid sample gives the cantilver deflection sensitivty, S_{defl}, in units of nm/V. This will allow δ_c to be calculated for the indentation of any sample based on the product of V_c and V_c, as shown in eq. 2.16.

$$\delta_c = V_c S_{defl} \tag{2.16}$$

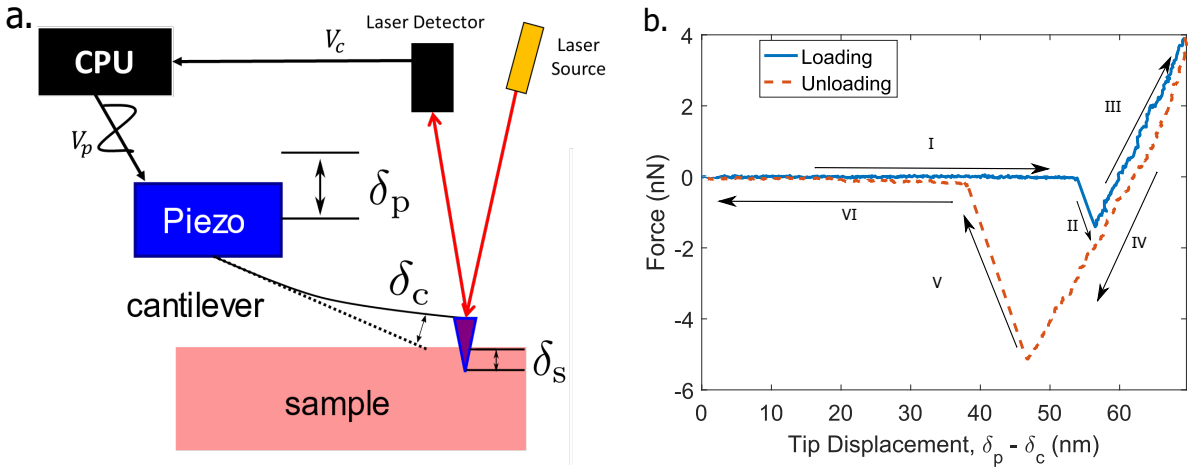

Figure 2.4: (**a**). Schematic of an AFM indentation during a SFS indentation. (**b**). Schematic of a force-displacement curve of an AFM indent in the matrix of a 10wt% carbon black styrene-butadiene rubber composite, showing the approach (I), the "pull-down" of the tip when it gets near the surface (II), the loading indent (III), the unloading (IV), the adhesive pull-off force needed to separate the tip from the surface (V), and the retraction of the tip from the sample (VI). Hysteresis due to viscoelasticity is also evident in the force-displacement curve.

Thus, with δ_c known, δ_s can be calculated by rearranging eq. 2.15 and subtracting δ_c from δ_p. For the rest of this thesis, sample indentation, δ_s, will simply be referred to as δ.

Finally, the applied force on the surface can be measured by eq. 2.17, by multiplying δ_c by the cantilever spring constant, k_c.

$$P = k_c \delta_c \tag{2.17}$$

Although a nominal cantilever stiffness is provided by the manufacturer, there is a third-power dependence of k_c on the cantilever thickness, t, as determined by Euler-Bernoulli beam theory in eq. 2.18, where E is cantilever material modulus, W is the width of the cantilever, and L is its length [41]. This makes the true k_c highly variable with each cantilever as the t is very small ($< 1\mu m$) and difficult to measure.

$$k_c = \frac{EWt^3}{4L^3} \tag{2.18}$$

So, k_c must be calibrated independently for each cantilevers. For cantilevers with a nominal spring constant of less than 6N/m, the spring constant can be found using a thermal tuning method available with the AFM software that fits a Gaussian curve to the cantilever response around its resonance frequency [40]. Unfortunately, thermal tuning methods are less accurate for stiffer tips due to the amount of noise that is produced around the resonance peak. Thus, the Sader method was used instead to calculate k_c for stiffer tips, given by eq. 2.19 [42].

$$k_c = 0.1906 \rho_f b^2 L Q_f \Gamma_i(\omega_f) \omega_f^2 \tag{2.19}$$

Where ρ_f is the density of the fluid (air in this case), b is the cantilever width, L is the cantilever length, ω_f is the resonance frequency of the cantilever, Q_f is the quality factor of the cantilver's oscillation at resonance, and $\Gamma_i(\omega_f)$ is the imaginary term of the hydrodynamic function evaluated at ω_f. L and b can be measured using optical microscopy, and Q_f and ω_f can be found by tuning the tip with the AFM software. The benefit of this method, is that it allows the calculation to be done without measuring the thickness, t. Additionally, the Bruker Dimension Icon holds the tip at a 12° angle from the sample, the spring constant from this calculation must be divided by $cos^2(12^o)$ [40, 42].

With the calibration of S_{defl} and k_c as described above, the $P - \delta$ curves can then be extracted from the AFM for further analysis. Figure 2.4b shows an example of a $P - \delta$ indenting into a polymer material

[6, 38]. The tip approaches the surface, not feeling any forces far away from the surface (I), then when the tip becomes close enough to the surface of the material to experience attractive molecular interaction, the tip will "pull down" to the surface of the material (II). Then, the tip will start to indent into the surface of the material for the duration of the loading cycle (III). After, the tip will start the unloading cycle (IV), but due to adhesion forces between the tip and the sample, require a much larger force to pull the tip out of the sample (V). The tip will then continue moving away from the surface without any additional forces acting on it (VI). Additionally, the time dependent nature of polymers can result in hysteresis, as shown by the separation between the loading and unloading curves. How to address adhesion and hysteresis in mechanical property analysis will be addressed in 2.2.3, as well as in **Chapters 3** and **4**, for specific applications of rubbers and rubber composites.

2.2.2 AFM Force-Spectroscopy Mapping Modes

The Bruker Dimension Icon has two main modes for the collection of force-curve maps. The first, and more established method is called Force Volume Mode, approaches the sample at a user defined linear ramp speed until a defined "trigger" force is reached. There are four main control parameters for this mode: number of samples, trigger threshold, ramp size, and ramp speed [39]. The number of samples defines the number of force curves in each scan line and number of lines that will be scanned. More samples gather more force-curves and is therefore higher resolution, but consequently more acquisition time is required for the whole scan. The trigger threshold determines the maximum force the tip will experience before reversing direction, which is directly related to the depth the tip indents into the material surface. The ramp size is the distance the tip will travel during the ramp, which must be large enough to overcome the adhesive forces from rubbery material to make sure the tip separates from the surface during the indent. Lastly, the ramp speed sets the time it takes for the tip to complete a loading/unloading cycle, which in Bruker's FASTForce Volume™ mode is between 0.1 and 300 Hz. However, higher speeds can create a lot of noise in the force-displacement curve, so it is important to choose a frequency that is fast enough to collect many force displacement curves in a reasonable time, but not so fast that the force curves are too noisy for accurate analysis. At 30 Hz, a 256×256 pixel force volume map can be taken in approximately 30 minutes.

Peak Force Quantitative Nanomechanical Mapping™ (PF-QNM™) is a SFS method developed by Veeco Instruments Inc. (now Bruker) that utilizes a peak force feedback mechanism. The cantilever oscillates at a specific frequency with a user-defined amplitude. After defining a peak force, the piezo will adjust itself so that it indents into the surface far enough to experience the defined peak force. Thus, adjusting the peak

force will adjust the penetration depth into the sample. The method has pico-Newton resolution, allowing the analysis of delicate soft samples and the reduction of tip wear. The defining feature of the method is that it uses a sinusoidal ramp rate instead of a linear ramp rate. The high frequency operation of 1-2kHz allows for thousands of force displacement curves to be recorded over a two-dimensional area in a matter of minutes as opposed to the hours required in linear ramp SPM. This allows for two-dimensional areas to be mapped much faster than ever before, drastically reducing the acquisition time of force-displacement curve collection. The software instantly processes the force-displacement curves allowing for mapping of a variety of properties, such as height, modulus, dissipation, adhesion, and deformation.

Additionally, this thesis also makes use of Asylum Cypher-ES and MFP-3D AFM's as well, which both have their own force volume, linear ramp rate mode, and a sinusoidal ramp rate mode (FastForceMapping), that work similarly with Bruker. There are two main differences between Bruker's PF-QNM and Asylum's FastForceMapping. First, the Ayslum instruments have a linear variable differential transformer (LVDT) attached to the piezo, and so it can more accurately measure the piezo displacement, δ_p, without the need for extra calibration. And second, PF-QNM can only operate at discrete frequencies (125, 250, 500, 1000, $2000Hz$), whereas FastForceMapping can operate at ANY frequency between 10 and 1000 Hz.

2.2.3 Contact Mechanics

2.2.3.1 Hertzian Contact Mechanicas

As discussed in **section 2.1.2**, modulus measurements from indentation experiments using equation 2.8 or 2.14 require knowledge of the tip-sample contact area, A. However, in atomic force microscopy, the given the nanometer length-scale size of the AFM tips, the tip-surface contact area is impossible to monitor directly through optical analysis. So, contact mechanical models must be used to determine this contact area, and some geometrical assumptions must be made [43]. The first is that the geometry of the tip can be estimated as a parabola, shown in figure 2.5. The AFM tip in the Scanning electron microscope (SEM) image in 2.5b is superimposed with a parabola (red), showing that this geometric approximation is acceptable. The contact mechanics of a parabolic indenter into a flat surface was first investigated by Heinrich Hertz in 1882 who derived it from the analytical solution of elasticity theory equations under half-space approximation [44, 45]. Hertz showed that the vertical elastic surface displacement, u_z, at a radial distance, r, from the tip of a

parabolic indenter that applies a load, P, is given by eq. 2.20.

$$u_z(r) = \frac{3P}{8E_r a^3}(2a^2 - r^2), r \leq a \tag{2.20}$$

where a is the circular area contact radius, as shown in, figure 2.5a. From this schematic, it can be seen that the total indent, δ, is separated into a contact region and a non-contact region. However, since the shape of the contact region is estimated to be a parabola with a radius of curvature R, this elastic displacement can also be defined geometrically as eq. 2.21.

$$u_z(r) = \delta - \frac{1}{2R}r^2, r \leq a \tag{2.21}$$

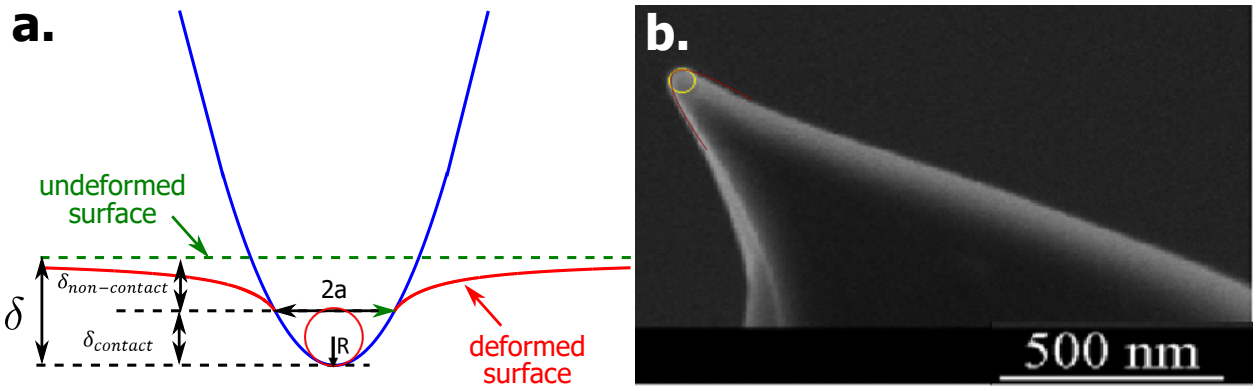

Figure 2.5: (a). Schematic of Hertzian contact mechanics of a parabolic-tip with tip radius of curvature R intenting a distance δ into the surface of a material with a contact radius a. (b). Scanning Electron Microscope (SEM) image of an Olympus OMCL-AC240TS-R3 silicon nitride tip A parabola (red) is superimposed over the

Setting equations 2.20 and 2.21 equal to each other at $r = 0$ yields the following relationship for δ in 2.22.

$$\delta = \frac{3P}{4E_r a} \tag{2.22}$$

The same two equations can then be set equal to each other at $r = a$, and using equation 2.22, the contact radius can be defined using eq. 2.23.

$$a_{hertz} = \sqrt{R\delta} \tag{2.23}$$

Therefore, a can be calculated using two measurable parameters. R can be measured by an SEM image

of the AFM tip and superimposing a parabola or circle on the end, as in figure 2.5b, or it can be estimated using the topology of a roughness sample (see Appendix: A.1), and δ is measured as described in 2.2.1. Substituting eq. 2.23 into 2.22 and solving for P yields eq. 2.24, the expected $P-\delta$ relationship of a parabolic indenter of radius R indenting into a surface of a materiel with modulus E_r. This equation is plotted in figure 2.6a. Differentiating this expression by δ yields the original equation for stiffness in eq. 2.8, where $A = \pi a^2 = \pi R\delta$.

$$P = \frac{4}{3} E_r R^{1/2} \delta^{3/2} \tag{2.24}$$

The Hertz equation can be fit to $P-\delta$ curves to determine modulus, provided there is minimal adhesion, which is can be fine for rigid materials at larger scale indentation and large tip radii ($>10^{-6}$m). However, AFM $P-\delta$ curves deal with very small loads and depths, and AFM tips are on the order of 10^{-9}m - 10^{-8}m [6]. Additionally, many polymers, especially soft and elastomeric polymers, typically show adhesion over even larger length scales, so attractive forces cannot be ignored [35, 46, 47]. This is manifested in AFM in the form of the "pull-down" in the loading curve (II), and the "pull-off" force in the unloading curve (V), as shown by the example AFM curve in figure 2.4b. So, the contact mechanics equations need to take this into account to improve quantitative accuracy.

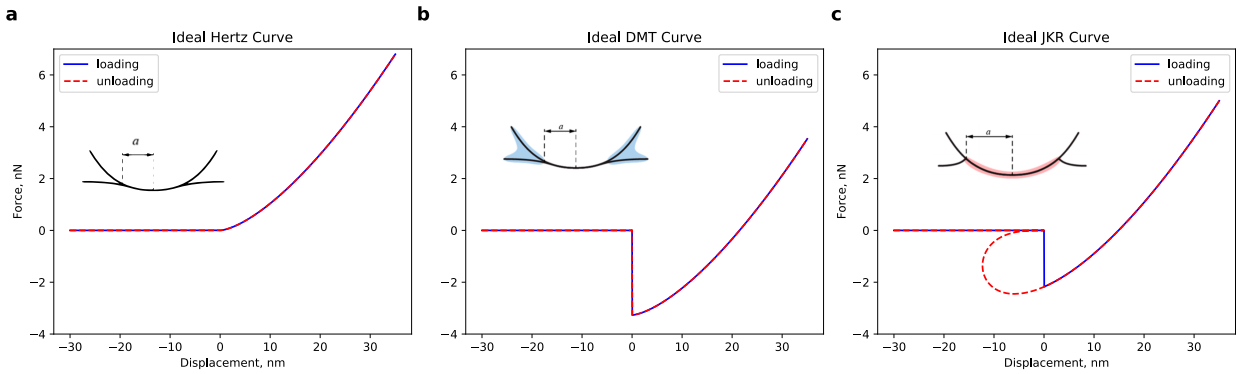

Figure 2.6: Theoretical $P-\delta$ curves as determined by (a) Hertz model using eq. 2.24, (b) DMT Model using eq. 2.25, and (c) JKR Model using eqs. 2.26 and 2.27. Each $P-\delta$ shows a schematic of the tip-sample contact region and adhesive forces assumed in the corresponding model, reproduced from Chyasnavichyus, *et al.* [6]. Each $P-\delta$ curve the parameters $E_r = 5.5$MPa, $R = 20$nm, and $\mathcal{G} = 2.6$mJ/m^{2}were used.

2.2.3.2 Adhesive Contact Mechanics

Adhesive contact is a complex subject that can manifest itself differently in different materials, but ultimately it is related the interactions between the two materials in contact as a result of van der Waals forces, hydrogen bonds, and ionic bonds [48]. The adhesion between two materials is typically quantified by the amount of energy needed to separate the materials in contact per unit area, known as the energy release rate, $\mathcal{G}$ (in units J/m^2), which is a geometry-independent property characteristic of the difference in surface energy of the two separated surfaces and the two materials in contact [49]. However, exactly how the energy release rate, $\mathcal{G}$, affects the $P-\delta$ curve in an indentation experiments depends on not just the magnitude of G, but also the geometry of contact , compliance of the surface, and length-scale of the adhesive interaction [50].

Different adhesive contact mechanical models have been developed to take into account tip-sample adhesive interactions, such as the Derjaguin-Muller-Toporov (DMT) [51], Johnson-Kendall-Roberts (JKR) [52], and Maugis-Dugdale (MD) [50]. For more rigid materials, where surface of the material is too stiff to deform due to adhesion and the adhesive forces are dominated by long range forces, the DMT model is typically used [51, 53]. The DMT model assumes no additional adhesive effect in the region of contact, but the adhesive interaction between the tip and the surface just outside the area of contact, as seen by the tip schematic in figure 2.6b. Since there is no change in surface deformation, the contact area is still described by eq. 2.23, however, the long range adhesive forces will apply a tensile force on the surface of the material that is felt even when $\delta = 0$, which will compete with the applied compressive force and change equation 2.24 into equation 2.25.

$$P = \frac{4}{3} E_r R^{1/2} \delta^{3/2} - 2\pi \mathcal{G} R \tag{2.25}$$

The DMT equation can therefore be thought of as just a vertical shift in the Hertz equation by $-2\pi\mathcal{G}R$, which can also be thought of as the DMT force of adhesion, $P_{adh} = 2\pi\mathcal{G}R$, or the maximum tensile force felt by the surface. This can be seen by the theoretical $P-\delta$ curve in figure 2.6b, as well as the plot of $a-P$ in 2.7a, which shows that the same trend in a vs. P for the DMT equation, just shifted by P_{adh}.

However, for softer, adhesive elastic materials, the contact is typically described by the Johnson-Kendall-Roberts (JKR) model [43, 52]. Unlike the DMT model, the JKR model takes into account surface deformation toward the tip due to the strength of adhesion in the contact region and compliance of the material surface, and is described by eqs. 2.26 and 2.27.

$$a_{JKR}^3 = \frac{3R}{4E_r}\left(P + 3\pi R\mathcal{G} + \sqrt{6\pi R\mathcal{G}P + (3\pi R\mathcal{G})^2}\right) \tag{2.26}$$

$$\delta = \frac{a_{JKR}^2}{R} - \sqrt{\frac{2\pi\mathcal{G}}{E_r}a_{JKR}} \tag{2.27}$$

The theoretical JKR $P-\delta$ curve is shown in figure 2.6c. The big difference here is that the tensile force continues to exist even $\delta < 0$, due to the tip pulling the surface with it during unloading. Additionally, the maximum tensile force during unloading is slightly lower than in the DMT, $P_{adh} = \frac{3\pi}{2}\mathcal{G}R$, since only the adhesive forces in the region of contact are taken into account. This surface warping due to adhesive forces leads to a much larger contact radius at similar forces, as plot of $a-P$ in figure 2.7a, compared to the hertz model, as well as at similar displacements, namely $\delta = 0$, as seen in figure 2.7b.

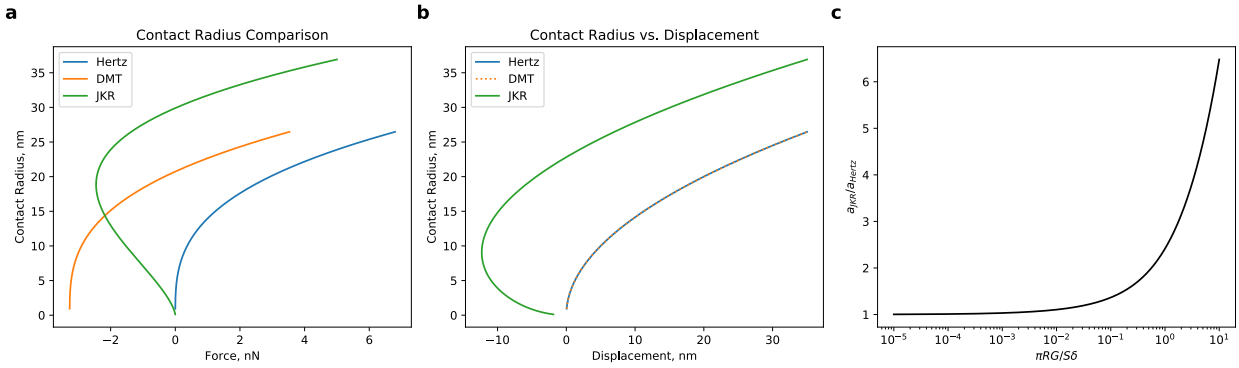

Figure 2.7: Comparison of Contact Radius, a , vs. (**a**) Applied Force, P, and (**b**) surface displacement, δ from Hertz, DMT, and JKR models whose $P-\delta$ curves are shown in figure 2.6. Note, The $a-\delta$ curves of Hertz and DMT are exactly the same. (**c**) Plot of ratio of a_{JKR} to a_{Hertz} vs. $\pi R\mathcal{G}/S\delta$, per eq. 2.29. Adhesive models assume constant $\mathcal{G}$.

The JKR contact radius can be written in terms of the Hertzian contact radius, eq. 2.23, first by replacing E_r with $\frac{S}{2a}$ as determined by eq. 2.8, in eq. 2.27. This leaves an easily solvable quadratic equation in a_{JKR} shown in eq. 2.28.

$$a_{JKR} = R\left(\frac{\pi\mathcal{G}}{S}\right)^{1/2} + R\left(\frac{\delta}{R} + \frac{\pi\mathcal{G}}{S}\right)^{1/2} \tag{2.28}$$

Dividing by the Hertz radius, $a_{Hertz} = \sqrt{\delta R}$ gives eq. 2.29

$$\frac{a_{JKR}}{a_{Hertz}} = \left(\frac{\pi R\mathcal{G}}{S\delta}\right)^{1/2} + \left(1 + \frac{\pi R\mathcal{G}}{S\delta}\right)^{1/2} \tag{2.29}$$

The JKR model deviation from the simple Hertzian prediction is given by the quantity $\pi R\mathcal{G}/S\delta$, shown in figure 2.7c. From this relation, it is apparent that the JKR contact radius is reduced to the Hertz radius when $S\delta >> \pi R\mathcal{G}$, namely when the material is very stiff, the indent is very deep, the indenter is large, and the energy release rate is low. Understanding this can allow Hertzian approximations of adhesive materials in specific conditions.

In reality, many adhesive materials behave somewhere in between the DMT and JKR cases, something the Maugis-Dugdale model tried to connect based on material stiffness and shape of the adhesive regime [50]. In general, stiffer materials such as metals and glassy polymers tend to follow the Hertz or DMT model where softer, more compliant adhesive materials like rubber typically follow close to the JKR model [53, 54]. However, these models are purely elastic contact models; they do not take into account the time dependent viscoelastic nature of polymers, particularly hysteresis, which is seen in most polymers like the example curve in figure 2.4b. Another problem occurs in unloading, where the models as described don't take into account the resistance to separation of the two surfaces, so the contact radius doesn't reduce monotonically with displacement and force in unloading until a critical force is reached [36], this will be discussed more in section 3.2.0.1. So, some modifications and assumptions need to be made to these models to address these concerns. Later in this thesis, two different arguments will be described in applying the JKR model to adhesive rubber where there is significant hysteresis. In 3, the strong adhesive interactions will be shown to signify a constant contact radius in unloading using a fracture mechanics based argument. In Chapter 4, it will be shown that the JKR model can provide a reasonable fit of the loading curve of the AFM force curves on rubber−carbon composites due to the high speed of the indentation.

Chapter 3

Quantitative Viscoelastic Property Mapping in Rubber Composites and Blends using Atomic Force Microscopy

Abstract

This chapter will describe the development of a novel and fast AFM based dynamic scanning indentation (DSI) nano-DMA method which relies only on the commonly available capabilities of commercial AFMs to provide quantitatively accurate high-resolution (∼15 nm) spatial maps of local viscoelastic mechanical properties (E', E'', and $\tan\phi$) in heterogeneous soft adhesive material systems. Quantitative agreement between DSI nano-DMA and bulk DMA measurements is demonstrated for two different homogeneous elastomers: styrene butadiene rubber (SBR) and synthetic natural rubber (SNR). The capability of the DSI methodology in acquiring quantitatively accurate viscoelastic property maps of heterogeneous soft solids was validated through experiments on an SBR-SNR blend sample. Experimental factors affecting DSI data quality, such as shift factor and AFM tip size, are also discussed. Finally, the application to rubber-composite systems is also discussed. This chapter reproduces work from "AFM-based Dynamic Scanning Indentation (DSI) Method for Fast, High-resolution Spatial Mapping of Local Viscoelastic Properties in Soft Materials" published in *Macromolecules* in 2018 [4]. This work was published by myself with co-authors Dr. Pavan V. Kolluru, David W. Collinson, Dr. Xu Cheng, Dr. David E. Delgado, Dr. Kenneth R. Shull, and Dr. L. Catherine

Brinson, where myself and Dr. Pavan Kolluru contributed equally to the work. All of the experiments were conducted by me.

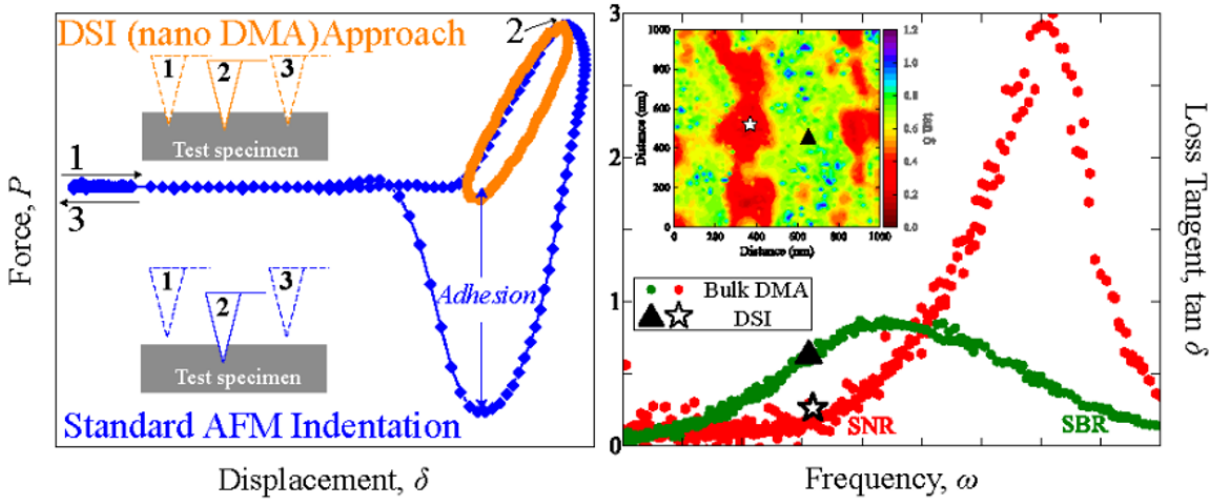

3.1 Introduction

3.1.1 Motivation: Interface Effects in Polymer Composites

Soft materials, such as elastomers, polymers, and gels, are finding increasing utility in a wide range of engineering applications owing to the ability to control their composition and microstructure and, in turn, their properties. Heterogeneous soft material systems such as polymer nanocomposites and blends and biomaterials such as tissues, which include a second (or even multiple) phase material, provide significant material design opportunities to achieve target properties by controlling a wider selection of material and microstructural parameters. Interface engineering is a particularly important design approach in such material systems [12, 55–60]. In the vicinity of an interface, macromolecular materials experience spatial confinement effects, resulting in the formation of a tertiary interphase region having distinct properties from those of the far-field bulk material [61, 62]. For materials with microscale complexity such as polymer blends and composites, the assessment of their bulk mechanical properties can be difficult to predict with mathematical models. Often residual stresses arising from dissimilar thermal stresses during manufacturing, or other imperfections such as voids can also contribute the development of a tertiary interphase-like region [63, 64]. Global or average

experimental measurements of physical properties and other analytical or computational studies have often estimated the interphase regions to be on the order of tens to hundreds of nanometers in length scale and to possess complex spatially graded material properties that are distinctly different from the bulk-like far field macromolecular behavior [65, 66].

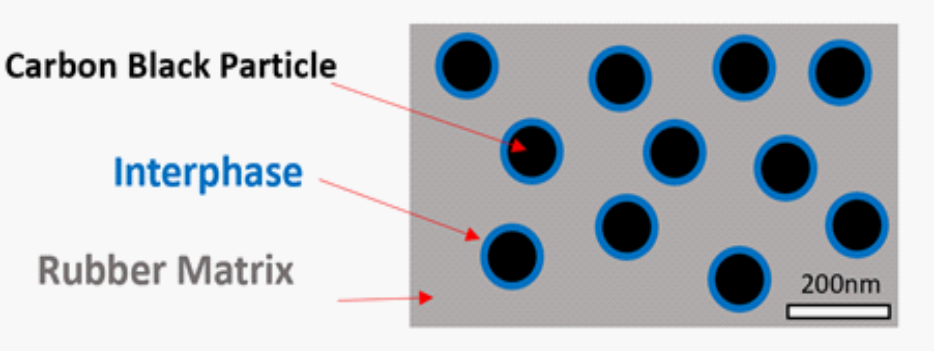

Figure 3.1: Simple schematic of interphase within a carbon black-rubber composite.

Rubber nanocomposites are particularly interesting due to the interphase effects on viscoelastic behavior, where the increase in the strength, toughness, and durability of the material while maintaining the flexibility of a rubber is desired. Rubber blends allow the optimization of the matrix phase in terms of improving of the technical properties of the matrix rubber, achievement of better processing behavior, and cost reduction [67]. The interphase effects of rubber composites are very pronounced, for example, traditional continuum mechanics would suggest that for a linearly viscoelastic rubber, the storage modulus, E', should approach a constant value of $(1 + 2.5\varphi)E'$, where φ is the filler concentration. However, measurements of filled rubber systems show deviations of 2 to 10 times the expected value [68]. Figure 3.1 shows a hypothetical schematic of what this interphase looks like in carbon black-rubber composite, but the exact length scale and extent is still debated. Some researchers suggest that the interphase in rubber composites actually consists of two regions: a thin, very still bound phase $<$10 nm around the particle, and less stiff "loosely bound" region that can extend another 40-50 nm away from the particle [13, 69]. However, more accurate and direct experimental characterization of local material property gradients across the interphase regions in heterogeneous soft material systems, are needed for: (1) determination of the length scale and shape of the property gradients in interphase regions to aid the development of reliable predictive models to design advanced heterogeneous materials with tailored properties and (2) studying the fundamental aspects of macromolecular confinement such as the local changes in polymer dynamics in spatially confined polymer volumes.

3.1.2 Viscoelastic Property Mapping Using AFM

The ability to accurately map the local interphase mechanical behavior is crucial to understanding spatial confinement effects in macromolecular systems, as well as for the optimization of material design and engineering advanced multiphase soft materials [12, 55, 70–74]. Given the nanoscale dimensions of the interphase region, AFM scanning force spectroscopy (SFS) is an appealing tool for the mechanical characterization of this region. AFM force curve analysis, as described in 2.2.1, relies on the use of elastic mechanical models to measure mechanical behavior of a probed material, and such experiments on model nanocomposite sampless have been developed to obtain high-resolution spatial maps of local elastic properties in soft heterogeneous materials [13, 75, 76]. However, these elastic models do not take into account the time-dependent viscoelasticity of these materials, that result in hysteresis of the force curves, and therefore can lead to errors in the calculations, and an incomplete picture of the mechanical response.

Research has been conducted in trying to measure viscoelastic properties from AFM indentation, such as multi-frequency AFM methods [77, 78] and contact resonance [79], and are either qualitative or semi-quantitative. For instance, contact resonance methods provide viscoelastic properties relative to those of a calibration sample, by measuring the resonance frequency shifts and amplitude damping of the AFM cantilever upon contacting a sample [79]. The choice of a calibration sample and an accurate and independent knowledge of the viscoelastic properties of the calibration sample are critical to the success of quantitative measurements. This latter aspect is in fact extremely difficult to establish experimentally. Additionally, the method is slow, with moderate resolution scans requiring many hours. Even more importantly, the contact resonance method is reliably applicable only in the case of stiff polymers, where $E' > 1\text{GPa}$, where there is minimal tip-sample adhesion. Thus, this approach is not an option for the viscoelastic characterization of very soft, adhesive materials such as elastomers or biological tissues.

By contrast, quasi-static indentation experiments, such as creep and relaxation experiments, have been better developed to provide direct measurements of viscoelastic properties and phenomenological time-dependent responses of soft materials [80, 81]. However, in addition to the major controls challenges of performing an indentation creep/relaxation experiments with an AFM (e.g., maintaining force/displacement control with a compliant AFM cantilever, or accounting for the finite initial force/displacement ramp), such experiments where the tip needs to spend many minutes at one location (to collect a creep/relaxation curve) is unsuitable for spatially mapping the viscoelastic properties of heterogeneous materials.

Recently, high resolution contact-mode AFM-based dynamic indentation methods capable of providing

quantitatively accurate viscoelastic property measurements on soft macromolecular materials such as cells and elastomers, have been developed [82–85]. These methods operate on the principle of adding a secondary piezoelectric actuator that oscillates the sample/stage across 2−4 decades of frequency. However, these methods require significant modification of commercial AFMs, such as the addition of external instrumentation (high bandwidth piezoelectric actuators and high power amplifiers) to dynamically oscillate the sample and associated control features (such as syncing the operation of the external piezoelectric actuators with that of the AFM piezoelectric actuator used for initial engagement into the sample and scanning), thus creating very expensive solutions that are not generally accessible to typical users. More importantly, these methods are still very slow for producing viscoelastic property maps of moderate, 64 × 64 pixels resolution; they require anywhere between 5 and 20 hr for about 10 different frequencies, spanning a frequency range of 2 to 4 decades [81–85]. At these extremely long time-scales (and the contact mode conditions represented in these experiments) even the lowest lateral drifts rates, on the order of ∼1−10 pm/s [86, 87], can produce significant lateral distortions (particularly in the slow scan direction) on the order of tens or hundreds of nanometers. Additionally, the temperature sensitive nature of the external actuators also limit the range of temperature-dependent experiments, thus precluding the ability to perform important thermorheological studies on the nature of relaxation dynamics in spatially confined soft material volumes such as the interphase regions [88].

This chapter describes a novel and versatile AFM-based **fast** dynamic scanning indentation (DSI) nano-DMA methodology that is capable of providing **quantitative viscoelastic** measurements of **soft materials**. Importantly, this method **does not require any modifications** to AFM instrumentation and can be easily and inexpensively performed using the existing mechanical testing modes that are available on commercial AFMs, such as the PeakForce Quantitative Nanomechanical Mapping (PF-QNM) mode or the FastForceMapping (FFM) mode, featured on the Bruker and Asylum AFMs, respectively. PF-QNM and FFM are SFS modes that operate under a peak/maximum force feedback mechanism. The defining feature of these modes is their use of smooth sinusoidal force ramp for the AFM tip oscillation in an intermediate frequency regime (10−2000 Hz) which is orders of magnitude greater than the range of frequencies employed in linear force ramp SFS modes (e.g., Force-Volume mode), yet orders of magnitude lower than the cantilever resonance frequency. Operation at these intermediate frequency ranges allows for thousands of force−displacement curves to be recorded over a two-dimensional area in a matter of a few seconds/mins as opposed to the hours/days required in other methods.

The novel DSI methodology reported here exploits these unique features of commercial SFS modes such

as PF-QNM or FFM to conduct dynamic indentation experiments that can quickly provide high-resolution spatial maps of quantitatively accurate viscoelastic properties for soft, adhesive heterogeneous materials. In fact, the DSI methodology will be demonstrated to be ∼10 times faster compared to existing methods [82–85] with the ability to capture a viscoelastic property map of 64 × 64 pixels resolution (at each frequency) within 1 min. Additionally, the ability to perform thermo-rheological DSI experiments is shown to result in an effective frequency span of 5 decades. The ensuing sections of this manuscript describe the specifics of the new DSI method and its quantitative validation by comparing the results from the DSI experiments against corresponding bulk-scale viscoelastic property measurements for two homogeneous soft materials: styrene−butadiene rubber (SBR) and synthetic high cis-1,4-polyisoprene (98%) (also known as synthetic natural rubber, SNR), as well as a heterogeneous blend of SBR and SNR. Moreover, the uniquely important thermorheological capabilities of this novel DSI methodology and the associated capability to produce nano-DMA viscoelastic master curves, which will open doors to quantitative characterization of local relaxation dynamics in heterogeneous soft materials, will also be described.

3.2 The Dynamic Scanning Indentation (DSI) Method

The operation of an atomic force microscope (AFM) in the tapping mode typically involves monitoring the interaction forces (P) as a function of distance (δ) between the AFM probe tip and the surface being probed, while rastering across to image the surface topology. During standard operation, Bruker's PeakForce Quantitative Nanomechanical Mapping (PF-QNM) mode as well as Asylum's FastForceMapping (FFM) mode, combine the high-resolution image acquisition (up to 256 × 256 pixels) process with a simultaneous recording of the entire $P-\delta$ curve at every pixel, all achievable at spatial scanning rates of ∼1 Hz (∼1 min to collect an image with 64 × 64 pixels resolution), thus enabling the AFM to serve as an instrumented indenter with high spatial resolution. Importantly, these modes operate the cantilever with a sinusoidal displacement drive, at relatively low oscillation frequencies of 10−2000 Hz (well below the resonant frequency of AFM cantilevers), under a feedback loop that can keep the maximum forces of indentation down to 10 pN, thus providing exceptional control to dynamically indent soft materials such as elastomers.

The sinusoidal displacement drive of these modes was exploited in the current study to a new viscoelastic experimental protocol termed dynamic scanning indentation (DSI). The DSI methodology is verified on two leading brands of commercial AFMs: Asylum (Cypher ES and MFP-3D Infinity) AFMs, and Bruker's Dimension Icon AFM. A primary difference between the two sets of AFMs was the ability of the two Asylum

AFMs to operate over a relatively continuous range of frequencies between 10−1000 Hz (Cypher ES) or 10−300 Hz (MFP-3D Infinity) respectively, where the lower limit of this frequency range is comparable to the upper limit of bulk-scale DMA experiments. The corresponding temperature ranges of these two AFMs are 0 to 120 °C and −30 to + 150 °C respectively. Thus, conventional frequency sweep DSI experiments and the associated construction of a nanoDMA viscoelastic master curve was achieved with these AFMs. Contrastingly, Bruker's Dimension Icon version used in this investigation operates only at the discrete frequencies of 1000 and 2000 Hz. Because of issues with noisy data at 1000 Hz, all data taken with the Dimension Icon for this study was at the 2000 Hz frequency and at multiple temperatures. It is however important to note that a vast number of the DSI nano-DMA experiments reported in this study were performed using Bruker's PF-QNM mode, owing to the better application programming interface (API) available for this AFM (as compared to the Asylum AFMs) which made it easy to batch process large sets of raw force−displacement data using MATLAB or Python and perform customized viscoelastic data analyses as described later in this section. As most experiments reported in this study were run in the PF-QNM mode of operation, the experimental methodology is primarily described based on this mode of operation. Important differences encountered during the application of the DSI methodology on Asylum AFMs are explicitly mentioned where necessary.

Before viscoelastic DSI scans, a "standard" PF-QNM pre-scan was performed on the chosen sample area of interest. The prescan utilized the desired spatial resolution settings and total oscillation distance, or "peak-force amplitude", ($2\delta_0$) of more than 200 nm, to establish the reference values of P and δ, thus ensuring the quantitative accuracy of subsequently measured viscoelastic (DSI) $P-\delta$ curve. Moreover, the standard PF-QNM curve, schematically illustrated, in blue, in figure 3.2a, is the only way to measure important quantities such as maximum indentation depth (δ_{max}) and adhesion force (P_{adh}), that are required in subsequent calculations of viscoelastic moduli from DSI experiments. The standard PF-QNM indent, the orange curve in 3.2a, is similar to a traditional instrumented indentation experiment used to study the elasto-plastic mechanical properties of materials, with the AFM tip starting the oscillatory cycle in air (1) until it engages with the sample surface and penetrates into the sample, eventually reaching a user-input peak force set point (P_{max}) (2), then reversing course and retracting from the sample until it completely disengages from the sample surface to reach the original starting position (3). On the basis of the standard PF-QNM $P-\delta$ curve, one can clearly identify the reference value for P ($P=0$ at the plateau in region 1 before engagement) and the instant the tip engages the surface, thus establishing the reference position of the sample surface ($\delta=0$). The reference $P-\delta$ curve enables the identification of a quantitatively accurate δ_{max}

and the absolute minimum force value of this curve as P_{adh}. In the current study, the standard PF-QNM mode of operation was used by manually adjusting the peak force set point (P_{max}) to the desired value instead of using the automated control settings. Consequently, the peak force also controls maximum depth of the penetration, as a larger force will indent the tip deeper into the material. For the materials reported here, the peak force set point was adjusted to be 5−25 nN when using AFM tips with ∼5 N/ m cantilever stiffness, 30−100 nN for ∼40 N/m stiff tips and 100−1000 nN for ∼250 N/m stiff tips.

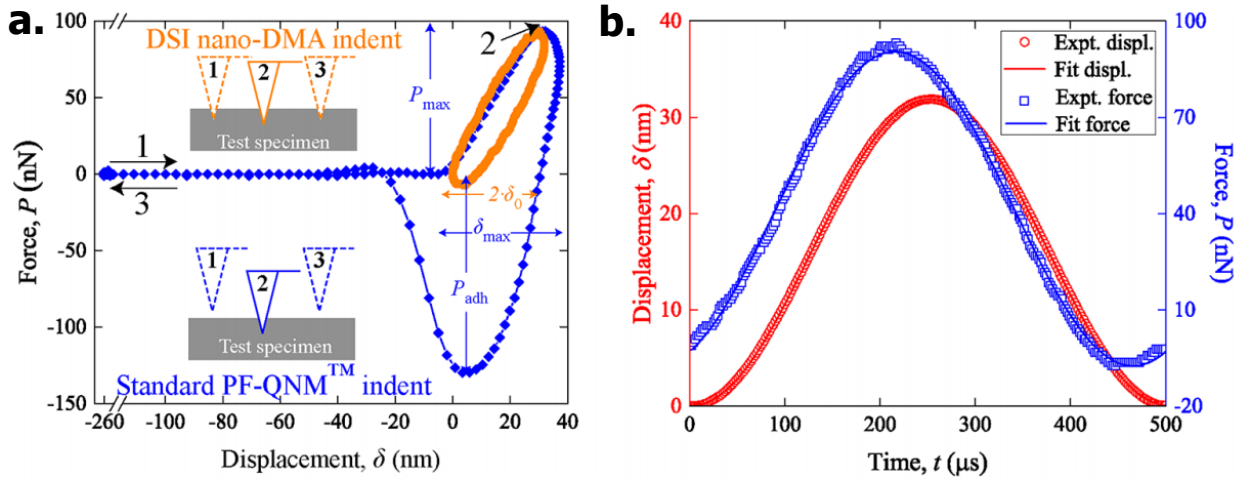

Figure 3.2: (**a**) Comparison of the force vs displacement curves obtained from the same location on SBR (at a temperature of 16 °C) using the standard PeakForce QNM operation as well as the modified DSI nano-DMA protocol developed in the current study to measure viscoelastic properties. The accompanying schematic illustrations describe the difference between the standard and dynamic (DSI) nanoindentation experiments. Important AFM control parameters of peak force (P_{max}) and displacement oscillation amplitude (δ_0) that can be varied to perform standard QNM and DSI indentation experiments, as well as the important measured quantities such as the adhesion force (P_{adh}) and maximum indentation depth (δ_{max}) that are used in subsequent data reduction process are schematically labeled. It should be noted that the standard $P-\delta$ curve was translated along the displacement axis such that both the standard and modified curves reach their Pmax at the same displacement. (**b**) Individual force vs time ($P-t$) and displacement vs time ($\delta-t$) data from the modified DSI nano-DMA experiment (whose $P-\delta$ data were shown in (a)) are plotted along with the corresponding fit lines that represent fits to eqs. 3.1 and 3.2, respectively.

Once the standard force-displacement curve map was performed, the aforementioned DSI technique could be conducted. The DSI scan uses the same spatial resolution settings as the aforementioned standard PF-QNM prescan over the same region, although the oscillation amplitude, of the AFM cantilever is progressively reduced, while maintaining a constant peak force set point, P_{max}, until the $P-\delta$ curve turns into a smooth, closed, cyclic curve, as shown in orange in Figure 3.2a. It should be noted that this is done in real-time as the tip continues to scan the surface, so as to be able to monitor the quality of the $P-\delta$ curve and ensure that the AFM controller is stable and properly controlling the AFM tip. The process of amplitude reduction

is stopped once a stable, fairly symmetric looking DSI viscoelastic indent is observed. A DSI scan composed of such cyclic indents at each pixel is then obtained. Careful observation of Figure 3.2a reveals that the DSI viscoelastic indent data, in isolation, cannot provide the baseline/ reference values of P or δ, thus visually reiterating the need for a standard PF-QNM indentation prescan. It should be noted that in Figure 3.2a, the standard $P-\delta$ curve was translated along the displacement axis such that both the standard and modified curves reach their P_{max} at the same displacement value because the same peak force setting is both scans is expected to result in the same displacement.

Figure 3.2b shows the temporal distribution of P and δ oscillation measurements obtained from the cyclic DSI indentation in Figure 3.2a. The overlaid fits in Figure 3.2b represent the least-squares regression lines to sinusoidal equations of the form expressed in eqs. 3.1 and 3.2.

$$P = P_0 \sin(2\pi\omega t + \varphi_P) + P_{avg} \tag{3.1}$$

$$\delta = \delta_0 \sin(2\pi\omega t + \varphi_\delta) + \delta_{avg} \tag{3.2}$$

where P_0 and δ_0 represent the force and displacement oscillation amplitudes respectively, ω is the frequency of oscillation, P_{avg} and δ_{avg} represent the difference between the maximum and minimum force and displacement, respectively, and φ_P and φ_δ are the phase offsets for the force vs time and displacement vs time curves. The sinusoidal displacement drive of the PF-QNM mode is evident from the smooth displacement vs time data and the extremely good fit of eq 3.2 to the experimental data. Moreover, the viscoelastic nature of the sample is evident from the phase lag between the force and displacement data, providing a direct measurement of the phase angle (ϕ) as eq. 3.3.

$$\phi = |\varphi_\delta - \varphi_P| \tag{3.3}$$

The $P-\delta$ data obtained from DSI nano-DMA experiments also enable independent measurements of the magnitude of the viscoelastic complex modulus $|E^*|$, which can can be calculated using eq. 3.4 which comes eqs. 2.14 and2.9as described in the previous chapter, assuming a circular contact area of $A = \pi a^2$, where a is the contact radius, and assuming $\upsilon = 0.5$, the typical value for rubbers.

$$|E^*| = \frac{3P_0}{8\delta_0 a} \tag{3.4}$$

The complex modulus can then be parsed into the storage modulus (E') and loss modulus (E''), once the phase angle ϕ is determined from eq. 3.3, using the equations from Chapter 2, eq. 2.3.

The measurement of contact radius, a, during the dynamic indentation of soft, rubbery materials is difficult due to the significant tip−sample adhesive interactions and the relatively large oscillation amplitudes of DSI nano-DMA. However, using a fracture mechanics analysis based on the Johnson−Kendall−Roberts (JKR) model [36, 52], two contact mechanics assumptions are made that enable the use of eq 3.4:

(i) Owing to the relatively deep indents ($\delta \geq R$) and high frequency of indentation into the sample ($\mathcal{G} \longrightarrow 0$) [89, 90], use of the expression for Hertzian contact radius of a paraboloid of revolution with tip radius R, eq 3.5, is applicable, as described in section 2.2.3.2.

$$a_{JKR} \sim a_{Hertz} = \sqrt{R\delta_{max}}, S\delta >> \pi R\mathcal{G} \tag{3.5}$$

(ii) During the oscillatory indentations, a is assumed to remain constant due to the significant adhesion between the tip and the sample, and the relatively low strain energy release rate at the maximum depth of indentation (See 3.2.0.1).

It should be noted that for the necessarily deep indentations ($\delta \geq R$), required for stable DSI experiments, relatively high characteristic strain can be experienced directly under the indenter tip, which could locally depart from linearized Hertz/JKR theories. However, using Tabor's relation for indentation strain [91], all indentation data reported in this study were ensured to be significantly below the typically reported linear viscoelastic strain limits for elastomers [92].

3.2.0.1 Constant Contact Radius Assumption

Application of eq. 3.4 for calculating $|E^*|$ requires the assumption of a constant contact area to in an oscillatory indent [35]. However, in the initial discussion of the JKR adhesive contact mechanical model of a parabolic tip in section 2.2.3.2, the model assumes that the contact radius, a, follows the same relationship with tip displacement, δ, during loading and unloading, suggesting that a increases and decreases with δ, as shown in figure 2.7b. This would cause a problem in the DSI method, as the tip oscillates a distance $2\delta_0$over the course of the indent, and some of the oscillation amplitudes can be rather large, since decreasing too much can create a cyclic DSI curve that is too noisy for good sinusoidal fits. However, this assumes that the energy release rate, $\mathcal{G}$, of the tip-samples systems is constant throughout the indent, which is likely the case during loading, but not necessarily during unloading [36]. During unloading, a reduction in a

requires the separation of two surfaces, which can be modeled as a propagating crack and analyzed using fracture mechanics arguments. According to linear elastic fracture mechanics, the surfaces will not separate unless the system $\mathcal{G}$ surpasses a critical energy release rate, $\mathcal{G}_c$, which represents the strength of the adhesive interactions of the tip and the sample. The energy release rate of the system according the JKR model can be expressed as eq. 3.6, by taking eq. 2.27and solving for $\mathcal{G}$.

$$\mathcal{G} = \frac{S}{4\pi a^2}\left(\frac{a^2}{R} - \delta\right)^2 = \frac{P_0}{4\pi\delta_0 a^2}\left(\frac{a^2}{R} - \delta\right)^2 \tag{3.6}$$

where $S = \frac{P_0}{\delta_0}$, from the derivation of 3.4 from 2.8 for cyclic indents (assuming constant a) [35]. Our initial assumption that for these deeper indents $a_{JKR} \sim a_{Hertz}$, means that during loading $\delta \sim \frac{a^2}{R}$, and thus $\mathcal{G} \sim 0$. However, once the tip reaches the maximum depth $\left(\frac{a^2}{R} \sim \delta = \delta_{max}\right)$ and reverses direction, the adhesive force between the tip and the sample will resist separation, and the contact area will remain constant at $a_{max} = \sqrt{R\delta_{max}}$ as long as $\mathcal{G}$ is below $\mathcal{G}_c$. Eq. 3.6becomes eq. 3.7.

$$\mathcal{G}_{unload} = \frac{P_0}{4\pi\delta_0\delta_{max}R}\left(\delta_{max} - \delta\right)^2, \mathcal{G}_{unload} < \mathcal{G}_c \tag{3.7}$$

With a constant, $\mathcal{G}$will now increase while δ decreases. For the contact area to be constant during the whole unloading cycle, the maximum $\mathcal{G}$, or $\mathcal{G}_{max}$, must remain below $\mathcal{G}_c$. $\mathcal{G}_{max}$will occur at the minimum δ, which is when the tip has moved the length of the oscillation cycle from the maximum depth, at $\delta = \delta_{max} - 2\delta_0$, resulting in eq. 3.8.

$$\mathcal{G}_{max} = \frac{P_0}{4\pi\delta_0\delta_{max}R}\left(\delta_{max} - (\delta_{max} - 2\delta_0)\right)^2 = \frac{P_0\delta_0}{\pi R\delta_{max}} \tag{3.8}$$

It has been reported in the literature that $\mathcal{G}_c \sim 0.4\text{J/m}^2$ for elastomers [35, 36], so it was used as a limit for acceptable DSI data. Only DSI experiments having $\mathcal{G}_{max} \leq 0.4\text{J/m}^2$ were reported in this thesis. From 3.8, it can be seen that higher values of $R\delta_{max}$ and lower values of $P_0\delta_0$ will enable keeping $\mathcal{G}_{max}$ low. Additionally, the force curves reported at each pixel using the PF-QNM mode is actually an average of several curves, not a single curve [93]. Thus several oscillations are performed on each pixel before it moves to the next pixel (the AFM lifts the tip a little further as it moves between pixels). This minimizes the effects of the increasing contact area during loading in the first cycle, since it is averaged out by the subsequent cycles at constant contact area. This force curve averaging, however, does not occur with Asylum's FastForce Mapping module, but the sinusoidal fits of the data collected from those AFM did not seem to be noticeably

affected.

3.3 Material & Methods

3.3.1 Sample Preparation

3.3.1.1 Homopolymer Rubbers and Rubber Blends

Cross-linked, commercially available synthetic high cis-1,4-polyisoprene (98%) (SNR, Natsyn 2200), and anionically prepared styrene–butadiene rubber (SBR, SLF16S42) were provided by The Goodyear Tire & Rubber Company. Additionally, a peroxide crosslinked 75wt% SBR-25wt% SNR sample was also provided by The Goodyear Tire & Rubber Company. These samples were cured using 0.5 phr dicumyl peroxide, for 35 min at 160 °C. Bulk DMA samples were prepared by cutting approximately 20 mm long strips with a 2×2 mm^2 cross-section. For the DSI nano-DMA experiments, 1–2 μm thick slices of these rubbers were prepared using a Leica EM UC7 Ultramicrotome with FC7 cryo-chamber. Slices were cut with the chamber and the sample holder set to −120 °C, while the knife was held at −40 °C. Slices were cut and collected with a DiATOME Ultra 45° Diamond knife designed for wet sectioning, using a mixture of 3:2 dimethyl sulfoxide: deionized water.

3.3.1.2 Carbon Black Rubber Composite & Carbon Black Sandwich Sample

Uncrosslinked SBR was mixed with 0.5 wt% dicumyl peroxide dispersed in toluene with 10wt% total solids. After toluene is evaporated, a mixture of 10% carbon black particles in toluene and 1% rubber + 0.5wt% peroxide is sprayed on a piece of the uncrosslinked rubber. After, a second piece of rubber is laid on top of this sprayed rubber layer. This "sandwich" is then crosslinked by placing in an oven at 160°C for 1hr. A cross-section of this carbon black-rubber "sandwich" was cut with a a Leica EM UC7 Ultramicrotome with FC7 cryo-chamber perpendicular to the carbon black layer. Additionally, a 10 wt % carbon black and sulfur cross-linked, anionically prepared styrene–butadiene–rubber (SBR, SLF16S42) were provided by The Goodyear Tire & Rubber Company for *in-situ* composite examination. Cryotome slices were prepared similarly to homopolymer rubber and rubber blend samples.

3.3.2 Bulk Scale Dynamic Mechanical Analysis (DMA)

Frequency sweep tensile DMA experiments were performed on bulkscale rubber samples using an RSA3 dynamic mechanical analyzer (TA Instruments), spanning a frequency range of 0.1 to 10 Hz, at a constant tensile strain of 0.1, for each temperature. Each set of frequency sweep experiments covered a temperature range of −100 to +40 °C, in intervals of 5°C.

3.3.3 AFM

The force curve spectroscopy data collected via the procedure outlined in **section 3.2** using mostly a Bruker Dimension Icon in the Peak-Force Quantitative Nanomechanical Mapping (PF-QNM) mode. For experiments Deflection sensitivity was determined from the slope of piezo movement vs deflection on a stiff, sapphire calibration sample, as described in section 2.2.1, and cantilever stiffness was then calibrated using the Sader method, also described in section 2.2.1 [42]. Finally, the tip radius of sharp/small radius, parabolic AFM tips used in this study was estimated by using the "roughness sample" method (appendix A.1) [39], or SEM micrographs (figure 3.3). In case of large radius ($R \sim 250$nm) parabolic AFM tips (purchased from Team Nanotec) used in this study, scanning electron microscope images (SEM) provided by the manufacturer were used to identify the tip radius, as shown in Figure 3.3b. Additional details of these calibration procedures can be found in section 2.2.1 and appendix A.1.

Some of the DSI AFM experiments were also performed on Asylum's Cypher ES and MFP-3D Infinity AFMs using the FastForceMapping module. For calibration, these AFMs were also capable of a thermal tune and Sader Method based noncontact calibration procedure for calibrating the cantilever spring constant and deflection sensitivity [94], using the proprietary GetReal application developed by Asylum Research[95]. The latter approach was followed in this study. Subsequently, tip radius was still quantified using the aforementioned roughness sample and SEM imaging approaches. The AFM and tip used in each experiment will be indicicated with the corresponding data and discussion.

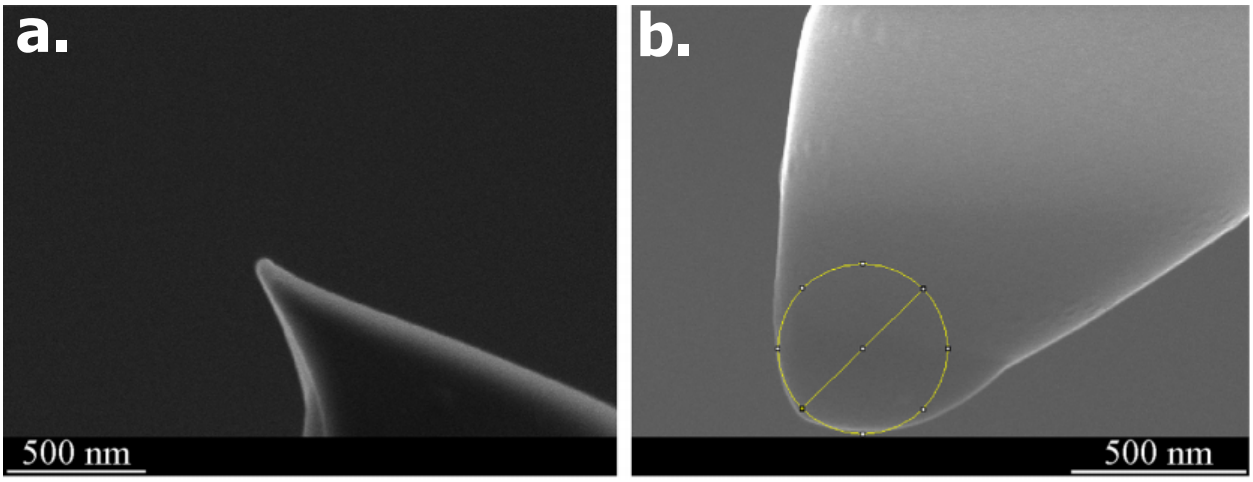

Figure 3.3: Representative scanning electron microscope images of (a) sharp parabolic AFM tips (Olympus OMCL-AC240TS-R3) and (b) large radius parabolic AFM tips (Team Nanotec LRCH 250) after a nano-DMA experiment.

3.3.4 Thermal Setup for Thermorheological DSI Experiments.

Thermorheological nano-DMA experiments performed in this study used different types of heating/cooling stages. Asylum's Cypher ES AFM has a built-in environmental control chamber and an associated heating/cooling stage with a range of $0 - 120$ °C. Similarly, for Asylum's MFP-3D Infinity AFM an Asylum CoolerHeater StageTM with a temperature range of -5 °C to +35 °C was used. For Bruker's Dimension Icon AFM, a custom-built heating/cooling system using a Instec mK2000 series high precision temperature controller, was used to adjust sample temperature between -30 °C and +50 °C using liquid nitrogen. Thin, cryotomed slices of the elastomer samples were placed on ~5 mm square silicon wafers. Good thermal contact between the metallic cooling stage and the silicon wafer was ensured by applying silver paint (Leitsilber 200, Ted Pella Inc., USA) to the base of the silicon wafers before mounting them onto the stage. Due to the low thickness (< 5 µm) and orders of magnitude lower thermal mass of the samples, the temperature of the elastomer samples was approximated to be the same as the steady-state thermocouple measurement. A nitrogen enclosure was built around the AFM using a polyethylene casing and zero-grade gaseous N_2 was supplied into the enclosure to create an inert, moisture-free atmosphere and prevent condensation on the sample.

3.4 Results & Discussion

The goal of this research was to develop and validate an AFM based nano-DMA methodology capable of quickly mapping the local viscoelastic properties in heterogeneous material systems such as polymer nanocomposites, using the readily available features of commercial AFMs. To this goal, the current section will focus on validating the quantitative accuracy of the DSI nano-DMA methodology described previously and discussing the likely impact of key experimental parameters on the quality of results. Initially, in section 3.4.2, the development of nano-DMA viscoelastic master curves (using DSI experiments on Asylum's Cypher ES and MFP-3D Infinity AFMs) and their comparison to bulk DMA data (in frequency space) will be presented. Section 3.4.3 will focus on validating the DSI nanoDMA methodology when using Bruker-type commercial AFMs, which only provide a single operating frequency or a few discrete operating frequencies, precluding the construction of an independent nano-DMA master curve through empirical frequency-space shifts of viscoelastic data. Subsequently, the use of van Gurp—Palmen (vGP) plots to address concerns associated with shift factor uncertainty in such experiments is presenteds This section also discusses the effect of ideal large radius parabolic AFM tips and high-resolution small radius parabolic AFM tips on the quantitative accuracy of the resulting DSI nano-DMA viscoelastic measurements. Finally, in section 3.4.4, the ability of the DSI nano-DMA method to map the viscoelastic mechanical properties of heterogeneous soft adhesive materials with high spatial resolution and quantitative accuracy is validated.

3.4.1 DMA Data

Master curves of the viscoelastic properties of $|E^*|$ and $\tan\phi$ were created following the time—temperature superposition (TTS) principle as described in section 2.1.1. Figures 3.4a shows the master curve for SBR at $T_r = -20°\text{C}$ and 3.4b is the master curve for SNR at $T_r = -40°\text{C}$ respectively. The reference temperatures were chosen as they were in the transition region of the curves. The shift factors were found using DMA software that optimizes the the overlap of the $|E^*|$ frequency sweep data, and these as plotted in 3.4c. The different regimes of the master curve, glassy, rubbery, and transition, are marked in these plots (figures 3.4a-c) to show that there is some noticeable uncertainty in the shift factors in the glassy and rubbery regions of the curves, particularly for SNR.

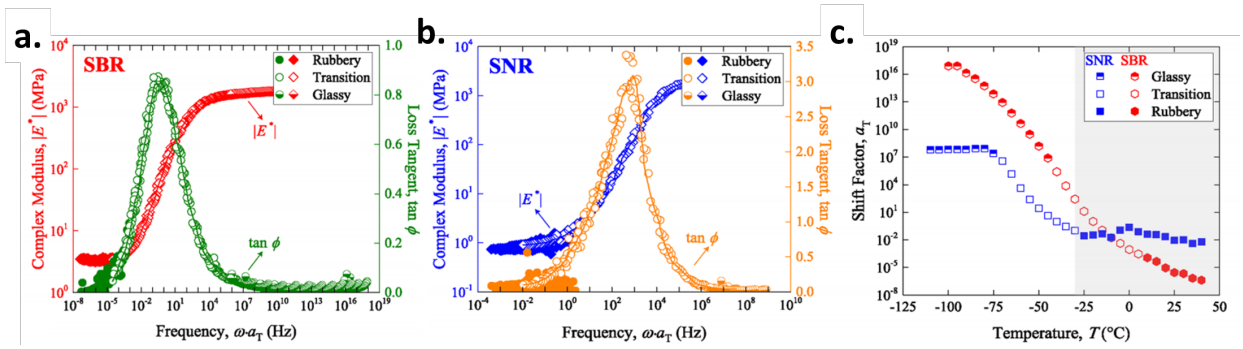

Figure 3.4: Results from bulk DMA experiments showing (**a**) complex modulus ($|E^*|$) as a function of temperature and frequency for SBR and (**b**) the corresponding complex modulus $|E^*|$ and loss tangent ($\tan\phi$) master curve data for SBR based on the time–temperature superposition principle (reference temperature = −20 °C). (**c**) Similarly constructed $|E^*|$ and $\tan\phi$ master curves for SNR (reference temperature = −40 °C). Solid lines in parts (**b**) and (**c**) are spline fits to the transition regime. (**d**) Experimental/empirically determined shift factor (a_T) values as a function of temperature, required for constructing the viscoelastic master curves of SBR and SNR, shown in parts (**b**) and (**c**). The gray region in part (**d**) represents the temperature range accessed by AFM DSI experiments in the current study.

It is important to note the uncertainty of the high temperature (rubbery regime) shift factors when comparing AFM-based DSI viscoelastic measurements to the corresponding bulk DMA measurements. One way to mitigate the issue of shift factor/master curve inaccuracy is to visualize viscoelastic data in the form of a van Gurp-Palmen (vGP) plot, which is a plot of $|E^*|$ vs. ϕ or $\tan\phi$, as shown in Figure 3.5a,b, for SBR and SNR respectively. vGP plots, which do not include the frequency/time component and corresponding time-temperature shifts associated with the frequency space viscoelastic master curves, were originally developed to visualize viscoelastic data from polymer blends where it was shown that even when relaxation times change slightly, $|E^*|$ - $\tan\phi$, plots remain unchanged [96]. This process will be utilized later this chapter to eliminate the frequency/time component of the viscoelastic master curves and enable a simpler comparison of bulk DMA data to the DSI results.

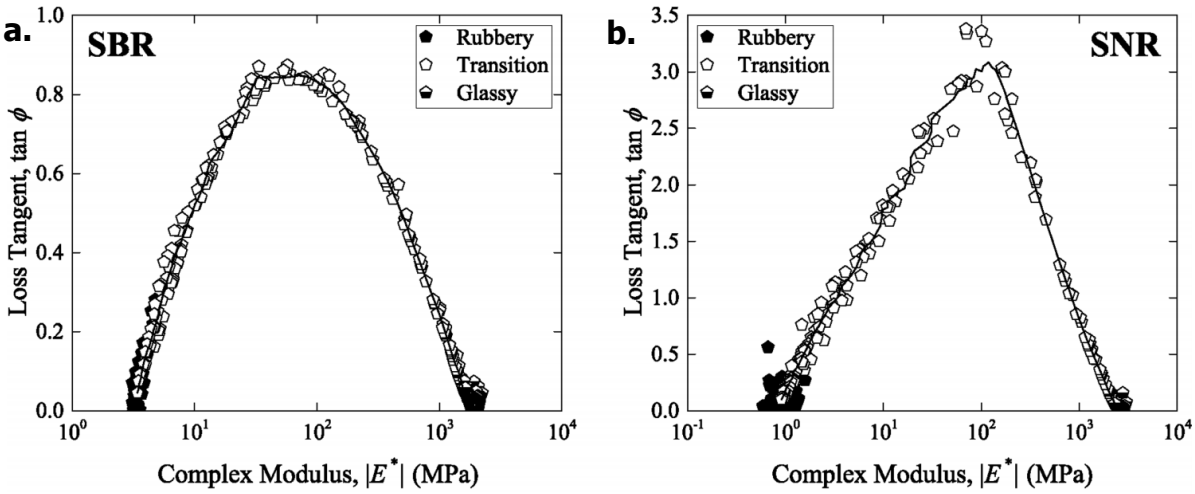

Figure 3.5: Van Gurp–Palmen (vGP) master curves from bulk DMA experiments for (**a**) SBR and (**b**) SNR. The solid lines represent spline fits to experimental data (scatter).

3.4.2 DSI Method Validation via Nano-DMA Viscoelastic Master Curves

The Asylum's Cypher and MFP-3D AFMs represent the most versatile commercial AFMs owing to their ability to control both the frequency of operation for mechanical testing and temperature. This versatility enables the acquisition of complete frequency sweep DSI nano-DMA curves. In the current study, DSI nano-DMA experiments on SBR and SNR were performed using the Cypher ES AFM, with the frequency sweeps spanning five discrete frequencies of 10, 32, 100, 320, and 1000 Hz, in 5°C temperature intervals, over a temperature range of 0°C (lower limit of the instrument) to 40°C (corresponding to the rubbery plateau regime). Figure 3.6a shows the frequency sweep $|E^*|$ data for SBR. Empirical shifting of data in Figure 3.6a results in the $|E^*|$ DSI nano-DMA master curve shown in Figure 3.6b. Room temperature (20°C) was used as the reference temperature for constructing the $|E^*|$ nano-DMA master curve. The empirical shift factors used to create the $|E^*|$ DSI master curve in Figure 3.6b are presented in Figure 3.6c. These same DSI shift factors were then used to create the nano-DMA $\tan\phi$ master curve illustrated in Figure 3.6d. It is important to note that the empirical shifting of the nano-DMA $|E^*|$ data, Figure 3.6b, was achieved only via horizontal shifting and in isolation, without trying to compare and match the emerging nano-DMA master curve to the bulk DMA data. This independent process allows us to judge the ability of the DSI method to provide reliable nano-DMA master curves in the future for materials or interphase regions for which a priori bulk DMA master curves would not be available.

In addition to being able to match the shapes of successive frequency sweep curves from thermorheological

DSI experiments and construct DSI nano-DMA master curves, Figure 3.6, temperature dependence of the shift factors, a_T should follow the Vogel−Fulcher−Tammann (VFT) equation (eq. 2.7, section 2.1.1). So, values of a_T determined during the creation of the $|E^*|$ master curve (Figure 3.6b), are presented in Figure 3.6c. Figure 3.6c demonstrates that the nano-DMA shift factors are very similar to the bulk DMA shift factors and also shows a fit of transition regime bulk DMA a_T to the VFT fit in eq 2.7 (see section 2.1) and its extrapolation to the rubbery regime [22]. This analysis establishes that the time−temperature superposition principle is applicable to the viscoelastic data collected from thermorheological DSI experiments using sharp parabolic AFM tips, and can be used to create nano-DMA master curves.

Figure 3.6b,d also compare the DSI nano-DMA master curves of the two viscoelastic functions ($|E^*|$ and $\tan\phi$, respectively) to the corresponding bulk DMA master curves. Excellent quantitative agreement between the bulk and nano-DMA master curves in Figure 3.6b,d validates the quantitative accuracy of the viscoelastic measurements obtained from the novel DSI methodology. Small differences between the DSI and bulk DMA $|E^*|$ master curves in Figure 3.6b, particularly in the rubbery regime can be attributed largely to the use of Hertzian contact mechanics model in these calculations, which ignores the tip− sample interaction forces and underestimates the indentation contact area, thus overestimating $|E^*|$. The DSI $\tan\phi$ master curve, Figure 3.6d, which is not affected by these concerns, still shows good quantitative agreement with bulk DMA data.

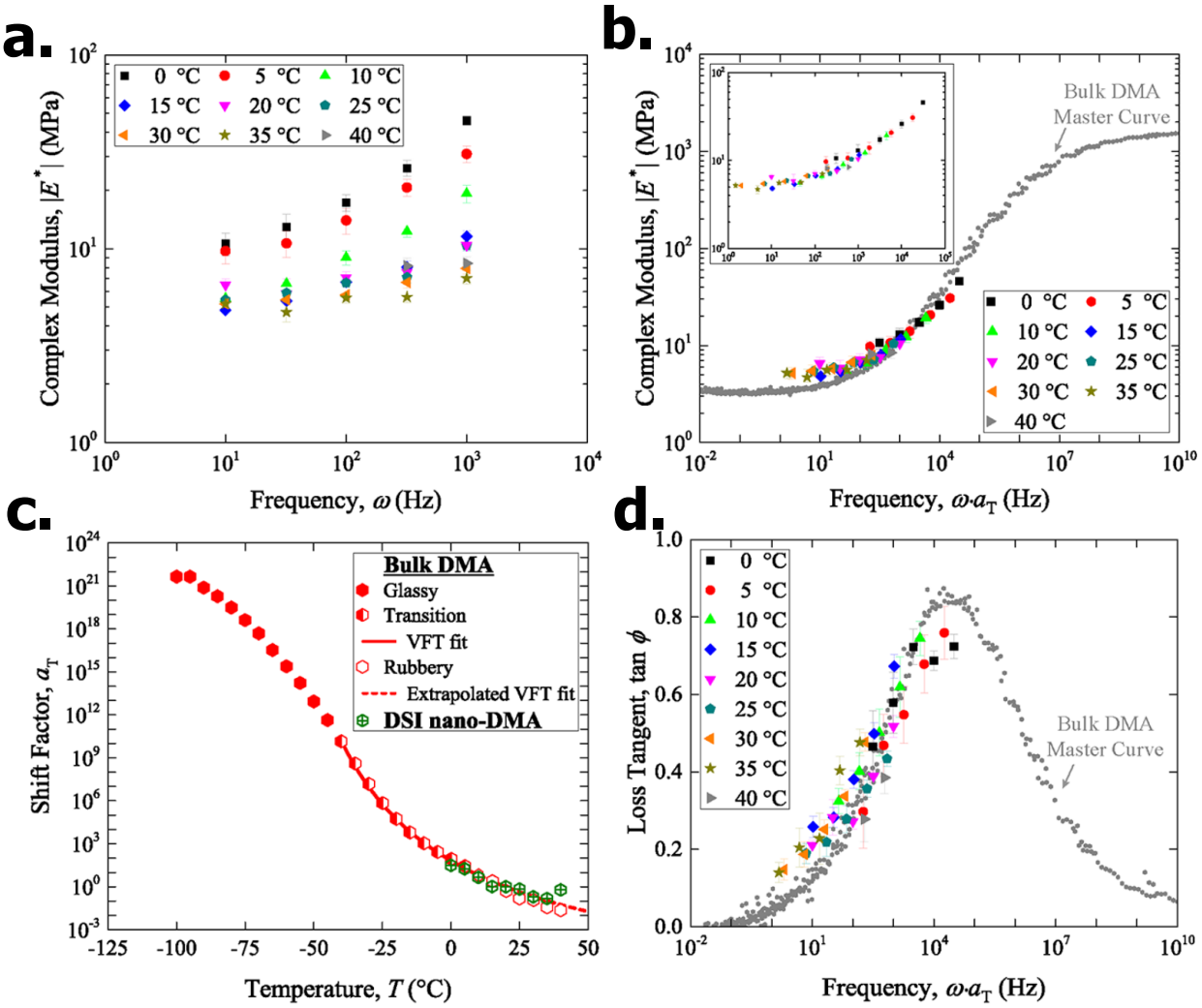

Figure 3.6: (**a**) Complex modulus, $|E^*|$, data from frequency sweep DSI nano-DMA experiments on SBR. (**b**) $|E^*|$ nano-DMA master curve (in the inset) created by empirical shifting of frequency sweep $|E^*|$ data (shown in part (**a**)) and compared to the corresponding bulk DMA master curve (both sets of master curves are referenced to 20°C). (**c**) Empirically determined DSI shift factors used to create the $|E^*|$ nano-DMA master curve shown in part (**b**). (**d**) Comparison of the DSI loss tangent ($\tan\phi$) master curve (obtained using the DSI shift factors shown in part (**c**)) to the bulk DMA $\tan\phi$ master curve. Error bars on DSI data in parts (**a**), (**b**), and (**d**) represent the standard deviation of the 10 measurements at each temperature and frequency. Theses DSI experiments were conducted on the Asylum Cypher ES AFM adapted from the FastForceMapping mode according to the DSI nano-DMA procedure.

Similar to the comparisons for SBR in Figure 3.6, Figure 3.7 depicts the generally good quantitative agreement between the DSI nano-DMA and bulk DMA master curves for SNR, thus reinforcing the validity of the DSI nano-DMA methodology. As noted earlier, the nearly uniform overestimation of DSI complex modulus in Figure 3.7a is a consequence using the Hertz contact mechanics model that does not account for

the significant adhesion observed in the rubbery regime.

Despite a slight overestimation of $\tan\phi$ by the DSI methodology in Figure 3.7b, a generally excellent overall agreement was observed between the bulk and nano-DMA loss tangent master curves. Owing to the low T_g of the SNR sample (relative to the SBR sample), and the frequency and temperature limits of the Cypher ES AFM, the DSI nano-DMA data from SNR, Figure 3.7, lie completely in the rubbery regime. In this regime, a comparison of the DSI nano-DMA and bulk DMA shift factors, depicted in the inset of Figure 3.7b, reveals an interesting observation: the DSI nano-DMA based shift factors continue to be very reliable, and are in excellent agreement with the extrapolated VFT fit to the bulk DMA shift factors from the transition regime. For the reasons mentioned earlier, the experimentally determined bulk DMA shift factors deep in the rubbery regime have significant uncertainty and a VFT extrapolation provides a more accurate estimation. While future improvements to the temperature and frequency capabilities of the commercial AFMs are to be expected and this will improve the ability to access the transition regime of low T_g materials, it is also extremely important to note at this stage that even with the current capabilities of commercial AFMs, the nano-DMA master curves generated by these novel thermorheological DSI experiments, Figures 3.6 and 3.7, already span an effective frequency range of 5 orders of magnitude, which supersedes the current state-of-the-art frequency range of 4 decades [82, 85]. Nevertheless, the time taken to collect all the data required to construct the nano-DMA master curves in Figure 3.6a is still 4–8 times lower than what has been previously reported.

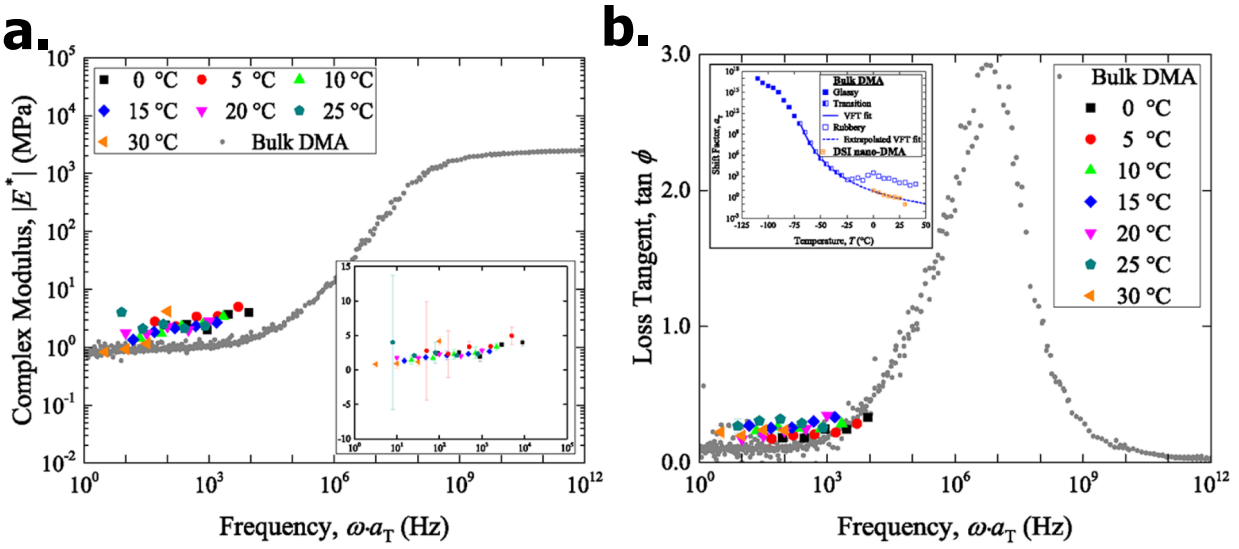

Figure 3.7: Results from DSI nano-DMA experiments on SNR rubber showing (**a**) the $|E^*|$ nano-DMA master curve created by empirically shifting the frequency sweep $|E^*|$ data shown in the inset (with a linearly scaled ordinate) and compared to the corresponding bulk DMA master curve (both sets of master curves are referenced to 20°C). (**b**) Comparison of the DSI based $\tan\phi$ master curve, which are obtained using the DSI shift factors shown in the inset (these shift factors were determined through the development of the $|E^*|$ master curve shown in part (a)). Theses DSI experiments were conducted on the Asylum Cypher ES AFM adapted from the FastForceMapping mode according to the DSI nano-DMA procedure.

3.4.3 DSI Methodology with only Temperature Sweep Capability

Many commercial AFMs such as the Bruker AFMs provide little to no frequency sweep capability in their mechanical mapping mode. In this section, it is shown that the DSI methodology continues to be very useful under these circumstances to obtain the local viscoelastic properties of soft materials while resorting to temperature sweep DSI experiments at a single frequency. DSI experiments on SBR and SNR reported in this section were conducted on Bruker's Dimension Icon AFM. The DSI experiments were performed at 2 kHz across a wide range of temperatures ranging between −35 and +50 °C. Owing to the lack of a frequency sweep capability, comparison of the DSI based viscoelastic properties to the corresponding bulk DMA data can only be achieved by shifting the DSI data using shift factors determined from bulk DMA experiments. As noted earlier through Figure 3.4d, for low T_g materials, such as the soft elastomeric materials being considered in this current study, most of the temperatures used in DSI experiments correspond to the rubbery regime, wherein the shift factors have greater uncertainty. Therefore, DSI nano-DMA and bulk DMA results will be initially compared through van Gurp−Palmen (vGP) plots to estimate the quantitative accuracy of the DSI nano-DMA measurements. As the calculation of $|E^*|$, which is the abscissa of vGP

plots, can depend on the tip shape/geometry and size, the impact of these parameters on the quality of DSI nano-DMA calculations will also be discussed in this section.

3.4.3.1 Tip Size Effects: Large Radius vs Small Radius Parabolic Tips

Hertzian contact mechanics models rely on the assumptions of ideal tip geometry with large radii (section 2.2.3.2 & eq. 3.5). However, practical considerations of maximizing spatial resolutions during AFM scans (even for nano-DMA experiments using DSI methodology), require the use of the sharp parabolic tips, with smallest possible tip radii. The primary concern associated with the use of small radius AFM tips is that the tip geometry is not well-defined, and may be altered during experimentation. As noted in section 3.2, this is likely to impact the accuracy of the complex modulus calculations, which are dependent on the accuracy of the underlying contact mechanics model used. Moreover, the use of sharp AFM tips is also expected to result in high local strains resulting from the relatively larger indentation depths, thereby inducing nonlinear effects that may invalidate the use of time–temperature superposition principle used to shift nano-DMA data . In the latter case, even the phase angle (ϕ) comparisons between bulk and nano-DMA experiments are expected to be impacted. To estimate the likely impact of these factors on the quality of the DSI nano-DMA measurements, the effects of tip geometry and radius on the reliability of nano-DMA measurements were studied.

Initially, DSI experiments were conducted with the AFM tips having an ideally large tip radius (of 250 nm) as shown in Figure 3.3b. Parts (a) and (b) of Figure 3.8 compare these nano-DMA results (obtained through DSI experiments on a Dimension Icon AFM over a temperature range of -15 to $+50$ °C) for SBR and SNR respectively, to the corresponding bulk DMA vGP master curves.

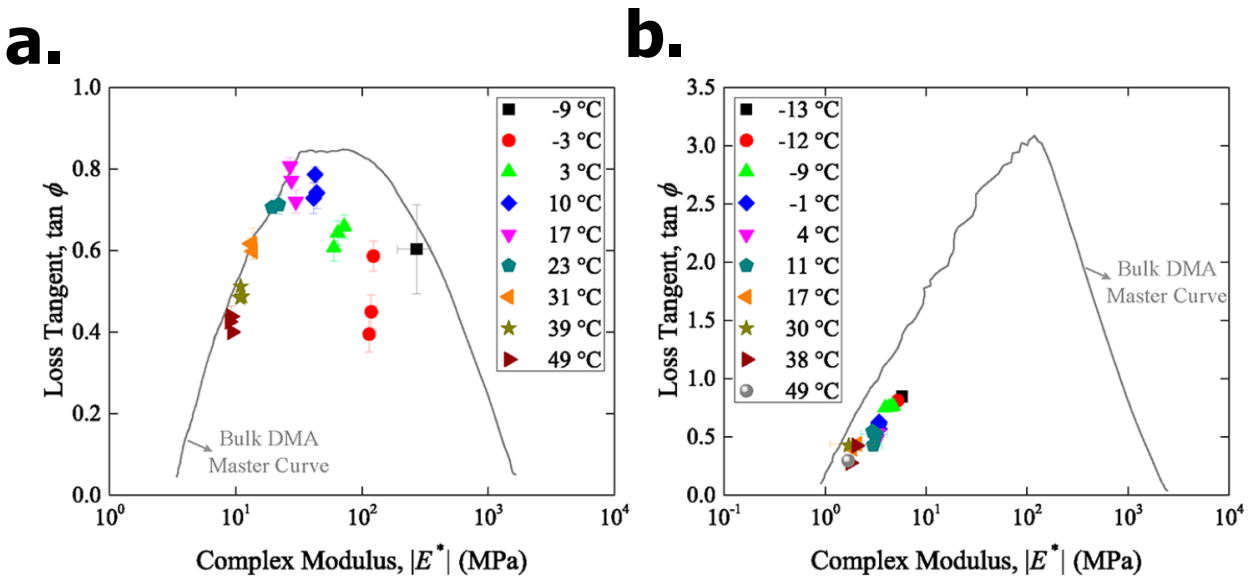

Figure 3.8: vGP plots comparing nano-DMA data (scatter) of (**a**) SBR and (**b**) SNR, obtained at 2 kHz frequency and different temperatures, using the DSI method on a Dimension Icon AFM with a large radius (~250 nm) circular AFM tip (and cantilever stiffness, k $\approx$ 250 N/m), to the respective bulk DMA master curves (solid lines). Bulk DMA master curves are the fit lines to the original raw data, previously depicted in Figure 3.5, parts (**a**) and (**b**), respectively. Error bars on DSI data represent the standard deviation of all the 1024 data points analyzed from a 32 $\times$ 32 pixels resolution DSI scan obtained at each temperature.

Generally, the DSI nano-DMA data in Figure 3.8a,b show the expected trend of increasing $|E^*|$ with decreasing temperature. Moreover, with the exception of some near-T_g measurements, the nano-DMA data for SBR in Figure 3.8a generally show good quantitative match with the bulk DMA master curve. The near T_g underestimation of loss tangent was reported earlier in Figure 3.6d, as well as by a previous study conducted by Nakajima and coworkers [82, 85], who suspected deviations from ideal contact mechanics conditions as the likely cause. However, it should be noted this issue persists in Figure 3.8a, despite the use of an ideally large radius, parabolic tip, thus suggesting that deviation from ideal contact mechanics conditions might not be arising from tip geometry/size concerns. The DSI nano-DMA measurements on SNR obtained from experiments with large radius tips, Figure 3.8b, also match the bulk DMA master curve fairly well, except for the small, yet consistent offset to the right of bulk DMA master curve. This offset can potentially be attributed to the overestimation of $|E^*|$ due to unaccounted adhesive effects in the Hertzian contact mechanics model. Accounting for adhesion would result in an increase of contact area and a consequent reduction in $|E^*|$, thus systematically shifting the nano-DMA data to the left. These adhesion effects are more prominent for DSI experiments on the low T_g SNR sample, which, despite the use of lower temperatures and higher frequency than the corresponding DSI experiments reported in figure 3.7, is still

largely in the rubbery regime.

Complementing the large radius tip data, a new set of DSI experiments were performed on both SBR and SNR, using sharp/small radius AFM tips: Bruker's recommended PF-QNM RTESPA probes. An RTESPA-300 with a nominal cantilever stiffness 40 N/m (experimentally measured value of 39.9 N/m) was used to probe the SBR sample while an RTESPA-150 with a nominal cantilever stiffness of 6 N/m (experimentally measured stiffness was 3 N/m) was used for the relatively softer SNR sample. Tip radii for these tips were determined to be ~35 and 32 nm respectively by the method described in section A.1. The resulting nano-DMA properties for SBR and SNR are shown in parts (a) and (b) of Figure 3.9, respectively, wherein they compare extremely well to the bulk DMA results, thus highlighting the ability of the DSI method to provide quantitatively reliable measurements. In fact, from Figure 3.9b, it is apparent that the DSI methodology is capable of providing reliable nano-DMA properties for the transition regime of SNR when the requisite low-temperature regime ($\sim -35°C$) could be experimentally accessed. At the same time, it is important to note that in case of SBR, although the temperature stage could go lower in temperature, the material became too stiff at lower temperatures to perform stable DSI indents, indicating the likely limitation of this technique below a material's T_g.

Interestingly, DSI nano-DMA data on SBR, obtained with sharp parabolic tips, Figure 3.9a, are slightly offset to the right, similar to the nano-DMA properties of SNR obtained with large radius parabolic AFM tips, Figure 3.8b. Although this systematic offset was then attributed to ignoring the effect of adhesion in $|E^*|$ calculations for SNR, the nano-DMA properties of SNR measured with sharp tips, Figure 3.9b, do not reflect the same offset. It is thus apparent that other experimental factors (apart from the tip size) could be impacting the quantitative accuracy of DSI nano-DMA data. Further studies to understand the complex interrelation between the choice of AFM cantilever stiffness, peak force, indentation depth, and experimental temperature relative to sample T_g are currently ongoing.

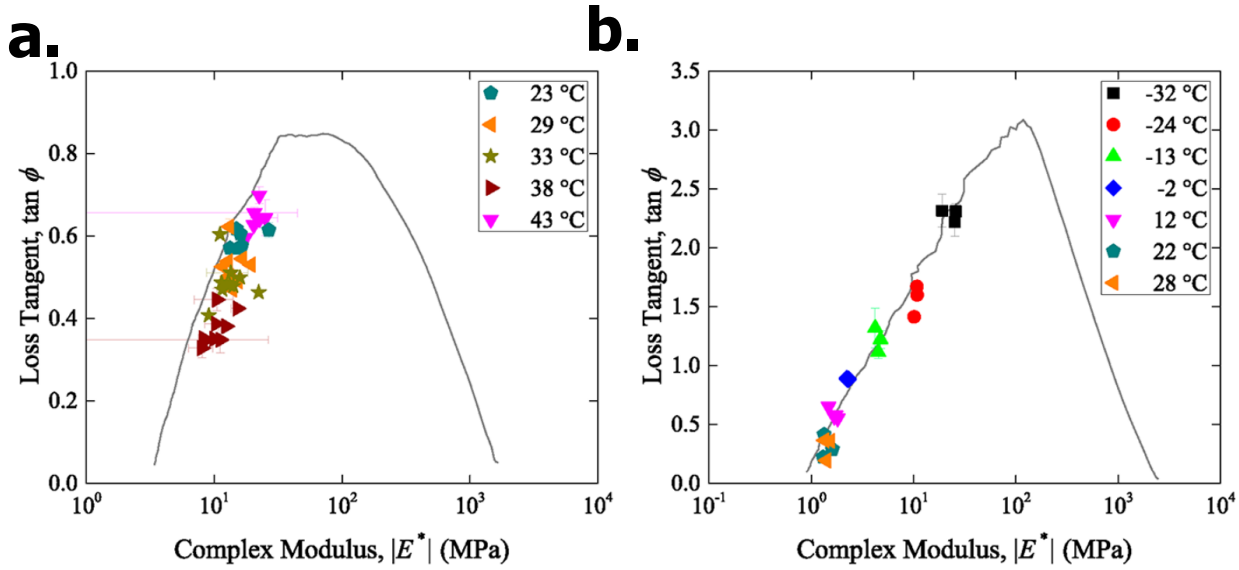

Figure 3.9: vGP plots comparing nano-DMA data (scatter) of (**a**) SBR and (**b**) SNR, obtained at 2 kHz frequency and at different temperatures using the DSI methodology on a Dimension Icon AFM, with sharp parabolic AFM tips (R = 30–35 nm, and k ≈ 40 and 3 N/m respectively), to the respective bulk DMA master curves (solid lines). Error bars on DSI data represent the standard deviation of all the 1024 data points analyzed from a 32 × 32 pixels resolution DSI scan obtained at each temperature.

3.4.3.2 DSI Data and Shift Factor (a_T) Evaluation.

To compare DSI nano-DMA data from AFMs having only temperature sweep capability to the bulk DMA master curves, the shift factor curve calculated from the bulk DMA data could be applied to the AFM data. However, the accessible DSI temperatures correspond to the rubbery regime temperatures of bulk DMA and, the bulk DMA determined shift factors in this regime are less accurate. Here we demonstrate an approach to use the DSI nano-DMA data itself to improve the accuracy of the rubbery regime shift factor fit from bulk DMA, even in this case where the AFM only has temperature sweep capabilities.

Per section 3.4.3.1, the $|E^*|$, $\tan\phi$ values pairs from the DSI experiments are consistent with the bulk DMA measurements at temperatures above T_g. As shown in Figure 3.6c, a VFT fit, eq 2.7, can be applied to the reliable bulk DMA shift factors from the transition regime and extrapolated to the rubbery regime (dashed lines in Figure 3.10a,c, which will henceforth be referred to as "extrapolated VFT" shift factors). The DSI data from figures 3.8 and 3.9 are then replotted in frequency space using these extrapolated VFT shift factors, figure 3.10c,d.

However, we can use additional information from the DSI data to improve the shift factors in the extrapolated region of the VFT fit. Since the DSI data used in this section were obtained at a frequency of 2000

Hz, which is 2 orders of magnitude higher than the highest frequency used in bulk DMA, DSI viscoelastic data that was obtained at temperatures corresponding to the rubbery regime of bulk DMA could still be in the transition regime and provide reliable shift factors. Hence, the rubbery regime DSI nano-DMA shift factors can be estimated by a simple mapping: for each AFM data point, find the closest point on the bulk DMA $\tan\phi$ master curve, take the corresponding shifted DMA frequency from the bulk DMA master curve, and divide by the AFM frequency ($\omega_{AFM} = 2000$ Hz), as given by eq 3.9:

$$(a_T)_{AFM} = \frac{(\omega a_T)_{bulkDMA}}{\omega_{AFM}} \tag{3.9}$$

This mapping provides an extended set of shift factors in the rubbery regime from the DSI nano-DMA data, which can be used in conjunction with the reliable transition regime bulk DMA shift factors, to cumulatively provide an improved "combination VFT fit" (solid lines in Figure 3.10a, b). DSI nano-DMA results obtained using large radius (figure 3.8) and small radius (Figure 3.9) parabolic tips were used to estimate these rubbery regime shift factors for SBR and SNR via eq 3.9, Figure 3.10a,b. Shift factors from DSI experiments at temperatures below 10 °C were ignored for SBR since they greatly deviated from the bulk DMA v-GP plot, as seen in figure 3.8a. The solid combination VFT fit lines show a small improvement over the dashed extrapolated VFT fit lines, Figure 3.10a,b. However, this small change in shift factors can have a measurable impact on the frequency dependence of the DSI nano-DMA data. In figure 3.10 (e) and (f), DSI nano-DMA data (for SBR and SNR respectively), now shifted in accordance to the combination VFT fits, are compared to their respective bulk DMA master curves. A comparison of of figure 3.10 (c) and (e) shows that a small difference in shift factors produces a noticeable difference in the frequency space nano-DMA master curves of SBR. Use of the refined combination shift factors results in an improved quantitative agreement between bulk and DSI nano-DMA master curves, figure 3.10e, which lasts until the peak of the loss tangent curve. Although the difference between extrapolated and combination VFT fits in SNR, Figure 3.10b, are similar to those observed in SBR, figure 3.10a, the impact of this difference on the DSI master curves for SNR is limited (comparing parts (d) and (f) of figure 3.10).

Owing to the relatively higher frequency of the DSI method, this methodology can provide high-temperature shift factors corresponding to the rubbery regime of bulk DMA experiments and help construct accurate shift factor curves and more reliable viscoelastic master curves for homogeneous materials. The methodology helps create DSI nano-DMA master curves when using commercial AFMs that only provide temperature sweeping capabilities under limited frequency settings.

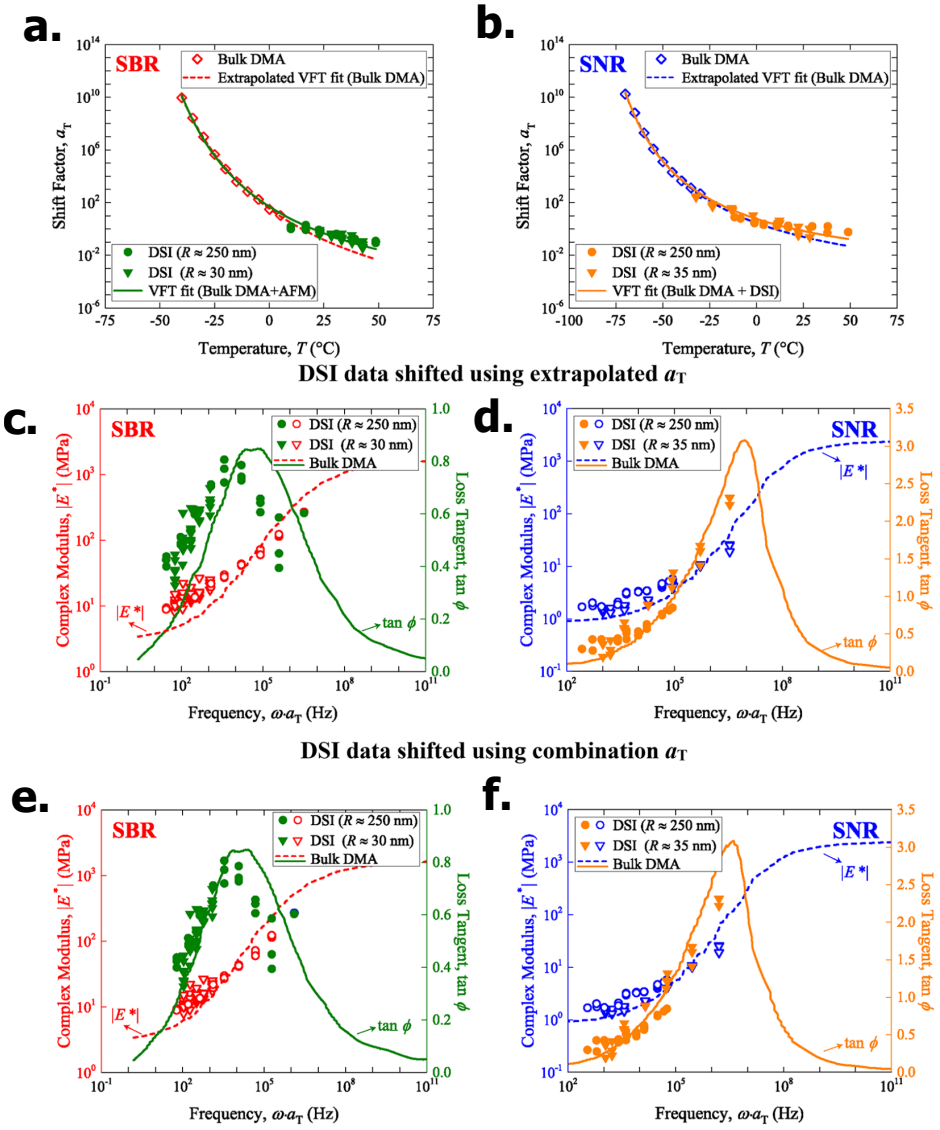

Figure 3.10: Empirical (scatter data) and VFT fit (lines) shift factors vs temperature for (**a**) SBR and (**b**) SNR, showing the different types of fits to the VFT equation eq. 2.7. Dashed lines in parts (**a**) and (**b**) represent the "extrapolated VFT fits" to eq 2.7, obtained by only using the bulk DMA transition regime shift factors (open diamonds) and extrapolating the fit to the (high temperature) rubbery regime. Solid fit lines in parts (**a**) and (**b**) represent the "combination VFT fits" to eq 2.7, obtained by fitting both the transition regime bulk DMA shift factors (open diamonds) and DSI nano-DMA shift factors (filled symbols that were calculated using eq. 3.9). Circles represent DSI data obtained with large radius parabolic AFM tips, while the inverted triangles represent DSI data obtained from DSI experiments with small radius/sharp parabolic AFM tips. Comparison of bulk vs nano-DMA $|E^*|$ and $\tan\phi$ master curves in frequency space for (**c**, **e**) SBR and (**d**, **f**) SNR was carried out for both sets of VFT fits identified in parts (**a**) and (**b**), respectively. Extrapolated bulk VFT fits (dashed lines in parts (**a**) and (**b**)) were used to shift DSI data in parts (**c**) and (**d**), whereas the revised, combination VFT fits (solid lines in parts (**a**) and (**b**)) were used to shift DSI data in parts (**e**) and (**f**).

3.4.4 Validation of DSI Nano-DMA Method for High Resolution Viscoelastic Property Mapping of Heterogeneous Soft Materials

The DSI method was developed to enable fast and quantitatively accurate, high resolution spatial mapping of viscoelastic property gradients in soft heterogeneous materials such as polymer blends and nanocomposites. Having established the quantitative validity of the DSI methodology in the earlier sections through experiments on homogeneous elastomers, the objective here is to demonstrate a preliminary validation of the applicability of the DSI methodology to spatially map the viscoelastic properties of a heterogeneous soft material system. Specifically, the viscoelastic properties of an elastomeric blend sample (constituted of 75 wt % SBR and 25 wt % SNR) were quantitatively mapped with the DSI nano-DMA methodology by performing a room temperature nano-DMA scan across a 1×1 μm^2 area with 64 $\times$64 pixels resolution (spatial resolution of ~15 nm). Figure 3.11a,b illustrate the spatial maps of $\tan\phi$ and $|E^*|$ and measured from this nano-DMA experiment, alongside the standard PF-QNM log(DMT modulus) map, Figure 3.11c, taken prior to the nano-DMA scan (as described in section 3.2). Clearly, an excellent contrast was achieved within the DSI viscoelastic property scans, particularly the loss tangent scan in Figure 3.11a, reproducing the same local microstructure visualized with Bruker's standard PF-QNM DMT modulus map. This consistency indicates the ability of the DSI approach to successfully capture the local microstructural heterogeneity of the sample, without inducing any damage to it despite performing relatively deep ($\delta > R$) dynamic indentations (similar to contact mode scanning) with a sharp AFM tip, in the material's rubbery state. It also highlights the method's ability to produce real-time spatial maps when implemented into commercial AFM software, at least when considering the simplicity and directness of the phase angle (or loss tangent) calculations involved with this method.

The first approach to verify that this high-resolution DSI scan produced quantitatively accurate nano-DMA properties, involved the selection of two random pixels in the DSI scan such that each lay deep within one phase. The two representative points are depicted in Figure 3.11a with a black triangle (embedded deep within the SBR phase) and a white star (embedded deep within the SNR phase). The corresponding $|E^*|$ and $\tan\phi$ measurements at these two locations were compared to the corresponding bulk DMA master curve for SBR and SNR in parts (d) and (e) of Figure 3.11. An excellent agreement between the two sets of data can be clearly observed. It is important to note that even the apparent overestimation in the DSI measurement of SNR $|E^*|$ is similar to the previously observed discrepancy for homogeneous SNR samples, in Figure 3.7a and Figure 3.10e,f.

To further ensure that the viscoelastic properties measured across the scan were within reasonable limits, $|E^*|$ and $\tan\phi$ values at each of the 4096 pixels in the DSI scan, shown in Figure 3.11a,b were plotted in Figure 3.11f and compared to the bulk DMA master curves of homogeneous SBR and SNR. Every single point from the DSI nano-DMA scan of the blend sample fall in between the bounds of SBR and SNR master curves, and are clearly closer to the SBR phase, due to its dominant weight fraction (of 75%). It is also important to note that the nanoDMA data from the two pixels corresponding to pure SBR and SNR phases, Figure 3.11d,e, are also plotted in Figure 3.11f. Clearly, these DSI data from the two phases more closely represent the upper and lower bounds for the band of blend properties depicted in Figure 3.11f, as should be expected, thus validating the quantitative reliability of the DSI methodology for capturing high-resolution viscoelastic property maps of heterogeneous soft materials.

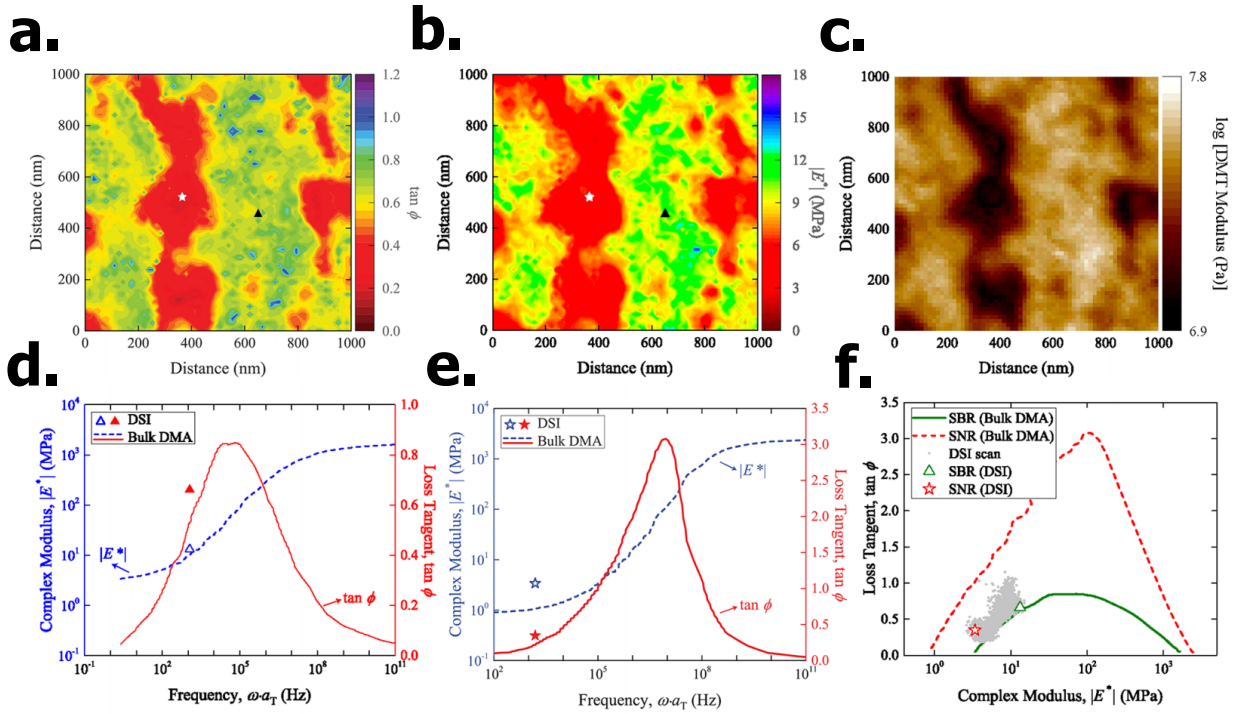

Figure 3.11: Spatial maps of (**a**) $\tan\phi$ and (**b**) $|E^*|$ obtained by performing a high-resolution (64 × 64 pixels) DSI nano-DMA scan over a 1 × 1 μm^2 area of an SBR-SNR blend sample (75/25 wt %). The centers of the star (white) and triangle (black) symbols in parts (**a**) and (**b**) depict the locations of the coordinates for pure SBR and pure SNR regions respectively, that were used for quantitative validation of the DSI methodology for heterogeneous materials in parts (**d**) and (**e**). (**c**) Standard PF-QNM modulus map scan performed over the same region, taken immediately prior to the performing the DSI scan, is also provided as a reference image to compare the spatial blend morphology revealed by the two methods. The nano-DMA properties measured at the two pixels depicted in parts (**a**) and (**b**), corresponding to SBR and SNR phases, are quantitatively compared to their corresponding bulk DMA master curves in parts (**d**) and (**e**), respectively. (**f**) Nano-DMA properties for all 4096 pixels in the scan are compared to the bulk DMA master curves through a vGP plot. Image taken with Bruker Dimension Icon adapting PF-QNM mode with DSI procedure.

3.4.5 Initial Results for Rubber Composites

Initial work on the viscoelastic properties of rubber composites have been shown to be quite tricky due to many reasons. The first is the fact that since AFM is a 2D surface measurements, particles underneath the surface of a material could result in local modulus changes that are not strictly due to interphase effects. One of the ways we tried to get around this was by making a "sandwich" sample, as described in section 3.3.1.2. A cross section of this "sandwich" can then be prepared using a cryo-microtome. Figure 3.12a shows an optical image of the sandwich sample after cryo-microtoming. The carbon black layer can clearly be seen on the left side of the image. Scanning the AFM tip across this layer allows individual particles to be found

without having to worry about the effects of neighboring particles hidden beneath the surface, as seen by the PF-QNM modulus map image in Figure 3.12b.

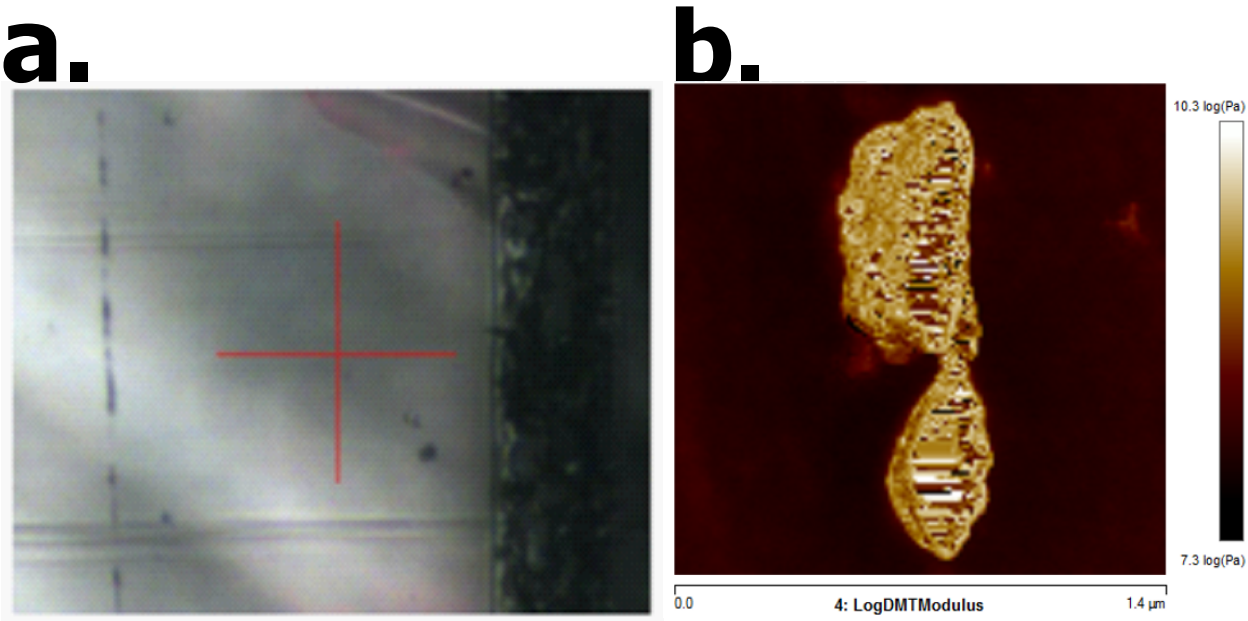

Figure 3.12: (**a**). An Optical microscope image of carbon black-rubber slice. Carbon layer is clearly seen in left side of image. (**b**). AFM image of a CB black particle found in the layer.

With a particle identified, the DSI viscoelastic property technique could be performed on the zoomed in area on the right of the particle in Figure 3.12b, shown in Figure 3.13a using a peak force of 5nN and an amplitude of 7.8nm. However, not all of the viscoelastic measurements can be trusted. Analysis of the force curves in the DSI technique of the matrix area (marked by the red dot in figure 3.13a) shows a nice cyclic force-displacement curve needed for the DSI analysis to work, shown in in Figure 3.13b. However, on the particle, (marked by the blue dot in figure 3.13a), since the particle itself is orders of magnitude stiffer than the matrix and not inherently viscoelastic , the resulting indent is not cyclic (see Figure 3.13c), and thus viscoelastic properties cannot be measured using the DSI method. However, the analysis software will still try to find a measurement from these curves, resulting in a loss tangent line scan as seen in Figure 3.13d across the middle of the image. As seen, to the right of this plot, most of the data is around a loss tangent of 0.9, and relatively consistent. This regular data corresponds to the matrix. However, as it gets closer to the particle on the left, the measured loss tangent values are now all over the place. Thus, the data needs to be filtered to remove bad data from non-cyclic force displacement curves.

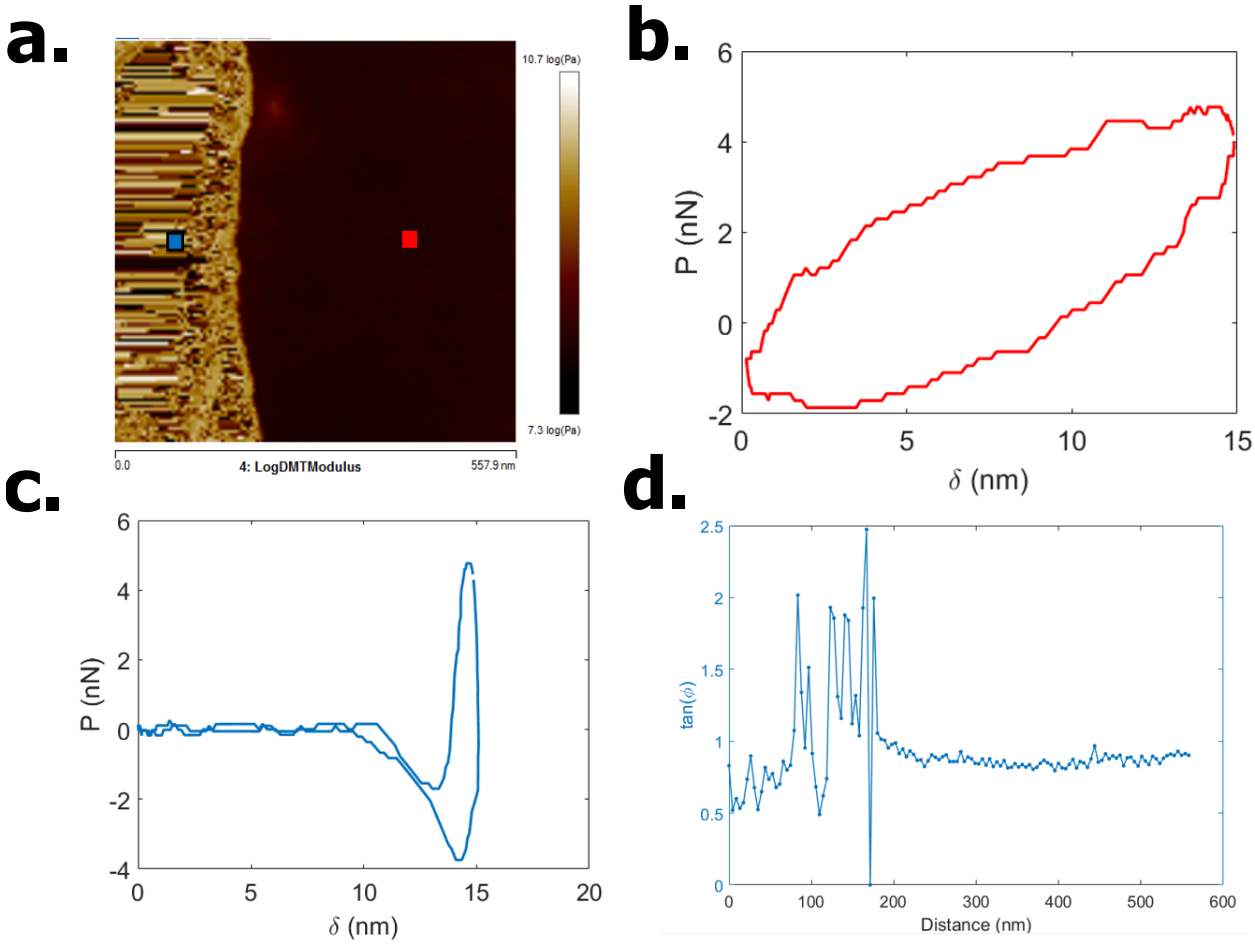

Figure 3.13: (**a**). Zoomed in region (558nm x 558nm) of the particle shown in Figure 3.12b. (**b**), DSI Force Displacement curve for the red pixel in (a), representing the matrix. (**c**). DSI Force Displacement curve for the red pixel in (a), representing the particle. (**d**) Loss Tangent map from DSI method across the center of the map in (a).

The best way to filter this data is to look at the sine fit for the force vs. time , eq. 3.1. A poor fit would mean that the tip is pulling out of the sample, and so the data should be ignored. The quality of the fit can be evaluated by the normalized root mean square error described in eq. 3.10 where N is the total number of experimental data points used in the fit, P_j, is experimental force measurement at $t = t_j$, $\hat{P}_j$, is force predicted by the sine fit at $t = t_j$. The summation is normalized by is the force amiplitude,P_0, so that resulting value is unitless. Figure 3.14a shows the same loss tangent line scan in Figure 3.13c in blue as well as the corresponding relative root mean square error of the sine fit of the force vs. time curve (normalized to the matrix value). This sets the relative error in the matrix to be about 1. As you approach the particle, the error in the fit will start to shoot up rapidly. This point can be used as the estimate of where the rubber

meets the particle (marked by the vertical red line). Once this is marked, there is clearly a slight increase in the loss tangent near the particle compared to the bulk loss tangent data. Where the data starts to deviate from the matrix loss tangent values by 5% is marked by the green vertical line, as an estimate as the end of the interphase. For this line scan, this interphase length was measured to be 52.72nm. This analysis was repeated on every line in the loss tangent map in Figure 3.14b, showing an average of 50.83±25.45nm. The average interphase measurement from this loss tangent map has a few concerns. First, the standard deviation is very large (50% of the measured value), thus there is quite a spread in the data, this could be due to the fact that the particle is still an irregular shape, and may lead to different tip interactions in different areas. Second, the tip radius is around ~30nm which is not much smaller than the measured interphase length, thus there is a likely possibility that some of the bulk measurement deviation is due to tip-substrate probe effects due to the physical interaction of the probe indenting near a hard substrate, which will overestimate any true interphase effects [13, 97]. Thus, in order to get any interphase information from these experiments, these geometry and probe effects need to be deconvoluted, which will be the focus of the next chapter.

$$NRMSE = \frac{1}{P_0}\sqrt{\frac{1}{N}\sum_{j=1}^{N}\left(P_j - \hat{P}_j\right)^2} \tag{3.10}$$

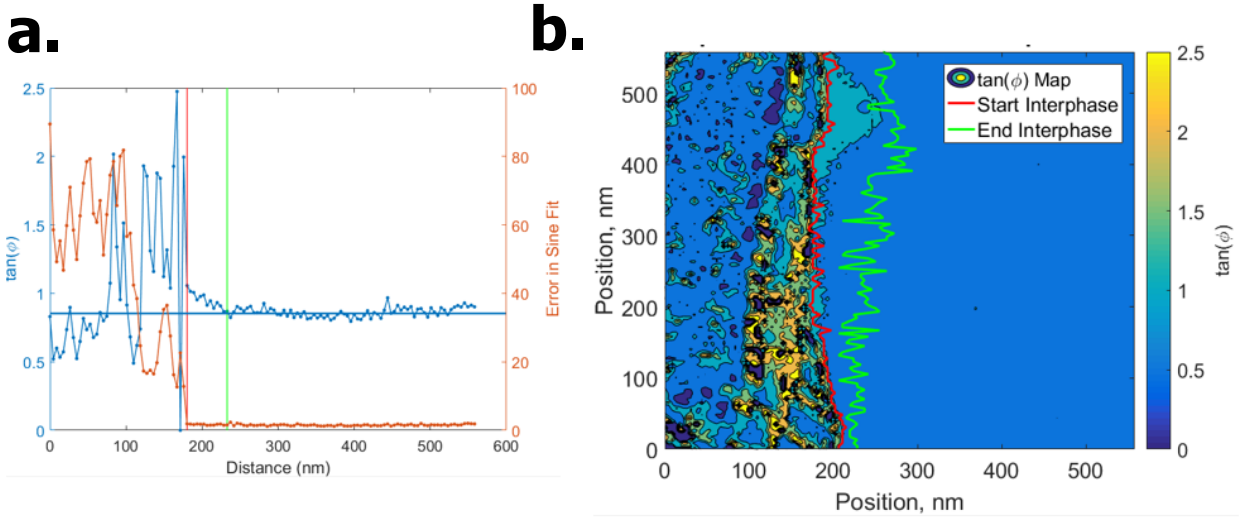

Figure 3.14: (**a**). Same loss tangent line scan as in 3.13d (blue) as well as the corresponding NRMSE (eq. 3.10) in the sine fit at each point (red). The red vertical line corresponds to the point where the error starts to increase and the green vertical line is when the loss tangent data starts to deviate from the baseline. The distance between these lines is 52.72nm. (**b**). This same analysis applied to every line of the loss tangent map around particle shown in figure 3.13a. Average interphase length is 50.83±25.45nm.

Nevertheless, preliminary investigations of the DSI technique were conducted on *in-situ* carbon black-SBR composites. Figure 3.15a shows a 2μmx2μm PF-QNM elastic modulus map scan of a 10wt% carbon black in SBR where the DSI technique was applied. The resulting viscoelastic maps of $\tan\phi$ and $|E^*|$ are shown in 3.15b and c, respectively, with regions of high RMSE of the sine fit of the force vs. time curve (>5x the average matrix value) set to zero (dark blue). In both cases, these dark blue regions correspond presicely with the high modulus particles in the PF-QNM modulus map in 3.15a, although they are noticeably larger, suggesting that some of the matrix/interphase region near the particles are lost due tip size affects. Nevertheless, regions near the particles but sufficiently far away from the paricles that are less likely to be caused solely by geometric effects show increases in both modulus and loss tangent when compared to the regions furthest away from particles. An increase in both loss tangent and complex modulus is consistent with a shift of the SBR master curve towards higher frequency (towards the glassy regime) by approximately 1.3 orders of magnitude, and similar behavior has been seen in other AFM viscoelastic investigations of rubber-carbon black nanocomposites [98]. A shift towards the glassy regime for rubber near a rigid particle makes sense since the molecular motions of the rubber are constrained by the rigid particles. These are very preliminary results, and more work needs to be done to verify these trends are consistent, and to better understand tip effects. However, the initial results can be used for preliminary investigations in predictive computational models, some of which will be discussed in the future work section of chapter 8.

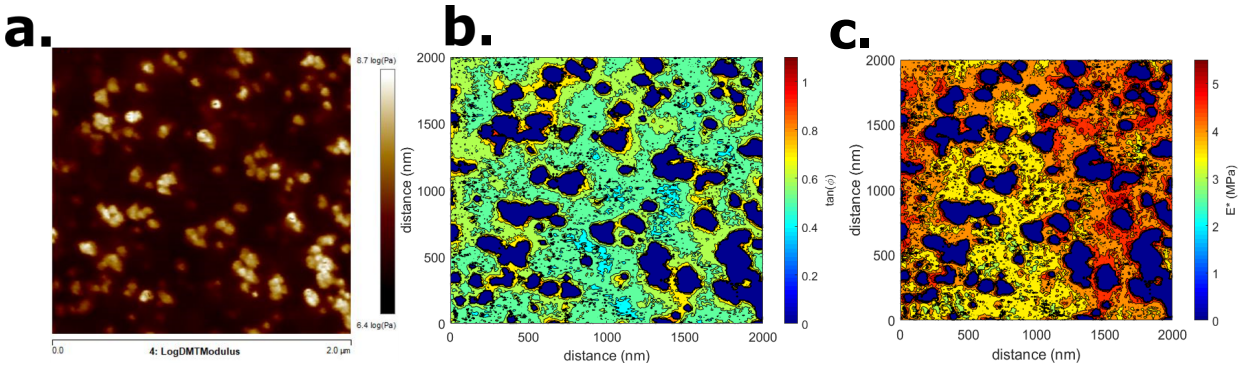

Figure 3.15: (a) Standard 2μmx2μm PF-QNM elastic modulus map scan of a 10wt% carbon black in SBR, taken immediately prior to the performing the DSI scan. The viscoelastic maps of $|E^*|$

3.5 Conclusion

A novel, versatile, quantitatively accurate and temporally fast AFM-based dynamic scanning indentation (DSI) nano-DMA method, which enables real-time, high-resolution spatial mapping of the local viscoelastic

properties of heterogeneous soft materials, using the existing capabilities of commercial AFMs is presented. This novel approach exploits the recent developments in low-frequency sinusoidal force ramp-based, force-curve capturing nanomechanical mapping modes of commercial AFMs, through simple, yet elegant control of the operational parameters of peak indentation force and tip oscillation amplitude. The quantitative accuracy of the DSI nano-DMA methodology was validated by demonstrating an excellent agreement between the viscoelastic properties obtained from DSI experiments on two different homogeneous elastomers (SBR and SNR) and a heterogeneous elastomer (SBR-SNR blend sample) to the corresponding bulk-scale viscoelastic master curves of SBR and SNR (for frequencies below and temperatures above T_g). In case of the elastomeric blend sample, it is shown that quantitatively accurate DSI nanoDMA scans with a spatial resolution of $\sim$15 nm could be achieved.

These extremely favorable quantitative comparisons between nano-DMA properties measured from AFM-based DSI experiments and standard bulk DMA measurements were possible despite relying on relatively simple viscoelastic property calculations for DSI data; as a first-order approximation basic Hertzian contact mechanics were assumed, while the assumption of constant contact area during dynamic indentation was demonstrated to be valid using a fracture mechanics-based energy release rate calculation. Incorporating future improvements and complexity of contact mechanics models used for nano-DMA analyses of the data provided by the DSI method should be relatively trivial and could only enhance the quality of the viscoelastic measurements from the DSI methodology.

Using state-of-the-art commercial AFMs that provide reasonably good temperature and frequency sweep capabilities, such as the Asylum's Cypher ES and MFP-3D Infinity AFMs, the full potential of the DSI method to enable the empirical and independent construction of quantitatively accurate nano-DMA viscoelastic master curves was demonstrated. These nano-DMA master curves spanned an effective frequency range of 5 decades, which is at least an order of magnitude better than the previously reported high-resolution nano-DMA methods. It was further shown that, despite the restricted availability of only one or two discrete operating frequencies on some commercial AFMs (such as the Bruker AFMs), the DSI method could be still applied successfully over multiple temperatures and continue to provide quantitatively reliable viscoelastic data over a similarly effective frequency span of 5 decades. A relatively simple, custom-built thermal enclosure and heating/cooling stage was shown to be useful in accessing temperatures between -35 and $+50$ °C in this study. In the case of the latter experiments, on AFMs without frequency sweeping capabilities, independent construction of frequency space nano-DMA master curves was not possible; instead, AFM data at different temperatures had to be shifted based on a priori knowledge of viscoelastic shift factors. A

methodology that relies on the use of the van Gurp–Palmen representation of viscoelastic data (i.e, plots of $|E^*|$ and $\tan\phi$) to analyze the quantitative accuracy of the DSI data, and to augment/correct DMA shift factors in the rubbery regime was developed and demonstrated.

Preliminary investigations have also been performed on model composite and *in-situ* carbon black rubber composite systems, showing increased loss tangent and complex modulus values around the carbon black material, consistent with a shift of the matrix properties towards the glassy regime. This data can be used as a reference for improving computational rubber composite models, but more work needs to be done to determine the effect of geometric tip constraints, and the temperature/frequency dependence of this interphase regime. Cumulatively, these capabilities of this novel DSI methodology render it a powerful and easily accessible tool for studying the local thermorheological behavior of complex soft materials, which opens the doors to study important nanoscale phenomena such as the viscoelastic response of spatially confined polymers and biomaterials.

Chapter 4

Understanding AFM Indentation Data in Rubber Composites using FEA Simulations

Atomic force microscopy (AFM) is a powerful technique for imaging polymer nanocomposites as well as other systems with heterogeneous material properties on the nanoscale. However, the quantitative measurement of modulus is highly susceptible to convoluting structural effects due to the finite tip radius and stress field interactions with particles and substrates which are often termed the "substrate effect" or "thin film effect". We present an empirical master curve that can model the change in measured modulus (E_{MC}) due to structural effects in an AFM indentation on a soft material near a stiff filler, using N121 and N660 carbon black−styrene−butadiene rubber nanocomposites as examples. Finite element analysis is combined with experimental AFM data across an interface at increasing indentation depths to create a robust method for confirming or rejecting the presence of an interphase layer in AFM. From the raw data, which is initially inconclusive, we reasonably estimate the width of the loosely bound layer (ξ_{int}) surrounding each (strongly interacting) N121 particle to be 50−60 nm after deconvolving the substrate effect. In comparison, we found no significant loosely bound layer around the (weakly interacting) N660 particles. While this technique is demonstrated for polymer nanocomposites, the strategy could also be applied to multiphase soft materials.

This chapter reproduces work from "Deconvolution of Stress Interaction Effects from Atomic Force Spectroscopy Data across Polymer−Particle Interfaces" published in *Macromolecules* in 2019 [14]. This work

was published by myself with co-authors, David W. Collinson, Dr. Kenneth R. Shull, and Dr. L. Catherine Brinson, where myself and David W. Collinson contributed equally to the work. All of the AFM experiments were conducted by me, while David W. Collinson conducted the FEA simulations. We worked together in analyzing and connecting the experiments and simulation data.

4.1 Introduction

Rubber nanocomposites are an important engineering material with many industrial uses. Engineering rubbers are typically filled with carbon black or silica nanoparticles as a reinforcing agent, and the nanoscale reinforcement is responsible for the high strength and toughness of rubber nanocomposites compared to that of pure rubber systems [99–101]. The reinforcement of the rubber also leads to macroscale behavior that deviates significantly from continuum scale predictions of the elastic [99] and viscoelastic [101] mechanical properties based on properties of constituents alone. Nanoparticles are able to reinforce rubber through multiple mechanisms including hydrodynamic reinforcement [68, 102], altering the polymer network [103], filler–filler interactions [101], and polymer–filler interactions [104]. Of these, the rubber–filler interactions best explain the observed viscoelastic[105, 106] and elastic [107] behaviors of rubber nanocomposites at the bulk scale. The rubber–filler interactions are typically described as a layer of "bound rubber" or an "interphase", which manifest as a region of rubber surrounding the particles with properties different from the bulk rubber phase due to chemical and physical interactions between the filler particle and the rubber matrix.

Atomic force microscopy (AFM) is a promising tool for characterizing polymer nanocomposites at the nanoscale [108]. Measurement artifacts associated with indentation, particularly the "structural indentation effect", also known as the "stress interaction effect" or "substrate effect", can convolute the measurement of material modulus in multiphase composites. While finite element analysis (FEA) techniques have been developed to deconvolute the interphase in model systems [13, 109], many commercially important nanocomposites have highly irregular morphology, which cannot be replicated easily in FEA. Therefore, techniques that provide a simple framework to extract the interphase extent (ξ_{int}) present in in situ polymer nanocomposites free from stress interaction effects will improve our understanding of the processing–structure–property relationship that results in a bound rubber layer.

4.1.1 Rubber Nanocomposites and the Bound Rubber Layer

The bound rubber layer has been shown to exhibit higher stiffness and longer relaxation times compared to the matrix and, as such, can be thought of as an interphase between the particle and the matrix. This interphase region is often considered to exist as a bilayer with a stiff glassy region that directly interacts with the particle, which is surrounded by a loosely bound, softer layer, and both may contribute to the overall properties of the composite [104, 110].

The extent of the bound rubber and its impact on the bulk scale properties is the result of the strength of the rubber interaction with the carbon particle. The interaction strength between the particle and the rubber is affected by the surface area of the particle and the number of chemically active sites for rubber molecules to interact with the surface of the carbon [111]. The resulting impact of the bound rubber layer on the bulk mechanical properties of the composite will also depend on the particle size or agglomerate [100]. A larger particle size will reduce the particle surface-area-to-volume ratio in the composite, lowering the overall volume fraction of the bound rubber layer in the composite and reduce the contribution of the bound rubber layer to the properties of the composite. Understanding the extent and magnitude of the bound rubber layer in situ is of vital importance for material design and development [112].

While there have been numerous studies to quantify the extent and strength of the interphase region both directly [13, 69, 70, 113–115] and indirectly [116, 117], a quantification of the interphase extent free from stress interaction effects in AFM remains elusive for in situ carbon black particle−matrix composites, where high geometric complexity due to the nature of carbon black makes analysis difficult. Multiple studies have indirectly measured the extent of the interphase region within uncross-linked rubber composite systems. Solution techniques that dissolve unbound rubber in toluene or another suitable solvent leave the insoluble bound rubber layer attached to the particle from which the wt % of bound rubber can be calculated. The extent of the remaining bound rubber layer can be highly dependent on the choice of solvent and experimental conditions [118]. Small-angle X-ray and neutron scattering, as well as nuclear magnetic resonance (NMR), can estimate the interphase extent to be between 1 and 10 nm [115–117, 119]. However, the sensitivity of such methods to the loosely bound layer varies [119] with the work of Tadiello, *et al.* [115], suggesting disagreement between NMR and AFM as to the true extent of the bound rubber layer. Complicating the matter further, the extent of the bound rubber layer as measured by NMR can increase by an order of magnitude when the temperature during measurement is close to the T_g of the polymer [120]. With careful treatment of the stress interaction effects associated with AFM indentation in multiphase composites, the

extent and magnitude of the bound rubber layer can be characterized in in situ composites with greater confidence.

4.1.2 Previous AFM Studies on Rubber Nanocomposites and Existing Challenges

The contrast in stiffness in the interphase layer compared to that in the bulk matrix along with the 1−100 nm length scale makes AFM a suitable technique for the direct measurement of the extent and stiffness change of the bound rubber. Limiting the accuracy of the measurement are structural effects, which can convolute indentation measurements and are a major factor limiting the accuracy of local modulus as measured in AFM. The most severe artifact occurs when two different phases are directly contacted simultaneously by the AFM tip, which then measures a single contact stiffness with direct contributions from both phases. However, important indirect structural effects arise when the AFM tip is wholly in the polymer phase because the force−displacement curve measured is a convolution of the response of a finite volume of material surrounding the tip, as opposed to a discrete infinitesimal material point. Therefore, near a surface or particle, the volume probed in the force−displacement relation includes that foreign body and changes the effective compliance of the probed volume [97, 121], impacting the local modulus measured for the polymer. This particular behavior is commonly termed as the substrate effect or "thin film effect". The size and extent of structural effects are highly dependent on the size of the tip used and indentation depth [122], the relative stiffness and location of neighboring phases relative to the indentation [13, 70], the viscoelastic state [123], and the incompressibility of the indented material [124]. In particle−matrix composites, the indentation measurement can be further complicated due to the shape of the particle targeted for analysis or the presence of other nearby or subsurface particles [113]. The particle geometry itself can influence the magnitude of the stress interaction effect if the particle shape and subsurface geometry are such that the material between the particle and the indenting tip becomes highly confined [123]. In addition, a nanoparticle is a nonideal substrate and is expected to deflect or rotate under load.

Several previous studies have sought to address, remove, or account for these structural effect issues in the interphase modulus profile as measured by AFM by iterating a material profile input into FEA until the modulus as measured by simulated indentations matches the experimental profile [13, 76, 109, 113]. However, this technique is limited to simple model geometries and cannot be applied to complex in situ composites due to the highly variable and unknown filler geometries and is especially difficult for fillers with complex

particle morphology such as carbon black.

4.1.3 Challenges in High-Speed Indentation Modes of Polymer Nanocomposites

High-resolution spatial maps of local elastic properties in soft heterogeneous materials have been obtained from experiments on model nanocomposite samples, using scanning force spectroscopy techniques (SFS), which use a force setpoint (P_{max}) for feedback [75, 76, 109]. SFS techniques have the ability to collect thousands of force−displacement curves per second and map out local mechanical properties in two dimensions without having to manually set x and y positions at each point in the array [125]. A number of studies have shown that in the best-case scenario, one can still expect errors in the absolute modulus at minimum to be between 10 and 15% due to uncertainty in the precise contact mechanical model and errors in cantilever stiffness and deflection calibration [126, 127]. This error is exacerbated for viscoelastic materials, since the time dependence of the material response, as well as the absence of robust and widely accepted viscoelastic contact mechanical models, leads to more uncertainty [128]. Thus, some studies have chosen to compare modulus values in multiphase systems, such as rubber blends and composites, by normalizing the modulus measurement to a bulk value, such as the comparison of an interphase region modulus measurement to the noninterphase bulk modulus measurement [75, 76, 109]. This allows the comparison of different AFM indentation responses related to the material stiffness and modulus in different regions of the same scan even with the uncertainty of the accuracy of the absolute measurement.

However, the accuracy of modulus maps produced of rubber composites is further complicated by the existence of structural interaction effects near the rubber−particle interface. In a two-dimensional modulus map, there are particles throughout the image, and the probed volume near the particle surface is the region of interest (ROI) for particle−matrix interphase effects. The structural indentation effect thus impacts the validity of any measured interphase modulus in these maps, which will report a larger and/or broader modulus magnitude variation near the stiff particles than the real values. Thus, this investigation explores a way to remove these modulus artifacts from indentations in the rubber to help improve the accuracy of AFM modulus maps of composite material interphases. Ideally, AFM indentation experiments would accurately measure the modulus magnitude and width of the interphase layer, but we will focus primarily on understanding the broadening of the measured interphase width and leave the modulus magnitude of the interphase layer to future investigations.

In this study, we develop a simple, easily applied technique to (**1**) determine whether the alteration of a modulus profile of a soft material near a rigid substrate or particle is due to the existence of one or

more interphase regions or just the stress interaction effects, and (**2**) estimate the width of the interphase regions when they are detected. The contact radius-dependent structural indentation effect is first established using the simulation of indentation experiments at different depths with an FEA model of known geometry and material properties. When there is no interphase, the modulus profiles of different indentation depths collapse on a single curve when normalized by the contact radius but will remain separated when there is an interphase. The structural indentation effect can be quantified and subtracted from the modulus profiles from simulations with interphase regions, and the interphase width can be determined by shifting the modified profiles laterally to collapse on a single curve. We then apply the technique developed to experimental data on a variety of carbon–styrene–butadiene rubber (SBR) composites with a variety of interaction strengths and geometries. The technique can successfully remove structural effects from inconclusive raw data profiles and estimate the interphase width even when multiple interphase layers exist. This study will look at only one-dimensional modulus profiles, but it will provide a basis for structural indentation effect removal to be applied in twodimensional AFM maps in future work.

4.2 Methods and Materials

4.2.1 Materials

4.2.1.1 Rubber Nanocomposite

Rubber composites of 10 wt % carbon black and sulfur cross-linked, anionically prepared styrene–butadiene–rubber (SBR, SLF16S42) were provided by The Goodyear Tire & Rubber Company. Two different carbon blacks were used to form the composites, N660 and N121. N660 particles are more spherical and less absorptive to phthalates, iodine, and nitrogen, whereas N121 is higher in surface area and more absorptive [129]. Thus, we expect higher chemical absorption onto the surface of N121, which should lead to stronger interfacial effects. The rubber composites formed using N660 carbon black and the N121 carbon black as the fillers are subsequently referred to as "N660" and "N121", respectively.

4.2.1.2 Model Graphite Sample

To simulate a model flat carbon– rubber interface, a rubber–graphite "sandwich" sample was made. SBR rubber was prepared by mixing 10 wt % uncross-linked SBR (SLF16S42, provided by The Goodyear Tire & Rubber Company) in toluene with 0.5 phr dicumyl peroxide. The toluene was then evaporated overnight

in a nitrogen flow chamber. A small, approximately 1 × 1 mm^2 piece of this rubber was masked with two pieces of tape, leaving an approximately 0.25 mm thick strip in the center. Then, the sample was placed in a sputter coater and coated with evaporated carbon from a graphite rod multiple times to ensure a thick deposition of the carbon layer. Afterwards, the masks were removed, and a second uncross-linked SBR layer was placed on top of the coated sample, creating a sandwich. The sandwich was then cured for 60 min at 160°C under nitrogen. A schematic of this process is shown in Figure 4.1.

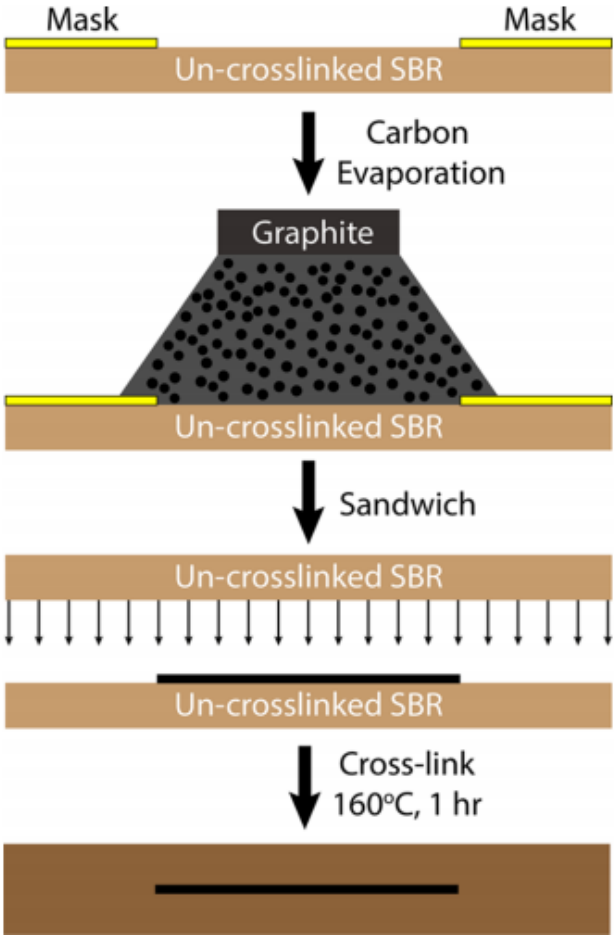

Figure 4.1: Schematic of the sample preparation procedure for the sputter-coated carbon–SBR sandwich sample. First, an uncross-linked SBR layer is masked with tape, leaving only a thin, ~0.25 mm thick region in the middle exposed. Then, the sample is placed in a sputter coater and coated with carbon from a graphite rod. The masks are removed, and a second SBR layer is placed on top of the coated sample, creating a sandwich. Finally, the sandwich is cured at 160°C for 1 h under nitrogen.

4.2.2 Cryo-ultramicrotomy

Thick slices of these rubbers were prepared using a Leica EM UC7 ultramicrotome with an FC7 cryochamber with the sample holder set to $-120°$C, while the knife was held at $-40°$C. Slices were cut and collected with a DiATOME Ultra 45° Diamond knife designed for wet sectioning, using a mixture of 3:2 dimethyl sulfoxide/deionized water [130]. The slices were cut to at least 300 nm thickness to ensure that the supporting substrate (a silicon chip) did not influence the measurement at the indentation depths probed.

4.2.3 Finite Element Analysis (FEA)

A finite element analysis model was developed to replicate a force-controlled indentation by an AFM cantilever. The created FEA model (Figure 4.2) was solved using ABAQUS software in a three-dimensional Cartesian space. An elastic model was chosen to represent the rubber to simplify analysis. The matrix modulus was adjusted to 15 MPa such that the indentation depth measured in the FEA was similar to typical indentation depths in rubber. The use of Hertzian contact mechanics in FEA instead of JKR contact mechanics due to the lack of adhesion results in a smaller contact radius, and less force is needed to reach the same indentation depth. The Poisson's ratio (ν) of the interphase and matrix was maintained at 0.495. The input interphase modulus if required was then scaled relative to the matrix modulus. The substrate properties are assigned to be typical of carbon black ($E = 15$ GPa, $\nu = 0.23$). The substrate properties were found to not affect the measured modulus during indentation in the rubber phases as long as the substrate modulus is $2-3$ orders of magnitude greater than the matrix. The tip was modeled as a perfectly rigid, analytical surface with a tip radius that matched the tip used in AFM experiments ($R \sim 20nm$). To replicate the cantilever deflection, a spring element was attached to the centroid of the tip. A nominal spring stiffness of 0.2 N/m was assigned to replicate the stiffness of the cantilever used in experiments. To perform indentations, a load was applied to the other end of the spring element as a concentrated nodal force at a linear ramp over a long enough time period to ensure a quasi-static indentation. A profile of modulus was collected by repeatedly relocating and indenting the tip so that indentation data could be collected. To calculate the modulus, a Hertzian model (eq. 2.23) is used. Using the radius of the tip, R as a reference, a set of model interphases were created for analysis in FEA.

Four different step interphase extents (ξ_{int}) were explored: $0.25R$ (5 nm), $0.6R$ (12 nm), $1.25R$ (25 nm), and $2.5R$ (50 nm). The four interphase lengths were chosen to encompass a range of length scales relative to the size to the far-field contact radii and span the full range of possible contact conditions between the

tip and the interphase layer. For $\xi_{int} = 0.25R$, the contact radius at each force setpoint is larger than the interphase width. For $\xi_{int} = 0.6R$, the two lowest forces (1–2 nN) have contact radii ($a/R = 0.45$ and 0.57, respectively) smaller than the interphase width, but the remaining force setpoints (3–5 nN) have contact radii larger than the interphase width. For both $\xi_{int} = 1.25R$ and $2.5R$, all contact radii are smaller than the interphase widths, but for $\xi_{int} = 2.5R$, the contact radius at each force setpoint is at most half the interphase width, ensuring that the full diameter of the tip can indent onto the interphase region. The range of ξ_{int} examined here will provide an understanding of how the relative size of the contact radius to the interphase extent influences how well the interphase can be resolved with AFM.

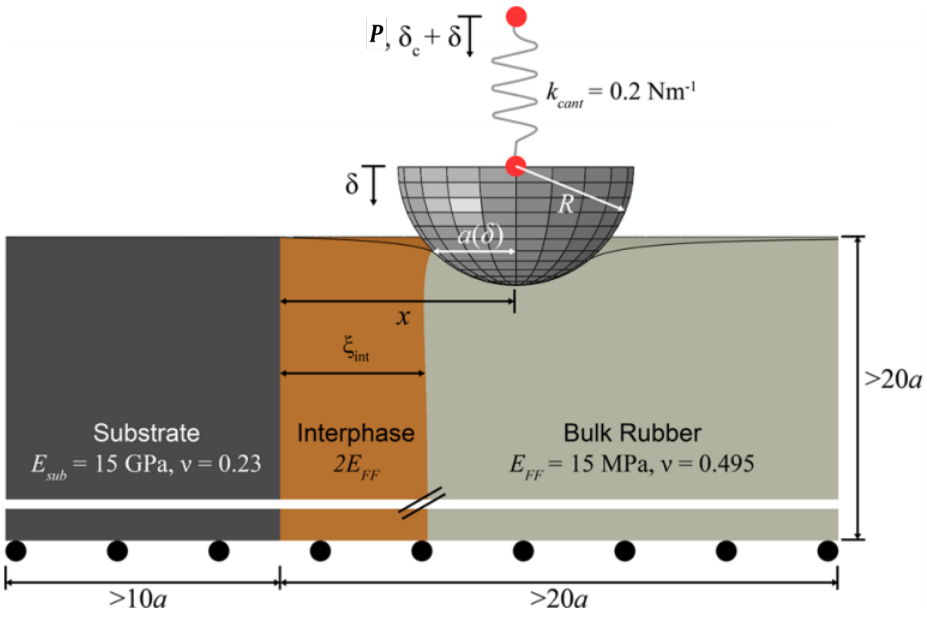

Figure 4.2: FEA model setup, including variables used to describe the position of the indenter relative to the substrate–rubber interface, the assigned material properties, the measured indentation depth, and "cantilever" deflection. Black circles refer to a roller boundary condition allowing horizontal motion in x and z, but not vertical motion in y.

4.2.4 Atomic Force Microscopy (AFM)

AFM experiments were conducted on a Bruker Dimension ICON using the FASTForce Volume mode. Experiments were conducted with either a biosphere B20-CONT, a high-density carbon tip with a well-characterized 20 nm tip radius and a nominal spring constant of 0.2 N/m for the experiments on the sputter-coated graphite–rubber samples, or a Bruker SCANASYST-Air AFM probe, a silicon nitride AFM probe with a nominal spring constant of 0.4N/m for the experiments with the in situ carbon black–rubber composite

samples. The tip radius was measured to be between 20 and 30 nm using the "roughness sample" method (see Appendix A.1), where a tapping mode height map of a Bruker titanium roughness sample (RS 15) was acquired with that particular AFM tip and inverse-analyzed using the AFM software, or measured via scanning electron micrographs. Deflection sensitivity of the cantilever was calibrated with a stiff sapphire sample, and the true spring constant was calibrated using a thermal tuning method according to the Bruker Dimension ICON user manual [40]. Force curves were collected using a linear ramp rate of 30 Hz. For interphase analyses on the 10% filled system or graphite–rubber sandwich sample, a single particle, or smooth graphite interface region was selected with the particle or graphite layer on one side of the image, for a total scan area between 500 × 500 and 800 × 800 nm^2 with 100 × 100 pixels. The small pixel size was chosen to ensure that in a scan the tip was contacting the region where an interphase may be present at multiple locations. For two-dimensional microstructure analyses, representative regions between 2 × 2 and 3 × 3 μm^2 were imaged with 256 × 256 pixels. Five different force setpoints (P_{max}) were used per sample, typically between 1 and 5 nN, while making sure the indentation depths did not exceed the elastic limit of the rubber. The resulting elastic modulus maps were calculated from analyzing the force curves using a custom script written in Python to fit the loading portion of the force–displacement curves with the JKR equations.

4.3 Results

The following sections isolate and describe the contact-radius dependent effects resulting from the stress interaction effect with an analytical function and then apply the function to modulus data acquired around reinforcing phases in polymer nanocomposites. First, idealized systems will be examined by solving finite element analysis models for a range of indentation locations. Indentations near a flat planar substrate without a model interphase layer are analyzed to establish the dependence of the stress interaction effect on the contact radius for a given indentation location and develop a model describing the behavior. A range of step interphase layers are then included in the FEA model to demonstrate the influence of the interphase on indentations and how the modulus profiles deviate from behavior expected from a pure stress interaction effect. The simulation results are then compared to *in-situ* carbon black–SBR composites that provide varying geometries and level of reinforcement.

4.3.1 Analysis of Ideal FEA Interface

4.3.1.1 Ideal, Flat Substrate with Step with No Interphase Model

The initial analysis focuses on the ideal case of a planar substrate to demonstrate the contact radius dependence of the apparent stress interaction effect. The simulation is first conducted without an interphase layer to measure the contribution from the substrate. Using the radius of the tip, R, as a reference, a set of raw data is created for analysis by indenting repeatedly at different distances away from the substrate, x, ranging from 0 to $5R$ for a range of force setpoints between 1 and 5 nN (Figure 4.3a). The measured modulus is then normalized to the far-field ($x > 5R$) measurement of the elastic modulus at each applied load to obtain a relative modulus. We find that near the substrate, the local modulus (E) can be up 1.4× the far-field modulus (E_{FF}), purely as a result of the change in effective compliance. When the tip begins to directly contact the substrate (represented with open symbols) during indentation, the relative modulus data increases dramatically. As the maximum indentation force is increased, the increase in modulus begins further away from the substrate, showing that the stress interaction effect is dependent on the depth of penetration as expected. With increasing load, the tip indents further into the material, and correspondingly, the probed volume will increase and is represented here by the contact radius, a. Normalizing the distance from the substrate (x) by the far-field contact radius (a_{FF}) (eq 2.23) using the measured far-field indentation depth, δ, and known tip radius, R, yields the plot in Figure 4.3b. This normalization causes the measured modulus from each sweep to collapse on a single curve, demonstrating that the scaling of the stress interaction effect is linearly proportional to a_{FF}. The "master curve" can be determined by fitting eq. 4.1 to the data (Figure 4.3b, inset)

$$\frac{E}{E_{FF}} = A\left(\frac{x}{a_{FF}}\right)^{-b} + 1, \text{ for } x > a_{cap} \tag{4.1}$$

Here, A and b are the fitting parameters which are found to be 0.64 and 1.48, respectively, and a_{cap} is the spherical cap radius, given by $a_{cap} = \sqrt{\delta(2R-\delta)}$. As $x \to 0$ and the tip contacts the substrate (Figure 4.3d, inset), the relative modulus increases rapidly, starting when $x/a_{FF} \sim a_{cap}/a_{FF}$. The point of tip–substrate contact ($x = a_{cap}$) is predicted in FEA through consideration of the tip geometry and indentation depth [14]. Once the tip encounters the substrate at a value close to $a_{cap}/a_{FF} = 1.25$, the data to the left of this point is the result of the tip directly touching the substrate and is not useful. The master curve, obtained by fitting eq 4.1 to the modulus data, can represent the stress interaction effect for every indentation depth examined until tip–substrate contact occurs. Comparing the master curves obtained from eq 4.1 for a range

of substrate moduli suggests that A and b are invariant if $E_{sub} \gg 10E_{FF}$, which is typical of most rubber nanocomposites [14]. Therefore, eq 4.1 has broad application for the calculation of the stress interaction effect for an indentation in an approximately incompressible rubber and a neighboring stiff phase and suggests that the behavior of the stress interaction effect in carbon black−rubber composites may not be significantly altered by even a multiple order of magnitude change in the local modulus as a result of a bound rubber layer. The validity of the Hertzian contact assumption was confirmed by measuring the contact radius directly from the displacement field output of the FEA model and compared to the predicted contact radius. Figure 4.3c shows a comparison of the true FEA contact radius of the 5 nN max force profile vs the contact radius obtained from the Hertz equation (eq 2.23). The Hertz equation slightly underestimates the true contact closer to the substrate, which is likely due to asymmetry in the contact region caused by the presence of the substrate bounding the surface of the rubber. However, it also shows that the true contact radius is relatively consistent until direct tip−substrate contact occurs. Far away from the substrate, the Hertz equation slightly overestimates the true contact radius; however, the measurement is within the error bars associated with the uncertainty of the simulated contact radius limited by the FEA model mesh size. Thus, using a single far-field contact radius should be reasonable to approximate the local contact radius up until tip−substrate contact. Additionally, it is important to note that the FEA model uses a spherical model where the Hertz equation for contact radius in eq 2.23 is the parabolic approximation solution. The spherical solution is identical to the parabolic solution for small δ/R, but begins to deviate as δ/R increases. At the maximum force examined here (5 nN), $\delta/R \sim 0.63$ and the difference between the spherical and parabolic solution is around 15% [50]. However, the error in the true simulated contact regime due to meshing limitations is greater than the deviation between the spherical and parabolic solutions to the Hertz equation.

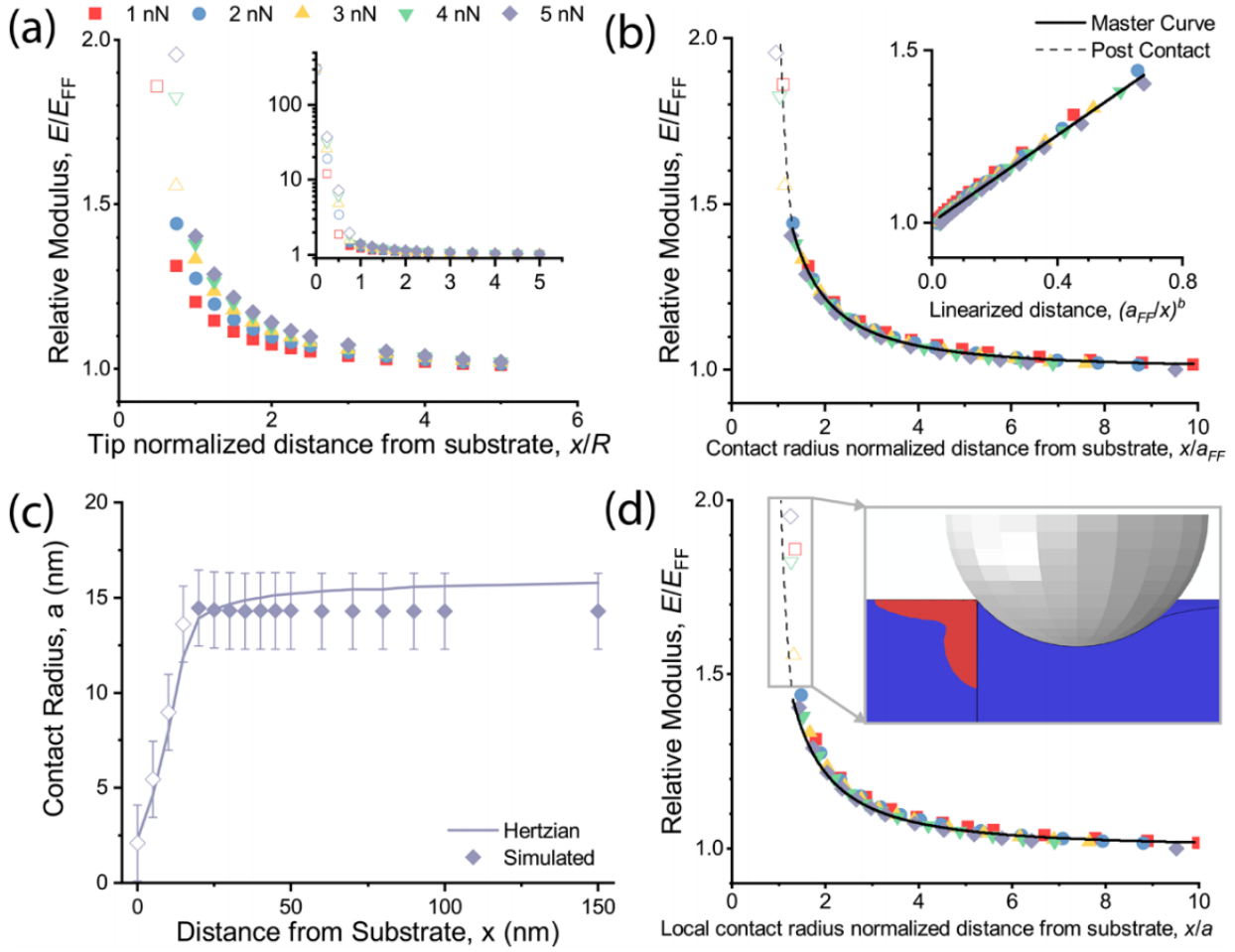

Figure 4.3: Normalized modulus profiles for indentation moduli of a simulated soft material near a rigid substrate (with no interphase) as a function of the distance of the tip from the substrate normalized by (**a**) tip radius, (**b**) contact radius as calculated by eq 2.23 and δ at $x = 7.5R$. The black line is the fitted curve to the normalized data. The solid line is the fit until tip–substrate contact; the dashed line is the fit post tip–substrate contact. Inset: linear fit of E/E_{FF} to $(a_{FF}/x)^b$ for values of E/E_{FF} greater than $1.05E_{FF}$ until the tip contacts the substrate. (**c**) Contact radius at each indentation location, x, for a 5 nN force setpoint as measured directly in the FEA model and the calculated contact radius using eq 2.23. Deviations likely due to mesh size and asymmetry of the indentation close to the substrate. (**d**) Modulus profiles normalized by the local contact radius calculated by the Hertz equation compared to the master curve generated from (**b**). Inset: schematic of tip–substrate contact. Red indicates where the von Mises stress exceeds 10 MPa for the exemplary indentation. Once tip–substrate contact is initiated, the force–displacement curve is dominated by the substrate stiffness even if most of the tip indents into the rubber.

The benefit of using the far-field contact radius rather than the local contact radius at each point is that it simplifies the analysis of experimental data, which will be further explained in the next section, even though the contact radius may decrease closer to the substrate, as shown in Figure 4.3c. To demonstrate that the

far-field contact radius is a valid approximation, Figure 4.3d shows the profiles normalized using the local contact radius, measured at each location for each max force, and compares it to the master curve (dark solid line) from Figure 4.3b. It shows that the collapsed data for the local modulus-normalized plot is nearly identical with the far-field-normalized master curve up until the point of contact with the substrate, which was the limit for the original master curve. Thus, the far-field contact radius is sufficient for normalizing the contact profile in the region where the structural indentation effect is relevant.

4.3.1.2 Ideal, Flat Substrate with Interphase Model

With a better understanding of the contact radius dependence of the stress interaction effect, the impact of a step interphase with a modulus twice that of the matrix on the behavior of the measured modulus was investigated, as shown in Figure 4.2. Four different step interphase sizes were explored: $0.25R$, $0.6R$, $1.25R$, and $2.5R$. These four different lengths were chosen since their relative size to the far-field contact radii spans a range of possible cases in experimental samples.

The far-field contact-radius-normalized modulus profiles for each of these cases are shown in Figure 4.4a–d, and each are compared to the master curve, which is represented by the black line plot in each figure. For the case of an interphase of size 0.25R, shown in Figure 4.4a, the interphase width is small and the far-field contact radii for each applied load are larger than the width of the interphase. As a result, the probe volume under the tip contains material outside the interphase regime even at the closest indents to the surface. Therefore, the impact of the interphase is negligible, and there is only a minor shift in the modulus profiles for the $0.25R$ interphase compared to that of the master curve, and the modulus profiles generated at each force setpoint still collapse on each other. When the width of the interphase increases to $0.6R$ (Figure 4.4b), the deviation from the pure stress interaction effect is more apparent and the profiles produced from the different max forces begin to separate. The separation of the profiles after normalization by contact radius becomes more apparent in Figure 4.4c,d, where the interphase width is $1.25R$ and $2.5R$, larger than the far-field contact radius for each applied load. Since the location of where the interphase meets the matrix is a fixed distance from the interface, it occurs at different values of x/a_{FF} for each applied force, as shown by the colored interphase input step functions (ξ_{int}/a_{FF}) in all figures. Note that the smallest load results in the broadest ξ_{int}/a_{FF} so that the relative modulus curves plotted in this manner are ordered with the smallest applied load having the broadest profile. Note also that while the curves are distinct as they approach the substrate, once the tip contacts the substrate, the collected data collapses back onto the master curve (dashed line). These results show that the impact of the interphase can be distinguished from

pure stress interaction effect by visualizing the data in this manner:

- If the a_{FF}-normalized modulus profiles from different force setpoints collapse onto a single curve as in Figure 4.3b, then no interphase is present.
- An observed separation in a_{FF}-normalized modulus profiles collected at different force setpoints indicates that the tip is indenting in multiple phases with significantly different moduli and provides strong evidence for the presence of an interphase layer in in situ rubber nanocomposites.

The contact-radius-normalized modulus profiles of the interphase models in Figure 4.4 show how the existence of an interphase with various extents can induce deviations from the master curve, but they do not directly provide the stiffness or shape of the interphase. However, if we assume that **1**) the increase in measured modulus in these interphase systems is a superposition of the stress-interaction effect of the rigid substrate and the interphase, and **2**) the stress intereaction effect of the substrate is mostly the same regardless of interphase width (which was verified through additional FEA, if $E_{sub} \gg E_{int} > E_{FF}$), then the master curve determined from Figure 4.3b can be subtracted from the raw profiles collected across the four-step interphases investigated, as shown in the insets for each of Figure 4.4a–d, where $\Delta E_{MC} = E_{MC}/E_{FF} - 1$. ΔE_{MC} is the substrate contribution to the increase in modulus (E) above the far-field modulus (E_{FF}). Removing ΔE_{MC} results in an approximate measurement of the local modulus profile of the polymer near the substrate; however, the finite-sized tip causes a smearing of the local modulus from the step input to a sigmoidal function. For a case with no interphase, a flat profile is returned (not shown).

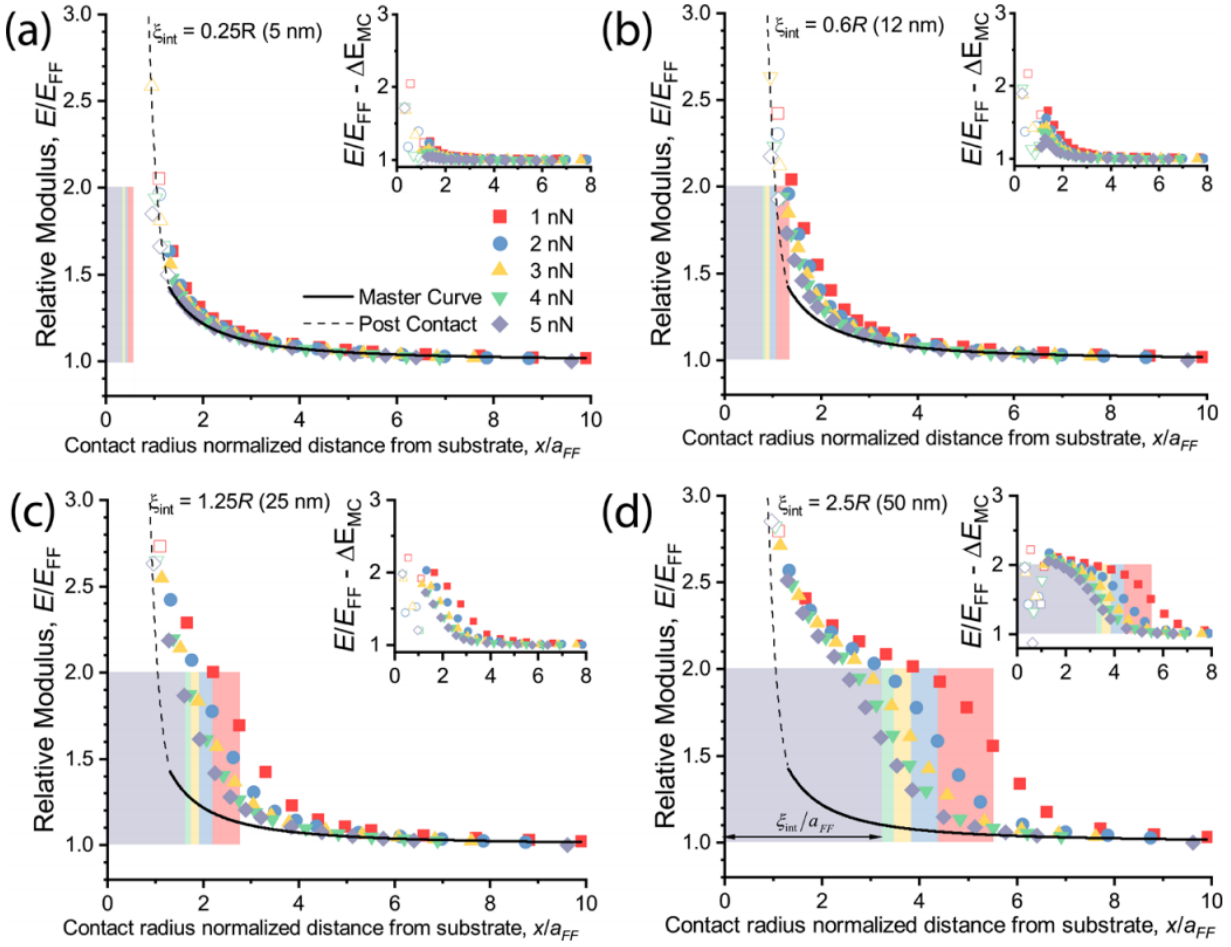

Figure 4.4: Far-field contact radius normalization of FEA-simulated indentation modulus profiles near a rigid substrate with a step interphase of modulus twice the matrix modulus ($2E_{FF}$) and increasing interphase thickness of (**a**) $0.25R$, (**b**) $0.6R$, (**c**) $1.25R$, and (**d**) $2.5R$. Each plot shows indentation profiles at five different force setpoints, as well as a comparison to the master curve from Figure 4.3b (black line). A smaller force setpoint results in a smaller contact radius, a_{FF}. As such, when the distance from the substrate is normalized by a_{FF}, the smallest force setpoint (1 nN) results in the largest interphase extent. Inset: the resulting profile with the substrate contribution removed, where $\Delta E_{MC} = E_{MC}/E_{FF} - 1$ and E_{MC}/E_{FF} is the master curve from the fit of Figure 4.3b. The dashed portion indicates when tip–substrate contact begins for the substrate effect master curve. Open symbols indicate that tip–substrate contact has occurred at this indentation depth. Shaded boxes in each figure show the shape of the input interphase layer for each max force as a function of x/a_{FF}.

To remove the shift of each curve due to the changing a_{FF} value for each force setpoint, we use eq. 4.2 to locate the origin of the x axis data at the interphase–matrix boundary, where ξ_{int} is the input interphase width. The profiles acquired at each indentation force and for each of the model interphases collapse to a single profile, the gray line in Figure 4.5.

$$\frac{x_{int}}{a_{FF}} = \frac{(x - \xi_{int})}{a_{FF}} \tag{4.2}$$

The scattered data that does not sit on the collapsed profile is due to small errors between the master curve and individual data points when the tip contacts the substrate. As such, a slight deviation from the master curve during tip–substrate contact can cause noticeable deviation in individual data points once the master curve is subtracted from the data. The stress interaction effect between the interphase layer and the matrix allows for interphase layers ($0.25R$ and $0.6R$) smaller than a_{cap} to be differentiated from a system with no interphase (Figure 4.5a,b), which returns a flat line of E_{FF} at all values of x/a_{FF} after the master curve is subtracted from the simulation data. As the interphase width increases, more of the interphase can be measured before tip– substrate contact, and only in the case of $\xi_{int} = 2.5R$ does the curve begin to plateau at $2E_{FF}$, the true modulus of the interphase region. The shape of the collapsed interphase profile for $\xi_{int} = 2.5R$ is still sigmoidal instead of the true step interphase that was input in the model due to the tip sampling both the matrix and interphase layer as it indents across the interface. Although determining the modulus and shape of the interphase is still a coarse approximation at this resolution, the fact that the data at all interphase widths collapses when shifted by eq 4.2 at the true value ofξ_{int} for a single interphase region suggests that the interphase extent could be estimated even when the ξ_{int} value is unknown a priori or if there are multiple interphase regions, such as in experimental data. This approach can be used in an iterative manner as mentioned in section 4.3.2.2 to provide insight into the interphase extent in experimental samples.

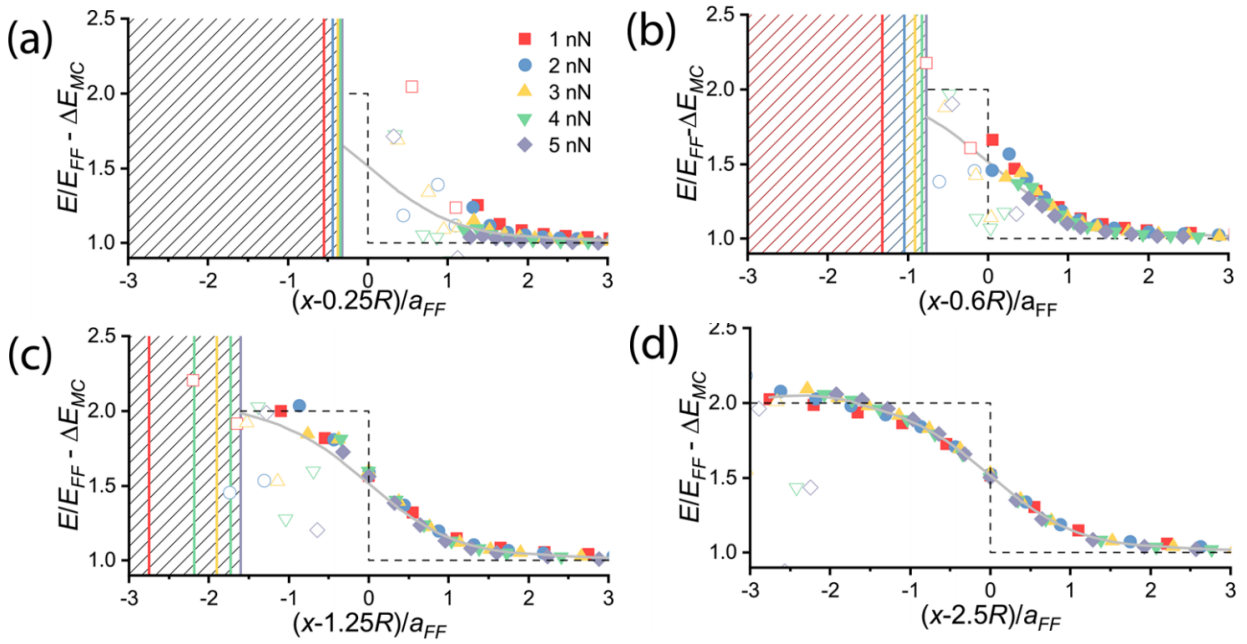

Figure 4.5: Simulated indentation profiles after shifting by (**a**)$\xi_{int} = 0.25R$, (**b**)$\xi_{int} = 0.6R$, (**c**) $\xi_{\text{int}} = 1.25R$, and (**d**)$\xi_{int} = 2.5R$ to locate the interphase–matrix boundary at 0 on the x-axis. The dashed black line indicates the input modulus profile, which is identical for each case after this transformation. The gray line indicates the observed trend acquired by fitting a high-order polynomial from the $\xi_{int} = 2.5R$ simulation data and subsequently overlaid on the other data to compare the behavior across each interphase layer. Open symbols indicate that tip–substrate contact has occurred at this indentation depth. The shaded region indicates the region occupied by the substrate with the colored vertical lines indicating the relative position of the substrate to the interphase–matrix boundary for each force setpoint. For the $\xi_{int} = 2.5R$ case, the substrate is far enough away from the matrix interphase boundary that it does not appear within the bounds of the plot.

4.3.2 AFM Analysis of Interacting and Noninteracting Systems

With the establishment of stress field interaction effect, as well as the influence of a model interphase on the modulus profile, the results of the FEA simulations can now be used in conjunction with real systems for interpretation of the experimental data. The first experimental system examined includes a planar, graphite substrate created as described in Section 4.2.1.2, Graphite was chosen because it is a carbon derivative, but typically has a poor reinforcement performance as a filler material for rubber when compared to other carbon derived filler materials like carbon black, graphene, and carbon nanotubes due to its tendency to agglomerate and very low surface-area-to-volume ratio and should, for these reasons, have a minimal bound rubber layer [131–134]. Then, as described in Section 4.2.1.1, systems that include interacting (N121) and weakly interacting (N660) carbon black particles are examined to determine if a bound rubber interphase

can be detected.

4.3.2.1 Analysis of AFM Force Curves

Before modulus profiles across SBR–carbon interfaces can be analyzed in the experimental systems, a correct contact mechanical model needs to be applied to accurately measure the modulus values. Unlike the simulated FEA curves, the experimental rubber composite systems are adhesive, which will increase the tip– sample contact area compared to that predicted by the Hertz model. As discussed in, section 2.2.3.2, for softer adhesive systems, typically, the Johnson–Kendall–Roberts (JKR) model is used, because it takes into account adhesive forces that can cause the surface to wrap up the sides of the tip [36, 50, 52]. The JKR contact model is described by eqs 2.26 and 2.27, where the contact radius a_{JKR} is a function of $\mathcal{G}$, the energy release rate, or the energy per unit area needed to separate the two materials. It can be shown that as $\mathcal{G}$ approaches 0, Hertzian contact mechanics is returned (section 2.2.3.2). The analytical solutions to the JKR equations (eqs 2.26 and 2.27) for some arbitrary parameters yield the plot shown in Figure 2.6c. As a perfectly elastic material, the loading and unloading curves overlap. The main difference is that in the unloading section, some of the material is pulled up beyond $\delta = 0$ until the material completely separates from the tip. However, as can be clearly seen by the experimental AFM force–displacement curve on a matrix region of the N660–SBR composite in figure 4.6a, the force curves are complicated by hysteresis, which can be caused due to dissipative effects (in this case, viscoelasticity) during indentation. No plasticity was observed during imaging. However, a few JKR studies on viscoelastic, rubbery materials have shown that the value for G varies greatly between the loading and unloading portions of the curve. The value of $\mathcal{G}$ during loading is much lower (and constant with indentation depth) than that during unloading, with the thermodynamic work of adhesion being an upper bound during loading [36, 89]. During unloading, $\mathcal{G}$ is a function of indentation depth, and the adhesive nature of the material holds the contact radius constant [4, 135] until a certain critical $\mathcal{G}$ is reached and allows the contact area to reduce, behavior that is not accounted for by eq 2.26. JKR contact mechanics assumes that $\mathcal{G}$ is constant with indentation depth and that aJKR changes as described by eq 2.26, which better describes the indentation behavior during loading. Therefore, we calculated the local modulus by fitting the JKR equations to the loading portion of the force curves (Figure 4.6a). Figure 4.6b shows the comparison of the measured contact radius, a_{JKR}, resulting from the JKR fit of the loading curve in Figure 4.6a, as well as the predicted Hertz contact radius. The contact radius calculated by the JKR fit of the loading curve is about 1.4× the Hertzian contact radius.

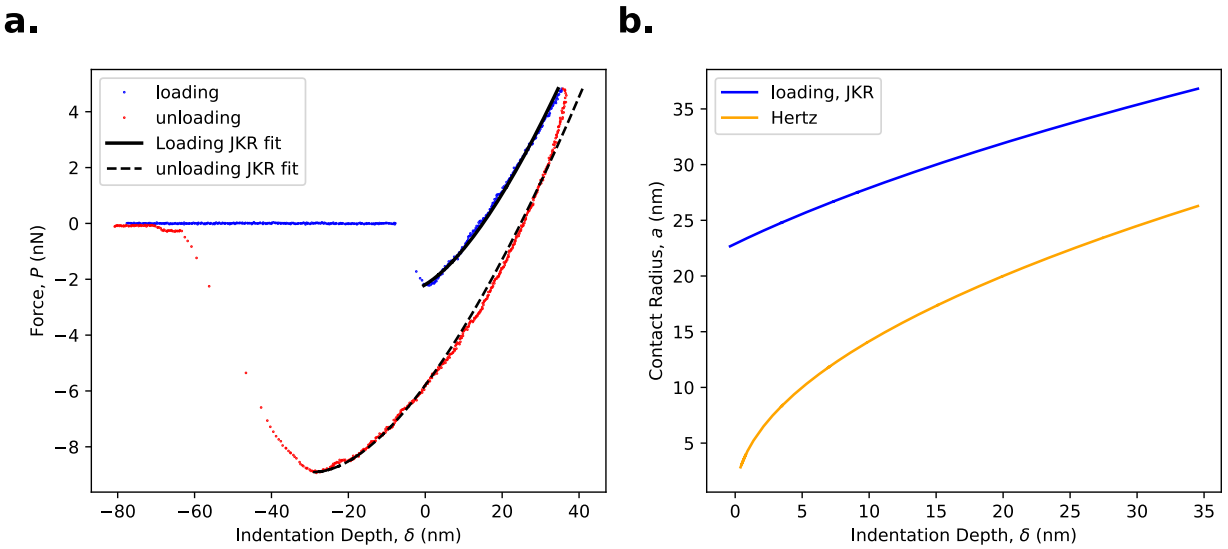

Figure 4.6: (**a**). Experimental force–displacement curve of a matrix (SBR) region of the 10 wt % N660–SBR composite with the corresponding fit of the JKR model to both the loading portion of the curve. The force setpoint was 5 nN. (**b**). Comparison of the contact radius as a function of force for the JKR fit of the loading curve and the predicted Hertz contact radius of the force curve in (a).

The JKR model fits the AFM force–displacement loading curves well for force curves collected on the rubber matrix (as represented by Figure 4.6a), but it is important to check that JKR mechanics describes the force curves well near the filler where the environment is more complex. Figure 4.7 shows the JKR fit for the loading curves at three points for each SBR– carbon system: a point in the matrix, a point near the matrix– particle/carbon interface, and a point on the filler, with the corresponding JKR fits for E_r, $\mathcal{G}$, a_{JKR}, and a_{Hertz} and the maximum indentation depth δ_{max} for each curve provided in Table 4.1. Fitted $\mathcal{G}$ values compare well to literature values of the thermodynamic work of adhesion limit for rubbery materials [36]. The corresponding E_r values are reasonable in the rubber but are orders of magnitude smaller than what is expected for the carbon black. This is due to particles being softly suspended in the rubber, providing some additional compliance. However, since the measurements made on the filler are not useful for the measurement of any interphase layer, they can be excluded. With this, we can have reasonable confidence in the modulus measurements in the SBR systems for the subsequent profile analysis. Figure 4.7a,c,e shows the topography maps of the investigated areas after a first-order flattening procedure with the filler masked to prevent erroneous fitting. There is very little topography variation as a result of the ultramicrotomy. The difference in height between the filler and the rubber observed is at least, in part, due to the additional

deformation of the rubber affecting the height measurement [136].

It is important to note that the matrix SBR region is not always consistent between the samples, with the N121−SBR matrix modulus value being more than twice that of the N660 and sputter-coated carbon−SBR matrices, as shown in Table 4.1. However, this deviation is likely due to differences in crosslinked density that can be the result of the filler identity, matrix−filler interaction, or the cross-linking process [137]. These differences in moduli should not affect the analysis of the relative moduli profiles as will be described in the subsequent section. To normalize the profiles collected for each experimental sample and force setpoint, the far-field modulus (E_{FF}) is estimated by first converting E_r to E assuming $\nu = 0.495$ and then fitting a Gaussian peak to the histogram of matrix modulus values to find the average value and standard deviation (Table 4.1). The average surface roughness (R_a) of the rubber matrix is approximately 2.5 nm for all samples.

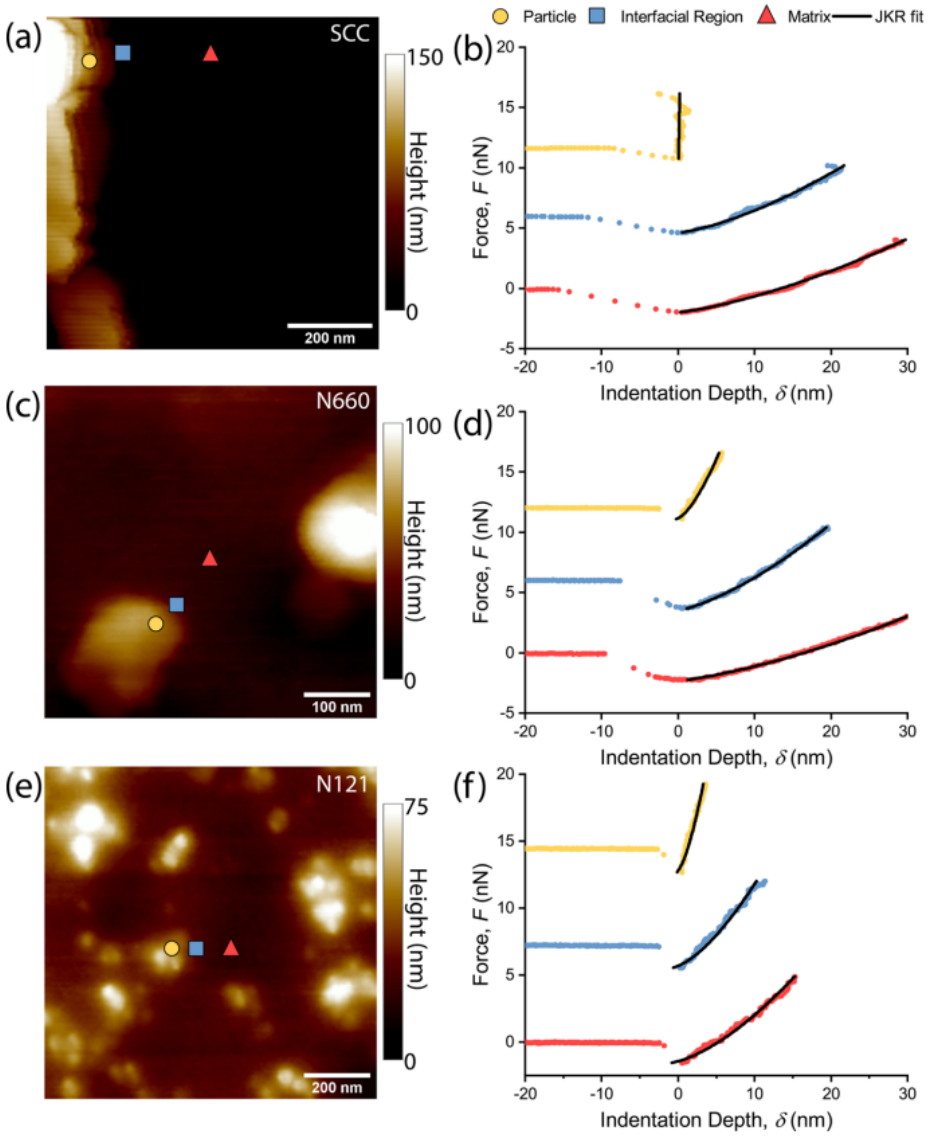

Figure 4.7: (**a**, **c**, **e**) Height maps of regions selected for analysis: (**a**) sputter-coated graphite–SBR model system (SCC), (**c**) 10 wt % N660–SBR composite (N660), and (**e**) 10 wt % N121–SBR (N121) composite. Locations of force curves displayed in (**b**), (**d**), and (**f**) are indicated with a yellow circle for the filler, a blue square for the interfacial region, and a red triangle for the matrix. (**b**, **d**, **f**) Loading curves from the AFM experiments showing representative curves from the matrix (red curve), near the matrix–carbon interface (blue curve), on the particle/carbon (yellow curve) for (**b**) sputter-coated graphite–SBR model system ($P_{max} = 4nN$), (*d*) 10 wt % N660–SBR composite ($P_{max} = 5nN$), and (**f**) 10 wt % N121–SBR composite ($P_{max} = 5$ nN). Curves are offset, and the unloading portion is removed for clarity. The fit of the JKR model is provided in black.

	SCC–SBR (4 nN)			N121–SBR (5 nN)			N660–SBR (5 nN)		
	matrix	interfacial region	substrate	matrix	interfacial region	particle	matrix	interfacial region	particle
E_r (MPa)	5.88[b]	8.87	10^4	13.9[c]	25.3	141.1	5.09[d]	12.7	71.3
G (J m^{-2})	0.024	0.017	0.019	0.011	0.012	0.013	0.028	0.031	0.010
δ_{max} (nm)	29.30	21.39	0.21	15.34	11.42	3.62	36.28	20.14	5.76
a_{JKR} (nm)	34.46	28.38	2.81	28.65	23.74	13.54	37.66	28.35	13.25
a_{Hertz} (nm)	24.21	20.68	5.34	21.46	18.51	10.42	26.94	19.82	10.73

Table 4.1: JKR Fitting Parameters E_r and $\mathcal{G}$ for the Loading Curves Shown in Figure 4.7 as well as Max Indentation Depth for Each Curve. For the sputter-coated carbon and N660 systems, $R = 20nm$. For the N121 system, $R = 30nm$. [b] $E_{FF} \pm \sigma$ for the collected forces in the matrix of the SCC sample is 6.4 ± 0.6 MPa. [c] $E_{FF} \pm \sigma$ for the collected forces in the matrix of the N121 sample is 14 ± 2 MPa. [d] $E_{FF} \pm \sigma$ for the collected forces in the matrix of the N660 sample is 5.2 ± 0.4 MPa.

4.3.2.2 Analysis of Modulus Behavior near the Interface

In the experimental systems, the exact location of the carbon– rubber interface is not precisely known as it is in the FEA simulations. However, the most rational choice to use for $x = 0$ is the location of the inflection point (x_{IP}) of the modulus profile, since the point where the measured modulus will change most rapidly is when the tip is in contact with equal amounts of rubber and substrate (i.e., the tip center is aligned with the interface). While it has been established that the inflection point in the modulus agrees with the true interface between a substrate and a polymer for an idealized substrate [109], a finite particle is expected to undergo rigid body motion under load, which may affect the accurate determination of the interface location with this method. Additional simulations across a particle–rubber interface, suggest that at the range of peak loads examined (1–5 nN), there is a 1–3 nm error associated with using the inflection point of the modulus profile as the location of the interface. This small error is less than the AFM resolution and not considered significant.

Figure 4.8 shows the relative modulus data from the experimental AFM across the N121 carbon black particle into the SBR matrix. The profile across the particle can be described well by a sigmoidal function (solid line) from which the inflection point location (x_{IP}) can be found for each profile collected (indicated in Figure 4.8 with a dashed line). The x-coordinate axis for each modulus profile is then shifted according to the $x_{IP}(a_{FF})$ so that $x = 0$ lies on the substrate– rubber interface for all experimental data.

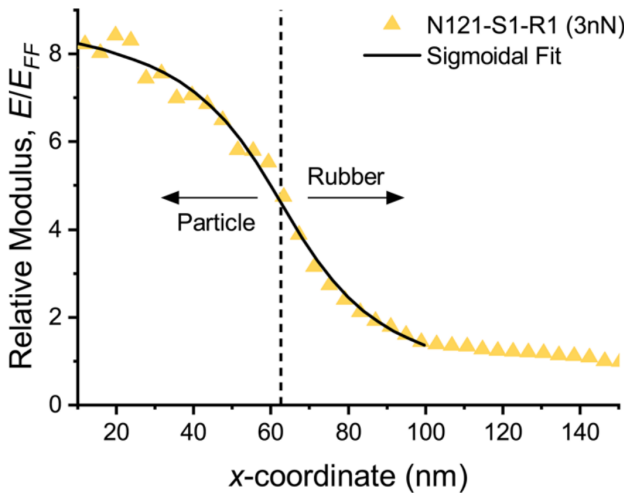

Figure 4.8: Relative modulus profile of the experimental AFM data across a N121 particle and the SBR matrix. Transition region is fit to a sigmoidal function, and the estimated boundary between the particle and the rubber is indicated by the dashed line.

Figure 4.9 provides the modulus profile data from the experimental AFM analysis. Profiles of the calculated modulus were extended away from the interface until the moduli were comparable to the far-field matrix modulus (E_{FF}). The entire profile acquired at each P_{max} was then normalized by the E_{FF} calculated for that P_{max}. The region of the collected profiles deemed to be in the far-field ($E \approx E_{FF}$) was examined to ensure there was no significant increase in modulus with the applied load, which would suggest that subsurface geometry could be affecting the measurement [124]. The profiles acquired at each applied load were then translated horizontally so that the inflection point of each profile was aligned, providing a single coordinate system for all of the profiles across the graphite–rubber interface. Even though the modulus measurements are made assuming JKR contact mechanics, the scaling of the substrate effect with x and P_{max} is effectively described by the Hertzian contact radius (a_{FF}), as calculated by eq 2.23, consistent with the recent MD simulations that show the substrate effect is not affected by changes to tip–sample adhesion strength [123].

When the profiles collected at each indentation force across the graphite-SBR interface (Figure 4.9a) are normalized by their corresponding far-field contact radius, a_{FF}, the data collapses to the master curve determined from the FEA simulation in figure 4.3 until the tip is predicted to contact the substrate directly (Figure 4.9b). The master curve of the flat substrate geometry from the FEA experiments in Figure 4.3 is an appropriate comparison because, as described in section 4.2.3, the mechanical properties chosen for the substrate and matrix of the FEA were typical of SBR and carbon black, respectively, and the geometry of the

sputtered system closely mimics a flat substrate. The collation of the experimental AFM profiles onto the master profile implies that there is no significant interphase present in the sputter-coated graphite system, as expected.

With the successful application of the technique to the idealized model planar sputter-coated graphite system, more complex *in situ* carbon black–SBR composite systems were then explored for two different carbon black particles: N660 and N121. The analyzed areas and plots of the respective line scans are shown in Figure 4.9c–f for N660 and N121, respectively. From the unnormalized line scans of the N660 data (Figure 4.9c, there is a broadening of E/E_{FF} profile with increasing applied load.

Before normalizing the profiles with respect to the far-field contact radius, it is important to note that the geometry of a particle is different from that of a flat substrate, and so the master curves for each may differ slightly. Modulus profiles across an FEA model of a particle suspended in a polymer matrix show that the resulting structural indentation effect master curve does not differ significantly from an ideal flat substrate but is slightly less pronounced in magnitude. When the modulus profiles for the N660 samples are normalized to the contact radius, the line scans collapse to a single profile (Figure 4.9d) that agrees well with the master profile. However, a slight offset in the measured profile is observed compared to that of the master profile, likely due to the suspended particle providing a smaller stress interaction effect compared to a fixed substrate similar to the FEA data.

The analysis is repeated for the interacting N121 composite (Figure 4.9e,f). The raw data curves are noticeably broader compared to the N660 data, and a significant increase in modulus is observed at 80 nm away from the substrate. When the acquired profiles are normalized by the contact radius, the profiles do not collapse onto the master curve. Instead, a significant increase in modulus remains near the particle. In addition, when $2 < x/a_{FF} < 6$, we see a separation between the profiles as seen for the FEA models that included an interphase–matrix boundary (Figure 4.4c,d).

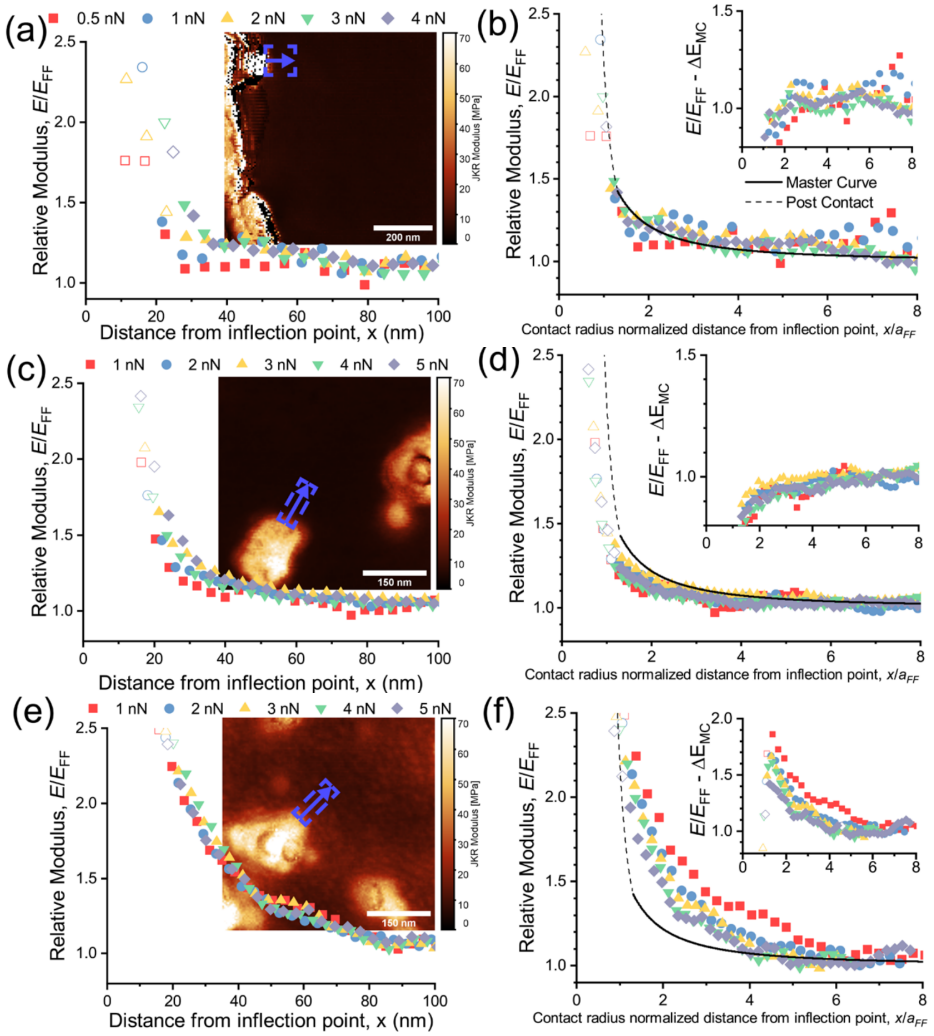

Figure 4.9: (**a**, **c**, **e**) Raw modulus profiles and modulus map of (**a**) sputter-coated graphite–SBR sandwich, (**c**) 10 wt % N660–SBR, and (**e**) 10 wt % N121–SBR sample. The region of analysis in each image is indicated by the blue box. Profiles are obtained by averaging the modulus data across the window perpendicular to the arrow direction. The profiles were collected with a high enough resolution so that there were approximately 10pixels/nm^2 with line scans at different force setpoints taken from the representative region of the composite, ensuring the indentation depth did not exceed the elastic limit of the SBR. (**b**, **d**, **f**) Contact-radius-normalized profiles compared to the master curve for (**b**) sputter-coated graphite– SBR, (**d**) 10 wt % N660–SBR, and (**f**) 10 wt % N121–SBR. Inset: the resulting profile with the substrate effect contribution to the measured modulus removed. For all figures, the dashed portion of the master curve indicates when tip–substrate contact occurs in the FEA. The open symbols indicate which data points are the result of tip–substrate contact as predicted by the spherical cap radius and indentation depth.

The N121 AFM data showing evidence of a possible interphase by the broadening of the depth dependent profiles in 4.9f leads to the question: can the length of the interphase region be approximated from this data? The analysis of the FEA simulation of the indentation experiments of an elastomeric polymer near an ideal,

flat substrate with defined interphase region in section 4.3.1.2 showed that the a_{FF}normalized profiles at different indentation depths would collapse on a single curve when 1) the stress-interaction effect master curve, E_{MC}, determined from the no-interphase simulation in section 4.3.1 is subtracted from each curve, and 2) the curves were shifted on the x-axis according to eq. 4.2 so that the location of where the interphase meets the matrix is defined as $x = 0$. However, for experimental systems, the location of this boundary is not known *a priori*. However, an algorithm could can be written that varies ξ_{int} in eq. 4.2 for each profile until the variance between data at the same x is minimized, a method defined as the "reduced variance score method" or RVS [14]. This analysis on multiple regions of the 10wt% N121 carbon black-SBR sample predicted an ξ_{int} of approximately 50-60nm, but with a non-negligible amount of uncertainty that is likely due to the irregular geometry of the N121 particles. Further experimental work on model samples with known geometries will help refine and validate the experimental applicability of the RVS method.

This study focused on large nanoparticles significantly larger than the tip radius dispersed in a relatively dilute sample. As particle size decreases, we expect a decrease in magnitude and the extent of the master curve. And while we expect that the scaling of the stress interaction effect master curve with particle radius should be predictable assuming no rigid body motion of the particle in response to an indentation, in all realistic cases, a particle with a radius on the order of the contact radius will deflect and rotate significantly under an indentation load. This would make the determination of the particle boundary as presented in figure 4.8 challenging. For composites that contain a larger filler fraction, as long as the tip is able to only contact a single particle−rubber interface at a time, the sigmoidal function should maintain a suitable approximation for the filler−matrix boundary. To ensure a quantitative analysis, judicial choice is needed for the interface to be analyzed so that the measured effects are not the result of contributions from multiple particles/interfaces.

4.4 Conclusions

This study provides a means to estimate the extent of the bound rubber layer in complex, in situ carbon black−rubber nanocomposites free from convoluting stress interaction effects or the "substrate effect" as a result of the stiff particles. We treat the substrate effect as a result of increased effective compliance in the volume probed during indentation. As such, the Hertzian contact radius is used as a measure of the displaced volume and successfully captures the scaling of substrate effect with the tip radius and indentation depth, while JKR contact mechanics is used to determine the local modulus. We present:

- A method to produce a master curve of the substrate effect, which collapses AFM data from different force setpoints to a single curve. This process defines a single response for the change in modulus as a function of distance in a polymer near a surface or particle due to the stress interaction effect alone.

- A robust method to confirm or reject the presence of an interphase layer around stiff particulates in soft, rubbery systems, using in situ carbon black–SBR nanocomposites as an exemplary case. By modeling the stress interaction effects as a change in the effective compliance of the probed volume, the effects should be independent of tip–sample adhesion and thus scale with the Hertzian contact radius. When AFM modulus data collected near an interface at multiple indentation depths is plotted with the modulus profiles normalized by the far-field Hertzian contact radius for each depth [E(x/aFF)], systems that contain an interphase layer will deviate from the master curve profile. In addition, the contact-radius-normalized profiles collected at different indentation depths will separate from each other when the tip is indenting an interphase layer and the matrix simultaneously.

- Once the presence of an interphase is established, an iterative algorithm is used to estimate the extent of an interphase without prior knowledge of the size of the interphase layer. To estimate the extent of an interphase layer, the algorithm searches for an interphase extent that minimizes the variance as measured by a metric we term the reduced variance score between modulus profiles collected at different force setpoints. The algorithm is validated in ideal FEA systems that included mono- and bilayer interphases.

- When the method outlined above is applied to in situ composites, clear differentiation in the measured interphase layer is achieved between a nonreinforcing N660 carbon black and a reinforcing N121 carbon black. The master curve is found to describe the modulus data obtained in an SBR near an N660 particle and graphite layer well. Across multiple N121 measurements, the loosely bound rubber layer is found to extend approximately 50–60 nm.

- The intrasample variance and complexity of the bound rubber layer profile introduces additional complexity into the analysis, and further development is needed for reliable estimates of the shape and extent of the bound rubber layers.

Continued work is ongoing to apply this method to entire modulus maps to remove structural indentation effects and map out deconvoluted interphase properties in two dimensions.

Chapter 5

Exploring Effect of Nanoscale Heterogeneity in the Temperature Dependent Fracture Behavior in a Model Epoxy System

This investigation looks at the temperature dependence of the fracture properties and mechanisms of model epoxy systems using diglycidyl ether of bisphenol A (DGEBA) as the epoxide with a stoichiometric amine mixture of a rigid cycloaliphatic diamine (PACM) and a more flexible, polypropylene glycol based diamine (Jeffamine) at different molar ratios. The molecular weight (MW) of the Jeffamine was adjusted to further tailor the epoxy properties. By changing the ratio of PACM to Jeffamine, the rheological behavior of the epoxy changes by either a shift in glass transition temperature, T_g, for low MW Jeffamine, or the appearance of multiple T_g's (phase separation) in the case of high MW Jeffamine. In the latter case, the epoxies are still optically transparent but exhibit heterogeneity on the submicron scale, a property that has been shown previously to correlate with enhanced impact toughness. Using single edge notched bend toughness testing and Vicker's hardness indentation testing, the fracture behavior as a function of temperature for these model epoxy systems was further explored for temperatures as low as -100 $^\circ$ C to above ambient temperatures. Distinct trends are shown between dynamically heterogeneous and homogeneous

(single T_g) systems. Fracture toughness is also shown to have opposite trends in temperature for each epoxy set: increasing with temperature as the glass transition is approached for the homogeneous systems, while decreasing with temperature for the heterogeneous systems. At very low temperatures the fracture toughness reaches a temperature-independent plateau. The relationship between the fracture toughness and the resulting morphology of the fracture surfaces was also explored.

This chapter reproduces work to be published in "Temperature Dependent Fracture Behavior in Model Epoxy Networks with Nanoscale Heterogeneity," submitted to *Polymer* in 2020 with co-authors L. Catherine Brinson and Kenneth R. Shull.

5.1 Introduction

Fiber-reinforced epoxy matrix composites are of increasing interest in low temperature applications such as in superconducting magnets, aerospace engineering, and cryogenic liquid containers due to their excellent strength to weight ratio [138–141]. However, epoxy resins tend to be brittle and can undergo large changes in size from temperatures due to the thermal expansion mismatch between the fibers and the matrix, leading to the development of large internal stresses, microcracking, and failure [142, 143]. Thus, there is much desire to improve the low-temperature toughness of epoxy resins.

The fracture behavior of epoxy resins has been studied extensively, with a goal of developing a universal model of fracture behavior in these materials. The development of such a model is very complex, due to the wide variety of variables that can affect the fracture behavior. These variables include the temperature [144–152], testing rate [146–149, 152], cure conditions [146], crosslink density with respect to resin/hardener ratio [146, 150, 153–155], and resin-hardener identity [144, 147, 149, 156, 157]. It is generally accepted that crack propagation in epoxies is controlled by a crack tip blunting mechanism, where localized plastic deformation ahead of the crack tip is the prevailing energy dissipation mechanism [152]. This mechanism is closely tied to the overall yield behavior of the epoxy, where conditions that increase the ability of the material to plastically deform (higher temperature, slower testing rate, lower crosslink density, more flexible hardeners) increase the fracture toughness of the epoxy. This approach is limited by the competing desire to avoid ductile failure at low stresses, thereby preserving the load-bearing capacity of the epoxy [157]. The optimum toughness regime of an epoxy is typically obtained in a narrow range of temperatures, 10-40 $^\circ$C below the glass transition temperature for the corresponding strain rate, below which the toughness decreases [144, 148–150].

This narrow optimum toughness window can pose a problem for epoxies to be used for low temperature

and high strain rate applications, and so methods to broaden the optimal toughness regime and increase low temperature toughness have been explored, such as the toughening of epoxies by the addition of rubber particles [145, 158, 159]. Rubber particles act as stress concentrators for the nucleation of shear deformation zones within the epoxy matrix [160]. Additionally, rubber particles can deflect, branch, pin, and bridge cracks, which all help to increase the toughness of the epoxy matrix. However, the addition of rubber particles has deleterious effects as well, including a reduction in the material stiffness and the development of non-uniformities in sample properties due to poor particle dispersion [159, 160]. In addition, the effectiveness of rubber toughening tends to decrease with increased strain rate and decreasing temperature as the conditions surpass the glass transition of the rubber filler [161, 162]. Also, the addition of rubber particle reduces the transparency of the composite, limiting the materials utility in applications for which optical clarity is a requirement.

Another, more recent approach to epoxy toughening is to modify the resin chemistry to incorporate nanoscale heterogeneity into the epoxy matrix, resulting in an expanded regime of temperatures and strain rates for which high toughness is observed. Recently, Masser, *et al.* developed a well-characterized model system to investigate this effect, consisting of diglycidyl ether of bisphenol A (DGEBA) crosslinked with a mixture of two different diamines, a rigid diamine, 4-4′-methylenebis(cyclohexylamine) (PACM), and a more flexible propylene oxide-based Jeffamine [159, 163–165]. The mechanical response of these materials was controlled by changing both the molar ratio of PACM to Jeffamine and the molecular weight (MW) of the Jeffamine used. For low MW Jeffamines, MW = 230 g/mol (D230) and MW = 400 g/mol (D400), the glass transition temperature, T_g, of the epoxy resin decreased in a straightforward way with increasing Jeffamine fraction. However, dynamic mechanical analysis of DGEBA/PACM/Jeffamine epoxies with of longer chain Jeffamines, 2000 g/mol (D2000) and 4000 g/mol (D4000), show multiple or broadened glass transition regions. Although a multiple/broadened T_g is typical of heterogeneous materials, the epoxies with Jeffamine D2000 were optically transparent, compared to the more expected opaque and phase separated D4000 systems, suggesting that for DGEBA/PACM/D2000 epoxies there is no macroscale phase separation. X-ray scattering confirmed the existence of structural heterogeneity with characteristic size of 1.5-4.5 nm, which is on the order of the radius of gyration of D2000 [164].

This nanoscale-phase separation with macroscale optical transparency, with corresponding heterogeneity of the polymer dynamics on the nanoscale, results in a material with very interesting performance in ballistic impact tests. For the low MW Jeffamine epoxy systems (DGEBA/PACM/D230, DGEBA/PACM/D400), the ballistic impact resistance was correlated in a straightforward way with the difference between the tem-

perature of the impact experiment and the epoxy T_g, showing an increase in penetration resistance about 60 °C below the T_g, behaving similarly to single amine systems [166]. However, the dynamically heterogeneous DGEBA/PACM/D2000 systems showed dramatic improvement in the ballistic impact resistance relative to the neat components when the total amine component corresponded to approximately 50% of the total sample volume [163]. Performing these ballistic tests at different temperatures showed that this sample had a temperature region of increased ballistic behavior that was twice as wide as epoxy systems using either D2000 or PACM as the sole diamine component [165]. Thus, these epoxy systems with nanoscale dynamic heterogeneity were concluded to have great potential for new transparent resin formulations for high impact applications, given their unique ballistic properties compared to homogeneous, single T_g formulations .

It is important to note that these ballistic tests provide a relative measurement of ballistic performance in comparison to a reference material, which in these previous studies was the DGEBA/PACM system. To better understand the intrinsic mechanical properties, it is necessary to do more quantitative investigations of the epoxy fracture properties, and to see how the fracture properties change with temperature, particularly at low temperatures when the material is the most brittle. Therefore, this study examines quasi-static single edge notch bend toughness testing and Vicker's hardness indentation on the epoxy samples from -100 °C to ambient temperatures in order to make a quantitative comparison of the fracture and deformation behaviors, comparing the single T_g DGEBA/PACM/D400 materials with the dynamically heterogeneous DGEBA/PACM/D2000 materials.

5.2 Materials & Methods

5.2.1 Epoxy Materials

The procedure for curing the model epoxy system used in this investigation was adapted from the experimental procedure in Masser, *et al.* [163]. The chemical structures of the epoxy components are shown in Figure 5.1. The diepoxide, diglycidyl ether of bisphenol-A (DGEBA), and rigid diamine, 4-4'-methylenebis(cyclohexylamine) (PACM), were bought from Sigma-Aldrich. Additionally two molecular weights (MW) of poly(propylene glycol) bis(2-aminopropyl ether), also known as Jeffamine, were also bought from Sigma-Aldrich. These are referred to as D400 (MW=400 g/mol) and D2000 (MW=2000 g/mol).

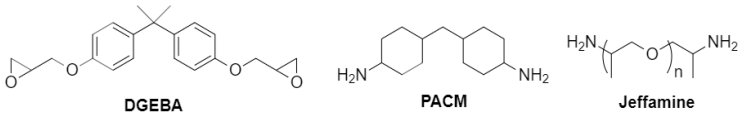

Figure 5.1: Chemical structures of the model epoxy system constituents used in this investigation. Two different molecular weights of Jeffamine were used, D400 (MW: 400g/mol) where n = 6, and D2000 (MW: 2000g/mol) where n = 33.

For each formulation explored a constant stoichiometric ratio of 2:1 DGEBA:total diamines was maintained to ensure maximum crosslinking, since each amine group can bond with two epoxide groups. PACM was melted at 80 °C, and then filtered using vacuum filtration and a Whatman filter to remove any impurities. Once melted, PACM was mixed with the Jeffamine in the following to give samples with a mole percentage of Jeffamine (relative to the total amine content) of 0, 25, 50, 75 and 100 for Jeffamine D400 and 10, 20, 30, 40, and 100 for Jeffamine D2000. We refer to the samples by mole fraction of amine that corresponds to the Jeffamine. For example, the diamine content in a D400-25 sample consists of 25 mol% Jeffamine D400 and 75 mol% PACM. The mole fractions and overall weight fractions of the components for each sample, are listed in Table 5.1 along with the corresponding sample name used to refer to them in this manuscript.

The amine mixture was then vigorously mixed together to ensure complete mixing of the component amines. Then, the appropriate stoichiometric amount of DGEBA, heated to 60-80 ° C to reduce viscosity, was added to the amine mixture. The DGEBA-amine mixture was then vigorously mixed. After mixing, the systems were degassed under a vacuum until all bubbles were removed. The degassed mixture was then carefully poured into a Dragon Skin^{TM} 10 VERY FAST silicone mold of the desired geometry for either hardness, toughness, or DMA tests. Curing was carried out under nitrogen at 80 °C for 2 hr, followed by 150 °C for 8hr. The samples were then allowed to sit at room temperature overnight before undergoing a final post-cure step at 200 °C for 2 hr. Samples were then removed from the mold after cooling, and polished on a polishing wheel to final geometry.

Table 5.1: Compositions of the different epoxy formulations used in these investigations.

D400 Series

	mol% (all Constituents)			wt. % (all Consituents)		
Sample	**DGEBA**	**PACM**	**D400**	**DGEBA**	**PACM**	**D400**
PACM	66.67	33.33	0.00	76.40	23.60	0.00
D400-25	66.67	25.00	8.33	72.54	16.81	10.65
D400-50	66.67	16.67	16.67	69.05	10.67	20.28
D400-75	66.67	8.33	25.00	65.88	5.09	29.03
D400-100	66.67	0.00	33.33	62.99	0.00	37.01

D2000 Series

	mol% (all Consituents)			wt. % (all Consituents)		
Sample	**DGEBA**	**PACM**	**D2000**	**DGEBA**	**PACM**	**D2000**
PACM	66.67	33.33	0.00	76.40	23.60	0.00
D2000-10	66.67	30.00	3.33	63.62	17.69	18.69
D2000-20	66.67	26.67	6.67	54.51	13.47	32.02
D2000-30	66.67	23.33	10.00	47.67	10.31	42.01
D2000-40	66.67	20.00	13.33	42.37	7.85	49.78
D2000-100	66.67	0.00	33.33	25.40	0.00	74.60

5.2.2 Mechanical Property Testing

5.2.2.1 Dynamic Mechanical Analysis (DMA)

Epoxy samples with dimensions of 3.0mm x 1.0mm x 30mm were produced for the DMA experiments. Temperature sweep tensile DMA experiments were performed on each epoxy sample using an RSA3 dynamic mechanical analyzer (TA Instruments). Experiments were conducted at a frequency 1.0 Hz around a mean tensile strain of 0.1%. The experiments were conducted a temperatures from -120 °C to 225 °C. Samples were held at each temperature for 60 sec before the measurement was taken.

5.2.2.2 Vicker's Indentation Testing

Instrumented indentation and corresponding equations in polymer samples with a Vicker's indenter were described in section 2.1.2. Epoxy samples were prepared for hardness testing by polishing cylindrical epoxy sample with a diameter of ≈ 3 cm and a length of ≈ 1 cm, producing a smooth, scratch-free surface could be indented, with the resulting indent identifiable with optical microscopy. Indentation tests were conducted with a custom set-up of a TA Instruments Electroforce System with an ETx environmental chamber and cooled using liquid nitrogen. An ASTM certified Vicker's indenter was sourced from Gilmore Diamond Tools, Inc, and attached to the Electroforce set-up. The Vicker's indenter approached the epoxy sample at

a displacement rate of 0.05mm/s until contact. Once in contact, the tip indented into the sample using a linear force ramp to a set max force between 10-100N. The force ramp was selected to make sure that the loading time was equal to 5 seconds to avoid viscoelastic differences between tests at different forces [28]. After reaching the maximum force, P_{max}, the force was held for 15 seconds before ramping back to the original position at a rate equal to the loading rate. An example of a force displacement curve into one of the epoxy samples (D400-100) was shown in figure 2.3a.

The maximum force chosen was dependent on the temperature and stiffness of the epoxy, typically starting at 10 N for high temperatures, and increasing it if the indent size got too small, so all the indentation depths were within the range 50-200 μm. Literature has shown the hardness of epoxy to be invariant at these depths [30], and this was verified at room temperature for several samples as well. An image of the indent was then taken on an optical microscope to measure the diagonal of the indent, d, which is used to calculate the Vicker's indenter-sample contact area, A_v, by eq. 2.13, shown by the schematic in figure 2.3b. Although, the viscoelastic nature of polymer results in a significant amount of recovery of the indent even after the indenter is removed [31]. Research has shown that the viscoelastic recovery of the indentation of polymers is concentrated in the walls of the indent bowing inward [32]. Thus, for Vicker's indentation of polymers, recovery on the diagonals of the indent is negligible, so the hardness measurement from measuring the diagonal lengths remains fixed even as the indent recovers [30]. Therefore, hardness could then be calculated using eq. 2.10.

The indentation modulus, E_i, of the material can also be found by taking the slope of the unloading curve, $\frac{dP}{dh}$, as described by eq. 5.1, which is just a rearrangement of eq. 2.8 [26]. For these calculations, υ was estimated as 0.3 for all epoxy samples. For accurate measurements, the machine compliance must be accurately accounted for so that the sample compliance is accurately obtained. This was done by performing the indentation experiment on a sample of Al with a modulus of 69GPa.

$$E_i = \frac{(1-\upsilon^2)\sqrt{\pi}}{2\sqrt{A_V}}\frac{dP}{dh} \tag{5.1}$$

The indent was imaged using a Olympus OLS5000 3D Laser Confocal Microscope, from which the residual, or final, indentation depth, h_f, could also be measured.

5.2.2.3 Toughness Testing

Toughness tests were conducted with a custom set-up of a TA Instruments Electroforce System with an ETx environmental chamber and cooled using liquid Nitrogen. K_{Ic} fracture toughness measurements of the epoxy samples were conducted following ASTM D5045 − 14 guidelines for single edge notch bend (SENB) specimens [167]. Samples were designed for a support length, L, of 40 mm. A schematic of the sample is shown in 5.2, with the length of the sample slightly larger than the support length at 45mm, the width, W, at 10mm, the thickness, B, at 5mm, and initial notch length of 3.73mm. Using a razor blade and hammer, a precrack was made from the end of notch so that the total initial crack length, a_o, (notch + precrack) was between 4.5-5.5mm. Force was then applied to the sample above the notch at a displacement rate of 0.05mm/s. If the force displacement curve was linear, the maximum force, P_{max}, was used to calculate K_{Ic} using eqs. 5.2 and 5.3. If there was some yielding, shown by a deviation from linearity, a line with a 5% less steep slope than the initial force displacement curve is drawn from origin, and the point at which this line intersects the force-displacement curve is used as P_{max} in eq. 5.2. However, if the ratio of the true max force and this point is larger than 1.1, the K_{Ic} measurement was considered invalid. This is described in more detail in section 9 of ASTM D5045 − 14 [167].

$$K_{Ic} = \left(\frac{P_{max}L}{4BW^{\frac{3}{2}}}\right) f\left(\frac{a_o}{W}\right) \tag{5.2}$$

$$f(x) = 6x^{\frac{1}{2}}\left(\frac{1.99 - x(1-x)(2.15 - 3.93x + 2.7x^2}{(x+2x)(1-x)^{\frac{3}{2}}}\right) \tag{5.3}$$

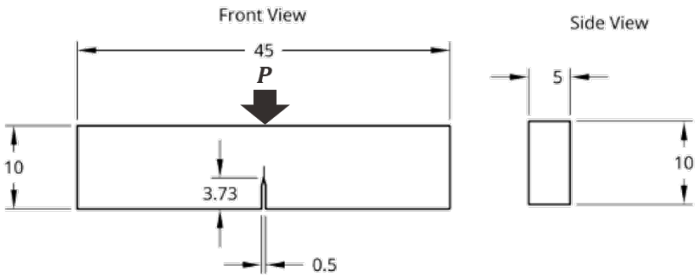

Figure 5.2: Schematic of the notched rectangular geometry of the epoxy samples used for K_{Ic} fracture toughness measurements. Dimensions in mm.

5.3 Results

5.3.1 Dynamic Mechanical Analysis

The dynamic mechanical analysis (DMA) results for model systems are shown in figure 5.3 for the D400 series (a, c) and D2000 series (b, d). They show good agreement with the DMA tests on the corresponding epoxies conducted by Masser, *et al.* [163], although the glass transition temperature, T_g, as determined by the temperature of the phase angle peak, for all samples are slightly lower by 10-20 °C. These differences may be due to different sourcing of the raw materials, or differences in the curing conditions, such as heating/cooling rates [168]. For the D400 series, increasing the D400 content causes the glass transition temperature to decrease, but maintains a narrow transition temperature range for each formulation, indicative of a homogeneous composition. The storage modulus in the glassy regime converges at low temperature for all formulations, but the rubbery modulus decreases with decreasing PACM since increasing the amount of the longer chain D400 decreases the crosslink density, υ_c, and thereby the rubbery plateau storage modulus, $E'_{rubbery}$, given by the following expression:

$$\upsilon_c = \frac{E'_{rubbery}}{3RT}, \tag{5.4}$$

where T is the corresponding temperature and R is the gas constant [169]. The calculated crosslink density values are plotted later in the next chapter in fig. 6.4**a-b.** The phase angle plot for the D400 series (5.3c) also shows a secondary transition around -40 °C, that seems invariant for each D400 formulation, however the magnitude of the peak is increased for the D400-100 system compared to the rest. For the D2000 series the transition regions for samples containing both D2000 and PACM are much broader than the PACM or D2000-100 systems suggesting some degree of heterogeneity in these materials. However, all samples are optically transparent, which verifies the small length scale of the heterogeneity.

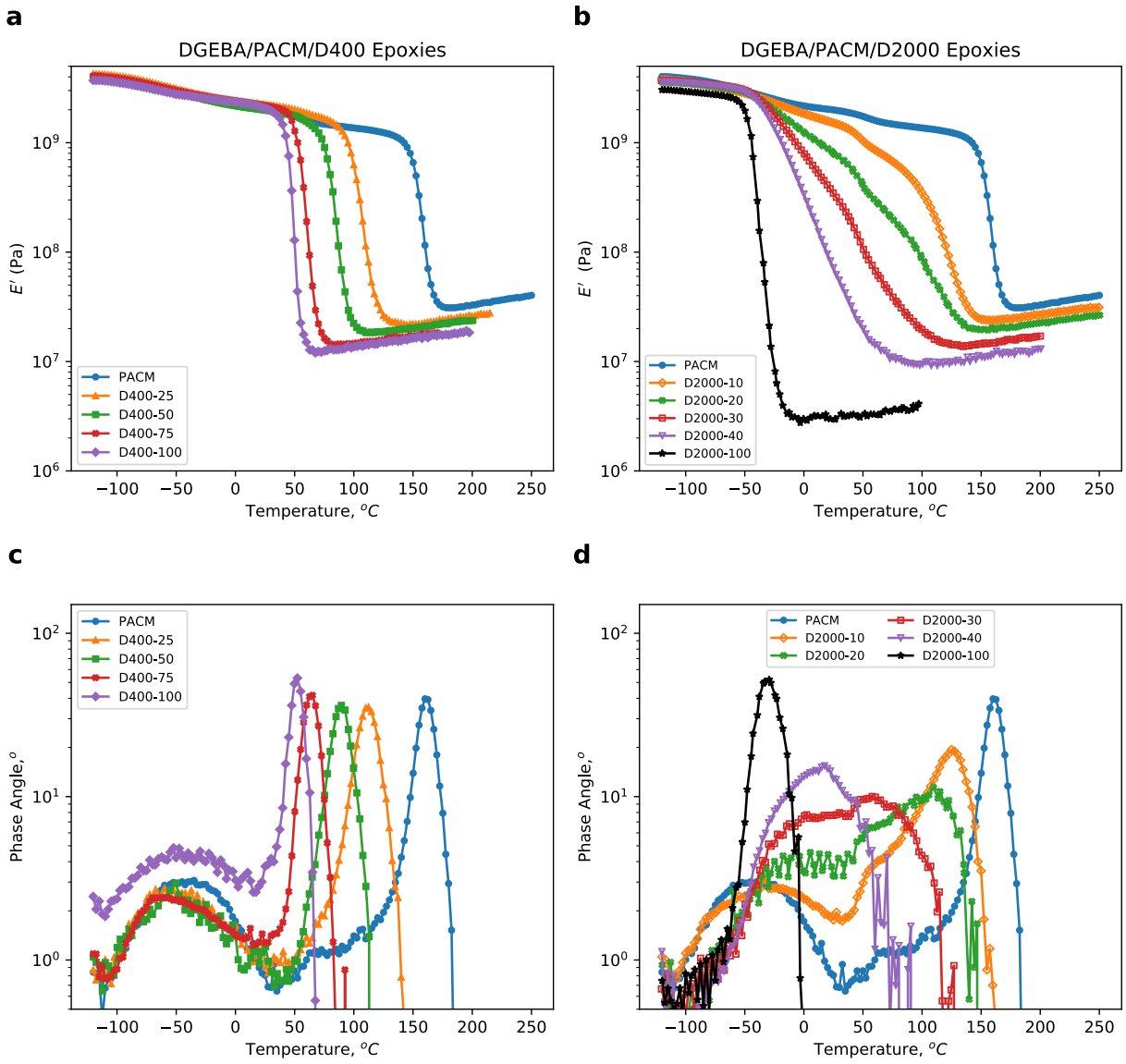

Figure 5.3: DMA characterization of Storage Modulus (**a**,**b**), and Phase Angle (**c**,**d**) for the DGEBA/PACM-Jeffamine epoxies with different PACM-Jeffamine molar ratios for (**a**,**c**) Jeffamine D400 series samples and (**b**,**d**) Jeffamine D2000 series samples. DMA conducted at 1Hz.

The nature of the glass transition in the different materials is illustrated by plotting the DMA data as a function of $T - T_g$, as shown in figure 5.4. For these purposes T_g is defined as the temperature for which the viscoelastic phase angle at 1 Hz is maximized. Although the limiting low temperature value of E' is ≈ 4 GPa in all cases, the temperature with respect to T_g at which the epoxy reaches this value is dependent on the

formulation. For the D400 systems in figure 5.4a, the glass plateau is reached at temperatures much closer to T_g for higher D400 content systems, likely due to the fact the secondary transition occurs at the same temperature for all systems, and therefore occurs closer to T_g for D400 systems (see 5.4c). For the D2000 systems, samples containing both PACM and D2000 show a broadened transition regime (figures 5.4b, d).

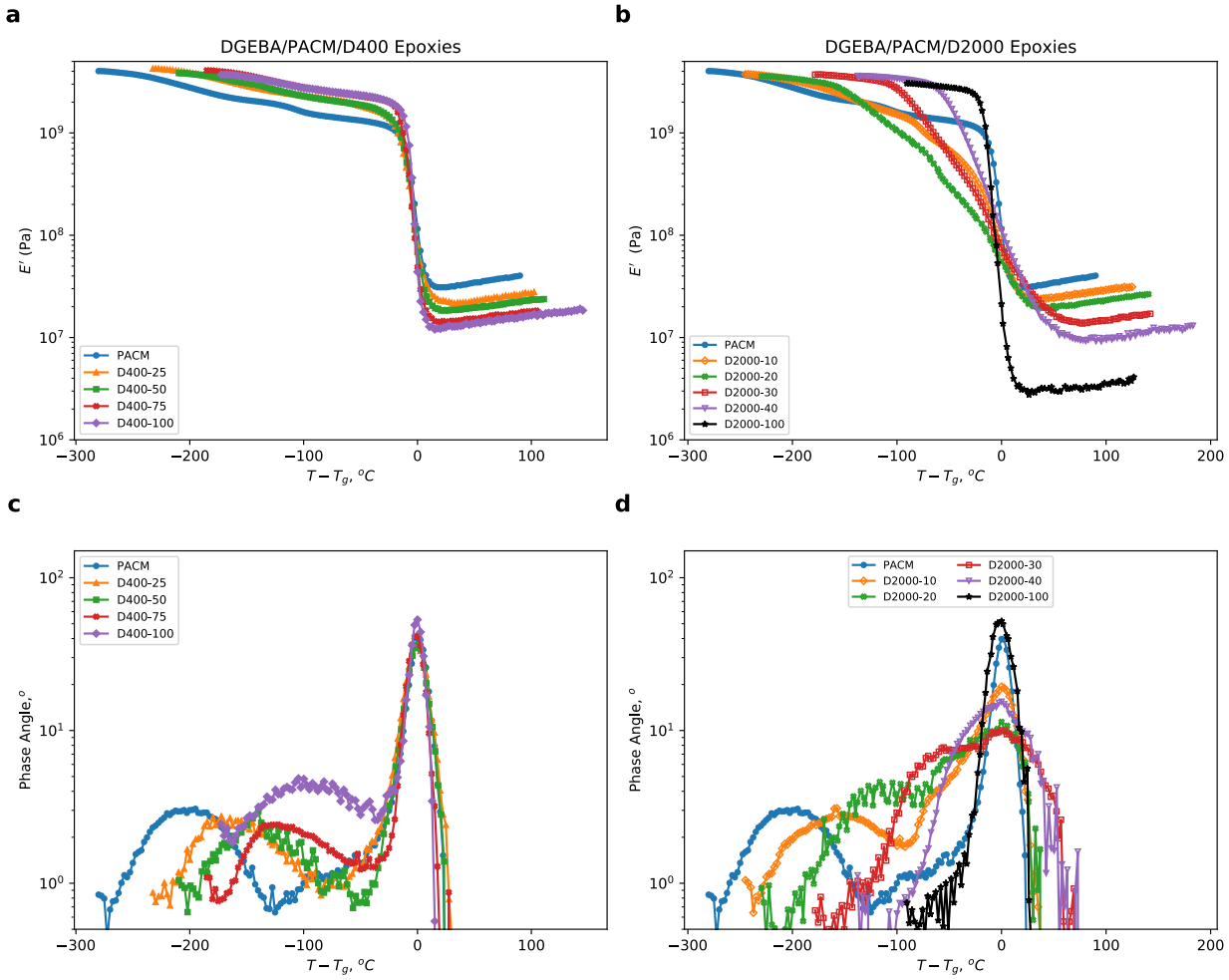

Figure 5.4: DMA characterization of Storage Modulus (**a**,**b**), and Phase Angle (**c**,**d**) plotted vs. $T - T_g$, where T for the DGEBA/PACM-Jeffamine epoxies with different PACM-Jeffamine molar ratios for (**a**,**c**) Jeffamine D400 series samples and (**b**,**d**) Jeffamine D2000 series samples. DMA conducted at 1Hz.

5.3.2 Vicker's Indentation Experiments

Results of the Vicker's Indentation hardness tests are shown in figure 5.5. For the D400 series of epoxies, seen in figure 5.5a, hardness steadily increases as temperature decreases. At higher temperatures, namely

0 °C and above, there is a clear trend of increased hardness with increasing PACM content. At lower temperatures, -20 °C and below, the hardness values of all PACM/D400 ratios start to converge in a way that is similar to the observed low-temperature dependence of the storage modulus. The hardness is not controlled simply by the difference below the glass transition temperature, as shown in figure 5.5c. At the same distance below T_g, the hardness increases with increasing Jeffamine content. A similar trend exists for the storage modulus, as seen in figure 5.4a, and so is likely tied to the temperature-invariant secondary transition as well, as described in the previous section. Qualitatively similar behavior is observed for the D2000 systems, as shown in figures 5.5b, d. There is no hardness data for the D2000-100 sample because the sample is too rubbery at room temperature to polish the surface.

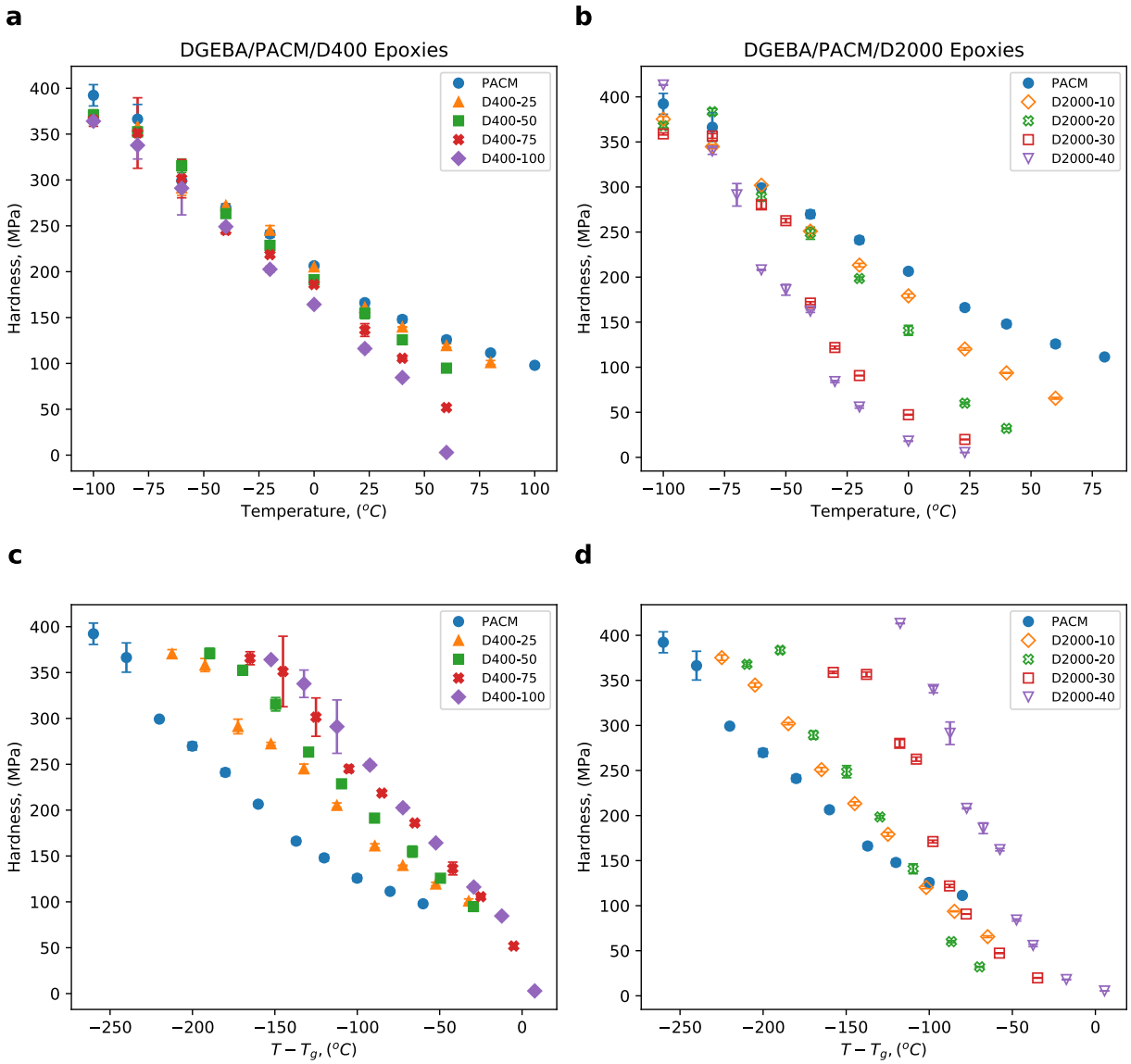

Figure 5.5: Hardness measurement as a function of temperature (**a, b**) and $T - T_g$ (**c,d**) for the DGEBA/PACM-Jeffamine epoxies with different PACM-Jeffamine molar ratios for (**a**,**c**) Jeffamine D400 series samples and (**b,d**) Jeffamine D2000 series samples.

Hardness is measure of how much a material deforms in response to a localized force. For materials such as metals and ceramics, it is an elastic-plastic measurement, meaning that both the elastic response and plastic deformation affect the measurement. Given the relationship between epoxy local plasticity and crack propagation, it is essential to deconstruct the effects of plasticity and elasticity on the hardness measurement

to better understand the fracture behavior of these epoxies [146, 152, 157]. The response becomes quite complex for polymers, due to the time dependent nature of the mechanical response and the very different yield and fracture mechanisms.

In an effort to understand the different intrinsic property contributions to the hardness measurement, the hardness value at each temperature was compared to the modulus at that same temperature. Moduli measured from the nanoindentation experiment using Equation (5.1) have larger errors than moduli obtained from DMA because of the relatively large machine compliance (~1μm/N) for our indenter, although the moduli measured by the two techniques correlate well with one another (figure 5.6a). We use the DMA storage modulus (E') as the most accurate measure of the temperature-dependent Young's modulus, E, for these systems. This ratio of hardness, H, to elastic modulus, E, has been used in the past as a measure of the relative importance of materials yielding in the deformation behavior [170–172]. A high value of H/E indicates that more of the deformation is elastic. The expected range of H/E for different polymers has been shown to be between 0.1 and 0.05, [173, 174]. Figures 5.6b and c show how H and E' are correlated to one another for D400 series epoxies and D2000 series epoxies, respectively. The value of H/E for both sets of epoxies is not constant with temperature. At lower temperatures, where the moduli and hardness values of the epoxies are the highest, $H/E \approx 0.1$, which is the upper limit of this ratio typically found for polymer systems. The value of H/E decreases with increasing temperature, reaching a limiting low-temperature value of ≈ 0.5. This would suggest greater plasticity as the epoxies near the T_g, which is expected. The nature of the transition between these two limiting values of H/E depends on the details of the formulation. For the D400 series an increased D400 content results in an decreased vale of H/E in the glass transition region. A more complicated composition dependence of H/E is observed for the D2000 systems, perhaps because of the more heterogeneous nature of these materials..

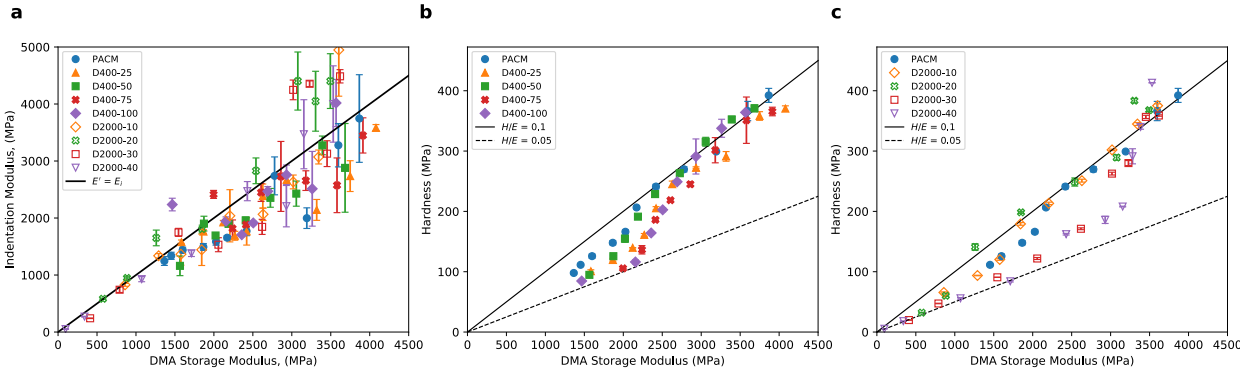

Figure 5.6: **(a)** A plot comparing the indentation modulus, E_i, to the DMA storage modulus at 1Hz, E'. Black line indicates $E_i = E'$. **(b, c)** Plots indentation hardness vs. DMA storage modulus of DGEBA/PACM/Jeffamine epoxies for **(b)** Jeffamine D400 series and **(c)** Jeffamine D2000 series. Solid line indicates the $H - E$ relationship at the low temperature (glassy) limit, with slope of 0.1. Dashed line indicates $H - E$ relationship in the higher temperature limit, with a slope of 0.05.

To verify the relationship between H/E and plastic deformation, the residual indentation depth can be used as measure of plasticity [175]. As shown by the indent schematic in 2.3c, at the maximum indentation depth, h_{max}, the depth of contact h_c, is slightly less, due to the elastic deformation of the material surface outside the contact area[5, 26]. When the load is removed, the depth of the indent will elastically recover to a final, residual depth of h_f.

Without permanent, plastic deformation, the surface would recover to its original position. For purely elastic-plastic materials, like metals, the residual depth will be equal to the displacement at which the unloading curve reaches 0 load (marked by the dot on the force-displacement curve from figure 2.3a, for example). However, the deformation in polymers is time dependent, and thus, the polymer surface can continue to recover once the indenter is removed [31]. Although research has shown that recovery can last over few days, the bulk of the recovery occurs in the first few seconds, then proceeds gradually [31]. Additionally, crosslinked thermoset polymer networks like epoxies are known to have thermally activated shape memory properties [176–178]. When heated above a certain temperature, normally the epoxy's T_g, the deformed epoxy material can return to its original shape, which in this case would mean complete recovery of the indent. In our experiments the residual depth was measured at room temperature, and we refer to the recovery as 'room temperature recovery' for this reason. In cases where the indent temperature is well below room temperature, additional recover can occur as the material is warmed back to room temperature.

Given that the residual indent depth is also dependent on the applied force, h_f was normalized by the

contact depth h_c, which would be the depth of the indent if no recovery occurred. For a Vickers indenter h_c is calculated from the following expression [179]:

$$A_V = 26.43 h_c \tag{5.5}$$

The indent recovery is defined as $1 - \frac{h_f}{h_c}$, where perfect recovery corresponds to $1 - \frac{h_f}{h_c} = 1$. Figures 5.7**a** and **b** show the indent recovery vs. amine mol%PACM at room temperature, -40 °C, and -100 °C for DGEBA/PACM/D400 epoxies and DGEBA/PACM/D2000 epoxies, respectively. These values for the recovery generally correlate with H/E, as shown in figures 5.7**c** and **d** for DGEBA/PACM/D400 epoxies and DGEBA/PACM/D2000 epoxies, respectively. The solid lines in these figures represent the following relationship between the recovery and H/E:

$$recovery = 0.2 + 7.55 \frac{H}{E} \tag{5.6}$$

Exceptions to this scaling for the samples with high D2000 content can be explained in terms of their shape memory effect. For systems for which T_g is well above room temperature, the room temperature recovery is expected to be equal to the recovery obtained at the indentation temperature. This equivalence is valid for all of the D400 samples, and for the D2000 samples with large PACM content. The three D2000 samples with high D2000 content show very broad T_g behavior, with an onset T_g that is at or below room temperature. The anomalously large recovery values obtained for these polymers are attributed to additional relaxation that occurs when the sample is warmed from the indentation temperature to room temperature.

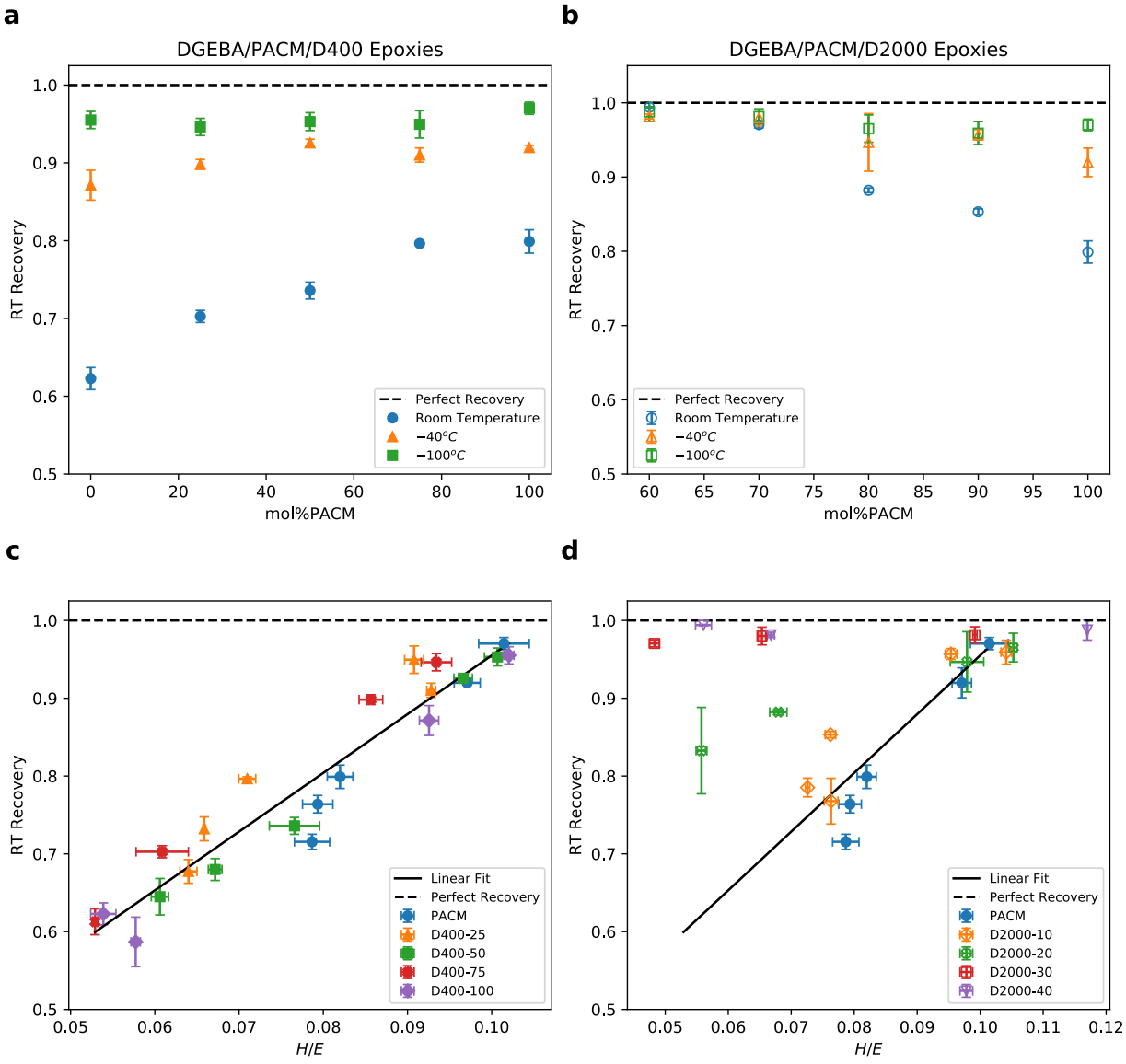

Figure 5.7: (**a**,**b**) Plots of indent recovery vs. amine mol%PACM at room temperature, -40 °C, and -100 °C for (**a**) D400 series epoxies and (**b**) D2000 series epoxies. (**c**,**d**) Plots of indent recovery vs. H/E for (**c**) D400 series epoxies and (**d**) D2000 series epoxies. Black line in **c** show linear relationship with slope of 7.55 (Eq. 5.6).

With this in mind, we can summarize our indentation results as follows:

- For homogeneous systems, there is a direct relationship between H/E, and indent recovery when temperatures are kept below T_g .

- Substantial recovery in the dynamically heterogeneous systems takes place at temperatures well below the temperature corresponding to the maximum in the phase angle, but within the temperature range corresponding to the transition between rubbery and glassy behavior.

5.3.3 Single Edge Notched Bend Toughness Testing

5.3.3.1 K_{IC} Measurements

The results of the single edge notched bend (SENB) toughness tests are shown in figure 5.8. Tests were conducted at temperatures from -100 °C to room temperature for all samples, and some of the more rigid samples were tested up to 100 °C. For the D400 series samples in figure 5.8**a**, several trends emerged. First, the relationship between K_{Ic} and T for each D400 formulation behaved similarly to literature descriptions of epoxy resins: a K_{Ic} plateau at low temperatures, followed by an increase in K_{Ic} near T_g [144, 145, 150]. When K_{Ic} is plotted as a function of $T - T_g$, as shown in figure 5.8**c**, all D400 formulations showed a low temperature plateau value of K_{Ic} for temperatures around 80 °C below the T_g. What was interesting was that the plateau value for the D400 systems system seemed to be one of two values, a low K_{Ic} of $\sim 0.65\,\mathrm{MPa}\sqrt{\mathrm{m}}$ for low D400 formulations (PACM, D400-25, D400-50), a value consistent with much literature data on epoxy resins. High D400 formulations (D400-75, D400-100), on the other hand, had a higher K_{Ic} of $\sim 1.5\,\mathrm{MPa}\sqrt{\mathrm{m}}$. The general trend was for the low-temperature fracture toughness to increase with a decreasing crosslink density. The measured K_{Ic} increased as the temperature approached T_g, but at different rates. Values of K_{Ic} for the D400-50, D400-75, D400-100 materials increased quite rapidly with T. A smaller increase in the fracture toughness was observed for the D400-25 system as T_g was approached, and now measurable increase in $K_{Ic}$was observed for the PACM system near T_g.

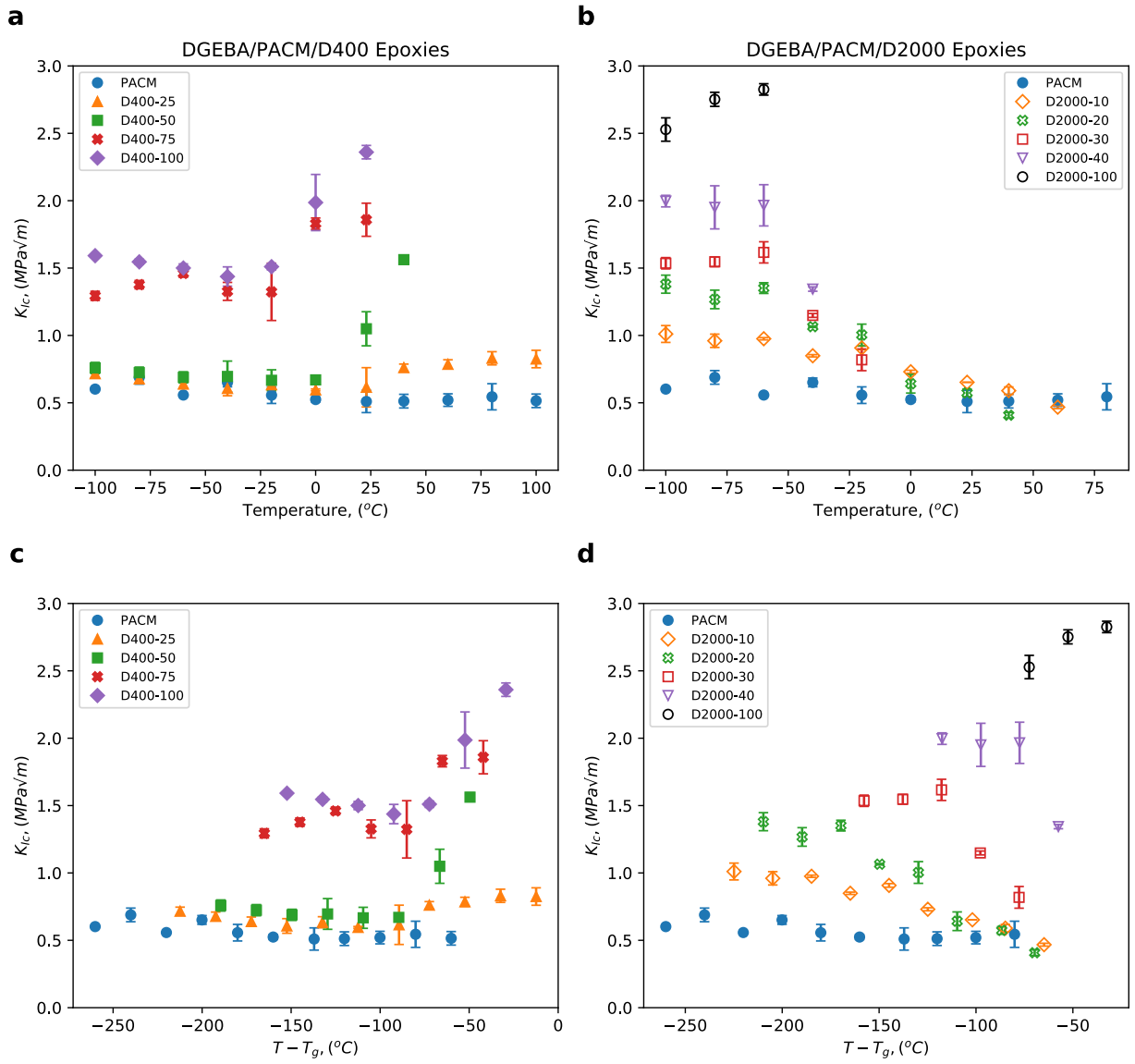

Figure 5.8: Toughness as a function of temperature (**a, b**) and $T - T_g$ (**c,d**) for the different epoxy materials: (**a**,**c**) D400 series epoxies and (**b,d**) D2000 series epoxies.

The D200 series epoxies shown in figure 5.8**b** exhibit trends that differ from those observed for the D400 systems. Like the D400 systems, K_{Ic} reaches a low-temperature plateau value that increases with decreasing crosslink density. However, the low temperature K_{Ic} steadily increases with increasing D2000 content, as opposed to having two distinct values for low and high PACM content. Also, as the temperature increases

from this plateau region, K_{Ic} for D2000 systems decreases as it approaches the glass transition regime, in direct opposition to the trends of the D400 systems. This behavior, with K_{Ic} increasing as the temperature decreases below T_g, is not typical of neat epoxy resins, but has been seen for epoxy resins toughened with rubber fillers [145]. This similarity suggests that the nanoscale heterogeneity in the D2000 epoxy resins systems induces a toughening effect akin to a rubber filled system, but without the need for actually incorporating a second phase material. However, as with the incorporation of a rubber filler, increasing the D2000 content decreases the yield stress. This decreased yield stress is accompanied by an increased plastic zone size in the vicinity of a propagating crack. When this plastic zone size is comparable to the sample size, K_{Ic} measurements can no longer be obtained accurately, as described in the ASTM standard [167]. Thus, as the D2000 content increases, the temperature range for the reported values of K_{Ic} decreases. For the two mixed PACM/D2000 systems that could reach ambient temperatures without significant yielding, D2000-10 and D2000-20, their room temperature K_{Ic} values were nearly identical to the values obtained for the PACM reference system. For completeness, we plot K_{Ic} for the D2000 systems as a function of $T - T_g$ in figure 5.8**d**. Also, we plot the critical energy release rate, $\mathcal{G}_{Ic}$, obtained from the measured values of K_{Ic} and E according to Eq. (5.7) in figure 5.9. This quantity is often used as a measure of material toughness, and is often more relevant than K_{Ic} for applications requiring a high energy dissipation as opposed to a high load-bearing capacity.

$$\mathcal{G}_{Ic} = \frac{K_{Ic}^2}{E} \tag{5.7}$$

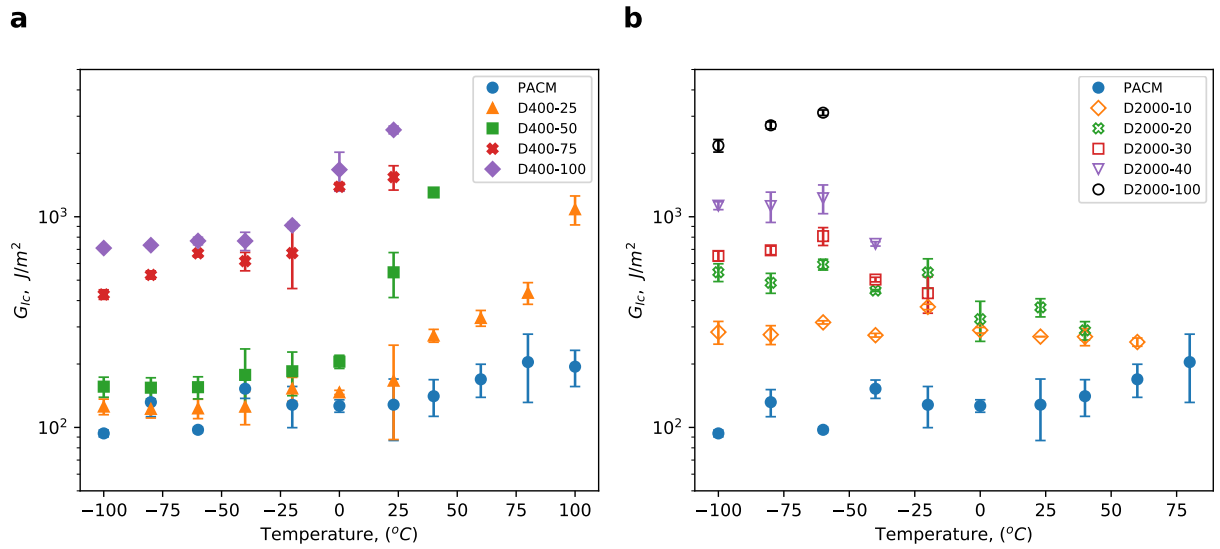

Figure 5.9: Critical energy release rate, G_{Ic}, as a function of temperature for the DGEBA/PACM-Jeffamine epoxies with different PACM-Jeffamine molar ratios for (**a**) Jeffamine D400 and (**b**) Jeffamine D2000.

The results of the SENB toughness tests can be summarized by these three primary points.

- The K_{IC} values reach a low-temperature plateau at temperatures well below the T_g for all epoxy formulations.
- The value of this low-temperature K_{IC} increases with Jeffamine content (decreasing overall crosslink density). For the D400 systems the increase is a continuous function of the D400 content, but for the D2000 systems there are two distinct toughness values of K_{IC}that differ from one another by a factor of 2.
- The toughness in the glassy regime increases with temperature for the homogeneous D400 systems, but decreases with temperature for the D2000 systems with nanoscale heterogeneity.

5.3.3.2 Plastic Zone Size Estimation

The following size criteria of the samples must be met in order for accurate values of K_{IC} to be obtained:

$$B,\ a,\ (W-a) > 2.5\left(\frac{K_{Ic}}{\sigma_y}\right)^2 \tag{5.8}$$

Here B is the sample thickness, a is the initial crack length, W is the sample width (see figure 5.2), and σ_y is the tensile yield stress. The value of B must be large enough to ensure plane strain and the region behind crack, $(W - a)$, must be large enough to avoid excessive plasticity. Given the sample geometry of $W = 10$mm, $B = 5$mm and $a \sim 0.5W$, the limiting dimension is ≈ 5 mm. The factor on the right side of eq. 5.8 is the approximate size of the plastically deformed region in front of the crack, referred to commonly as the 'plastic zone' or 'Dugdale zone' [150]. Given that crack blunting resulting from the size of this plastic zone is the main toughening mechanism in epoxies, this plastic zone size is important for understanding the fracture behavior in these systems.

The value of the tensile yield stress is difficult to measure for brittle samples, although it can often be correlated with the hardness, H. Koch and Seidler showed that for a number of thermoplastic polymers with shear dominated deformation behavior, the indentation hardness is about 3 times the tensile yield stress [180]. Here we use this approximation to obtain an estimate for the plastic zone size from the measured values of H and K_{IC} The results are plotted as a function of temperature in figure 5.10a for the D400 series and figure 5.10b for the D2000 series. The same data are plotted as a function of $T - T_g$ in parts c and d of figure 5.10. In some cases the plastic zone size approaches the limiting dimension of 5 mm, but is generally well below this value. These estimates of the plastic zone size validate the values obtained for K_{IC} and also serve as a point of reference for interpreting the images of the fracture surfaces shown in the following section.

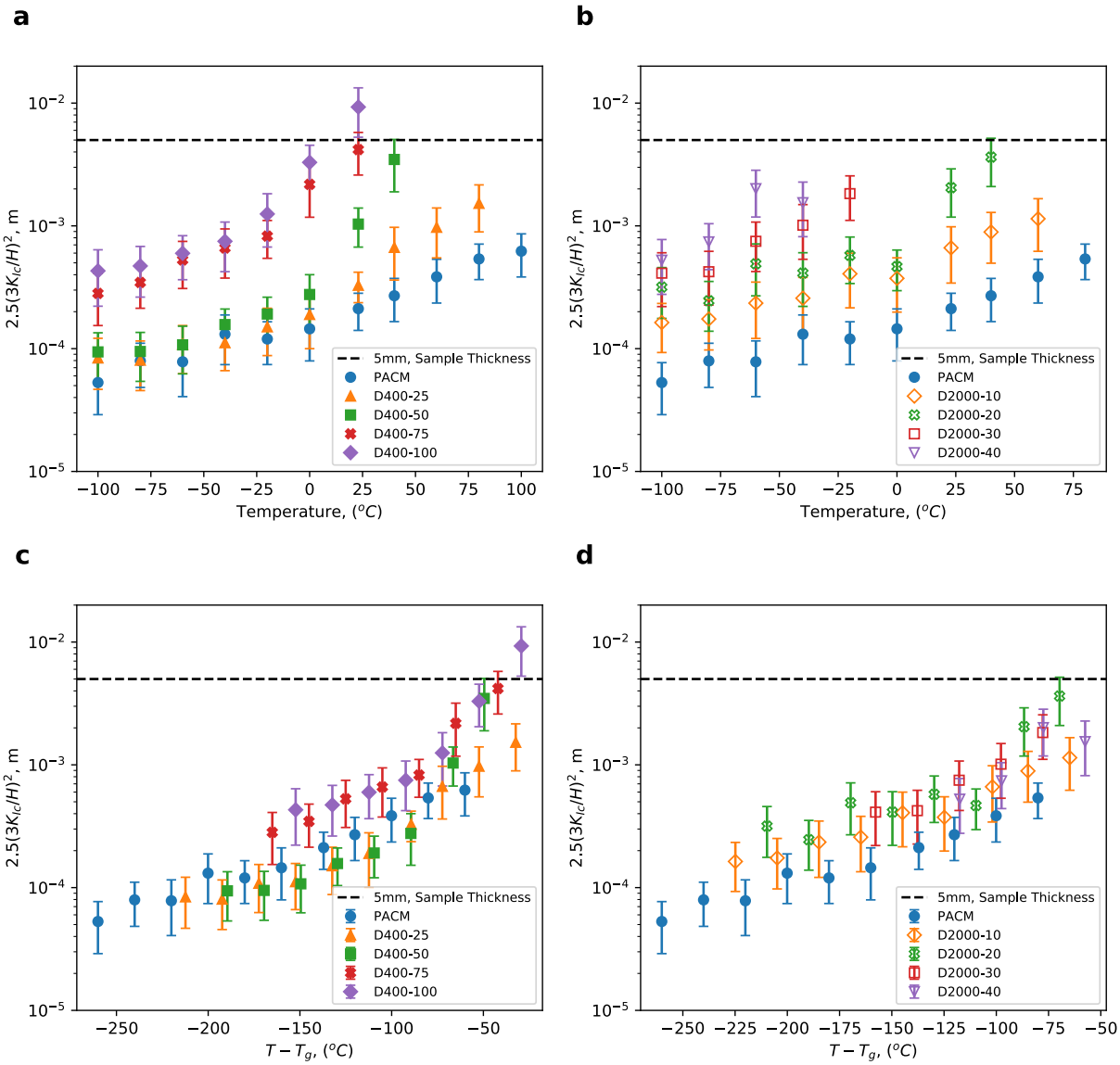

Figure 5.10: Plastic zone size estimation, vs. temperature for **(a)** D400 series epoxies, and **(b)** D2000 series epoxies. The same data is plotted vs. $T - T_g$ for **(c)** D400 series epoxies, and **(d)**D2000 series epoxies. The sample thickness B of 5mm is marked by the dotted line. Points below the dotted line satisfy the inequality.

5.3.3.3 Fractography

To better understand how fracture differed between the different epoxy systems, the fracture surface of each SENB sample was observed under a 3D laser confocal microscope. All images are shown in **Appendix A.2**,

but a few of the most informative images are explored in this section. The cross-section of a fractured SENB polymer sample generally has five distinct regions, indicated in the SENB schematic in figure 5.8a:

1. Initial Notch. This is formed in the mold
2. Razor blade inserted region. The region is formed by wedging the razor blade into the notch. The region was physically in contact with the blade during wedging.
3. Wedge-induced pre-crack. This crack forms in-front razor blade-inserted region, but does not physically come in contact with the blade. This crack is present before running the SENB test. This is not always present, as softer epoxies will not form a pre-crack in front of the razor blade.
4. Deformation during sub-critical crack growth (slow growth region). This region is typically rough as the result of localized yielding and resistance to crack prorogation.
5. Deformation from fast-growth region (unstable crack growth). This region is typically smooth.

Special attention is given to region 4, the slow growth region, which gives the most information in regards to toughening mechanisms, and has been shown to be on the order of magnitude of the plastic (Dugdale) zone [157]. From this region, the fracture can generally be described as "brittle" for a small slow growth region, "tough," for a larger slow growth region, and "ductile," for when the bulk of the fracture surface displays yield behavior and linear elastic fracture mechanics no longer applies. Although the fracture surfaces of the epoxies can generally be described by these three modes of failure, the exact morphology can differ substantially with epoxy formulation and temperature, suggesting different mechanisms are at play for different formulations.

5.3.3.4 Fractography in Homogeneous D400 Series Samples

The low temperature K_{Ic} plateau from figure 5.8a of the PACM-rich (amine content of 50% or more PACM) D400 formulations all had crack surface morphologies similar to the PACM sample at -100 °C, shown in figure 5.11b. This surface is similar to fracture surfaces obtained for other brittle epoxy resins [146, 147, 150, 157, 181]. Due to the stiff and brittle nature of these epoxies, region 2 is very small, and hard to discern from region 1. However, the pre-crack (region 3), consists of multiple curved arrest lines in the direction of crack propagation, that are due to the precrack moving and stopping from hammering the blade into the notch multiple times [152]. These arrest lines are curved due to the change in stress state in the SENB sample: there is plane strain in the center of the sample, and plane stress near the edges [182]. Magnifying the crack front in figure 5.11d shows that in front of each arrest line there is a coarse "hackled" region with numerous

striations, which is representative of the slow growth region (region 4) in these brittle epoxies. In front of this hackled region, the striations coalesce into longer lines known as "river markings" that correspond to the increased crack velocity as the crack exceeds the critical length and rapidly moves across the remainder of the sample, resulting in a smooth, featureless region far ahead of the initial crack front (region 5). These features are not observed for the D400 samples with high D400 content. In particular, there is no crack extension in front of the razor blade as it is inserted in to the sample, so region 3 does not exist. Figure 5.11c for the D400-100 sample at -100 °C is a representative example. From a higher resolution image of the slow growth region for this sample, shown in figure 5.11e, we see a higher degree of roughness, consistent enhanced plastic deformation in the plastic zone and higher measured values of K_{Ic} for these samples.

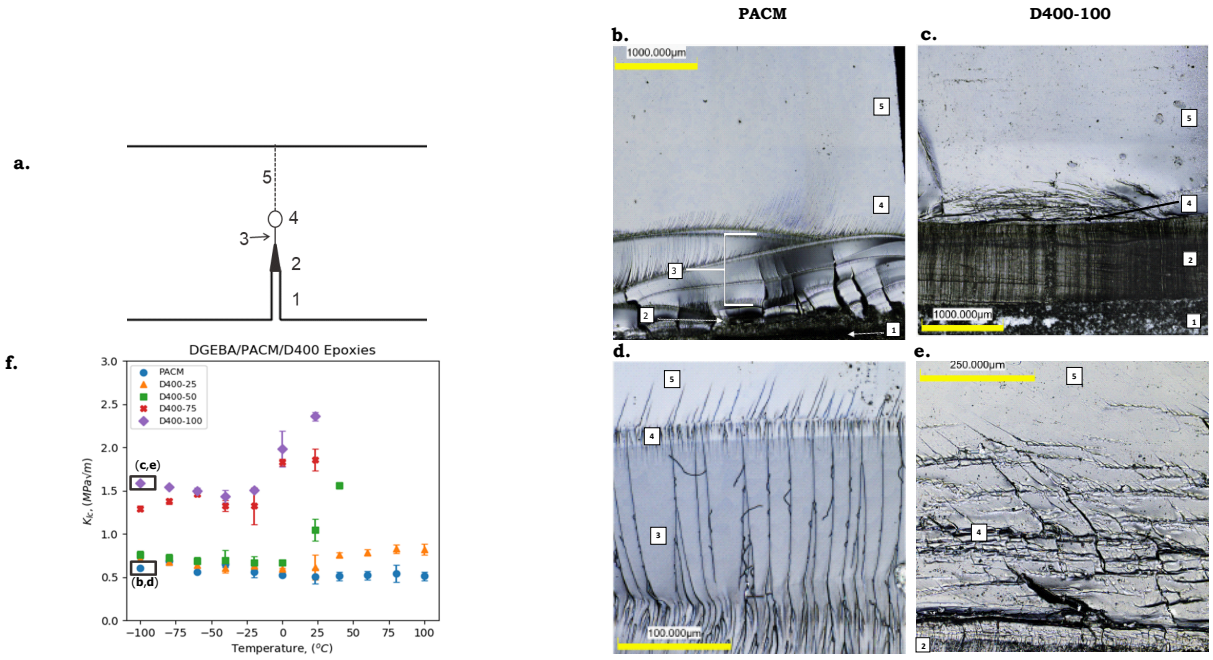

Figure 5.11: **(a)** Schematic of the notch region of the SENB toughness sample indicating the regions of the fractured surface: (1) initial notch, (2) razor blade inserted region (contact with blade), (3) wedge-induced pre-crack, (4) slow growth region, and (5) critical, fast growth region; **(b-e)** 3D laser confocal microscope images of the fracture surfaces of a PACM sample (b, d) and a D400-100 sample (c, e) at two magnifications. The notch of each sample is located at the bottom of each image, and the fracture direction goes from the bottom to the top of each samples. **(f)** Plot of K_{Ic} vs. Temperature (from fig. 5.8a) with the corresponding images indicated shown in this figure enclosed by black boxes.

Figure 5.12 shows a representative fracture surface for each D400 formulation in high temperature regime, where K_{Ic} increases as T_g is approached. For the PACM sample at 80 °C, K_{Ic} was about the same as for the low temperatures. However, the morphology of the fracture surface, shown in 5.12a, is much different

than the low temperature surface in 5.11a. First, the hackled region above the crack front (labeled 4) is noticeably larger than at low temperature, consistent with the increasing plastic zone size with temperature. However, the river markings that extend from the hackled region to the fracture surface (5) are much more numerous, and extend through the entire length of the fracture surface. The inset of 5.12a magnifies the hackled region, showing that these river markings do not intersect. The D400-25 sample at 60 °C, shown in 5.12b, which has a slightly higher K_{IC} than at low temperature, similarly shows a large hackled region at the crack front, but the width of this region is larger than for the PACM sample. Additionally, the river markings are longer than at low temperature, but they do not extend for the entirety of the fracture surface and are more widely spaced. Additionally the region directly above the hackled region is very rough for about 2mm, before becoming relatively smooth. Such roughness are also seen on fracture surfaces of PACM samples at 60 °C, 40 °C and room temperature (see **Appendix A.2**), but for a much smaller region than seen on the D400-25 sample at 60°C. For D400-50 sample at 40 °C, shown in 5.12c, the measured K_{IC} is about $1.5\,\mathrm{MPa}\sqrt{\mathrm{m}}$, more than twice the value obtained for the PACM sample at 80 °C (figure 5.12a). This D400-50 sample shows a larger hackled region above the initial crack front. Additionally, the river markings are thicker, shorter, and seem to be pushed towards the edges of the sample. Finally, fracture surfaces for D400-75 and D400-100 fractured at room temperature are shown in figures 5.12d and e, respectively. They both show very rough surfaces that are likely the result of macroscale yield behavior, which is consistent with a plastic zone size that exceeds the sample size (fig. 5.10).

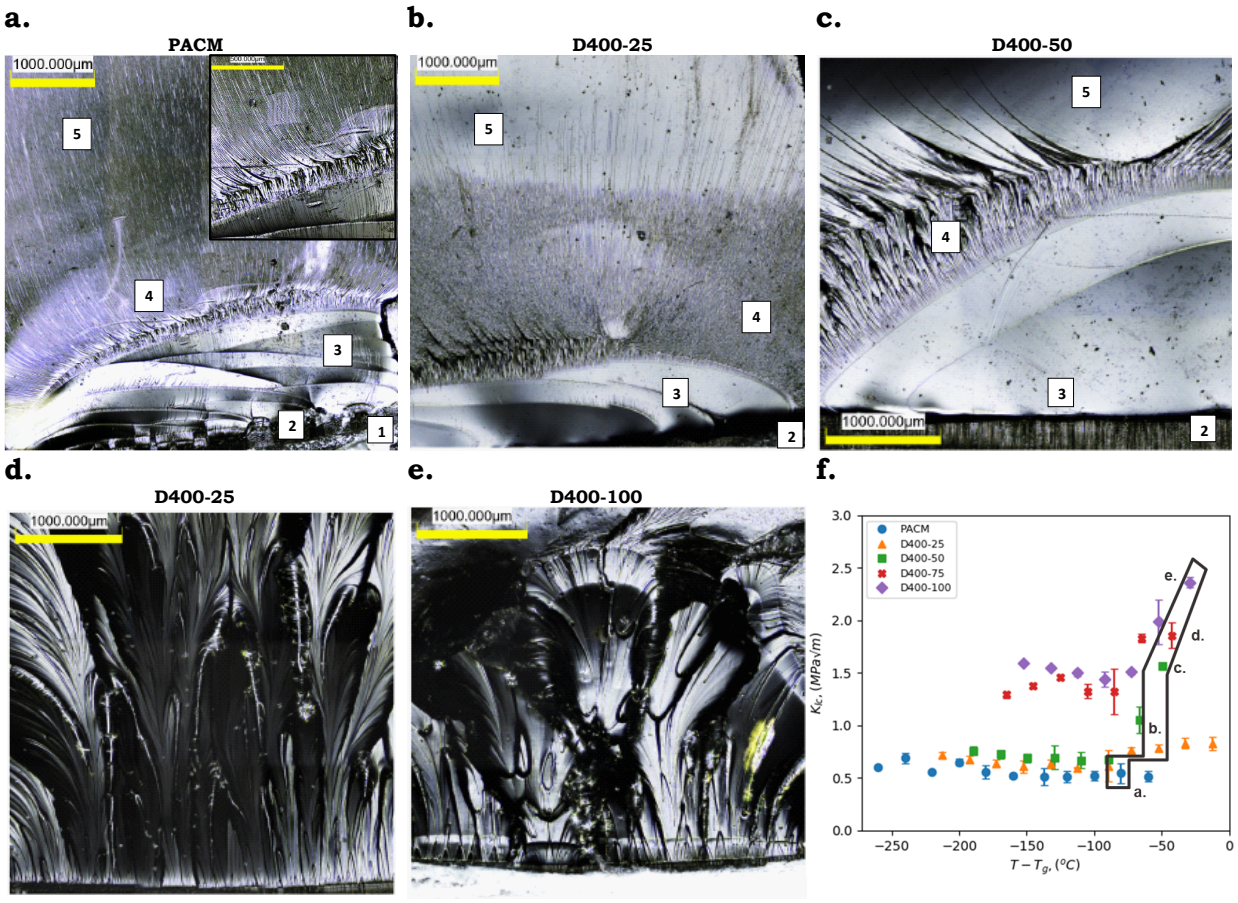

Figure 5.12: 3D laser confocal microscope images of the fracture surfaces of D400 series epoxies in the high temperature limit: (**a**) PACM at 80 °C , **(b)** D400-25 at 60°C, **(c)** D400-50 at 40 °C, **(d)** D400-75 at room temperature, and **(e)** D400-100 at room temperature. The notch of each sample is located at the bottom of each image, and the fracture direction goes from the bottom to the top of each samples. (**f**) Plot of K_{Ic} vs. $T - T_g$ (from fig. 5.8c) with the corresponding images indicated shown in this figure enclosed by black box.

5.3.3.5 Fractography in Dynamically Heterogeneous D2000 Series Samples

The D2000 series epoxies have strikingly different fracture surface morphologies than their D400 counterparts. Fracture surfaces at the low temperature limit (-100 °C) for the D2000 formulations are shown in figure 5.13a-e. In all tested D2000 formulations, a large, well defined rough arch appears in front of the pre-crack region, with a size on the order of magnitude of the plastic zone size. This zone, however, is morphologically distinct from the well "hackled" regions shown in the D400 formulations. The roughness within this plastic arch increases with increasing D2000 content, which correlates with increased fracture toughness. Above this plastic arch, the surface is relatively smooth for the lower D2000 content formulations. D2000-40 fracture

surface exhibits parabolic-features above the plastic arch, which have been shown to be the result of secondary crack initiation in front of the primary crack front[139].

Fracture surfaces for samples fractured at higher temperatures are shown in figure 5.13f-i. The D2000-10 sample fractured at 40 °C (figure 5.13f), shows a similarly rough surface for both the area directly above the precrack and the main fracture surface, similar to what is seen in the high temperature fracture of the PACM sample (figure 5.12a) without the hackled region. For D2000-20 fractured at 40 °C (Figure 5.13g), thick river lines originating from the crack front appear, but soon disappear into a uniformly smooth surface, despite having a similar measured K_{IC} to the D2000-10 sample at the same temperature. The D2000-30 sample fractured at 0 °C (fig. 5.13h) and D2000-40 sample fractured at -20 °C (fig. 5.13i) show similar crack surface morphologies, and in both cases result in an invalid K_{IC} due to bulk material yielding. However, the fracture surface morphology of these yielded samples, for which the K_{IC} value was low at the next measurable temperature, is different from the fracture surfaces of the high temperature yielded samples of D400-75 and D400-100, shown in figures 5.12d and e, where the previously measurable K_{IC} (at 0 °C) was relatively high.

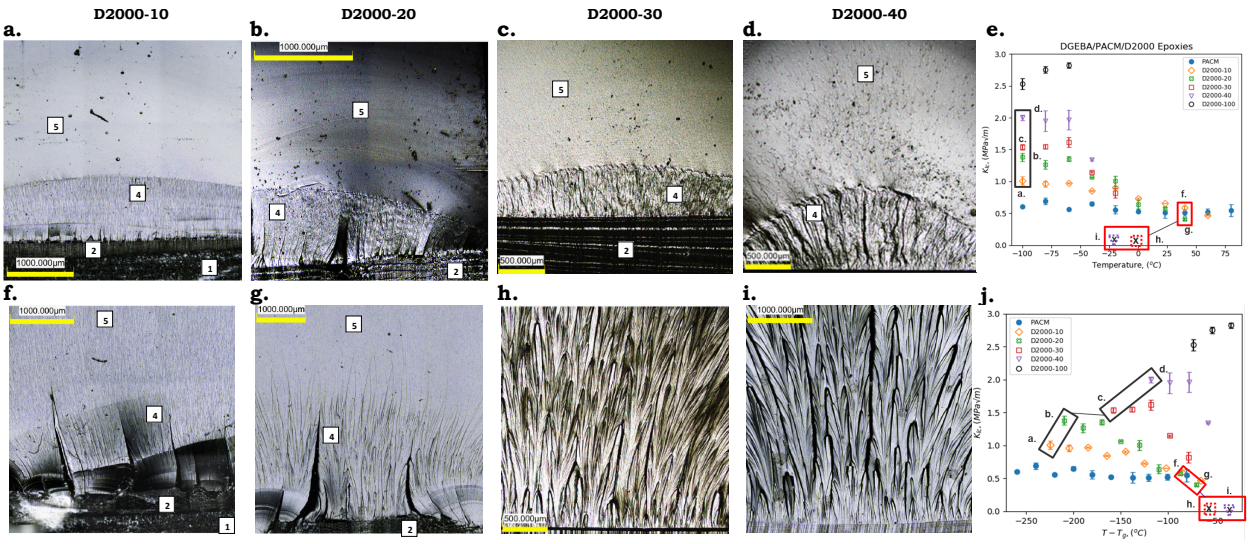

Figure 5.13: Fracture surfaces for D2000 series epoxies at both ends of the measured temperature range. D2000-10 at (**a**.) -100 °C and (**f**.) 40 °C; D200020 at (**b**.) -100 °C and (**g**.) 40 °C; D2000-30 at (**c**.) -100 °C and (**h**.) 0 °C; D2000-40 at (**d**.) -100 °C and (**i**.) -20 °C. Plots of K_{Ic} vs (**e**.) T and (**j**.) $T - T_g$ (from fig. 5.8b,d) with the data corresponding to the images enclosed in black boxes (-100 °C) or red boxes (higher temperatures). Note that since K_{Ic} could not be measured accurately for D2000-30 at 0 °C and D2000-40 at -20 °C because the samples are too ductile, they are indicated by x's and dashed markers at $K_{Ic} = 0$.

The most distinct change in fracture surface morphology for the D2000 series epoxies occurs for the

D2000-20, D2000-30 and D2000-40 systems between -40 °C and -60 °C, shown by the fractographs in figure 5.14. This temperatures correspond to to the temperature where all three of these samples reach their low temperature plateau value (-60 °C), as shown in figure 5.8c, and the temperature (-40 °C) where the K_{IC} starts to reduce with increasing temperature. In the low temperature plateau at -60 °C in figures 5.14b,d, and f the characteristic slow growth region, similar to 5.13b-d at -100 °C described above, is apparent in these samples. However, when the temperature increases to -40 °C, the outline of the slow growth region is still seen on the fracture surface above the initial crack front, but this region becomes smooth, as seen in figure 5.14a,c, and e. This result indicates once again that increased roughness in the slow growth region leads to higher K_{IC}. However, the smooth morphology here is very distinct from the high temperature fracture surfaces seen in 5.13g-i where more ductile behavior dominates. As mentioned previously, the expected nano-scale heterogeneity in these systems, likely leads to local T_g heterogeneity. Given that this morphology change occurs ~10 °C below the T_g for the D2000-100 sample, the smoother regions between the low temperature "tough" regions and the higher temperature "ductile" regions, are likely due to these local differences in T_g.

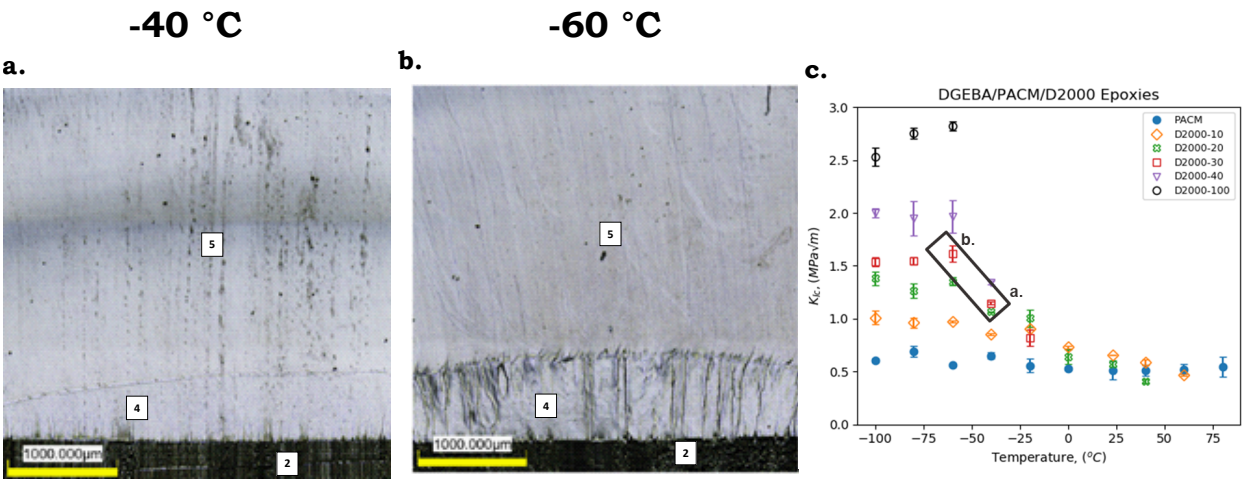

Figure 5.14: Fracture surfaces of D2000-30 at (**a**) -40 °C and (**b**) -60 °C. K_{IC} drops as the temperature is increased from -60 °C to -40 °C, which corresponds to the disappearance of the rough slow growth region. Similar morphology changes are seen for D2000-20 and D2000-40 at the same temperatures. (**c**) Corresponding K_{Ic}vs. T plot from fig. 5.8b, with the data corresponding to the images enclosed by black box.

Examination of the fracture surfaces of these samples shows that the K_{Ic} fracture toughness data from the previous section is closely tied to fracture surface morphology. While the fracture surface morphology in the D400-based systems is consistent with much of the literature on epoxy fracture surfaces, such as arrest

lines and river markings, the fracture surfaces of the D2000-based systems are more unique. A rough, but contained plastically deformed zone around a crack tip is indicative of higher fracture toughness for the dynamically heterogeneous D2000-based systems. These features disappear at higher temperatures, likely due to local T_g heterogeneity. Although plastic yielding is the key mechanism of epoxy fracture toughness in all cases, plasticity manifests itself very differently in the fracture behavior of epoxies with nanoscale heterogeneity. Information from these fracture surfaces can potentially be used to better understand the deformation mechanisms, perhaps leading to the development of new machine learning tools to enable a more rapid materials design and validation process.

5.4 Conclusions

This report outlines an in depth investigation in the temperature dependence of the fracture and deformation behavior of a model epoxy system that consists of a DGEBA epoxide with a stoichiometric amine mixture of a rigid cycloaliphatic diamine (PACM) and a more flexible, polypropylene glycol based diamine (Jeffamine) at different molar ratios, exploring the effect of nanoscale heterogeneity by varying the molecular weight of the Jeffamine used. Vicker's Indentation hardness experiments were conducted at different temperatures from -100 °C to 80 °C, and measured hardness trended well with the DMA storage modulus for all epoxy systems. Measurement of the residual indent after the indentation experiments showed a distinct linear correlation between the ratio H/E, and indentation recovery for the homogeneous D400-based epoxies that was independent of the ratio of PACM to D400 when temperatures were held below the epoxy's T_g. However, the D2000-based epoxies showed more recovery at lower H/E values with increasing D2000 content after returning to room temperature, exhibiting partial shape memory recovery that increased with increasing D2000 content. This showed that H/E is very predictive of permanent plastic deformation in the homogeneous epoxy materials at temperatures below T_g, but not so much in the D2000-based epoxies where broadened glass transition regime, as a result of nanoscale heterogeneity increases shape memory recovery even at temperatures below the phase angle peak.

Single edge notched bending tests were also performed on these samples in the same temperature range to measure K_{IC} and showed distinct trends for each set of epoxies. The results can be summaries as follows:

- K_{IC} for the homogeneous D400 series epoxies were constant at low temperature for all formulations, for all temperatures 80 °C or more below the T_g.
- The low temperature K_{IC} for the D400 series epoxies separated into two distinct values, depending

on D400 content: 0.65 MPa$\sqrt{\text{m}}$ for low D400 formulations, and about 1.5 MPa$\sqrt{\text{m}}$ for higher D400 formulations. Analysis of the fracture surfaces of these samples suggest the initial crack tip of the higher D400 content samples is more blunt than the lower D400 content epoxies, due to lack of arrest lines and hacked regions.

- At high temperatures, K_{IC} for the D400 series epoxies increased as the T_g is approached.
- K_{IC} for the D2000 series epoxies also reached a low-temperature plateau. The low temperature K_{IC} increased with increasing D2000 content. The fracture surfaces of these epoxies fractured at low temperature show a characteristic plastic zone arch that increases in roughness with increasing D2000 content.
- K_{IC} for the D2000 series epoxies decreased with increasing temperature and was accompanied by a decrease in the roughness of the fracture surface. The fracture surface morphology in these D2000-based systems is distinct from that of the homogeneous D400-based systems, even in situations where the values of K_{Ic} are quite similar.

This investigation shows that the fracture behavior of an epoxy can be tailored based on careful selection of epoxide and ratio of hard to soft hardener, which opens many doors for the use of epoxy composites in applications requiring exposures to cryogenic temperatures and wide temperature ranges.

Chapter 6

Exploring Effect of Nanoscale Heterogeneity in the Temperature Dependent Fracture Behavior in for Epoxy-PMMA Semi-Interpenetrating Polymer Network Systems

This chapter explores the sequential synthesis of semi-interpenetrating polymer networks (semi-IPN) using the same model DGEBA/PACM/Jeffamine epoxy system described in chapter 5 with thermoplastic poly(methylmethacrylate) (PMMA) to investigate the effect of nano-scale heterogeneity found in DGEBA/PACM/Jeffamine-D2000 systems on the temperature dependent mechanical and fracture properties of the corresponding semi-IPN compared to that of the homogeneous DGEBA/PACM/Jeffamine-D400 systems. The DGEBA/PACM/D2000 epoxies swelled with much more PMMA than the DGEBA/PACM/D400 systems, even at similar crosslink densities. Dynamic mechanical analysis showed that the uptake of PMMA in the epoxy networks generally lead to an increase in T_g, and for the dynamically heterogeneous DGEBA/PACM/D2000 systems with broadened transition regimes, an extension of the glassy plateau to higher temperatures for the epoxies in their DMA curves. Further fracture and indentation tests were explored for the 100mol%D400,

70mol%PACM 30mol%D2000, and 60mol%PACM 40mol%D2000 systems. The low temperature K_{Ic} fracture toughness decreased for the epoxy-PMMA semi-IPN and characteristic fracture surface morphology of the neat polymers disappeared, but there was less temperature variation of the fracture toughness values for all three systems. Additionally, indentation tests showed a reduction in the shape memory effect for the DGEBA/PACM/D2000-IPNsystems, but no noticeable change for the 100%D400 system. The experimental work described in this section was done collaboratively with Ruiqi Xiao.

6.1 Introduction

The previous chapter (5) explored the temperature dependence of the fracture, elastic, and plastic properties of model epoxy systems with and without nano-scale heterogeneity. The epoxy system, consisting of diglycidyl ether of bisphenol A (DGEBA) as the epoxide with a stoichiometric amine mixture of a rigid cycloaliphatic diamine (PACM) and a more flexible, polypropylene glycol based diamine (Jeffamine) at different molar ratios, exhibits nanoscale heterogeneity, evidenced by broadened glass transition regime with DGEBA/PACM/Jeffamine systems using high molecular weight (MW) Jeffamine, MW=2000g/mol (D2000). It was shown that the the toughness of the dynamically heterogeneous DGEBA/PACM/D2000 epoxy systems at very low temperatures ($<-60°C$) increased monotonically with increasing D2000 content at low temperature. Thus, the dynamically heterogeneous systems shows great potential for a system with improved fracture toughness at low temperature compared to ambient temperatures with more control over desired low temperature properties. For applications such as matrix materials for fiber-reinforced composites in cryogenic liquid containers where significant thermal cycling can lead to significant thermal stresses [142, 143], a matrix material where there is high low temperature toughness is desired to avoid microcracking in failure. However, the dynamic heterogenous DGEBA/PACM/D2000 epoxies show reduced toughness and significant temperature dependence of modulus and hardness as a result of the broadened transition regime and local heterogeneity, leading to a reduction in structural integrity and utility in high performance applications[163–165].

From a design stand-point, the ideal epoxy system would have a very high toughness at low temperature to prevent low temperature catastrophic failure in addition to a high modulus or stiffness at ambient conditions (or even higher) to maintain structure rigidity. This can be visualized in the plot shown in figure 6.1 that plots the measured K_{Ic} at -100C determined from the SENB tests in section 5.2.2.3 vs. the corresponding measured room temperature DMA storage modulus (E') at measured at 1Hz. An optimal epoxy would have properties in the top right corner: high stiffness at room temperature, and high toughness at low temperature. Thus,

this chapter aims to find a method to increase the range of glassy modulus in the dynamically heterogeneous epoxy systems while maintaining their low temperature fracture toughness performance.

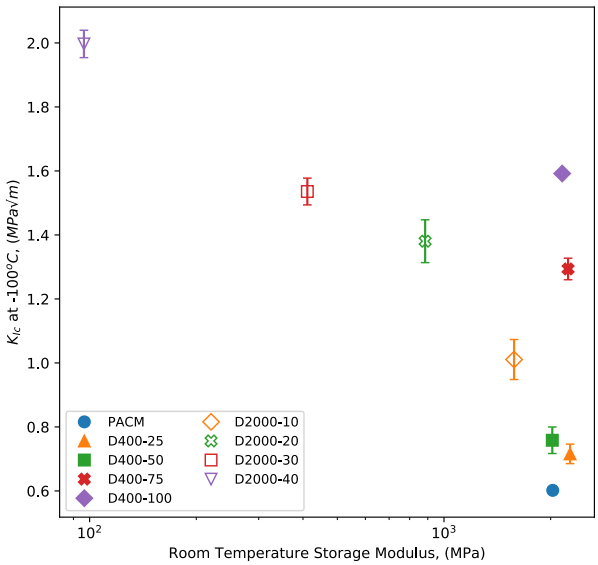

Figure 6.1: Plot of the K_{Ic} fracture toughness at -100°C vs.vs. the room temperature time DMA E' value at 1Hz for different formulations of the DGEBA/PACM/Jeffamine model epoxy system described in chapter 5. Optimum structural and fracture performance would push data to the top right corner.

Interpenetrating polymer networks (IPNs) have been explored to improve the mechanical properties of polymer systems like epoxies [183, 184]. IPNs are a type of polymer blend where at least two different polymers are interwoven together, as the result of crosslinking in one or both of the polymers, but are not covalently bonded with each other [185]. For full IPNs, each of the polymer species are crosslinked, and the crosslinked networks of each polymer are interwoven, and thus cannot be separated without breaking the crosslinks, despite the lack of covalent bonds between the two polymers, whereas semi-IPNs have only one crosslinked polymer, with the other polymer being linear (and thus more mobile), but polymerized within the network of the crosslinked polymer. IPNs can be synthesized simultaneously, where the monomers of each constituent polymer are mixed together and polymerized at the same time, or sequentially, where one polymer is synthesized first, then the monomers is swollen into the first polymer before subsequent polymerization [186]. The type of polymerization and relative quantity of each polymer component can effect the phase morphology and properties of the resulting IPN [187]. A schematic of the sequential preparation of a semi-IPN is shown in fig. 6.2.

Previously, full and semi-IPN's of homogeneous epoxy resins with high performance ductile thermoplastics such as poly(methylmethacrylate) (PMMA) have been explored as a method for improving epoxy toughness, resulting in improved thermal stability, as well as mechanical and damping properties [188–190]. Given the relative high glass transition temperature of PMMA (85-165 °C), the relatively high fracture energy due to its large free volume [190], and good miscibility of PMMA with DGEBA resin [191], PMMA appears to be a good candidate to add to the model DGEBA/PACM/Jeffamine epoxy network to improve the ambient stiffness of the epoxy while hopefully maintaining toughness behavior. This chapter examines the temperature dependent mechanical properties of DGEBA/PACM/Jeffamine - PMMA semi-IPNs and evaluates their potential for improved extreme temperature performance. Although it will be shown that the aforementioned method of IPN formulation does not maintain the desired toughness characteristics of the neat epoxies, it shows some promising results in terms of improved stiffness behavior and lays the groundwork for future investigations of epoxy-IPNs.

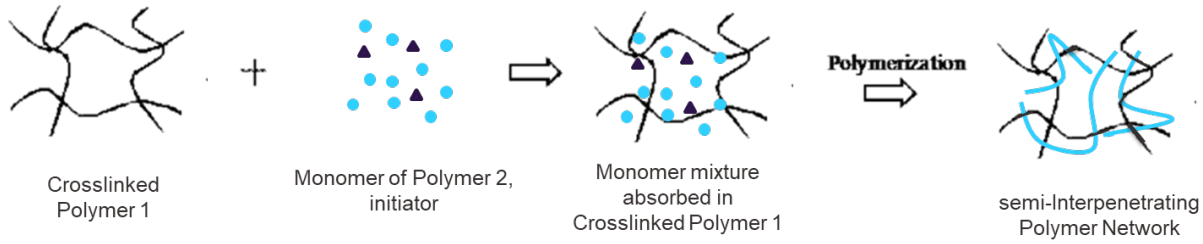

Figure 6.2: Schematic of sequential semi-IPN formation. Schematic adapted from Goswami, *et al.* [7].

6.2 Materials and Methods

6.2.1 Epoxy Materials

Epoxies consisting of diglycidyl ether of bisphenol-A (DGEBA), 4-4'-methylenebis(cyclohexylamine) (PACM), and poly(propylene glycol) bis(2-aminopropyl ether), a.k.a. Jeffamine, were prepared in stoichiometric 2:1 DGEBA:total amine formulations according to the procedure described in section 5.2.1. The same set of 10 epoxies described in table 5.1 were used: PACM, D400-100, D2000-100, D400-25, D400-50, D400-75, D2000-10, D2000-20, D2000-30, and D2000-40.

All formulations were performed for DMA in a rectangular geometry of approximately 3.0mm x 1.0mm x 30mm. For further Vicker's hardness and single edge notched bending (SENB) K_{IC} toughness testing, only D400-100, D2000-30, and D2000-40 were further investigated. Hardness samples were prepared by 3cm

diameter x 1cm cylindrical pucks, and SENB samples were prepared in the geometry described in section 5.2.2.3.

6.2.2 Interpenetrating Polymer Network (IPN) Formation

Methyl methacrylate (MMA) and the photointitiator, 2-Hydroxy-2-methylpropiophenone (Darocur 1173), were sourced from Sigma-Aldrich. A mixture of 1% by volume of Darocur 1173 in bulk MMA was prepared. The cured epoxy samples for DMA, hardness, and SENB toughness testing were weighed and then submerged in the MMA-Darocur 1173 mixture. The sample was left in the MMA bath for about 24hr to ensure the sample had swelled to completion. Afterward, the swollen epoxy was placed under a UV lamp under nitrogen for about 2hr. Then, the sample was weighed to determine mass change as a result of crosslinked poly(methylmethacrylate) (PMMA) in the epoxy stracture. This process is illustrated in figure 6.3

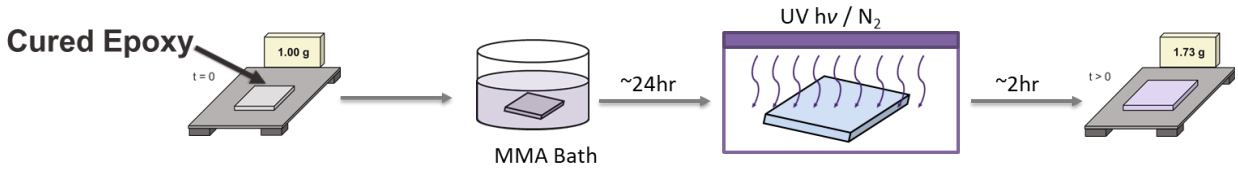

Figure 6.3: Schematic of the preparation of the epoxy-PMMA interpenetrating polymer network (IPN). The cured epoxy sample is weighed then placed in a bath of liquid methyl methacrylate (MMA) with photoiniator for 24hr. After swelling with MMA, the sample was irradiate with UV light under N_2 for 2hrs, and then weighed again to measure PMMA uptake.

6.2.3 Dynamic Mechanical Analysis

Epoxy samples of geometry of approximately 3.0mm x 1.0mm x 30mm for DMA. Temperature sweep tensile DMA experiments were performed on each epoxy DMA sample using an RSA3 dynamic mechanical analyzer (TA Instruments). Experiments were conducted at a frequency 1.0 Hz around a mean tensile strain of 0.1%. The experiments were conducted from -120 °C up to 225 °C. Samples were held at each temperature for 60 sec before the measurement was taken.

6.2.4 Toughness Testing

Toughness tests were conducted with a custom set-up of a TA Instruments Electroforce System with an ETx environmental chamber and cooled using liquid Nitrogen. K_{Ic} fracture toughness measurements of the

epoxy samples were conducted following ASTM D5045 − 14 guidelines for single edge notch bend (SENB) specimens [167]. See section 5.2.2.3 for more information.

6.2.5 Hardness Testing

Top surface of epoxy-IPN cylindrical hardness samples were polished after IPN formation so that the surface was smooth and scratch free and indents left from hardness experiments were easily visible. Indentation tests were conducted with a custom set-up of a TA Instruments Electroforce System with an ETx environmental chamber and cooled using liquid Nitrogen. An ASTM certified Vicker's indenter was sourced from Gilmore Diamond Tools, Inc, and attached to the Electroforce set-up. The indent was imaged using a Olympus OLS5000 3D Laser Confocal Microscope. The maximum indentation force was held constant for 15sec for each indent. See section 5.2.2.2 for more information.

6.3 Results

6.3.1 Swelling of Epoxy during IPN Formation

To determine the extent of the incorporation of PMMA in the epoxy-PMMA interpentrating polymer network (IPN), the weight change due to the swelling of the epoxy with PMMA was calculated from the initial mass, $M_0$and the mass of the sample after UV curing, M_f, per equation 6.1. The amount of swelling was compared to the crosslink density, υ_c, of the epoxy matrix determined by eq. 5.4, from the rubbery modulus of the DMA data presented in figure 5.3, since it is expected that epoxies with lower crosslink densities can absorb more MMA monomer [192]. The density is plotted vs. mol%PACM in fig. 6.4a, which unsurprisingly shows lower crosslink density for DGEBA/PACM/D2000 systems compared to DGEBA/PACM/D400, given the longer chain length of D2000.

$$\text{PMMA swelling } (\%) = \frac{M_f - M_0}{M_0} \times 100 \tag{6.1}$$

The plot of swelling vs. crosslink density for all the samples is shown in 6.4b. For DMA samples there is a clear difference is the swelling behavior of the PACM/D2000 and PACM/D400, even at comparable crosslink densities. The swelling of the DMA samples of PACM/D2000 increases from over 20% for D2000-10 to over 60% for D2000-100. For the PACM/D400 samples, all but the D400-100 sample have less than 10%, and PACM has negligible PMMA swelling. In addition to higher crosslink density, the PACM

and mixed PACM/D400 samples likely have lower free volume than the PACM/D2000 systems due to the shorter segments of jeffamine. With the relatively higher swelling of D400-100, it seems that the addition of PACM to the DGEBA/D400 significantly lowers the free volume and therefore swelling capability of the DGEBA/PACM/D400 epoxy networks.

Given the similar amount of swelling of IPN, the formulations of D2000-30 and D400-100 were chosen for further analysis for toughness and hardness testing, in addition to D2000-40 which was chosen due to the high low-temperature toughness of the neat resin. The swelling of the SENB toughness samples (open markers in fig. 6.4c) was noticeably less than in the much smaller DMA samples. The difference in swelling is smallest for the D2000-40 sample, and most pronounced for the D400-100 sample, which only swells half as much as the DMA sample. Thus, the free volume difference in these samples is likely more pronounced for the larger SENB samples, which may lead to inhomogeneous swelling. Evidence of inhomogeneous swelling is shown later this chapter in the fracture surfaces of the SENB samples in figure 6.8.

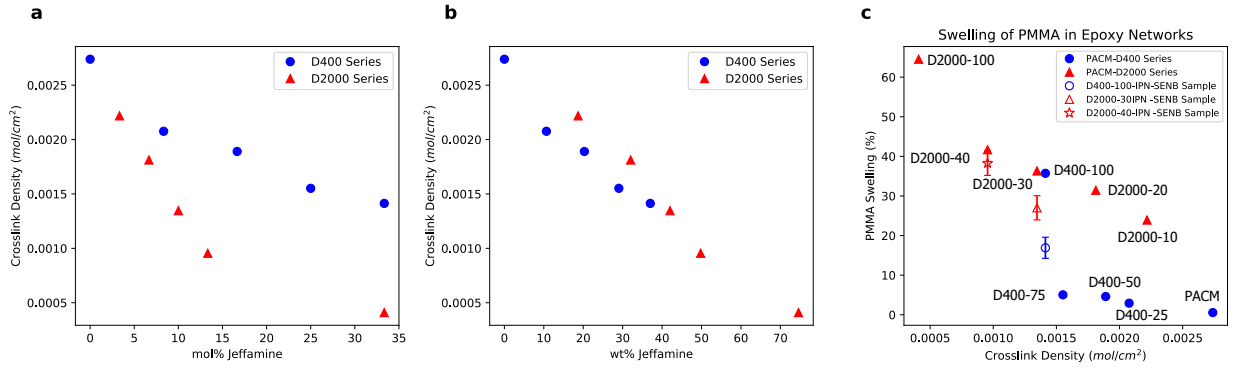

Figure 6.4: Plot of crosslink density vs. (**a**). mol%Jeffamine and (**b**). wt%Jeffamine for the DGEBA/PACM/Jeffamine epoxies as determined by eq. 5.4. (**c**) Plot of total PMMA swelling (eq. 6.1) vs. crosslink density of the DGEBA/PACM/Jeffamine epoxies. Epoxies with Jeffamine D400 are in blue while the epoxies with D2000 are read. Closed markers signify the swelling of the rectangular DMA samples, while the open marks are the swelling of the SENB toughness samples.

6.3.2 Dynamic Mechanical Analysis

All the epoxy-PMMA IPN samples were analyzed using dynamic mechanical analysis, except for the PACM sample, which had negligible swelling, and the D2000-100 sample, where the >60% swelling resulted in swelling induced fracture of the IPN. The DMA data of the PACM/D400-PMMA IPNs are plotted in figure 6.5 in red and compared to the neat epoxy resin in blue. The D400-25 data in fig. 6.5a, which had <3% swelling, showed only a slight broadened shoulder towards lower temperature of the α-glass transition peak,

but no change in peak location. The D400-50 sample in 6.5b, which had slightly more PMMA, shows and even broader shoulder and a slight increase in in peak ϕ temperature, and the D400-75 sample in 6.5c has a larger, increase in peak ϕ temperature and broader transition peak width. In these three mixed PACM/D400 systems, the uptake of PMMA is small (all <6%) but all had slight, but noticeable changes in dynamic behavior. The effect of the IPN was more pronounced on the D400-100-PMMA IPN, shown in fig. 6.5d, which swelled by $\sim 35\%$. The peak ϕ temperature increased by $\sim 15.3°C$ with a clear shoulder to the left of the peak. Additionally the β-transition peak was noticeably damped out compared to the neat epoxy in this sample.

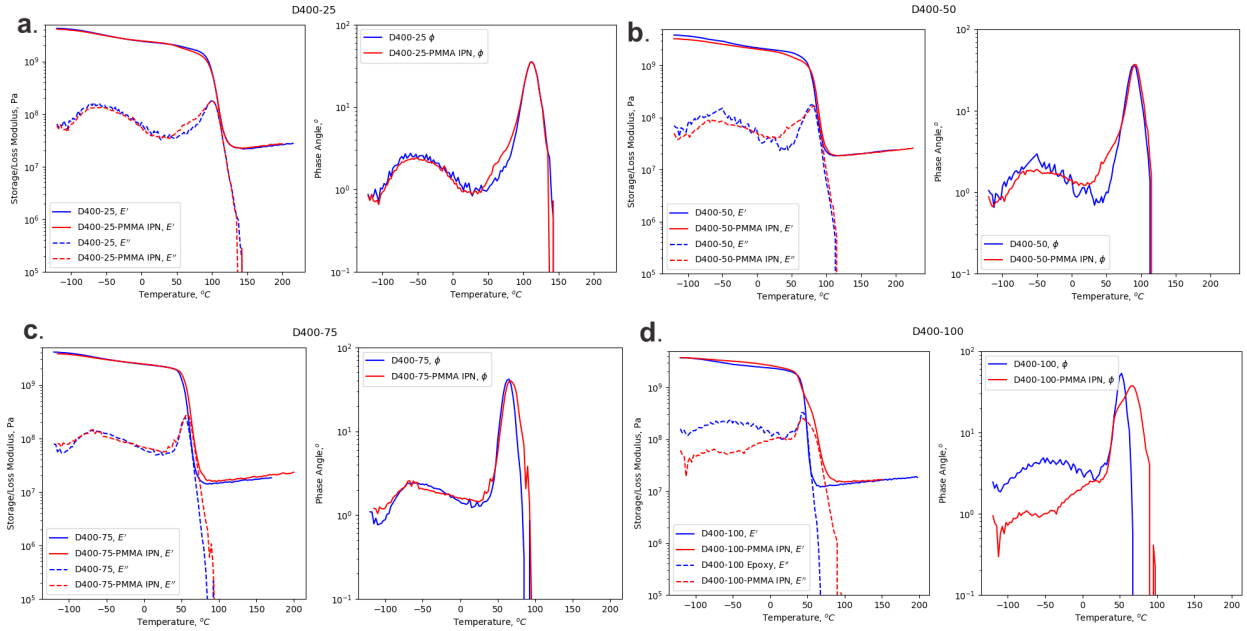

Figure 6.5: Plots of E', E'', and ϕ vs. temperature from tensile dynamic mechanical analysis for (**a**) D400-25, (**b**) D400-50, (**c**) D400-75, and (**d**) D400-100. The epoxy-PMMA IPN is plotted in red while the neat epoxy resin is in blue.

The DMA data of the neat DGEBA/PACM/D2000 epoxies was compared to their respective PMMA semi-IPNs in fig. 6.6. The D2000-10-PMMA IPN sample in fig. 6.6a, with about 24% PMMA swelling, showed a small shift in the α-transition regime to higher temperature, and a more dramatic reduction in the β-transition peak at -50°C. Changing the formulation to D2000-20-PMMA IPN in fig. 6.6b, where swelling is increased to 31%, a more significant change in dynamic mechanical behavior begins to emerge. The glass region of the E'extends to significantly higher temperatures. For the neat D2000-20, E'dropped below 10^9Pa at ~13.25°C, whereas the PMMA-IPN stays above 10^9Pa until ~51.5°C. Additionally, the E''

value remains above 10^8Pa until ~73°C. This change in viscoelastic moduli interestingly causes the peak in ϕ to decrease slightly, and the peak as a whole becomes slightly less broad. Similarly behavior is seen in the D2000-30 and D2000-40 - PMMA semi-IPNs in figs. 6.6c & d, respectively. The glassy E' plateaus are extended to higher temperatures, dropping below 10^9Pa at approx. 32.5°C for the D2000-30-PMMA semi-IPN and 25°C for the D2000-40-PMMA semi-IPN as opposed to -12°C and -20°C for the respective neat epoxies. Intestestingly, the E'' peak broadens, but the phase angle peak actually becomes more narrow and shifts to higher temperature as the D2000 content, and consequently PMMA content, increases. With more PMMA in the network the glass transition of the PMMA likely becomes more pronounced. Unlike the D2000-10 system, the β-transition at -50C was obscured by the broadened glass transition region of the higher D2000 systems, so it is unclear of the exact effects of the IPN on this transition for these systems. However, the narrowing of the glass transition peak suggests that this transition is also inhibited by the IPN.

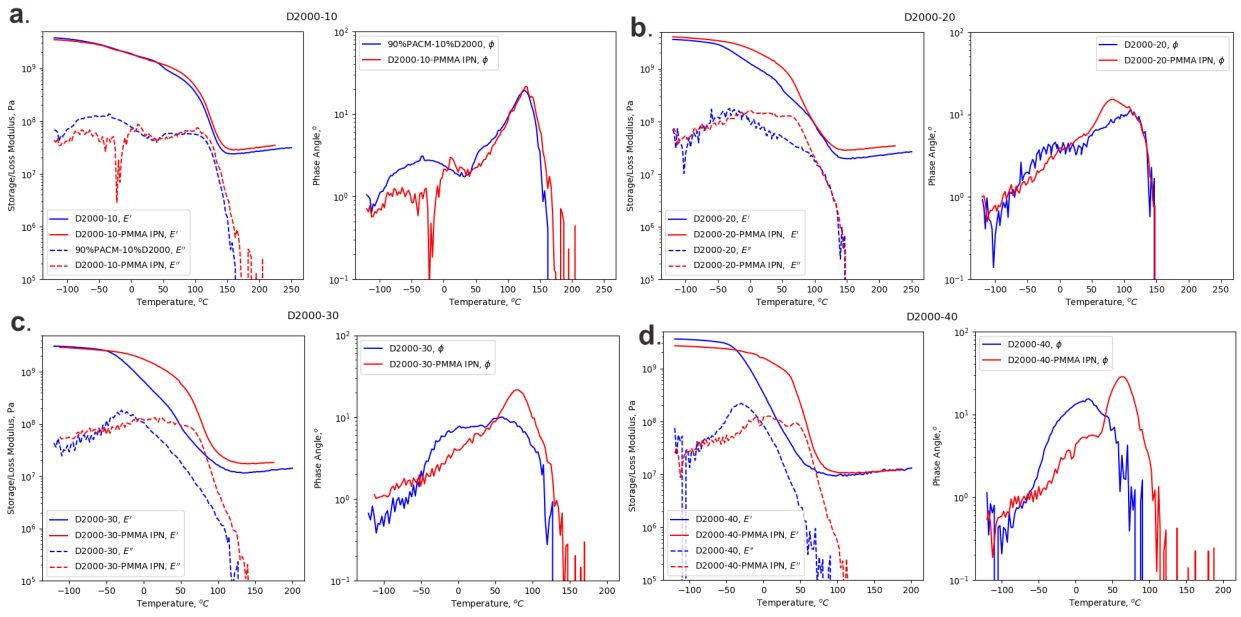

Figure 6.6: Plots of E', E'', and ϕ vs. temperature from tensile dynamic mechanical analysis for (**a**) D2000-10, (**b**) D2000-20, (**c**) D2000-30, and (**d**) D2000-40. The epoxy-PMMA IPN is plotted in red while the neat epoxy resin is in blue.

The DMA data of these epoxy-PMMA semi-IPNs show several interesting implications. **1**) Changes to dynamic mechanical behavior to mixed PACM/D400-PMMA semi-IPN are small due to small PMMA uptake, but show increasing and broadening ϕ peaks with increasing PMMA uptake. **2**) Increasing the PMMA content suppresses the β-transition in the epoxies, and **3**) the dynamically heterogeneous DGEBA/PACM/D2000-

PMMA semi-IPN show an extension of the glassy E' regime to higher temperatures, broadening of the $E''$to higher temps, but a narrowing of the ϕ peak region.

6.3.3 Toughness Testing

Single edge notched bend (SENB) K_{Ic} toughness tests were performed on the epoxy-PMMA semi-IPNs of 100mol%D400, 70mol%PACM30mol%D2000, and 60mol%PACM40mol%D2000 from -100°C to 40°C and plotted in fig. 6.7. Each of these plots compares the temperature dependent K_{Ic} value of the epoxy/PMMA IPN (red) to the neat epoxy resin (blue). As mentioned previously, D2000-30 and D400-100 were chosen for toughness testing since they had similar swelling of PMMA and crosslink density, so differences between the fracture behavior of the IPN of a dynamically heterogeneous system and homogeneous epoxy system could be compared. In addition, D2000-40 was also chosen due to the high low-temperature toughness of the neat resin.

However, it can be seen from the plot of the toughness data in fig. 6.7 that all of the epoxy–PMMA semi-IPN's showed lower toughness than their neat epoxy counter parts. For D400-100 in fig. 6.7a, the low temperature plateau drops from $\sim$ 1.5MPa$\sqrt{\text{m}}$ to $\sim 1.0MPa\sqrt{m}$, additionally, the K_{Ic} value the epoxy-PMMA IPN *decreases* as the temperature increases, a stark contrast to the neat epoxy where the K_{Ic} value increases as the T_g is approached. Similarly, the low temperature plateau of the D2000-30 and D2000-40 in figs 6.7b and c also drop to $\sim 1.0MPa\sqrt{m}$, but the the D2000-30-PMMA IPN K_{Ic} values are more or less constant with temperature, and the D2000-40-PMMA IPN shows a gradual decrease with temperature, but does not drop as low as the D400-100-PMMA IPN sample. Unfortunately, this is sharp drop from the low temperature toughness of the neat epoxies. However, the increased stiffness in the PACM/D2000 systems does allow the measurement of the $K_{Ic}$to be extended to much higher temperatures without deviating from linearity due to yielding, up to 40°C for the D2000-30-PMMA IPN and room temperature for D2000-40-PMMA IPN. Given reductions of the transition peak from the DMA of epoxy-PMMA IPNs with high PMMA content, and that polymer toughness has been tied to β and higher order relaxations [193], the drop in toughness may be due to a restriction of molecular mobility of the epoxy/PMMA IPN.

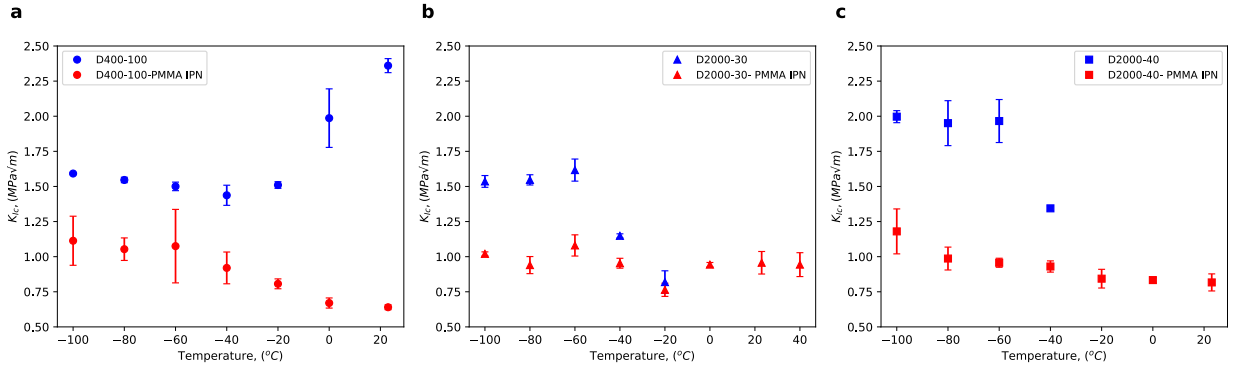

Figure 6.7: Plot of K_{Ic} vs. temperature as determined from SENB test per section 5.2.2.3 for networks of (a) D400-100, (b) D2000-30, and (c) D2000-40. Each plot compares the K_{Ic} values of the epoxy/PMMA semi-IPN in red to that of the neat epoxy resin (blue).

Examination of the fracture surfaces shown in fig. 6.8 show distinct fracture surface morphology differences compared to the neat epoxy resins discussed in section 5.3.3.3. One of the most apparent features that is present in the D400-100-PMMA IPN SENB samples and to a lesser extent in the D2000-30-PMMA IPN SENB samples is this inner "ring" in the center of the sample. This is likely due to incomplete or in-homogeneous swelling or curing of the PMMA in the IPN. This is evidenced by the stark difference in %swelling of the SENB samples compared to the DMA shown in fig. 6.4, and the size of this ring is correlated to the swelling dependency between the two types of samples. Nevertheless, the fracture surface morphology within the ring is not noticeably different than outside of the ring. Besides the ring, the fracture surfaces of D400-100-PMMA IPN SENB at room temperature and -100°Cwere strikingly similar and very smooth. The room temperature sample lacked the rough surface features characteristic of bulk yield behavior seen in the neat epoxy of D400-100 at room temperature.

For the PACM/D2000-PMMA IPN samples, the rough plastic zone arch seen in the neat epoxy resins at low temperatures has completely vanished. Instead, the -100°Csamples have multiple arrest lines along the fracture surface, with thin river markings extended from each arrest lines (these are less clear in the -100°C image of the D2000-40-PMMA IPN sample, but are still there). These features suggest some type of "stick-slip" fracture behavior, but there are no thick plastic deformation bands, typical of slow growth regions on the arrest lines seen in the neat PACM/D400 epoxies in section 5.3.3.3. The most distinct feature of these epoxy-PMMA IPNs are seen at the high end of the temperature range, where long streaks are seen along the fracture surface. In the neat-epoxies, when the epoxy began to yield too much for the SENB tests,

the fracture surface became very rough resulting in three-dimensional features as the result of crazing. In these epoxy-PMMA IPNs, the IPN may prevent 3-dimensional craze behavior between separated surfaces the fracture, resulting in these streaks.

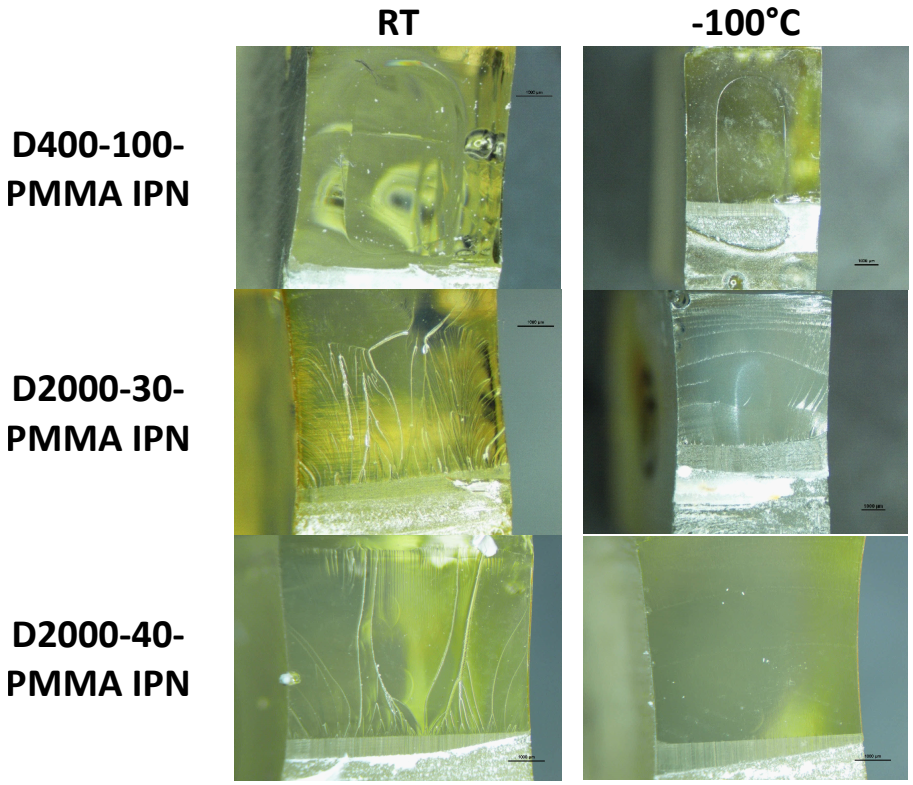

Figure 6.8: Optical Images of the SENB fracture surfaces of the epoxy/PMMA semi-IPNs at (left) room temperature and (right) -100°C for (top) D400-100, (middle) D2000-30, and (bottom) D2000-40.

Nevertheless, the SENB toughness tests show that the current epoxy/PMMA-IPN network lead to a reduced toughness when compared to the neat-resins for the formulations tested, likely as a result of restriction in molecular motions. Nevertheless, the range of temperatures for which valid K_{Ic} measurements was extended to higher temperatures for the PACM/D2000 systems.

6.3.4 Vicker's Hardness Indentation Testing

Vicker's indentation tests were also performed on the selected epoxy-PMMA IPNs in the same manner as the neat epoxies in section 5.3.2. The hardness data was unsurprising, based on the results of the the DMA storage moduli of the epoxy/PMMA IPN. No significant difference was seen between the measured hardness for the neat resin and PMMA-IPN for the D400-100, plotted in fig. 6.9a. The D2000-30 and D2000-40 -

PMMA semi-IPNs in fig. 6.9b showed a dramatic increase in hardness compared to the neat resins, and the measured hardness of all three of these IPNs were more or less the same at each temperature.

Additionally the residual indentation depth of the indents was measured to determine the extent of recovery of the indent and plotted versus the ratio of hardness to modulus, H/E, as described in section 5.3.2. The recovery of the indents in D400-100-PMMA IPN followed the same relationship of the homogeneous neat PACM/D400 epoxies as seen in fig. 6.9c. On the other hand, the recovery of the indents in D2000-30 and D2000-40 - PMMA semi-IPNs decreased at higher temperatures (lower H/E) compared to the neat resins, seen in fig. 6.9d. The two PACM/D2000-PMMA IPNs both followed a similar trend to the neat D2000-20 epoxy, suggesting reduced shape memory behavior, but still more than the PACM/D400 systems. The reduced recovery once again suggests that the molecular motions of the epoxy have been restricted by the IPN.

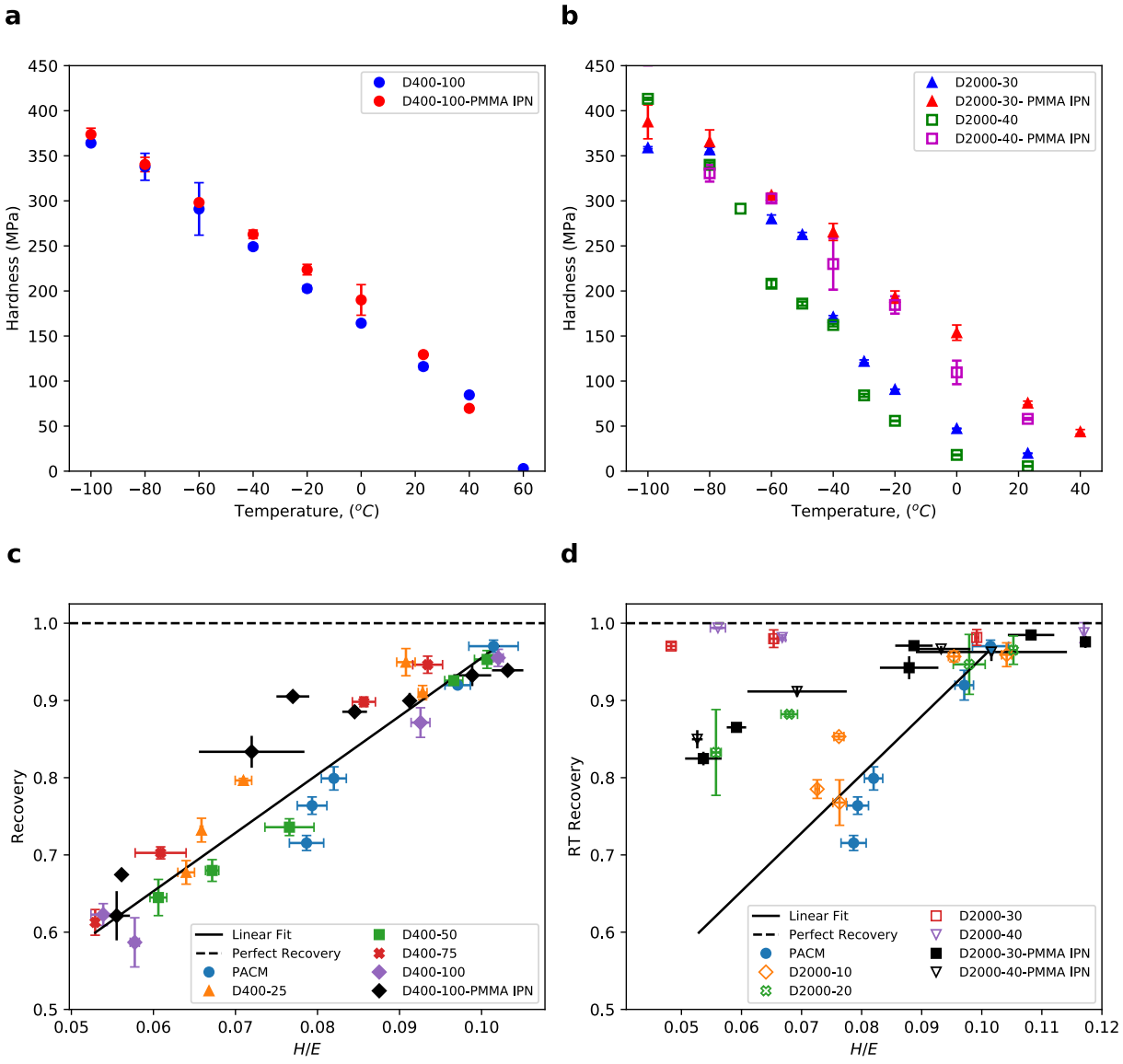

Figure 6.9: Indentation Hardness data vs. temperature for (**a**) D400-100, and (**b**) D2000-30 & D2000-40, comparing the hardness between epoxy/PMMA-IPNs to the neat epoxy data. (**c**,**d**) Plots of indent recovery vs. H/E for (**c**) DGEBA/PACM/D400 epoxies and (**d**) DGEBA/PACM/D2000 epoxies from chapter 5 with added epoxy/IPN data added, shown by black markers. Black line in **c** shows linear relationship with slope of 7.55.

6.4 Conclusions

This chapter describes the temperature dependent fracture and mechanical property characterization of semi-interpentrating polymer networks of the model DGEBA/PACM/Jeffamine epoxy systems investigated in the previous chapter with poly(methyl methacrylate) using the sequential method. Mixed PACM/D400 epoxies showed minimal swelling of PMMA due to low free volume, but D400-100, D2000-100, and all mixed PACM/D2000 epoxy systems could be swollen with significant amounts (20-65%) of PMMA that increased with decreasing crosslink density. DMA data showed that the uptake of PMMA into the epoxy network generally resulting in increased peak ϕ temperature and a suppression of the β-transition peak. But, the mixed PACM/D2000 systems showed an clear extension of the glassy plateau by approximately +40°C. Further K_{Ic} toughness testing of the 100mol%D400, D2000-30 and D2000-40 - PMMA semi-IPNs showed a drop in K_{Ic} at all temperatures, but the temperature range of valid K_{Ic} measurements was extended to higher temperatures for the PACM/D2000 systems. Hardness values from indentation experiments were similar for all three IPN formulations, resulting in increased hardness compared to the neat resins for the PACM/D2000 systems, but no change for the D400-100 system. Additionally, the D400-100-PMMA IPN maintained the same recovery-H/E relationship as the neat PACM/D400 formulations, but the IPNs of the PACM/D2000 systems showed reduced shape memory effect.

The goal of this investigation was to try to utilize the IPN structure to improve the ambient stiffness of the model DGEBA/PACM/Jeffamine epoxy systems, particularly the formulations with nano-scale heterogeneity, while maintaining their high low temperature toughness. Adding the data from IPNs characterized in this investigation to the design chart from fig. 6.1 to fig. 6.10, shows that goal has only partially been reached. Even though the room temperature moduli of the dynamically heterogeneous D2000-30 and D2000-40 samples greatly increased in the PMMA semi-IPN, the increase in stiffness was coupled with the aforementioned drop in toughness. From the DMA and recovery data, it is likely that this drop in toughness is due to decreased molecular mobility, and other IPN formulations could potential be investigated to improve the mobility. For instance, the scope of this work was limited to the Using the sequential method of creating semi-IPNs of epoxy-PMMA due to its relative ease of fabrication, but resulting in swelling the epoxy to its maximum. However, other processing conditions, such as using the simultaneous method of fabrication, should be investigated in the future for better control over PMMA content. Additionally, a better understanding of the extent of polymerization of the PMMA in the epoxy network could be helpful in optimizing the properties as well. This will be discussed more in chapter 8.

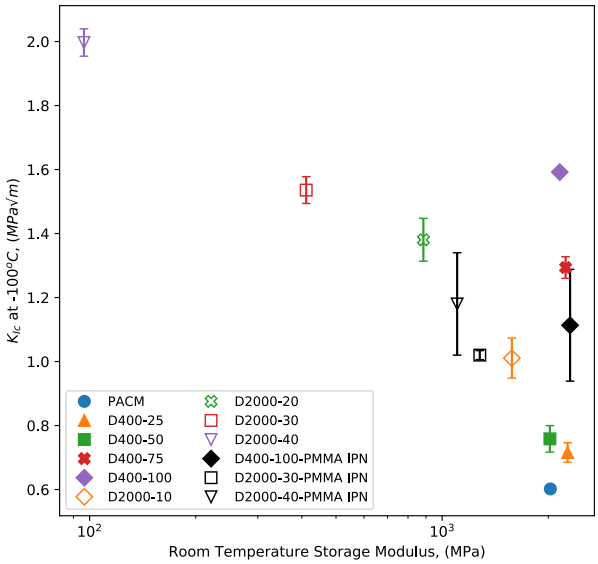

Figure 6.10: Plot of the K_{Ic} fracture toughness at -100°C vs. the room temperature time DMA E' value at 1Hz from figure 6.1 with Epoxy-PMMA IPN data points added (in black).

Chapter 7

Exploring the Effect of Humidity on Thermoplastic Starch Films using the Quartz Crystal Microbalance

This chapter investigates the utility of the quartz crystal microbalance (QCM) as a nondestructive, efficient characterization tool for thin thermoplastic starch (TPS) films. Thin TPS films (1-2μm) were prepared using 30 wt-% (w/w solids) plasticizers over starch using either glycerol or an ionic liquid, 1-ethyl-3-methylimidiazolium acetate ([emim$^+$][Ac$^-$]) as plasticizers, and the differences in the mechanical properties and environmental effects were explored. The QCM data showed evidence of retrogradation in starch-glycerol films but not in starch-[emim$^+$][Ac$^-$] by monitoring the film thickness over the course of a week. The modulus of starch-glycerol films was higher than starch-[emim$^+$][Ac$^-$], consistent with literature data and bulk AFM measurements, likely due to superior plasticization by the ionic liquid. Additionally, increases in the relative humidity (RH) of the environment resulted in an increased areal mass, an increased viscoelastic phase angle, and a decreased shear modulus. Property changes were moderate at low RH values, but increased substantially for RH values above 45%. Additionally, the starch-[emim$^+$][Ac$^-$] films were shown to have a relative stable properties at low humidity that may be due to some antiplasticization effects at low water content, despite absorbing more water than starch-glycerol films at higher humidity.

This chapter reproduces work from "Exploring the Effect of Humidity on Thermoplastic Starch Films using the Quartz Crystal Microbalance" submitted to *Carbohydrate Polymers* in 2020 with co-authors Daniel

Domene-López, Qifeng Wang, Mercedes G. Montalbán, Ignacio Martin-Gullon, and Kenneth R. Shull.

7.1 Introduction

Biodegradable and edible films made from renewable, abundant sources are increasingly of interest for sustainable applications such as coatings for food products and pharmaceuticals to increase shelf life [194–196], and to replace petrochemical based plastics for single-use packaging applications [197, 198]. Starch, in particular, has been extensively studied due to its abundance in nature, widespread use in industry, low cost, low oxygen permeability, and its ability to be readily cast into thermoplastic starch (TPS), which is odorless, colorless, and transparent [199–201]. Starch is a hydrophilic and semicrystalline polymer composed mainly of two polysaccharides, linear amylose and hyperbranched amylopectin, which are held in place by strong hydrogen bonds that result in microcrystalline regions of lattice like double-helical structures [8, 202–204]. In its native form, starch exists as granules which depends strongly on the botanical origin. with two types of allomorphs, Type A for grains like corn, wheat and other cereals; and Type B for tubers, like potato. These two configurations differ on the arrangement of crystallites in the lamellae, allowing more water amount and diffusion in hexagonal Type B [205].

Due to the hydrophilic nature and the intercrystallite space, water itself is a strong plasticizer [206]. It is relatively easy to suppress crystal formation altogether, leading to the formation of an amorphous, glassy and transparent material commonly referred to as (TPS). While non-equilibrium processes are extraordinarily important in the processing of starch, it is nevertheless useful to consider the equilibrium phase diagram for the starch/water system. This phase diagram has the general form shown in Figure 7.1, with detailed phase boundaries taken from the work of van der Sman and Meinders [8], and of Carlstedt, *et al.* [9]. At equilibrium, homogeneous, molecular solutions are only obtained at high temperatures and intermediate water contents (the AS, or amorphous starch region of the phase diagram). Starch films are generally prepared by heating starch/water mixtures into this region. Carlstedt *et al.* showed rather convincingly that the high temperature region of the phase diagram has the character of a eutectic system, where 3 phases are in equilibrium with one another at the eutectic temperature, T_e, and overall solution composition equal to the eutectic composition, w_e [9]. (Note that solution concentrations in our notation are expressed in terms of w, the weight percentage of water). When a homogeneous AS solution with a water content less than w_e is cooled below the solubility limit of crystalline starch (XS), crystalline starch forms with a lower water content than the amorphous starch solution with which it is in equilibrium. In the work of van der Sman and Meinders the upper boundary of the two-phase XS+AS region is referred to as the 'melting' curve and

the lower boundary of this two phase region is referred to as the 'gelatinization' curve.

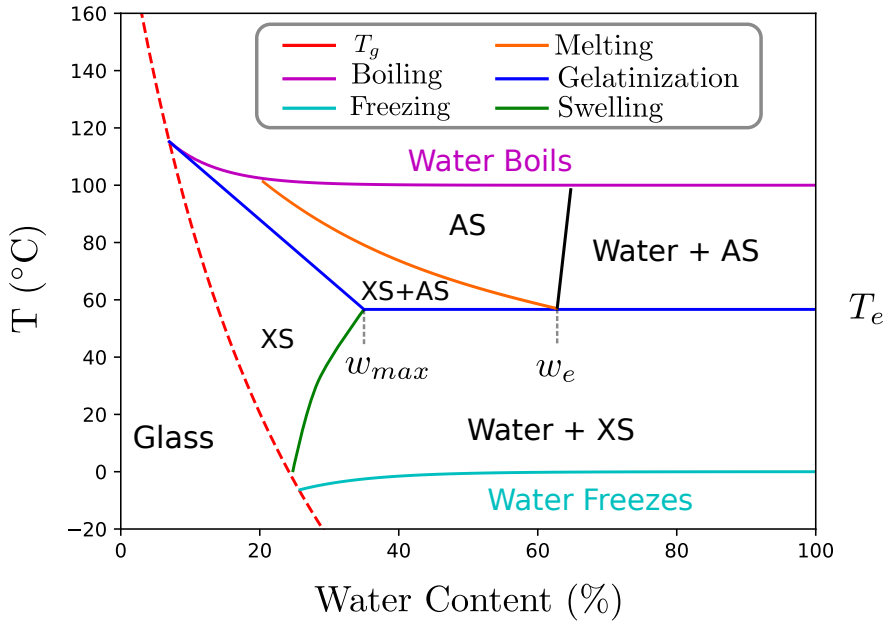

Figure 7.1: Equilibrium starch-water phase diagram. Phases are defined as XS for crystalline starch, and AS for amorphous starch. Adapted from van der Sman and Meinders [8], and Carlstedt, *et al.* [9].

The maximum equilibrium water concentration in the crystalline starch phase, w_{max}, is expected to occur at the eutectic temperature. This point on the phase diagram is the termination of a 'swelling' line that defines the amount of water in a crystalline starch sample in equilibrium with pure water. The ability for the system to reach this crystalline state is determined by the polymer mobility, which is in turn determined by the amount of water in the starch polymer, which acts as a plasticizer [8, 9]. The material is locked into a glassy state when the temperature is less than the glass transition temperature, T_g. The glass transition temperature is quite high for dry starch, but is reduced to room temperature for a water content of ≈20 wt.%. In the portion of the one-phase, crystalline starch (XS) region of the phase diagram that is above the T_g line, the material will slowly crystallize over time, a process referred to in the starch literature as retrogradation. Crystalline starch is quite brittle, and retrogradation generally has a substantial negative impact on the ductility of TPS [207]. As a consequence, the amount of water in a TPS film greatly affects its properties [206]. Unfortunately, glassy starch is also quite brittle, and additional plasticizers, such as polyols like glycerol are often used [208, 209]. These plasticizers increases the compliance, processability, and longevity of the resulting TPS material [209], but can migrate to the surface and evaporate over time, resulting in material embrittlement and failure [207, 210–212]. For this reason non-volatile ionic liquids,

such as 1-ethyl-3-methylimidazolium acetate ([emim$^+$][Ac$^-$]) have been utilized as plasticizers for TPS films [213–216]. Initial investigations into ionic liquid-starch films have shown better stability and an enhanced resistance to retrogradation attributed to inhibition of the migration of the plasticizer to film surface due to the the higher molecular weight, lower vapor pressure, and stronger electrostatic bonds of ionic liquids compared to polyols. [210, 214, 217, 218]. Overall, [emim$^+$][Ac$^-$] is an excellent choice as a plasticizer because of its high thermal stability, low density, low vapor pressure, and low toxicity [214, 215, 219], and because of the depth of its characterization in the literature [220–223]. The structure of [emim$^+$][Ac$^-$] is compared to glycerol in figure 7.2.

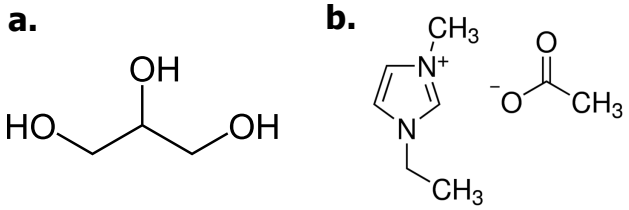

Figure 7.2: Chemical Structure of (**a**) glycerol and (**b**) 1-Ethyl-3-methylimidazolium acetate [emim$^+$][Ac$^-$], the two starch plasticizers used in this investigation

Even when additional plasticizers are added to TPS, the plasticizing effects due to absorbed atmospheric water play an important role. Although many different variables can affect the properties of TPS films, such as starch source [200, 224–226], plasticizer type [204, 213, 227–231], plasticizer content [227, 229, 232, 233], the presence of other polymers due to blending [234–236], and filler type/concentration [213], water adsorption affects the properties in all cases. Generally, the mechanical strength of TPS films decreases with increased plasticizer content and drops sharply with increasing water absorption, as a result of the aforementioned T_g reduction [208]. However, in some cases, small amounts of water or plasticizer can actually facilitate recrystallization, resulting in an increased modulus and decreased ductility [237–239]. Because of these complicating effects, the reported results of the humidity dependent TPS film moduli in the literature are not always consistent, showing drops in modulus by over an order of magnitude [204, 227, 240], smaller drops in modulus (by a factor of 2-3) [239], no substantial change in modulus [234], no clear trend (randomly increasing and decreasing) [228, 241], or even increasing with increasing humidity [230]. Given the potential of TPS to be used in very different relative humidity environments, understanding the humidity dependence of TPS mechanical properties and aging behavior is of critical importance.

The mechanical properties of TPS film are typically evaluated using tensile testing. Although tensile test methods are firmly established and standardized for material characterization, they are labor intensive, time

consuming, and destructive techniques. The tests can be particularly cumbersome when long equilibration times are needed in order to investigate humidity affects associated with the presence of adsorbed water [204]. Given the number of variables that can affect the properties of TPS films (starch source, plasticizer, plasticizer content, etc....), a non-destructive mechanical characterization technique that can be used to efficiently measure water content while also providing mechanical property information at different humidity levels is of considerable interest. In this paper we describe the use of the quartz crystal microbalance (QCM) for this purpose.

The quartz crystal microbalance produces a shear acoustic wave by oscillating a piezoelectric quartz crystal at its resonant frequency in the megahertz regime [242]. The shear wave propagates through a thin film deposited on the surface of the crystal, and the changes in acoustic impedance compared to a bare crystal can be used to calculate the film thickness and the linear viscoelastic properties of the film [243–246]. The QCM offers several advantages over traditional testing methods used for measuring the humidity effects on TPS films:

- The QCM can measure changes in film thickness and the viscoelastic mechanical properties simultaneously, and so the effects of water absorption on film properties can be linked unambiguously.
- The QCM is non-destructive, so the mechanical properties and thickness of the same film can be tested and monitored continuously over time and as a function of changing environmental condition, such as relative humidity.
- The QCM uses films with thicknesses in the micron range, which is thick enough so that bulk properties are measured, but thin enough so that sample equilibration with the local environment is rapid, typically over a time period of minutes to a couple hours at the most.

The use of the QCM to measure adsorption in thin films is widely understood [247, 248]. While moisture isotherms of TPS films have previously been measured with QCM-based techniques [249], QCM has not, to the best of our knowledge, been utilized extensively or coupled with viscoelastic property measurements for TPS. The calculation of viscoelastic properties from the QCM is more complex than than the mass measurements, but quantitative viscoelastic QCM methods have been developed in recent years [24, 245, 250, 251]. Here we demonstrate the utility of the QCM in evaluating the humidity response of the water content and mechanical properties of thin TPS films. Two TPS systems are investigated, one plasticized with glycerol since it is widely used, understood, and known to present quick retrogradation, and the other plasticized

with the promising higher molecular weight ionic liquid, [emim$^+$][Ac$^-$]. The effect of the plasticizer on the mechanical properties of the TPS films in different relative humidity environments is explored.

7.2 Materials & Methods

7.2.1 Preparation of Thermoplastic Starch

TPS films were prepared by the casting technique following the procedure described in Domene-López, *et al.* [200, 226]. Briefly, the film-forming solution was composed of potato starch (5 wt.%), plasticizer (glycerol or [emim$^+$][Ac$^-$]) (1.5 wt. %) and distilled water (93.5 wt. %). The solution was stirred at room temperature for 45 min and then heated up to 96 °C for 40 min, to guarantee complete starch gelatinization. The mixture was then cooled down, degassed under vacuum for 7 min and finally poured onto Petri dishes (0.34 g/cm^2). The plates were dried in an oven with circulating air at 50 °C for 48 h. The dried films were peeled off and used for the experiments. Potato starch (20.5% amylose) was provided by Across Organics (Geel, Belgium), glycerol was supplied by Fisher Chemical (Geel, Belgium) and [emim$^+$][Ac$^-$] was supplied by IoLitec (Heilbronn, Germany).

7.2.2 Thermoplastic Starch-QCM film deposition

The prepared TPS films were re-dissolved in water by placing 0.5g of the film in a beaker with DI water with $\sim$ 39.5mL of water (2.5wt% TPS). The mixture was heated to boiling and refluxed for about 45min until the starch seemed uniformly dissolved. The mixture was then diluted by a factor of 2 with DI water. The resulting 1.25wt% TPS mixture was then passed through a 0.4μm filter to removed large starch granules from the mixture and improve film uniformity. A calibrated QCM crystal was then placed on a hot plate set to 90-100 °C. After letting the crystal sit on the hot plate for 1-2 minutes, $\sim$ 20μL of the filtered 1.25wt% TPS mixture was pipetted onto the gold electrode of the QCM crystal and spread out with the pipette tip. The water was then allowed to evaporate, leaving behind a TPS film on the electrode surface. It's important for the film to be uniform and smooth over the center of the electrode for good quantitative QCM fit data. This includes controlling the rate of water evaporation through the heat of the hot plate. If the water is removed too fast, the film can become very rough and inhomogeneous, whereas if the water evaporates too slowly, the starch can concentrate at the edge of the film, resulting in a "coffee-ring" pattern, that is also rough and inhomogeneous [252].

7.2.3 Quartz Crystal Microbalance Experiments

7.2.3.1 Quartz Crystal Rheometry Set-up & Theory

QCM measurements were taken with 5 MHz AT-cut quartz disks with gold electrodes deposited on both sides, obtained from RenLux Crystal (Guangdong, China). To record measurements, the crystal was placed in a holder from Advanced Wave Sensors (Valencia, Spain), which was attached to a N2PK Vector Network Analyzer (VNA), that collected the impedance spectra of the crystals. Before film deposition on the QCM crystal, the bare crystal reference frequencies (f_n) and half width at half maximum of the resonance peaks (Γ_n) for the first three odd harmonics ($n = 1, 3, 5$) were measured at room temperature every minute for about 1 hour.

After the bare crystal was measured, the TPS film was deposited as described in section 7.2.2. After the QCM holder, crystal, and sample were placed in a sealed container over Drierite® desiccant (Alfa-Aesar), and the impedance spectra were collected. From the resulting impedance spectra, the change in resonance frequency Δf_n and change in the change in half width at half maximum of the resonance peaks ($\Delta\Gamma_n$) of the crystal + TPS film compared to the bare crystal are collected. These values both make up the complex frequency shift, Δf_n^*, given by eq. 7.1. From the Δf_n^* of two resonance harmonics, a system of three equations of the complex resonant frequency related to the viscoelastic properties, described in DeNolf, *et al.,* using in-house Python programs [245]. From this, the areal mass, ρd (where ρ is the density and d is the thickness), phase angle, ϕ_n, and product of the density and complex modulus magnitude, $\rho|G_n^*|$, can be calculated.

$$\Delta f_n^* = \Delta f_n + i\Delta\Gamma_n \tag{7.1}$$

As described in previous QCM literature [250, 253], the quality of the viscoelastic calculations depends on 1) the film thickness, and 2) film uniformity. In regards to thickness, if the film is too thin, the film is in the Sauerbrey limit, shifts in peak width, $\Delta\Gamma_n$, are quite small, Δf scales linearly with n, and sufficient information is not obtained for obtaining the viscoelastic properties [246]. The frequency shift is determined by the mass per are of the fillm and is given by eq. 7.2, where Δf_{sn} is known as the Sauerbrey shift, and $Z_q$is the electrical impedance of the bare quartz crystal.

$$\Delta f_{sn} = \frac{2nf_1^2}{Z_q}\rho d \tag{7.2}$$

On the other hand, if the film is too thick, and the film is very stiff, the conductance signal will become "overdamped", preventing collection of a reliable resonance signal, particularly at higher harmonics. As a result, only intermediate thicknesses can accurately measure both thickness and viscoelastic properties simultaneously. In this ideal region, the complex frequency shift deviates from the Sauerbrey prediction according to eq. 7.3. The response is determined by the viscoelastic phase angle, ϕ_n, and d/λ_n, the film thickness divided by the wavelength of the shear wave within the film [24, 245]. The shear wavelength within the film, λ_n, is related to the material complex shear modulus by eq. 7.4. To obtain the three properties of interest, ρd, ϕ_n, and $\rho|G_n^*|$, a set of three equations satisfying eq. 7.3 must be solved using the collected Δf_n and $\Delta\Gamma_n$ from at least two different harmonics. For example, according to the method described by, DeNolf, *et al.,* setting Δf_3 from the third harmonic and Δf_5 from the fifth harmonic equal to the real part of eq. 7.3, and $\Delta\Gamma_5$ from the fifth harmonic to the imaginary part of eq. 7.3, will allow, ρd, ϕ_n, and $\rho|G_n^*|$ to be determined. This solution is referred to as the 3:5,5 solution, but other solutions can also be solved, for instance, using $\Delta\Gamma_3$ for the third equation instead of $\Delta\Gamma_5$ would result in the 3:5,3 solution. Given edge effects that often complicate accurate measurement of f_1, and the greater possibility of becoming over damped for the higher order harmonics ($n = 7, 9, ...$), the 3:5,3 and 3:5,5 solutions are typically used [250].

$$\frac{\Delta f_n^*}{\Delta f_{sn}} = \frac{-\tan\left\{(2\pi d/\lambda_n)\left(1 - i\tan\left(\phi_n/2\right)\right)\right\}}{(2\pi d/\lambda_n)\left(1 - i\tan\left(\phi_n/2\right)\right)} \tag{7.3}$$

$$\lambda_n = \frac{1}{nf_1}\left(\frac{|G_n^*|}{\rho}\right)^{1/2}\frac{1}{\cos(\phi_n/2)} \tag{7.4}$$

Additionally, given the desire to measure water absorption in response to humidity, thickness will increase over the course of the experiment, causing the potential of entering the overdamped region at higher humidities. Given this, it is important that the sample is thick enough to avoid being in the Sauerbrey regime, but still given enough room to expand and still be in the viscoelastic regime. According to Sadman, et al., the optimum regime is when the measured value of $d/\lambda_n$for the harmonic whose $\Delta\Gamma_n$is used in the viscoelastic calculations (i.e. $d/\lambda_3$for 3:5,3 and $d/\lambda_5$for 3:5,5) is between 0.05 and 0.2 [253]. As such, a film with the most room to grow would be when the $d/\lambda_5 \sim 0.05$ using the 3:5,5 solution at 0% relative humidity, which will be shown to be $\rho d \sim 1.5 - 2.0\mu m \cdot g/cm^3$.

The second possible issue for good viscoelastic data is film roughness and uniformity. The validity of equation 7.3 assumes the film is homogeneous through the thickness of the film and laterally across the electrode surface, which could be a problem in a TPS film if large recrystallized granules exist in the film

[250, 254]. Large granules, inhomogeneities, and surface roughness can create interference in the propagating shear wave, which could lead to inflated measurements of $\Delta\Gamma_n$. Thus, careful attention needs to be paid to film deposition on the QCM as described in section 7.2.2. To determine if a newly cast film presented reasonable viscoelastic measurements from the processed QCM data, the resulting calculated measurements of ρd, ϕ_n, and $\rho|G_n^*|$ were used to predict the $\Delta\Gamma_n$ not used in the determination of the aforementioned properties ($\Delta\Gamma_3$ for the 3:5,5 solution). If the predicted $\Delta\Gamma_n$ deviates significantly from the measured the $\Delta\Gamma_n$ ($> 30\%$ difference), then the resulting viscoelastic measurements were not considered to be reliable.

Overall, before further QCM analysis of the TPS films in the subsequent study, two criteria of the films were met from the initial evaluation of the film using the 3:5,5 solution: 1) the initial values for d/λ_5 were approximately 0.05 to allow room for the film to grow over the course of the experiment, and 2) the values of $\Delta\Gamma_3$calculated using the 3:5,5 solution should not deviate from the measured values of $\Delta\Gamma_3$ by more than 30%. If a film did not meet these initial criteria, it was remade.

7.2.3.2 Saturated Salt Fixed Humidity Points

Saturated aqueous salt solutions were used as humidity fixed points in this investigation. Using a solubility reference guide [255], specified quantities of the salt were mixed with de-ionized water and stirred vigorously. Excess salt was added, so that some salt remained undissolved at the bottom of solution ensure saturation. A saturated salt solution will have a fixed vapor pressure, which will fix the humidity of a closed container holding the aqueous solution [10]. Table 7.1 shows the saturated salt solutions and the corresponding humidity at room temperature used in this investigation. The listed salts were sourced from Sigma-Aldrich.

Saturated Salt Solution	**Humidity (%)**
LiCl	11.3
$K[C_2H_3O_2]$	22.5
$MgCl_2$	32.8
K_2CO_3	43.2
$Mg(NO_3)_2$	52.9
NaBr	57.6
$NaNO_2$	65
NaCl	75.3
KBr	84.3

Table 7.1: Equilibrium Relative Humidity of Selected Saturated Salt Solutions at Room Temperature [10].

7.2.3.3 Controlled Humidity QCM Set-Up

To control the humidity affecting the TPS film on the QCM crystal, the QCM crystal holder was suspended over the saturated aqueous salt solution in a sealed beaker, as shown by the schematic in figure 7.3. As described earlier, the 0% humidity point was found by equilibrating above Drierite® desiccant for about a week before the humidity experiments. Then the aqueous solutions were added, starting with the lowest humidity first. Harmonics were analyzed every minute until measurements for thickness and mechanical properties stabilized, which took about 1-2hrs before moving on to the next one. Humidity experiments were done over the course of two days. In between the two sets of humidity experiments the film, was equilibrated back to 0% RH over desiccant overnight.

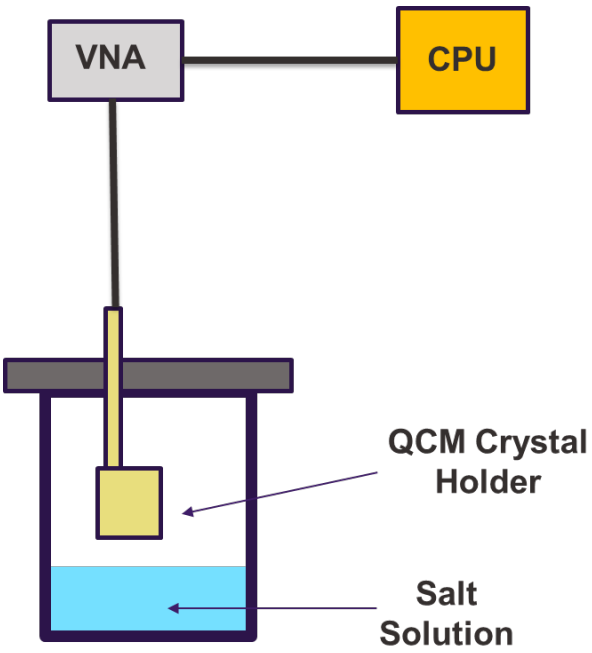

Figure 7.3: Schematic of QCM humidity experiments of the thermoplastic starch films. The QCM crystal holder with the sample is suspended above a saturated salt solution in a sealed container. Outside the container, the QCM holder is connected to the VNA (Vector network analyzer) and then the computer.

7.2.4 Atomic Force Microscopy (AFM)

AFM Force curve spectroscopy experiments were conducted on a Bruker Dimension ICON using the FAST-Force Volume mode. Experiments were conducted with a Bruker RTESPA-300 AFM probe, a silicon nitride AFM probe with a nominal spring constant of 40 N/m for the experiments. The tip radius was measured to be approximately 47.7nm using from the analysis of force-displacement curves of a polystyrene standard

sample from Bruker (PSFILM-12M) with a modulus of 2.7GPa using a JKR model [52]. Deflection sensitivity of the cantilever was calibrated with a stiff sapphire sample, and the true spring constant was calibrated using a thermal tuning method according to the Bruker Dimension ICON user manual[39]. Force curves were collected using a linear ramp rate of 30 Hz. AFM indentation scans were done on the TPS films on a 5μm x 5μm area with 128x128 force curves (16384 total curves), each was analyzed using JKR analysis of the loading curves, as described in Collinson, *et al.* [14]. AFM force curves with a poor fit of the JKR equation, determined by R^2 values less than 0.9, were removed from the subsequent analysis.

7.3 Results

7.3.1 Stability Experiments

7.3.1.1 QCM Rheometry Data for Thermoplastic Starch Films at 0% Relative Humidity over 1 Week

The starch films on the QCM crystal sat in a sealed contained filled with desiccant to remove the effects of moisture for about a week before any further tests were conducted. The results of this data are shown in figure 7.4. Some water was still in the film initially, so the data begins that plot at about an hour after the film is deposited. Figure 7.4a, shows the relative thickness, which is the measured areal mass normalized by the areal mass after the first hour of deposition,$1.95\mu\text{m} \cdot \text{g/cm}^3$ for starch-glycerol and $1.5\mu\text{m} \cdot \text{g/cm}^3$ for starch-[emim$^+$][Ac$^-$]. Assuming the density of the film is relatively constant, changes of this ratio will correspond to thickness changes. After 6 days, clearly the starch-[emim$^+$][Ac$^-$] system's thickness was stable for the entirety of these six days. The starch-glycerol film, however, showed a clear continuous drop in thickness over the course of the week, leading to a 2% drop in thickness, or from $1.95\mu\text{m} \cdot \text{g/cm}^3$ to $1.90\mu\text{m} \cdot \text{g/cm}^3$. This is likely attributed to the "retrogradation" of the starch-glycerol film, with the glycerol migrating to the film surface and evaporating [207]. Thus, it does show that the thickness of the [emim$^+$][Ac$^-$] /starch film is more stable than the starch-glycerol over this time period.

Looking at the phase angle (7.4**b**) and the modulus (7.4**c**) data, the mechanical properties of the both films seem to be stable in this time period, meaning the retrogradation of the starch-glycerol has not noticeably effected these viscoelastic properties in this period of time. Longer stability experiments may be necessary to detect these. The modulus data ($\rho|G^*|$) showed that the starch-glycerol system had a noticeably higher modulus ($\sim$ 800MPa) to the ionic liquid/starch system ($\sim$ 500MPa). This is consistent with [emim$^+$][Ac$^-$]

being a better starch plasticizer than glycerol, given the lower film modulus, which would indicate a lower degree of starch recrystallization. One thing that is a little confusing is that the starch-glycerol film has a higher phase angle than the ionic liquid starch film despite having higher stiffness. Higher phase angle would suggest higher dissipative properties, which would suggest better plasticization. However, both the starch films still have very low phase angles ($\sim 6°$ for starch-glycerol and $\sim 1.5°$ for starch-[emim$^+$][Ac$^-$]), so both films are still very glassy.

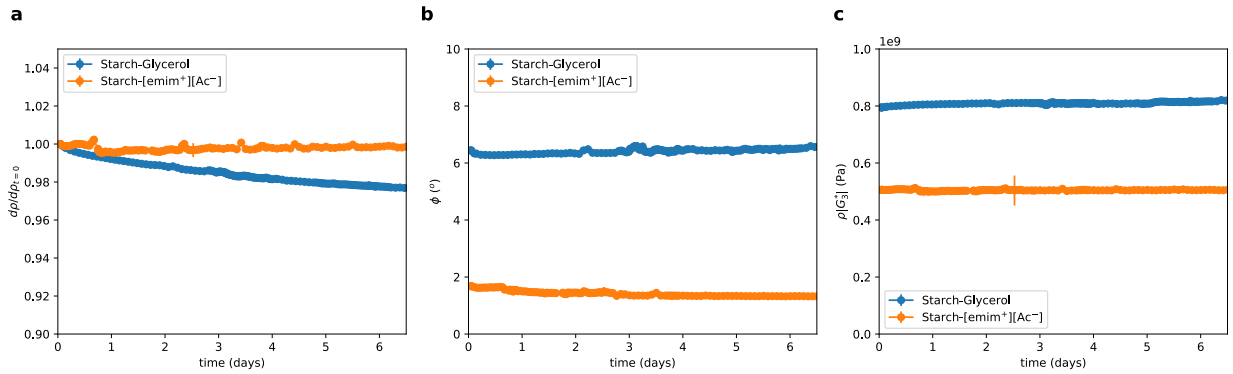

Figure 7.4: Plot of (**a**). relative thickness, normalized by areal mass measurement at $t = 0$ (**b**). phase angle, and (**c**) complex shear modulus at 15 MHz measured from 3:5,5 solution of QCM data of starch-glycerol and starch-[emim$^+$][Ac$^-$] films in a sealed container with Drierite dessicant (0% humidity) for 6.5days. Plots start an hour after film deposition.

7.3.1.2 Comparison to AFM Indentation Data

To assure the validity of the QCM modulus measurements the modulus results were compared to AFM-nanoindentation data, as described in section 7.2.4. AFM experiments were done on a Bruker Dimension Icon in the Fast Force Volume Mode. Scans were done on a 5µm x 5µm area with 128x128 force curves (16384 total curves), each was analyzed using JKR analysis using an 40N/m RTESPA-300 silicon nitride cantilever with a tip radius of approximately 47.7nm. The measured modulus distribution is shown in figure 7.5. Like the QCM data, it showed the starch-glycerol film as having a higher modulus than the starch-[emim$^+$][Ac$^-$] film. Likewise, the AFM showed a similar order of magnitude to the modulus data in figure 7.4c.

Converting the young's modulus, E, to the shear modulus, G, by $E = 2G(1 + \nu)$, where ν is Poisson's ratio, the modulus reported from AFM is still slightly lower than that of the QCM. The larger measured modulus in QCM is consistent with the fact that QCM is conducted at a much higher frequency (15MHz) than AFM (30Hz). Nevertheless, the two measurements are similar order of magnitude, and similar trend

helps give confidence in the QCM data. Additionally, there is noticeably more spread in the starch-glycerol data than the starch-[emim$^+$][Ac$^-$] data, which may be more evidence of film retrogradation.

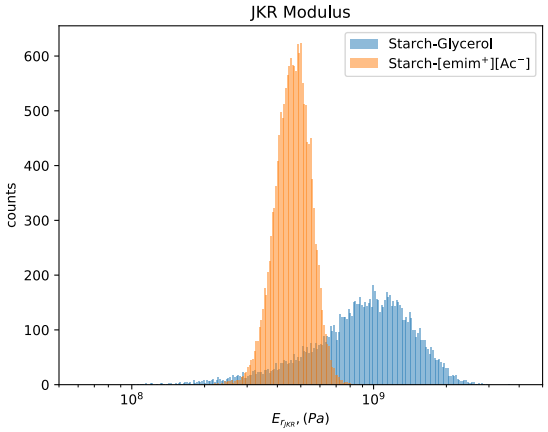

Figure 7.5: AFM indentation modulus distributions for the TPS films deposited on the QCM crystals.

7.3.2 Humidity Experiments

The resulting data collected from the humidity experiments described are section 7.2.3.3 is shown in figure 7.6. The first plot (7.6a) shows the relative thickness as a function of humidity, where the measured areal mass is normalized by the areal mass when the humidity is 0% (equilibrated in desiccant), which was $1.90\mu\text{m} \cdot \text{g/cm}^3$ for starch-glycerol and $1.5\mu\text{m} \cdot \text{g/cm}^3$ for starch-[emim$^+$][Ac$^-$]. Both the [emim$^+$][Ac$^-$] and glycerol plasticized starch films increase in thickness with increasing humidity linearly at approximately the same rate initially, consistent with other moisture isotherms of TPS with different plasticizers [204]. Above 45% humidity, the thickness seems to increase more rapidly with more humidity, marked by a sudden change in slope. Additionally, the starch-[emim$^+$][Ac$^-$] sample starts to increase in thickness more than the starch-glycerol sample, up to a 30% increase in thickness at 75% humidity for starch-[emim$^+$][Ac$^-$] compared to a 25% increase in thickness for starch-glycerol. The next fixed humidity point (84%), resulted in the 5th harmonic being over-damped for both films ($d/\lambda_5 > 0.2$, see section 7.2.3.1), and so accurate measurements could not be done above 75% on these films. Likewise, phase angle, (**figure 7.6b**), a measure of mechanical dissipation, increases with increasing humidity as more evidence of increasing water content in the film. Similar to the thickness trend, a noticeable change in slope of the phase angle with respect to humidity is seen around at 45% humidity. At 75% Humidity, the phase angle for both reach around 45°, which signifies the point where the loss modulus (dissipative component) surpasses the storage modulus (elastic component).

Examining the generalized phase diagram depicted in figure 7.1, it is likely that the saturation limit of water in the TPS film is being reached.

The humidity dependent stiffness, shown by the plot of $\rho|G^*|$ vs. humidity in figure 7.6c, likewise shows a decreasing stiffness of the film with increasing relative humidity, which is as expected for increased water uptake. Here, the initial decrease in stiffness is much less for both samples at lower humidity, and like the other properties, the stiffness begins to decrease rapidity above 45% humidity. Here, the decrease in stiffness at high humidity is much more in the starch-glycerol film than in the ionic liquid/starch film, as they both reach ∼100MPa, but the initial stiffness is higher in the starch-glycerol film, leading to almost an order of magnitude decrease in stiffness, This, combined with the large phase angle, could lead to loss in the structural integrity of the film. Although the films were unable to be tested above 75% relative humidity, the trends suggests that it would likely lead to moduli <100MPa and phase angles >45°.

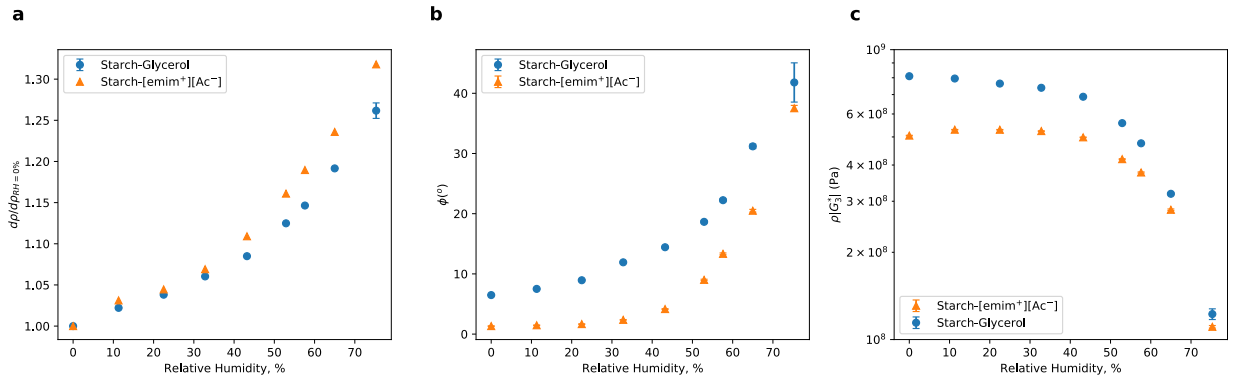

Figure 7.6: Plot of the (**a**). relative thickness, (**b**). viscoelastic phase angle, and (**c**) complex shear modulus at 15MHz vs. Relative Humidity for the Starch-Glycerol and Starch-[emim$^+$][Ac$^-$] films. Properties were calculated from the 3:5,5 solution of the QCM data.

With the ability to measure the areal mass, viscoelastic phase angle, and complex moduli simultaneous, each of these properties can easily be compared with each-other to better understand relationships between water-absorption and mechanical properties. Figure 7.7a and b plot the ϕ and $\rho|G^*|$ vs. the relative thickness, respectively. This effectively shows the change in properties as a function of water content. As expected, phase angle increases and modulus decreases with increasing water content. However, it is more apparent in these plots that the effect of water in the starch-glycerol films begins to change the mechanical properties immediately, with the phase angle increasing and the modulus decreasing monotonically with increasing water content. However, the starch-[emim$^+$][Ac$^-$] films seem to be more resistant to mechanical property

changes at low humidity/water content. The phase angle does not seem to change noticeably until the thickness has increased by more than 5%, at a relative humidity of 32.8%. $\rho|G^*|$, on the other hand, remains stable to a relative thickness increase of 11%, or for all data points below a RH of 45%. A closer look at the low humidity region actually shows the modulus slightly increasing from 0% RH to 11% RH, before beginning to decrease with further humidity/water content increase. The increase in modulus is very small, but was shown to be consistent with other starch-[emim$^+$][Ac$^-$] film. This would suggest that there is an antiplasticization effect for these starch-[emim$^+$][Ac$^-$]films at low humidity, when water is first introduced to the films. Lourdin, *et al.*. reported that antiplasticization occurs in starch-glycerol films at low humidity when the glycerol content is below 12% (w/w), where in these films, the plasticizer content is 30% (w/w) [237]. Antiplasticization of the film due to water at such high plasticizer content is very interesting, and further investigation is needed to verify and understand why this is the case. Regardless, this allows the modulus of the material starch-[emim$^+$][Ac$^-$] to maintain stability at low humidity. On the other hand, above 45% RH, the starch-[emim$^+$][Ac$^-$] begins to take up water more easily than the starch-glycerol film and the stiffness rapidly decreases.

Another way to look at the humidity data results is through a van Gurp-Palmen (vGP) plot, which plots the measured phase angle vs. the measured shear modulus, as seen in figure 7.7. This allows a comparison of both phase angle and modulus for both samples on a single plot. For both films, the data starts on the right: low phase angle and high modulus, at 0% humidity. With increasing humidity, the phase angle increases and the modulus decreases at approximately the same rate, despite the differences in magnitude for each property. Each film seems to follow a set curve on the vGP plot, except for a single point of the starch-[emim$^+$][Ac$^-$], the one at 0% humidity is slightly to the right of the main curve. This is again evidence of the antiplasticization of this film.

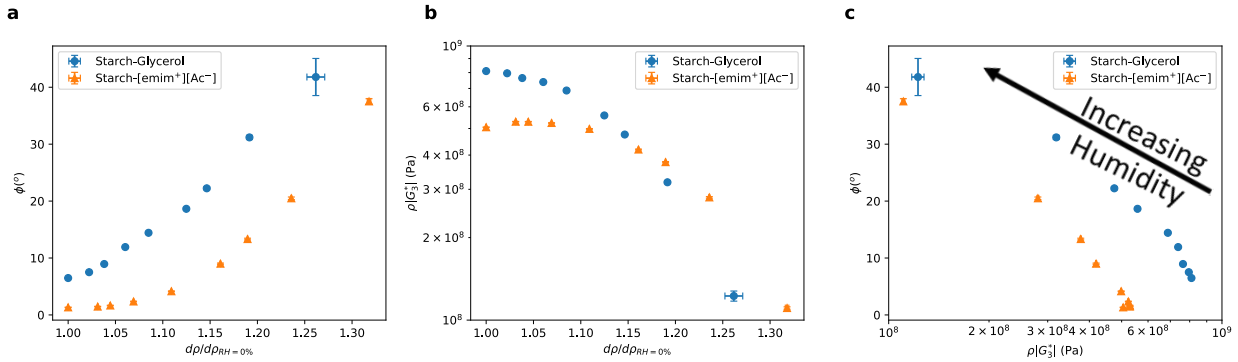

Figure 7.7: Plots of (**a**) viscoelastic phase angle and (**b**) complex shear modulus vs. the relative thickness of the 3:5,5 QCM data of the starch-glycerol and starch-[emim$^+$][Ac$^-$] films from the humidity experiments plotted in figure 7.6. (**c**) vanGurp-Palmen Plot of the QCM humidity experimental data for the same TPS films. The data at 0% humidity is on the right, then moves up in phase angle and down in modulus with increasing humidity.

The properties of the film post-humidity experiments were also of interest, to see if the absorbed water could be completely removed, and to see if there were permanent effects on the film properties. Since the humidity experiments took 1-2hr for each humidity point, the experiment had to be broken into two separate days. After each day of experiments, the aqueous solutions was replaced with desiccant and allowed to dry overnight, so the properties of the film during the humidity experiments at 0% humidity were assessed three times: before any humidity experiments, after measurement at 52.9% humidity ($Mg(NO_3)_2$ saturated salt solution), and then once again after the end of the humidity experiments (attempt of 84.3% humidity with KBr saturated salt solution). The plots of the relative thickness, phase angle, and shear modulus at each of these points are shown in figure 7.8. A few distinctions between the samples emerge. First, looking at the relative thickness in figure 7.8a, it's important to note that the thickness differences after the humidity experiments for both samples are very, very small, so the differences could be negligible. However, the data as is shows opposite trends for the two samples. The starch-glycerol thickness decreases by -1.42% after the humidity tests are completed, which is much faster than the rate of thickness loss found over the course of week before the humidity experiments. It is possibly that the absorption of water by the film and subsequent drying increases the rate of retro-degradation, but more experiments may need to be done to verify this.

On the other side, for the starch-[emim$^+$][Ac$^-$], the thickness actually increased after the humidity experiments, but by an even smaller amount, 0.5%. This could signify that the film hold on to a very small amount of water once exposed to very high humidity that doesn't come out easily. The increased phase angle

for the starch-[emim$^+$][Ac$^-$] sample (7.8b) could signify more water in the film. However, the starch-glycerol film also shows an increase in phase angle, despite showing mass loss. Additionally, the shear modulus data also show a very slight drop in the shear modulus for the glycerol starch film, and an even slighter increase in modulus for the ionic liquid starch film, which is kind of the opposite trend you'd expect for both cases given the thickness results. Another possible explanation is, that damage to the film has made the sample more rough, and caused more errors in the viscoelastic calculation. Examination of the $\Delta\Gamma$ fits (as discussed in section 7.2.3.1), shows that the deviation of the experimental data and the resulting viscoelastic solutions increases after the humidity experiments. It's important to note that these fitting errors cause error mostly in the viscoelastic property calculations (ϕ, $\rho|G^*|$), but shouldn't affect the thickness measurements as much, which depend more on Δf. Future investigations will likely look at the effects of these TPS films after much more humidity cycles to understand the long term effects of humidity exposure and drying.

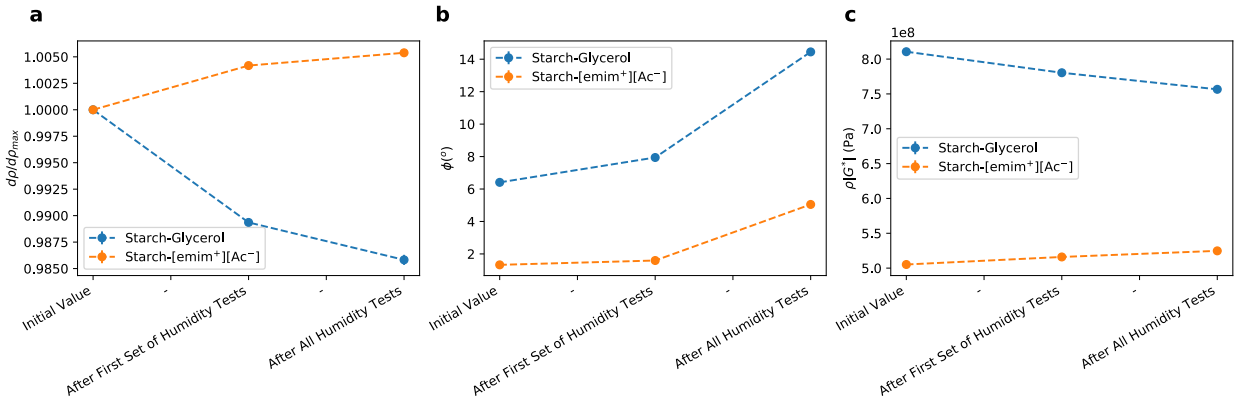

Figure 7.8: QCM measurements of TPS films at 0% humidity at three different points during humidity experiments: before humidity experiments, after the measurement of 52.9% humidity ($Mg(NO_3)_2$) saturated salt solution), and after the end of the humidity experiments (84.3%, KBr solutions). Measurements are (**a**) relative thickness, (**b**) phase angle, and (**c**) shear modulus ($\rho|G^*|$).

7.4 Conclusions

This investigation has shown QCM to be a versatile and useful tool to evaluate the mechanical properties of TPS films in response to environmental stimuli, and evaluate the use of different plasticizers, such as glycerol and 1-ethyl-3-methylimidazolium acetate ([emim$^+$][Ac$^-$]). Several advantages of QCM testing over previously used tensile testing methods for mechanical property analysis were shown, as QCM is a non-destructive technique that only requires a small amount of test material, allowing the study of the effect of

a wide range of environmental stimuli, such as humidity, on a single TPS film, that will equilibrate to its environment quickly.

Thus, using the QCM, several advantages of the ionic liquid, [emim$^+$][Ac$^-$], over glycerol as a plasticizer for TPS were demonstrated. Testing the TPS films over desiccant for 1 week showed evidence of a 2% mass loss for starch-glycerol films likely due to evaporation of glycerol from the film, but the film thickness of the starch-[emim$^+$][Ac$^-$] remained stable over the same time. As a better plasticizer, the measured modulus of starch-[emim$^+$][Ac$^-$] was noticeable lower than that of starch-glycerol, which agreed with complementary AFM indentation data. The AFM indentation also gave evidence of retrogradation in the glycerol-starch film shown by a wider distribution in the AFM modulus compared to that of the starch/ [emim$^+$][Ac$^-$].

In response to humidity, both films showed a similar increase in mass with relative humidity until about 45% RH, at which the starch/ [emim$^+$][Ac$^-$] film began to absorb more water than the starch-glycerol film, suggesting that [emim$^+$][Ac$^-$] is more sensitive to water absorption. This was coupled to similar trends in mechanical properties: increased phase angle and decreased modulus with increased water absorption, dropping by almost an order of magnitude over the tested humidity range, but with some key differences. Although the modulus of starch-glycerol decreased (and phase angle increased) monotonically with increased RH, the mechanical properties of the starch-[emim$^+$][Ac$^-$]remained relatively stable up until 45% RH, even showing a slight increase in modulus at low RH, evidence of some antiplasticization effect, before beginning to drop sharply above that point. The stability of TPS films in response to humidity is of great interest for potential applications in consumer packaging, and this shows some potential of ionic liquids like [emim$^+$][Ac$^-$]to maintain its properties better than polyol TPS films. However, the properties still begin to change very rapidly above 45% RH as a result of increased water absorption, and so future work will likely look to find different ionic liquids or additives that reduce water uptake into the TPS film at high RH. Additionally, both films showed some evidence of film quality depreciation after the conducting the humidity tests as a result of swelling and deswelling the film, but future investigations will be needed to show the effects of multiple cycles of humidity exposure and drying on these TPS films.

Overall, QCM has the potential to be used for future studies on temperature, humidity, and aging of the TPS films and the development of new TPS formulations. It will be a vital tool for evaluating and optimizing different plasticizers, hydrophobic polymer additives, and starch sources much more quickly and efficiently than traditional testing methods.

Chapter 8

Conclusions & Future Work

This thesis discussed design-driven mechanical property characterization approaches to polymer and polymer composite materials development for three different polymer materials systems: crosslinked rubbers, epoxies, and thermoplastic starch. Despite the unique motivations and distinct experimental investigations, the investigations of each system was connected with at least two out of the three major themes introduced in chapter 1:

1. Mechanical characterization technique development.
2. Understanding the structure-property relationships, and by extension, the link between bulk and local mechanical properties.
3. Bridging the gap between experiments and computational simulations.

In this final chapter, the work presented in this thesis is summarized for each other three polymer systems in terms of how the work relates to the aforementioned themes. Additionally, the suggested future work and direction of each project will be discussed.

8.1 Rubber Composite & AFM Work: Incorporating Interphase Data with Composite Simulations

In chapter 3, an AFM nanoindentation method was developed from accessible AFM indentation modes to measure and map the local viscoelastic properties of elastomeric blends and composites (theme 1). Quantitative agreement between DSI nano-DMA and bulk DMA viscoelastic master curves was demonstrated

for two different homogeneous elastomers: styrene butadiene rubber (SBR) and synthetic natural rubber (SNR), and the capability of the technique in acquiring quantitatively accurate viscoelastic property maps of heterogeneous soft solids was validated through experiments on an SBR-SNR blend sample (theme 2). However, as mentioned in section 3.1.1, the main motivation behind the development of the DSI-AFM viscoelastic property characterization technique was to characterize the viscoelastic behavior interphase regions in carbon black - rubber composites in order to improve computational models to predict bulk viscoelastic behavior (theme 3). The application of this method to computational models has yet to be fully addressed, but some initial "proof of concept" simulations have been conducted.

Initial investigations of carbon black - rubber composites with the DSI technique, shown in fig. 3.15, showed the rubber regions around the particle to be of higher modulus and higher loss tangent than the matrix-regions further from the particles, which would suggest a shift of approximate 1.3 orders of magnitude in frequency of the neat, unfilled SBR master curve towards the glassy regime with approximate interphase width of ~50nm. Some assumptions could be taken from this initial AFM data and applied to a rough 3-D voxelated rubber-composite model using finite element analysis (FEA) to simulate viscoelastic mechanical behavior. This model had three components, the carbon black particles, the rubber matrix, and an interphase region. The particles were assumed to be purely elastic, the matrix given the viscoelastic master curve from the DMA data corresponding to the unfilled SBR system (fig. 3.4a), and the interphase given the same mastercurve shifted towards the glassy regime ~1.3 orders of magnitude (shift of the peak to lower frequency), with interphase width ~50nm as estimated from the AFM experiments. The initial results are seen in figure 8.1a for the simulation of the loss tangent master curve for a 10wt% N121 carbon black-SBR rubber composite. The experimental loss tangent curve of the 10wt% carbon black-SBR composite is plotted in black, whose loss peak is at a higher frequency and lower magnitude than the unfilled rubber matrix material (blue). The results of the simulation when no interphase is input (only structural & geometric effects from particles) shows only a reduction in the peak loss tangent but no shift in frequency (green). However, the the system with the interphase as previously described results in the curve in red, showing a shift in phase angle peak to lower frequency, the opposite of what is seen in the true rubber composite data.

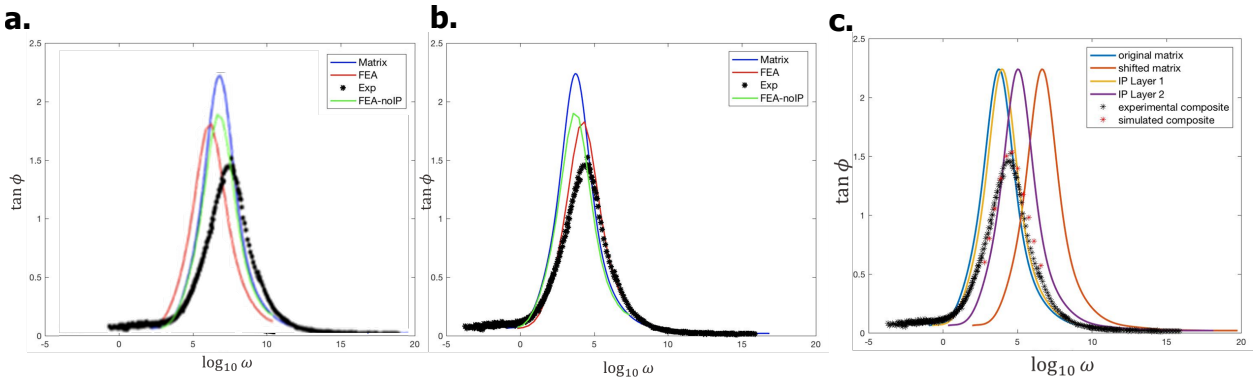

Figure 8.1: Comparison of experimental DMA $\tan\phi$ master curves of 10wt% N121 carbon black-styrene-butadiene tubber (SBR) composite (black stars) to a finite element analysis simulation of a 3-D voxelated composite composite model with ~50nm interphase red **(a,b)**. The blue **(a,b)** line shows the inputted $\tan\phi$ master curve of the matrix material, which was generally determined from DMA of the unfilled system, and the green line **(a,b)** shows the corresponding composite simulation when no interphase is included in the model. (**a**) shows the case when the interphase region is given the viscoelastic properties of the matrix master curve shifted towards lower frequencies (to the left) by 1.3 orders of magnitude, as the result of stiffening suggested by the AFM DSI data. (**b**). Shows the potential "interphase softening" case where the interphase is given properties of the matrix shifted towards higher frequencies (to the right). (**c**). Shows the "matrix softening" case where the input matrix master curve is shifted ~3 orders of magnitude towards higher frequencies (to the right). In this model the matrix master curve is red, and the output FEA is given by the red stars. This model used two step interphase regions, the stiffest, near the particle (yellow), and a less stiff region further from the particle (purple). *Simulations & Plots Courtesy of Dr. Xiaolin Li.*

Given the molecular motions of the rubber will be restricted near carbon black particles, and the AFM experimental data show a stiffening of near the carbon black particles, it should be expected that the addition of stiff particles result in a shift in the dynamics towards low frequency/high temperature, as the FEA model predicts. Instead the opposite is seen in the experimental DMA data. So, one of two things could be happening:

- The interphase region is softer than the matrix.
- The matrix region of the composite may be softer than the unfilled rubber system.

An FEA of the soft interphase case is shown in figure 8.1b, which shows the simulated peak matching the frequency of the experimental data (but not the magnitude). However, this soft interphase hypothesis is in direct violation with our AFM DSI findings from chapter 3, and investigation from other research in rubber composites have shown similar stiffening of the interphase rubber layer near fillers [98]. This leaves the soft matrix case, and some research has suggested that the process of curing elastomers like rubber with rigid fillers *in situ* reduces the crosslink density of the rubber in the composite [256–258]. Given that lower

crosslink density leads to lower stiffness [259], this hypothesis seems more probable, and the DSI technique is the perfect tool to test it.

Following a similar protocol from section 3.4.2, DSI was performed a 10wt% N121 carbon black - SBR composite at several temperatures between 0-25°C and frequencies between 20-1000Hz. A "matrix-only" region far away from any particles was selected to construct a DSI-master curve of the matrix viscoelastic properties. This is compared to the DMA master curve of the unfilled system in figure 8.2a, which shows that the SBR matrix region master curve in the composite system is shifted to higher frequency, which suggests a softening of the matrix. To overlap with the DSI, the unfilled SBR master curve frequencies must be multiplied by 25 (1.4 orders of magnitude), shown in figure 8.2b. This "matrix softening" situation was modeled in figure 8.1c, with 2 interphase layers instead of one with slightly different properties, and lead to good agreement with the experimental DMA data of the 10wt% carbon black composite. However, it required a shift in the matrix properties by 3 orders of magnitude, instead of the 1.4 seen in the initial experiments. However, a lot of assumptions were made in this initial FEA-interphase composite model, namely a uniform shift in the master curve for the matrix and interphase regions and a "step" interphase geometry (no gradient in properties).

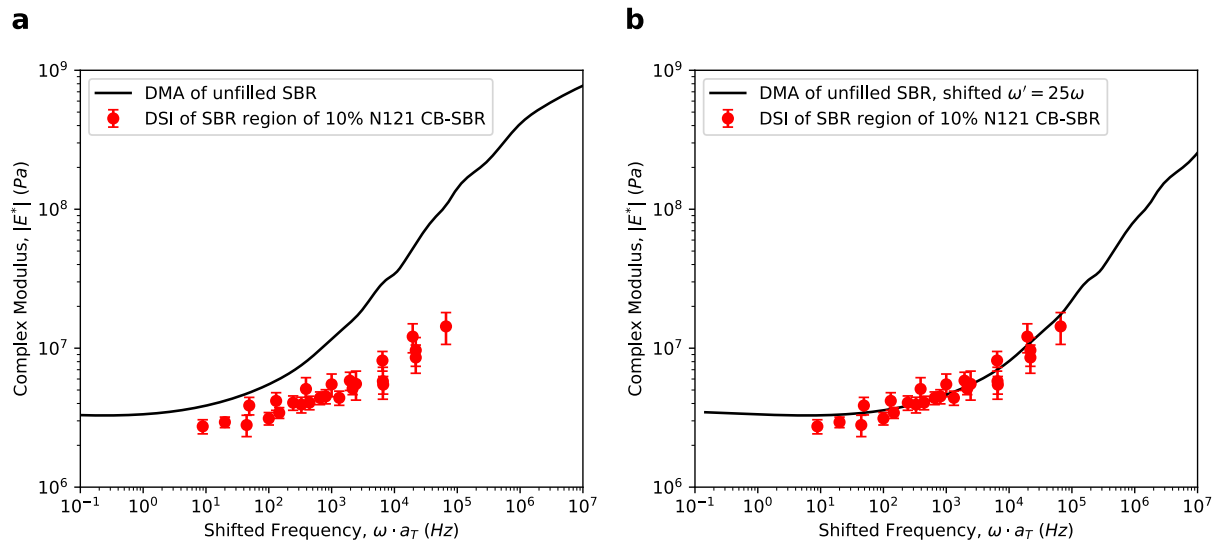

Figure 8.2: **(a)** Mastercurves of $|E^*|$ for styrene-butadiene tubber (SBR), reference temperature of 20°C, comparing bulk DMA data mastercurve (black) with a mastercurve constructed from AFM DSI nano-DMA data from the Asylum Cypher-ES (red) of 10wt% N121 carbon black-SBR, averaged only on the matrix regions, far from CB particles. **(b)** Same data, except the DMA mastercurve of SBR is shifted in frequency by a factor of 25, showing better agreement with the DSI master-curve data.

The fact that the general trends in matrix and interphase properties are consistent in the model and AFM experiments is promising. Future work related to the local viscoelastic property evaluation of rubber nanocomposites should focus on:

- The construction of viscoelastic property master curves of different phases in heterogeneous materials, such as the interphase region and the matrix region of composites, or each phase in a multi-rubber blend, and a comparison of these properties to that of corresponding homorubber systems, to verify the existence of matrix or phase softening due to crosslinking density changes when cured in multi-phase environments. This would help verify consistency of the results presented in fig. 8.2.
- Constructing a consistent time-temperature model of the geometry of the interphase region by collecting viscoelastic property data around rubber-particle interphases. Currently, the interphase region was assumed to be constant in shape with time and temperature, although some research suggests that the thickness can decrease with increasing temperature [113]. This also requires the removal of artificial increases in stiffness due to indentation artifacts.

In the case of the second point, the need to accurately measured the size and shape of the interphase is complicated by the potential of artificial measurement of stiffness due to the stress interaction effect as a result of indentation of a compliant material near a rigid substrate. In chapter 4, the stress interaction effect was demonstrated using FEA models, both with and without interphases for elastic, linear indentations. The extend of broadening of the interphase was directly related to the contact area of the indent (as of the result of a deeper indentation). Thereby a method was developed to estimate the interphase width based on the modulus profiles taken at different indentation depths. This method showed good agreement when applied to experimental AFM data (theme 3). However, there was still a lot of uncertainty in the data, particularly due to the geometric inconsistency around the particles. These experiments would also be helped by future work using a model, more controllable system, such as PDMS-silica composites, adding to the future work:

- Utilizing a model system that is easily reproducible, such as PDMS with silica particles (whose interaction with PDMS can be more easily controlled with surface treatment). The carbon-black rubber systems were proprietary formulations given by Goodyear, and their properties could vary widely in different batches. Using a system whose formulations we have complete control over would help tremendously with understanding the behavior of these composite systems.

Additionally, these FEA experiments were elastic indentation experiments. To improve the characterization of the interphase in rubber composites, if possible given the finite size of the tips, similar FEA experiments

need to be done for DSI-type dynamic mechanical indentation experiments to see if the stress inderaction effect deconvolution method discussed in chapter 4 can be applied to the DSI technique. This will then need to be coupled with AFM DSI indentation experiments near rubber-particle interphases at different peak forces/indentation depths. Thus, a lot of work still needs to be done to fully understand and characterize the local viscoelastic properties in these rubber composites to build accurate models for predicting bulk behavior. Nevertheless, the development of the DSI method and the FEA experiments modeling the stress interaction effect in indentation experiments have laid the ground work for these future investigations, and increased the understanding of both rubber composites and AFM indentation experiments in the polymer mechanics community.

8.2 Epoxies With Nanoscale Heterogeneity: Applications to Composite Systems

In chapter 5, the temperature dependent mechanical and fracture properties of the model DGEBA/PACM/Jeffamine systems required the application of standardized characterization techniques (Vicker's indentation tests, SENB K_{Ic} fracture toughness) to custom mechanical testing set-ups with temperature & environmental controllers (theme 1). These experiments demonstrated the unique low temperature fracture toughness behavior of the DGEBA/PACM/D2000 systems with nanoscale heterogeneity compared to homogeneous epoxy systems. The broadened glass transition regime as a result of the heterogeneity lead to the fracture toughness increasing as temperature decreased below the transition region, leading to a low temperature K_{Ic} plateau that scaled with increasing D2000 content (theme 2). Given the motivation to apply these or similar epoxies to low temperature structural applications as composite matrix materials, the high K_{Ic}at low temperatures is attractive due to the desire to inhibit crack propagation and failure as a result of thermal stresses. However, the high K_{Ic}at low temperature typically corresponded to low modulus and hardness at ambient conditions, limiting their utility for structural applications. In chapter 6, we tried to address this issue by forming semi-interpenetrating polymer networks (IPNs) of the epoxy with PMMA thermoplastic. The epoxy-PMMA IPNs showed great improvement in ambient stiffness and hardness, however, the low temperature toughness also seemed to decrease, which was the characteristic that we wanted to preserve.

Nevertheless, there is still much to learn about these epoxy-thermoplastic IPNs that could lead to improved low temperature performance. There are three main paths of future work in regards to these systems:

1. Understanding the chemisty of the polymerized PMMA in the epoxy systems.
2. Controlling the PMMA uptake in the epoxy resins (unsaturated IPN)
3. Studying other thermoplastics besides PMMA for epoxy-IPN formation.

In the case of (1), the free radical polymerization in the presence of the epoxy could inhibit the extent of reaction. It is known that oxygen is a major culprit free radical polymerization inhibition, and even though the UV curing takes place under nitrogen, there may be some effect of the epoxy chemistry, it is unclear if the polymerization within the matrix of epoxy has any inhibitive effects[251, 260]. Since it is not chemically bonded to the epoxy, the PMMA can be extracted from the semi-IPN by a compatible solvent like tetrahydrofuran (THF) to be analyzed by mass-spectrometer techniques. Initial MALDI investigations suggest low MW (∼2000), but the MALDI spectra do not show the characteristic features of PMMA, showing mass separation of only 58 instead of the expected 100 for PMMA, suggesting that there may be something else in the IPN or some cross product. Further analysis by gel permeation chromatography (GPC) needs to be done to very the exact identity of the polymer product. If there is some oxygen inhibition that is limiting the properties of the IPN, it may be beneficial to look at thiolene polymerization instead of acrylate free-radical polymerization. It has been shown that thiolene resist oxygen inhibition in their polymerization mechanism [251].

Secondly, the amount of the thermoplastic could potentially be controlled for more tailored properties. In the method presented in chapter 6, the cured epoxies were submerged in the MMA monomer until saturation, as in, as much MMA as possible. It is possible that complete PMMA saturation inhibits the molecular motions of the epoxy responsible, which is suggested by the quenching of the β-transition peak in the DMA data, and the lack of free volume limits the energy absorption capability of the network. As such, it would be beneficial to see how controlling the PMMA uptake in the epoxy matrix affects the IPN properties. There is evidence in the literature that there is an optimal range of thermoplastic content for improved mechanical performance in epoxy-PMMA IPNs [188, 189], for example. Barcia, *et al.* tried different PMMA content in their epoxy/PMMA IPNs from 5-30wt% PMMA, and the optimal mechanical properties were found at only 5wt%PMMA [188]. The low temperature K_{Ic}-ambient modulus relationship should theoretically change monotonically with PMMA content between the neat epoxy and saturated epoxy/PMMA IPN, as indicated in figure 8.3a in the case of D2000-40. Ideally, it would follow the purple dashed line, maintaining a high toughness while increasing in modulus until reaching a drop-off, but it could decrease linearly (red line), or worse, a steep drop in toughness at low PMMA content (green line). The reality is likely somewhere in

between, but future investigations need to work in filling out these intermediate points. Two main ways to control the PMMA content are either using simultaneous synthetic methods, where the PMMA is cured at the same time as the epoxy with a thermoinitiator, although this introduces another issue in controlling phase separation during curing [261], or mixing the MMA with some type of volatile solvent in different ratios before monomer absorption. The solvent will take up space in the epoxy network during PMMA polymerization, and evaporate afterwards, reducing the overall PMMA content. This option would be likely the first step since it doesn't change the epoxy synthetic process.

Additionally, there may be an issue of using PMMA, a glassy thermoplastic with low free volume, that reduces the toughness capability of the epoxy-PMMA IPN and other thermoplastic polymers may be more equipped to maintain low temperature toughness. Thermoplastics such as bisphenol A glycerolate dimethacrylate (bis-GMA), shown in fig. 8.3b, may be a better fit for this application, given is chemical similarity to DGEBA, and its widespread use as a tough dental composite material [262]. So, future investigation of heterogeneous epoxy-thermoplastic low temperature fracture behavior will likely look at these systems.

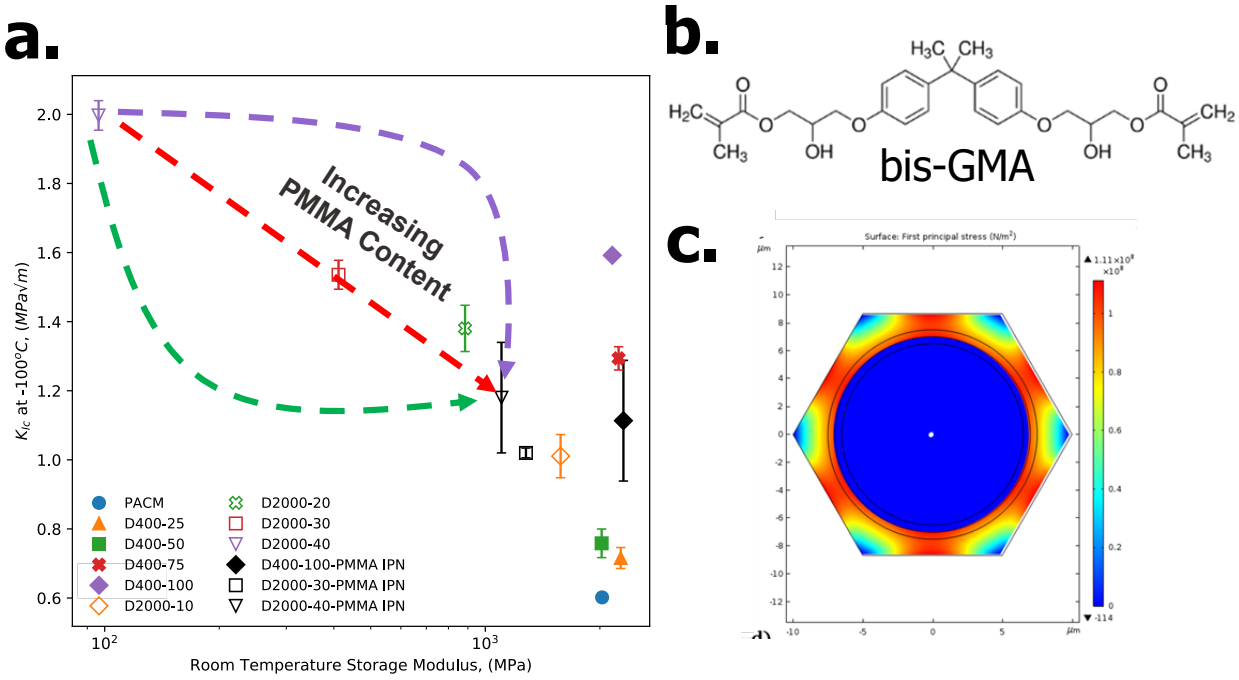

Figure 8.3: (**a**). Design Plot of K_{Ic} at -100°C vs. room temperature DMA storage modulus (1Hz) of DGEBA/PACM/Jeffamine epoxies as well as the select epoxy/PMMA IPNs from chapter 6, with potential pathways for the D400-40-PMMA IPNs to follow as the PMMA content is increased (**b**). Chemical structure of Bisphenol A glycerolate dimethacrylate (bis-GMA), a potential replacement for PMMA in the epoxy-thermoplastic IPN's that is chemically similar to DGEBA. (**c**). Hexagonal periodic FEA model of epoxy-fiber composite modeling thermal stresses as a result of differences in thermal expansion.

Despite the fact that this epoxy work has been motivated by potential applications for fiber composite, none of the characterization has been extended to composite systems yet. Thus, the logical direction of this project is to test the mechanical behavior of these epoxy systems in a fiber-reinforced composite. One such experimental technique of interest that could potential be very interesting to explore is fiber-fragmentation tests, which looks at the fragmentation of a single fiber embedded in an epoxy matrix as it is loaded, which help evaluate the fiber-matrix adhesion [263]. It would be very interesting to evaluate these fiber-matrix mechanical properties at different temperatures, particularly low temperatures, to see the effect of thermal loading.

However, designing these experiments with different epoxy formulations for destructive characterization would be very labor intensive task. Thus, it is likely beneficial to try to evaluate the performance of the model epoxy systems using computation models before moving to experiments to help decide which formulations are worth testing (theme 3). FEA simulations of thermal loading can easily be conducted using

readily available FEA software. Some initial FEA experiments have been conducted to look at the thermal stresses on an epoxy-fiber composite cross-section as a result of large changes in temperature, such as the first principle stress 2D plot in figure 8.3c, which shows high thermal stresses in the regions between fibers. These initial simulations were purely elastic, and did not take into account the temperature dependent properties of modulus and thermal expansion. Future FEA simulations will need to take into account the temperature dependence of these properties to compare how stresses may change in the different epoxy formulations, (especially the ones with a wide glass transition regions). Experimental investigations on the thermal expansion of these materials have already been done, and large changes in thermal expansion are seen in the transition regime. Thus, inputting the collected expansion data in these models will help evaluate the potential of these epoxies to be used in cryogenic applications.

Additionally, given the large amount of fracture surface data presented in sec 5.3.3.3 and Appendix A.2 showed interesting trends with respect to the K_{Ic} fracture toughness, another potential avenue of future work is to develop machine learning algorithms to connect and predict K_{Ic} fracture toughness from fracture surface morphology to enable a more rapid materials design and validation process.

8.3 Thermoplastic Starch

Chapter 7 presented a non-destructive, efficient method to measure the full range of humidity dependence of viscoelastic mechanical properties and moisture absorption of thermoplastic starch (TPS) films using a quartz crystal microbalance (QCM) (theme 1). The QCM allows for the mechanical characterization of a single film at different temperature and humidity environments, making the evaluation of different TPS film formulations more efficient. The resulting data showed that the mechanical starch sample plasticized with the ionic liquid, [emim$^+$][Ac$^-$], was relatively stable at low humidities compared to the starch/glycerol sample, but the starch/[emim$^+$][Ac$^-$] ultimately absorbed more water that starch/glycerol at higher humidities, likely as a result of a stronger affinity to water of the ionic liquid (theme 2). However, in order to be useful for packaging applications, the TPS films need to be able to withstand a wide range of humidity environments without becoming too weak, meaning resist falling apart due to too much water uptake. Careful selection of plasticizers that may be more resistant to water uptake, while maintaining the stability that an ionic liquid like [emim$^+$][Ac$^-$] brings to the TPS film, could help improve this issue.

There is a lot of interest in deep eutectic solvents (DES), a specific class of ionic liquids, that are formed by the eutectic mixture of Lewis or Brønsted acids and bases, and typically contain more anionic and/or

cationic species [217]. The wide variety of formulations, including food grade ingredients, make them an attract choice for examination as possible plasticizers for TPS films, and some literature has shown them used at plasticizers for other biomaterials, such as cellulose [264]. Understanding the starch-water phase diagram of specific TPS film, as presented in figure 7.1, is essential in the design of better TPS materials, and the QCM is well equipped to be able to evaluate the properties of new TPS-DES starch films at different points in the single phase region of the diagram. Given the push for more biodegradable and sustainable materials, the characterization and development of new TPS materials is a sensible direction to pursue in the future, and the QCM is well-equipped to continue to make meaningful contributions to the field.

8.4 Final Thoughts

This thesis presented materials characterization of a diverse set of polymer systems, namely rubber nanocomposites, epoxies with nanoscale heterogeneity, and thermoplastic starch. It is important to note that each of the three polymer systems discussed could be the subject of a whole thesis by themselves, and there is certainly much more to be explored in each of these systems, as discussed in this final chapter. Nevertheless, the characterization approach for each of these material systems was carefully executed with a mindset of new materials design, either by trying to develop a new experimental characterization technique to characterize the material for improving computational models, studying a model system to understand a wide range of possible behavior in a constituent material of a potential composite, or developing new methods that make complete characterization of a material more efficient. The materials design approach has shown to be very versatile, and with this thesis as evidence, meaningful contributions to polymer materials development have been made.

Bibliography

[1] Kenneth R. Shull and Jonathan Emery. *MSE: 332 Mechanical Behavior of Materials*. Northwestern Materials Science Series, Evanston, Illinois, USA, January 2020.

[2] Inc. PerkinElmer. Dynamic Mechanical Analysis (DMA): A Beginner's Guide, 2013.

[3] Hadi Tavakoli Nia, Lin Han, Iman Soltani Bozchalooi, Peter Roughley, Kamal Youcef-Toumi, Alan J. Grodzinsky, and Christine Ortiz. Aggrecan nanoscale solid–fluid interactions are a primary determinant of cartilage dynamic mechanical properties. *ACS nano*, 9(3):2614–2625, 2015.

[4] Pavan V. Kolluru, Matthew D. Eaton, David W. Collinson, Xu Cheng, David E. Delgado, Kenneth R. Shull, and L. Catherine Brinson. AFM-based Dynamic Scanning Indentation (DSI) Method for Fast, High-resolution Spatial Mapping of Local Viscoelastic Properties in Soft Materials. *Macromolecules*, 51(21):8964–8978, November 2018. ISSN 0024-9297. doi: 10.1021/acs.macromol.8b01426.

[5] R. Wimmer, B. N. Lucas, W. C. Oliver, and T. Y. Tsui. Longitudinal hardness and Young's modulus of spruce tracheid secondary walls using nanoindentation technique. *Wood Science and Technology*, 31 (2):131–141, April 1997. ISSN 1432-5225. doi: 10.1007/BF00705928.

[6] M. Chyasnavichyus, S.L. Young, and V.V. Tsukruk. Probing of polymer surfaces in the viscoelastic regime. *Langmuir*, 10:10566–10582, 2014.

[7] Kaustav Goswami, Frederikke Bahrt Madsen, Anders Egede Daugaard, and Anne Ladegaard Skov. Silicone resembling poly (propylene glycol) interpenetrating networks based on no pre-stretch as basis for electrical actuators. In *Electroactive Polymer Actuators and Devices (EAPAD) 2013*, volume 8687, page 86871Z. International Society for Optics and Photonics, 2013.

[8] R. G. M. van der Sman and M. B. J. Meinders. Prediction of the state diagram of starch water mixtures using the Flory–Huggins free volume theory. *Soft Matter*, 7(2):429–442, 2011. doi: 10.1039/C0SM00280A.

[9] Jonas Carlstedt, Joanna Wojtasz, Peter Fyhr, and Vitaly Kocherbitov. Understanding starch gela-

tinization: The phase diagram approach. *Carbohydrate Polymers*, 129:62–69, September 2015. ISSN 0144-8617. doi: 10.1016/j.carbpol.2015.04.045.

[10] Lewis Greenspan. Humidity fixed points of binary saturated aqueous solutions. *Journal of research of the national bureau of standards*, 81(1):89–96, 1977.

[11] P.M. Ajayan, P. Braun, and L.S. Schadler. *Nanocomposite Science and Technology*. Wiley-VCH, Weinham, 2003.

[12] L.S. Schadler, L.C. Brinson, and W.G. Sawyer. Polymer nanocomposites: A small part of the story. *Journal of Mechanics*, 59:53–60, 2007.

[13] P.F. Brune, G.S. Blackman, T. Diehl, J.S. Meth, D. Brill, Y. Tao, and J. Thornton. Direct measurement of rubber interphase stiffness. *Macromolecules*, 49:4909–4922, 2016.

[14] David W. Collinson, Matthew D. Eaton, Kenneth R. Shull, and L. Catherine Brinson. Deconvolution of Stress Interaction Effects from Atomic Force Spectroscopy Data across Polymer-Particle Interfaces. *Macromolecules*, 52(22):8940–8955, November 2019. ISSN 0024-9297. doi: 10.1021/acs.macromol.9b01378.

[15] Hongyao Ding, Xin Ning Zhang, Si Yu Zheng, Yihu Song, Zi Liang Wu, and Qiang Zheng. Hydrogen bond reinforced poly(1-vinylimidazole-co-acrylic acid) hydrogels with high toughness, fast self-recovery, and dual pH-responsiveness. *Polymer*, 131:95–103, November 2017. ISSN 0032-3861. doi: 10.1016/j.polymer.2017.09.044.

[16] Jingcheng Fu, Hadi M. Fares, and Joseph B. Schlenoff. Ion-Pairing Strength in Polyelectrolyte Complexes. *Macromolecules*, 50(3):1066–1074, February 2017. ISSN 0024-9297. doi: 10.1021/acs.macromol.6b02445.

[17] William W Graessley. The entanglement concept in polymer rheology. In *The Entanglement Concept in Polymer Rheology*, pages 1–179. Springer, 1974.

[18] A. KELLER. Morphology of Crystallizing Polymers. *Nature*, 169(4309):913–914, May 1952. ISSN 1476-4687. doi: 10.1038/169913a0.

[19] Shogo Saito. Transitions in Solid Polymers. In *Changes of State*, pages 555–592. Springer, 1975.

[20] L.C. Brinson and H.F. Brinson. *Polymer Engineering Science and Viscoelasticity*. Springer US, second edition, 2015.

[21] J.D. Ferry. *Viscoelastic Properties of Polymers*. Wiley, New York, 1980.

[22] L.S. Garcia-Coln, L.F. del Castillo, and P. Goldstein. Theoretical basis for the Vogel-Fulcher-Tammann equation. *Physical Review B*, 40:7040–7044, 1989.

[23] Malcolm L. Williams, Robert F. Landel, and John D. Ferry. The Temperature Dependence of Relaxation Mechanisms in Amorphous Polymers and Other Glass-forming Liquids. *J. Am. Chem. Soc.*, 77 (14):3701–3707, July 1955. ISSN 0002-7863. doi: 10.1021/ja01619a008.

[24] David E. Delgado, Lauren F. Sturdy, Craig W. Burkhart, and Kenneth R. Shull. Validation of quartz crystal rheometry in the megahertz frequency regime. *Journal of Polymer Science Part B: Polymer Physics*, 57(18):1246–1254, September 2019. ISSN 0887-6266. doi: 10.1002/polb.24812.

[25] Mark R VanLandingham. Review of Instrumented Indentation. *Journal of Research of the National Institute of Standards and Technology*, 108(4):249–265, 2003. ISSN 1044-677X. doi: 10.6028/jres.108.024.

[26] W.C. Oliver and G.M. Pharr. An improved technique for determining hardness and elastic modulus using load and displacement sensing indentation experiments. *Journal of Materials Research*, 7(6): 1564–1583, 1992. ISSN 0884-2914. doi: 10.1557/JMR.1992.1564.

[27] S.I. Bulychev, V.P. Alekhin, M.Kh. Shorshorov, A.P. Ternovskij, and G.D. Shnyrev. Determination of Young modulus by the hardness indentation diagram. *Zavodskaya Laboratoriya*, 41(9):1137–1140, 1975.

[28] Shuang Yang, Yong-Wei Zhang, and Kaiyang Zeng. Analysis of nanoindentation creep for polymeric materials. *Journal of Applied Physics*, 95(7):3655–3666, 2004.

[29] ASTM E384: Standard Test Method for Knoop and Vickers Hardness of Materials. 2017. doi: 10.1520/E0384-17.

[30] I. Low and C. Shi. Vickers Indentation Responses of Epoxy Polymers. *Journal of Materials Science Letters*, 17:1181–1183, January 1998. doi: 10.1023/A:1006517005082.

[31] Catherine A Tweedie and Krystyn J Van Vliet. On the indentation recovery and fleeting hardness of polymers. *Journal of materials research*, 21(12):3029–3036, 2006. ISSN 2044-5326.

[32] I. M. Low. Effects of load and time on the hardness of a viscoelastic polymer. *Materials Research Bulletin*, 33(12):1753–1758, 1998. ISSN 0025-5408. doi: 10.1016/S0025-5408(98)00179-2.

[33] B. N. Lucas, W. C. Oliver, and J. E. Swindeman. The dynamics of frequency-specific, depth-sensing indentation testing. *MRS Online Proceedings Library Archive*, 522, 1998.

[34] Roderic S. Lakes. *Viscoelastic Solids (1998)*. CRC press, 2017. ISBN 1-351-35565-1.

[35] K.R. Shull. Contact Mechanics and the Adhesion of Soft Solids. *Mat. Sci. and Eng. R.*, 36:1–45, 2002.

[36] D. Ahn and K.R. Shull. JKR studies of Acrylic Elastomer Adhesion. *Macromolecules*, 29:4381–4390, 1996.

[37] G. Huang, B. Wang, and H. Lu. Measurements of viscoelastic functions of polymers in the frequency-domain using nanoindentation. *Mechanics of Time-Dependent Materials*, 8:345–364, 2004.

[38] Peter Eaton and Paul West. *Atomic Force Microscopy*. Oxford University Press, New York, 2010. ISBN 978-0-19-957045-4.

[39] Veeco Instruments Inc. PeakForce™ QNM™ User's Guide, 2010.

[40] Bruker Corporation. Dimension Icon User Guide, 2010.

[41] O. A. Bauchau and J. I. Craig. Euler-Bernoulli beam theory. In O. A. Bauchau and J. I. Craig, editors, *Structural Analysis*, pages 173–221. Springer Netherlands, Dordrecht, 2009. ISBN 978-90-481-2516-6. doi: 10.1007/978-90-481-2516-6_5.

[42] J.E. Sader, J.W.M. Chon, and P. Mulvaney. Calibration of rectangular atomic force microscope cantilever. *Review of Scientific Instruments*, 70:3967–3969, 1991.

[43] Kenneth Langstreth Johnson. *Contact Mechanics*. Cambridge university press, 1987. ISBN 0-521-34796-3.

[44] Heinrich Hertz. Ueber die Berührung fester elastischer Körper. *Journal für die reine und angewandte Mathematik*, 1882(92):156–171, 1882. ISSN 0075-4102.

[45] Stepan Prokof'evič Timošenko and James Norman Goodier. *Theory of Elasticity*. McGraw-Hill, 1951.

[46] A.J. Crosby, K.R. Shull, Y.Y. Lin, and C.Y. Hui. Rheological properties and adhesive failure of thin viscoelastic layers. *Journal of Rheology*, 46(1):273–294, 2002.

[47] W.C. Lin, K.R. Shull, C.Y. Hui, and Y.Y. Lin. Contact Measurement of Internal Fluid Flow within Poly(n-isopropyl acrylamide) Gels. *Journal of Chemical Physics*, 127:094906, 2007. doi: 10.1063/1.2771167.

[48] R.S. Bradley. LXXIX. The cohesive force between solid surfaces and the surface energy of solids. *The London, Edinburgh, and Dublin Philosophical Magazine and Journal of Science*, 13(86):853–862, April 1932. ISSN 1941-5982. doi: 10.1080/14786449209461990.

[49] Fang Zhong Li, C Fong Shih, and A Needleman. A comparison of methods for calculating energy release rates. *Engineering fracture mechanics*, 21(2):405–421, 1985. ISSN 0013-7944.

[50] D. Maugis. Extension of the Johnson-Kendall-Roberts Theory of the Elastic Contact of Spheres to Large Contact Radii. *Langmuir*, 11(2):679–682, February 1995. ISSN 0743-7463. doi: 10.1021/la00002a055.

[51] B.V. Derjaguin, V.M. Muller, and Y.P. Toporov. Effect of contact deformations on the adhesion of particles. *Journal of Colloid and Interface Science*, 53:314–326, 1975.

[52] K.L. Johnson, K. Kendall, and A.D. Roberts. Surface energy and the contact of elastic solids. *Proceedings of the Royal Society of London A*, 324:301–313, 1971.

[53] A. E. Lee. The role of elastic deformation in the adhesion of solids. *Journal of Colloid and Interface Science*, 64(3):577–579, 1978. ISSN 0021-9797. doi: 10.1016/0021-9797(78)90400-9.

[54] R.G Horn, J.N Israelachvili, and F Pribac. Measurement of the deformation and adhesion of solids in contact. *Journal of Colloid and Interface Science*, 115(2):480–492, February 1987. ISSN 0021-9797. doi: 10.1016/0021-9797(87)90065-8.

[55] Béla Pukánszky. Interfaces and interphases in multicomponent materials: Past, present, future. *European Polymer Journal*, 41(4):645–662, April 2005. ISSN 0014-3057. doi: 10.1016/j.eurpolymj.2004.10.035.

[56] Benjamin J. F. Bruet, Juha Song, Mary C. Boyce, and Christine Ortiz. Materials design principles of ancient fish armour. *Nature Materials*, 7(9):748–756, September 2008. ISSN 1476-4660. doi: 10.1038/nmat2231.

[57] Kuangshin Tai, Ming Dao, Subra Suresh, Ahmet Palazoglu, and Christine Ortiz. Nanoscale heterogeneity promotes energy dissipation in bone. *Nature Materials*, 6(6):454–462, June 2007. ISSN 1476-4660. doi: 10.1038/nmat1911.

[58] Ming Fang, Zhen Zhang, Jianfeng Li, Hongdong Zhang, Hongbin Lu, and Yuliang Yang. Constructing hierarchically structured interphases for strong and tough epoxy nanocomposites by amine-rich graphene surfaces. *J. Mater. Chem.*, 20(43):9635–9643, 2010. ISSN 0959-9428. doi: 10.1039/C0JM01620A.

[59] James C. Weaver, Garrett W. Milliron, Ali Miserez, Kenneth Evans-Lutterodt, Steven Herrera, Isaias Gallana, William J. Mershon, Brook Swanson, Pablo Zavattieri, Elaine DiMasi, and David Kisailus. The stomatopod dactyl club: A formidable damage-tolerant biological hammer. *Science*, 336(6086):1275–1280, 2012. ISSN 0036-8075. doi: 10.1126/science.1218764.

[60] Jozsef Karger-Kocsis, Haroon Mahmood, and Alessandro Pegoretti. Recent advances in fiber/matrix interphase engineering for polymer composites. *Progress in Materials Science*, July 2015. doi: 10.1016/j.pmatsci.2015.02.003.

[61] J Jancar, J.F. Douglas, F.W. Starr, S.K. Kumar, P. Cassagnau, A.J. Lesser, S.S. Sternstein, and M.J. Buehler. Current issues in research on structure–property relationships in polymer nanocomposites. *Polymer*, 51:3321–3343, 2010.

[62] D. Ciprari, K. Jacob, and R. Tannenbaum. Characterization of polymer nanocomposite interphase

and its impact on mechanical properties. *Macromolecules*, 39:6565–6573, 2006.

[63] G.C. Papanicolaou and P.S. Theocaris. Thermal properties and volume fraction of the boundary interphase in metal-filled epoxies. *Colloid and Polymer Science*, 257:239–246, 1979.

[64] S.D. Gardner, C.U. Pittman, and R.M. Hackett. Residual thermal stresses in filamentary polymer–matrix composites containing an elastomeric interphase. *Journal of Composite Materials*, 27: 830–860, 1993.

[65] F.T. Fisher and L.C. Brinson. Viscoelastic interphases in polymer–matrix composites: Theoretical models and finite-element analysis. *Composites Science and Technology*, 61:731–748, 2001.

[66] M. Munza, H. Sturma, E. Schulza, and G. Hinrichsen. The scanning force microscope as a tool for the detection of local mechanical properties within the interphase of fibre reinforced polymers. *Composites Part A: Applied Science and Manufacturing*, 29:1251–1259, 1998.

[67] Urška Šebenik, Andreja Zupančič-Valant, and Matjaž Krajnc. Investigation of rubber–rubber blends miscibility. *Polymer Engineering & Science*, 46(11):1649–1659, November 2006. ISSN 0032-3888. doi: 10.1002/pen.20645.

[68] Gregor Huber and Thomas A Vilgis. On the mechanism of hydrodynamic reinforcement in elastic composites. *Macromolecules*, 35(24):9204–9210, 2002. doi: doi.org/10.1021/ma0208887.

[69] Dina Gabriel, Alexander Karbach, Doris Drechsler, Jochen Gutmann, Karlheinz Graf, and Saeid Kheirandish. Bound rubber morphology and loss tangent properties of carbon-black-filled rubber compounds. *Colloid and Polymer Science*, 294(3):501–511, 2016.

[70] Supinda Watcharotone, Charles D. Wood, Robert Friedrich, Xinqi Chen, Rui Qiao, Karl Putz, and L. Catherine Brinson. Interfacial and Substrate Effects on Local Elastic Properties of Polymers Using Coupled Experiments and Modeling of Nanoindentation. *Advanced Engineering Materials*, 13(5):400–404, 2011. ISSN 1527-2648. doi: 10.1002/adem.201000277.

[71] G. Constantinides, K.S. Ravi Chandran, F.-J. Ulm, and K.J. Van Vliet. Grid indentation analysis of composite microstructure and mechanics: Principles and validation. *Materials Science and Engineering: A*, 430(1):189–202, August 2006. ISSN 0921-5093. doi: 10.1016/j.msea.2006.05.125.

[72] Perla Rittigstein, Rodney D. Priestley, Linda J. Broadbelt, and John M. Torkelson. Model polymer nanocomposites provide an understanding of confinement effects in real nanocomposites. *Nature Materials*, 6(4):278–282, April 2007. ISSN 1476-4660. doi: 10.1038/nmat1870.

[73] J. A. Forrest, K. Dalnoki-Veress, and J. R. Dutcher. Interface and chain confinement effects on the glass transition temperature of thin polymer films. *Phys. Rev. E*, 56(5):5705–5716, November 1997.

[74] Christopher J. Ellison and John M. Torkelson. The distribution of glass-transition temperatures in nanoscopically confined glass formers. *Nature Materials*, 2:695, September 2003.

[75] X. Cheng, K.W. Putz, C.D. Wood, and L.C. Brinson. Characterization of local elastic modulus in confined polymer films via AFM indentation. *Macromolecular Rapid Communications*, 36:391–397, 2015.

[76] M. Zhang, S Askar, J.M. Torkelson, and L.C. Brinson. Stiffness gradients in glassy polymer model nanocomposites: Comparisons of quantitative characterization by fluorescence spectroscopy and atomic force microscopy. *Macromolecules*, 50:5447–5458, 2017.

[77] R. Garcia and R. Proksch. Nanomechanical mapping of soft matter by bimodal force microscopy. *European Polymer Journal*, (49):1897–1906, 2013.

[78] R. Proksch, M. Kocun, D. Hurley, M. Viani, A. Labuda, W. Meinhold, and J. Bemis. Practical Loss Tangent Imaging with Amplitude-Modulated Atomic Force Microscopy. *Journal of Applied Physics*, 119(134901):1–11, 2016.

[79] P.A. Yuya, D.C. Hurley, and J.A. Turner. Contact-Resonance Atomic Force Microscopy for Viscoelasticity. *Journal of Applied Physics*, 104(074916), 2008.

[80] M.R. VanLandingham, N.K. Chang, P.L. Drzal, C.C. White, and S.H. Chang. Visceolastic characterization of polymers using instrumented indentation. I . Qausi-static testing. *Journal of Polymer Science: Part B: Polymer Physics*, 43:1794–1811, 2005.

[81] L. Han, E.H. Frank, J.J. Green, H.Y. Lee, H.H.K. Hung, A.J. Grodzinsky, and C. Ortiz. Time-dependent nanomechanics of cartilage. *Biophysical Journal*, 100:1846–1854, 2011.

[82] T. Igarashi, S. Fujinami, T. Nishi, N. Asao, and K. Nakajima. Nanorheological mapping of rubbers by atomic force microscopy. *Macromolecules*, (46):1916–1922, 2013.

[83] H.K. Nguyen, M. Ito, S. Fujinami, and K. Nakajima. Viscoelasticity of Inhomogeneous Polymers Characterized by Loss Tangent Measurements Using Atomic Force Microscopy. *Macromolecules*, 47: 7971–7977, 2014.

[84] M. Dokukin and I. Sokolov. High-resolution high-speed dynamic mechanical spectroscopy of cells and other soft materials with the help of atomic force microscopy. *Scientific Reports*, 5(1):12630, July 2015. ISSN 2045-2322. doi: 10.1038/srep12630.

[85] Hadi Tavakoli Nia, Iman S Bozchalooi, Yang Li, Lin Han, Han-Hwa Hung, Eliot Frank, Kamal Youcef-Toumi, Christine Ortiz, and Alan Grodzinsky. High-bandwidth AFM-based rheology reveals that cartilage is most sensitive to high loading rates at early stages of impairment. *Biophys J*, 104(7):

1529–1537, April 2013. ISSN 1542-0086. doi: 10.1016/j.bpj.2013.02.048.

[86] Liansheng Zhang, Qian Long, Yongbin Liu, Jie Zhang, and Zhihua Feng. Correlation-steered scanning for scanning probe microscopes to overcome thermal drift for ultra-long time scanning. *Ultramicroscopy*, 166:16–26, July 2016. ISSN 0304-3991. doi: 10.1016/j.ultramic.2016.03.013.

[87] B. Mokaberi and A. A. G. Requicha. Drift compensation for automatic nanomanipulation with scanning probe microscopes. *IEEE Transactions on Automation Science and Engineering*, 3(3):199–207, July 2006. ISSN 1558-3783. doi: 10.1109/TASE.2006.875534.

[88] A. Serghei, M. Tress, and F. Kremer. Confinement Effects on the Relaxation Time Distribution of the Dynamic Glass Transition in Ultrathin Polymer Films. *Macromolecules*, 39(26):9385–9387, December 2006. ISSN 0024-9297. doi: 10.1021/ma061290s.

[89] D. Ahn and K.R. Shull. Effects of Substrate Modification on the Interfacial Adhesion of Acrylic Elastomers as Measured by the JKR Technique. *Langmuir*, 14(13):3646–3654, 1998.

[90] D. Ahn and K.R. Shull. Effects of Methylation and Neutralization of Carboxylated Poly(n-butyl acrylate) on the Interfacial and Bulk Contributions to Adhesion. *Langmuir*, 14(13):3637–3645, 1998.

[91] D. Tabor. *Hardness of Metals*. Clarendon Press, Oxford, U.K., 1951.

[92] I. V. Yannas. Nonlinear viscoelasticity of solid polymers (in uniaxial tensile loading). *Journal of Polymer Science: Macromolecular Reviews*, 9(1):163–190, January 1974. ISSN 0076-2083. doi: 10.1002/pol.1974.230090104.

[93] Georges Smolyakov, Cécile Formosa-Dague, Childérick Séverac, RE Duval, and Etienne Dague. High speed indentation measures by FV, QI and QNM introduce a new understanding of bionanomechanical experiments. *Micron*, 85:8–14, 2016. ISSN 0968-4328.

[94] M. J. Higgins, R. Proksch, J. E. Sader, M. Polcik, S. Mc Endoo, J. P. Cleveland, and S. P. Jarvis. Noninvasive determination of optical lever sensitivity in atomic force microscopy. *Review of Scientific Instruments*, 77(1):013701, January 2006. ISSN 0034-6748. doi: 10.1063/1.2162455.

[95] Roger Proksch, Roger C Callahan, Frank Stetter, Ted Limpoco, Sophia Hohlbach, Jason Bemis, and Jason Cleveland. Automated atomic force microscope and the operation thereof, July 2016.

[96] Marnix van Gurp and Jo Palmen. Time-temperature superposition for polymeric blends. *Rheology Bulletin*, 67:5–8, 1998.

[97] J. E. Jakes, C. R. Frihart, J. F. Beecher, R. J. Moon, P. J. Resto, Z. H. Melgarejo, O. M. Suarez, H. Baumgart, A. A. Elmustafa, and D. S. Stone. Nanoindentation near the edge. *Journal of Materials Research*, 24(3):1016–1031, 2009.

[98] Ken Nakajima, Makiko Ito, Hung Kim Nguyen, and Xiaobin Liang. Nanomechanics of the Rubber-Filler Interface. *Rubber Chemistry and Technology*, 90(2):272–284, June 2017. ISSN 0035-9475. doi: 10.5254/rct.17.82642.

[99] Y Fukahori, AA Hon, V Jha, and JJC Busfield. Modified guth–gold equation for carbon black–filled rubbers. *Rubber Chemistry and Technology*, 86(2):218–232, 2013. doi: doi.org/10.5254/rct.13.87995.

[100] Shao-Yun Fu, Xi-Qiao Feng, Bernd Lauke, and Yiu-Wing Mai. Effects of particle size, particle/matrix interface adhesion and particle loading on mechanical properties of particulate–polymer composites. *Composites Part B: Engineering*, 39(6):933–961, 2008. doi: doi.org/10.1016/j.compositesb.2008.01.002.

[101] Meng-Jiao Wang. Effect of polymer-filler and filler-filler interactions on dynamic properties of filled vulcanizates. *Rubber chemistry and technology*, 71(3):520–589, 1998. doi: doi.org/10.5254/1.3538492.

[102] JB Donnet. Nano and microcomposites of polymers elastomers and their reinforcement. *Composites science and technology*, 63(8):1085–1088, 2003. doi: doi.org/10.1016/S0266-3538(03)00028-9.

[103] Yoshihide Fukahori. New progress in the theory and model of carbon black reinforcement of elastomers. *Journal of applied polymer science*, 95(1):60–67, 2005. doi: doi.org/10.1002/app.20802.

[104] Jean L Leblanc. Rubber–filler interactions and rheological properties in filled compounds. *Progress in polymer science*, 27(4):627–687, 2002. doi: doi.org/10.1016/S0079-6700(01)00040-5.

[105] Rui Qiao and L Catherine Brinson. Simulation of interphase percolation and gradients in polymer nanocomposites. *Composites Science and Technology*, 69(3-4):491–499, 2009. doi: doi.org/10.1016/j.compscitech.2008.11.022.

[106] Rui Qiao, Hua Deng, Karl W Putz, and L Catherine Brinson. Effect of particle agglomeration and interphase on the glass transition temperature of polymer nanocomposites. *Journal of Polymer Science Part B: Polymer Physics*, 49(10):740–748, 2011. doi: doi.org/10.1002/polb.22236.

[107] GM Odegard, TC Clancy, and TS Gates. Modeling of the mechanical properties of nanoparticle/polymer composites. *Polymer*, 46(2):553–562, 2005. doi: doi.org/10.1016/j.polymer.2004.11.022.

[108] G. Binnig, C. F. Quate, and Ch. Gerber. Atomic Force Microscope. *Phys. Rev. Lett.*, 56(9):930–933, March 1986. doi: 10.1103/PhysRevLett.56.930.

[109] Min Zhang, Yang Li, Pavan V. Kolluru, and L. Catherine Brinson. Determination of Mechanical Properties of Polymer Interphase Using Combined Atomic Force Microscope (AFM) Experiments and Finite Element Simulations. *Macromolecules*, 51(20):8229–8240, October 2018. ISSN 0024-9297. doi: 10.1021/acs.macromol.8b01427.

[110] Irwin Pliskin and Noboru Tokita. Bound rubber in elastomers: Analysis of elastomer-filler interaction

and its effect on viscosity and modulus of composite systems. *Journal of Applied Polymer Science*, 16 (2):473–492, 1972. doi: doi.org/10.1002/app.1972.070160217.

[111] Yasuto Hoshikawa, Baigang An, Susumu Kashihara, Takafumi Ishii, Mariko Ando, Syuji Fujisawa, Koutarou Hayakawa, Satoshi Hamatani, Hiroshi Yamada, and Takashi Kyotani. Analysis of the interaction between rubber polymer and carbon black surfaces by efficient removal of physisorbed polymer from carbon-rubber composites. *Carbon*, 99:148–156, 2016. doi: doi.org/10.1016/j.carbon.2015.12.003.

[112] He Zhao, Xiaolin Li, Yichi Zhang, Linda S Schadler, Wei Chen, and L Catherine Brinson. Perspective: NanoMine: A material genome approach for polymer nanocomposites analysis and design. *APL Materials*, 4(5):053204, 2016. doi: doi.org/10.1063/1.4943679.

[113] Meng Qu, Fei Deng, Salmon M. Kalkhoran, Andrew Gouldstone, Agathe Robisson, and Krystyn J. Van Vliet. Nanoscale visualization and multiscale mechanical implications of bound rubber interphases in rubber–carbon black nanocomposites. *Soft Matter*, 7(3):1066–1077, 2011. doi: 10.1039/C0SM00645A.

[114] Hung K Nguyen, Xiaobin Liang, Makiko Ito, and Ken Nakajima. Direct Mapping of Nanoscale Viscoelastic Dynamics at Nanofiller/Polymer Interfaces. *Macromolecules*, 51(15):6085–6091, 2018.

[115] L Tadiello, M D'Arienzo, B Di Credico, T Hanel, L Matejka, M Mauri, F Morazzoni, R Simonutti, M Spirkova, and R Scotti. The filler–rubber interface in styrene butadiene nanocomposites with anisotropic silica particles: Morphology and dynamic properties. *Soft Matter*, 11(20):4022–4033, 2015. doi: 10.1039/C5SM00536A.

[116] Julien Berriot, Hélène Montes, François Lequeux, Didier Long, and Paul Sotta. Evidence for the shift of the glass transition near the particles in silica-filled elastomers. *Macromolecules*, 35(26):9756–9762, 2002. doi: doi.org/10.1021/ma0212700.

[117] Aurélie Papon, Kay Saalwächter, Kerstin Schäler, Laurent Guy, François Lequeux, and Hélène Montes. Low-field NMR investigations of nanocomposites: Polymer dynamics and network effects. *Macromolecules*, 44(4):913–922, 2011. doi: doi.org/10.1021/ma102486x.

[118] Sung-Seen Choi and Eunah Ko. Novel test method to estimate bound rubber formation of silica-filled solution styrene-butadiene rubber compounds. *Polymer Testing*, 40:170–177, 2014. doi: doi.org/10.1016/j.polymertesting.2014.09.003.

[119] Shiwang Cheng, Bobby Carroll, Vera Bocharova, Jan-Michael Carrillo, Bobby G Sumpter, and Alexei P Sokolov. Focus: Structure and dynamics of the interfacial layer in polymer nanocomposites with attractive interactions. *The Journal of chemical physics*, 146(20):203201, 2017. doi: doi.org/10.1063/

1.4978504.

[120] J Berriot, H Montes, F Lequeux, D Long, and P Sotta. Gradient of glass transition temperature in filled elastomers. *EPL (Europhysics Letters)*, 64(1):50, 2003. doi: doi.org/10.1209/epl/i2003-00124-7.

[121] Joseph E Jakes, Charles R Frihart, James F Beecher, Robert J Moon, and DS Stone. Experimental method to account for structural compliance in nanoindentation measurements. *Journal of Materials Research*, 23(4):1113–1127, 2008.

[122] Hung K Nguyen, So Fujinami, and Ken Nakajima. Elastic modulus of ultrathin polymer films characterized by atomic force microscopy: The role of probe radius. *Polymer*, 87:114–122, 2016. doi: doi.org/10.1016/j.polymer.2016.01.080.

[123] Jake Song, Ridvan Kahraman, David W. Collinson, Wenjie Xia, L. Catherine Brinson, and Sinan Keten. Temperature Effects on the Nanoindentation Characterization of Stiffness Gradients in Confined Polymers. *Soft Matter*, (15):359–370, 2019.

[124] Le Li, Lucas M. Encarnacao, and Keith A. Brown. Polymer nanomechanics: Separating the size effect from the substrate effect in nanoindentation. *Applied Physics Letters*, 110(4):043105, 2017.

[125] W.F. Heinz, Emad A-Hassn, J.H. Hoh, and F.M. Serry. Applications of Force Volume Imaging with Atomic Force Microscopes, 2010.

[126] Charles A. Clifford and Martin P. Seah. Quantification issues in the identification of nanoscale regions of homopolymers using modulus measurement via AFM nanoindentation. *Applied Surface Science*, 252(5):1915–1933, December 2005. ISSN 0169-4332. doi: 10.1016/j.apsusc.2005.08.090.

[127] Maxim E Dokukin and Igor Sokolov. Quantitative mapping of the elastic modulus of soft materials with HarmoniX and PeakForce QNM AFM modes. *Langmuir*, 28(46):16060–16071, 2012.

[128] E.G. Herbert, W.C. Oliver, and G.M. Pharr. Nanoindentation and the dynamic characterization of viscoelastic solids. *Journal of Physics D: Applied Physics*, 41:074021, 2008.

[129] ASTM D1765-17, Standard Classification System for Carbon Blacks Used in Rubber Products. Technical report, ASTM International, West Conshohocken, PA, 2017.

[130] Ruth N. Havemeyer. Freezing point curve of dimethyl sulfoxide—water solutions. *Journal of Pharmaceutical Sciences*, 55(8):851–853, August 1966. ISSN 0022-3549. doi: 10.1002/jps.2600550822.

[131] Guo-Hua Chen, Da-Jun Wu, Wen-Gui Weng, Bin He, and Wen-li Yan. Preparation of polystyrene–graphite conducting nanocomposites via intercalation polymerization. *Polymer International*, 50(9):980–985, 2001.

[132] Zanib Anwar, Ayesha Kausar, and Bakhtiar Muhammad. Polymer and Graphite-Derived Nanofiller

Composite: An Overview of Functional Applications. *Polymer-Plastics Technology and Engineering*, 55(16):1765–1784, November 2016. ISSN 0360-2559. doi: 10.1080/03602559.2016.1163598.

[133] Suneel Kumar Srivastava and Yogendra Kumar Mishra. Nanocarbon Reinforced Rubber Nanocomposites: Detailed Insights about Mechanical, Dynamical Mechanical Properties, Payne, and Mullin Effects. *Nanomaterials (Basel, Switzerland)*, 8(11):945, November 2018. ISSN 2079-4991. doi: 10.3390/nano8110945.

[134] Bryan Debelak and Khalid Lafdi. Use of exfoliated graphite filler to enhance polymer physical properties. *Carbon*, 45(9):1727–1734, August 2007. ISSN 0008-6223. doi: 10.1016/j.carbon.2007.05.010.

[135] K.J. Wahl, S.A.S. Asif, J.A. Greenwood, and K.L. Johnson. Oscillating adhesive contacts between micron-scale tips and compliant polymers. *Journal of Colloid and Interface Science*, 296:178–188, 2006.

[136] Dong Wang, So Fujinami, Ken Nakajima, and Toshio Nishi. True surface topography and nanomechanical mapping measurements on block copolymers with atomic force microscopy. *Macromolecules*, 43(7):3169–3172, 2010.

[137] Zhao Fei, Chen Long, Pan Qingyan, and Zhao Shugao. Influence of Carbon Black on Crosslink Density of Natural Rubber. *Journal of Macromolecular Science, Part B*, 51(6):1208–1217, 2012. doi: 10.1080/00222348.2012.664494.

[138] Jialiang Li, Zhiwei Li, Hongyu Wang, Zhanjun Wu, Zhi Wang, and Shichao Li. Liquid oxygen compatibility and cryogenic mechanical properties of a novel phosphorous/silicon containing epoxy-based hybrid. *RSC Adv.*, 6(93):91012–91023, 2016. doi: 10.1039/C6RA16641E.

[139] W.J. Cantwell and H Kausch. Fracture behaviour of epoxy resins. pages 144–174. January 1993. ISBN 978-94-010-5302-0. doi: 10.1007/978-94-011-2932-9_5.

[140] Emmett Crawford and Alan J. Lesser. The effect of network architecture on the thermal and mechanical behavior of epoxy resins. *Journal of Polymer Science Part B: Polymer Physics*, 36(8):1371–1382, 1998. doi: 10.1002/(SICI)1099-0488(199806)36:8<1371::AID-POLB11>3.0.CO;2-4.

[141] E. Grossman and I. Gouzman. Space environment effects on polymers in low earth orbit. *Nuclear Instruments and Methods in Physics Research Section B: Beam Interactions with Materials and Atoms*, 208:48–57, August 2003. ISSN 0168-583X. doi: 10.1016/S0168-583X(03)00640-2.

[142] J. Kulawik, Z. Szeglowski, T. Czapla, and J. P. Kulawik. Determination of glass transition temperature, thermal expansion and, shrinkage of epoxy resins. *Colloid and Polymer Science*, 267(11):970–975, November 1989. ISSN 1435-1536. doi: 10.1007/BF01410157.

[143] H. Thomas Hahn. Residual Stresses in Polymer Matrix Composite Laminates. *Journal of Composite Materials*, 10(4):266–278, October 1976. ISSN 0021-9983. doi: 10.1177/002199837601000401.

[144] Kiyoshi Mizutani and Minoru Yoshii. Temperature dependence of fracture toughness of epoxy resins cured with diamines. *Journal of Materials Science*, 23(10):3501–3504, October 1988. ISSN 1573-4803. doi: 10.1007/BF00540486.

[145] Zhao Bo, Li Jing-wei, Li Shu-guang, Lu Yi-hui, and Hao Ju-tao. Relationship between fracture toughness and temperature in epoxy coatings. *Polimery*, 60(4):258–263, 2015.

[146] Salim Yamini and Robert J. Young. Crack propagation in and fractography of epoxy resins. *Journal of Materials Science*, 14(7):1609–1618, July 1979. ISSN 1573-4803. doi: 10.1007/BF00569280.

[147] J. M. Scott, G. M. Wells, and D. C. Phillips. Low temperature crack propagation in an epoxide resin. *Journal of Materials Science*, 15(6):1436–1448, June 1980. ISSN 1573-4803. doi: 10.1007/BF00752123.

[148] R.A Gledhill, A.J Kinloch, S Yamini, and R.J Young. Relationship between mechanical properties of and crack progogation in epoxy resin adhesives. *Polymer*, 19(5):574–582, May 1978. ISSN 0032-3861. doi: 10.1016/0032-3861(78)90285-9.

[149] S. Yamini and R.J. Young. Stability of crack propagation in epoxy resins. *Polymer*, 18(10):1075–1080, October 1977. ISSN 0032-3861. doi: 10.1016/0032-3861(77)90016-7.

[150] Salim Yamini and Robert J. Young. The mechanical properties of epoxy resins. *Journal of Materials Science*, 15(7):1823–1831, July 1980. ISSN 1573-4803. doi: 10.1007/BF00550603.

[151] G. Hartwig. Low-Temperature Properties of Epoxy Resins and Composites. In K. D. Timmerhaus, R. P. Reed, and A. F. Clark, editors, *Advances in Cryogenic Engineering*, pages 17–36. Springer US, Boston, MA, 1978. ISBN 978-1-4613-9853-0. doi: 10.1007/978-1-4613-9853-0_2.

[152] A. J. Kinloch and J. G. Williams. Crack blunting mechanisms in polymers. *Journal of Materials Science*, 15(4):987–996, April 1980. ISSN 1573-4803. doi: 10.1007/BF00552112.

[153] R. Rahul and R. Kitey. Effect of cross-linking on dynamic mechanical and fracture behavior of epoxy variants. *Composites Part B: Engineering*, 85:336–342, February 2016. ISSN 1359-8368. doi: 10.1016/j.compositesb.2015.09.017.

[154] G Levita, S De Petris, A Marchetti, and Andrea Lazzeri. Crosslink density and fracture toughness of epoxy resins. *Journal of materials science*, 26(9):2348–2352, 1991. ISSN 0022-2461.

[155] Richard E Robertson, Viorica E Mindroiu, and Mo-Fung Cheung. Fracture in epoxy matrix resins. *Composites Science and Technology*, 22(3):197–207, January 1985. ISSN 0266-3538. doi: 10.1016/0266-3538(85)90033-8.

[156] D. C. Phillips, J. M. Scott, and M. Jones. Crack propagation in an amine-cured epoxide resin. *Journal of Materials Science*, 13(2):311–322, February 1978. ISSN 1573-4803. doi: 10.1007/BF00647775.

[157] U. M. Vakil and G. C. Martin. Yield and fracture behaviour of cross-linked epoxies. *Journal of materials science*, 28(16):4442–4450, 1993.

[158] S. C. Kunz and P. W. R. Beaumont. Low-temperature behaviour of epoxy-rubber particulate composites. *Journal of Materials Science*, 16(11):3141–3152, November 1981. ISSN 1573-4803. doi: 10.1007/BF00540323.

[159] Erich D. Bain, Daniel B. Knorr, Adam D. Richardson, Kevin A. Masser, Jian Yu, and Joseph L. Lenhart. Failure processes governing high-rate impact resistance of epoxy resins filled with core–shell rubber nanoparticles. *Journal of Materials Science*, 51(5):2347–2370, March 2016. ISSN 0022-2461, 1573-4803. doi: 10.1007/s10853-015-9544-5.

[160] Hanieh Kargarzadeh. Mechanical Properties of Epoxy/Rubber Blends. In *Handbook of Epoxy Blends*. January 2016. doi: 10.1007/978-3-319-40043-3_11.

[161] A.J. Kinloch, S.J. Shaw, D.A. Tod, and D.L. Hunston. Deformation and fracture behaviour of a rubber-toughened epoxy: 1. Microstructure and fracture studies. *Polymer*, 24(10):1341–1354, October 1983. ISSN 0032-3861. doi: 10.1016/0032-3861(83)90070-8.

[162] A. F. Yee and R. A. Pearson. Toughening mechanisms in elastomer-modified epoxies. *Journal of Materials Science*, 21(7):2462–2474, July 1986. ISSN 1573-4803. doi: 10.1007/BF01114293.

[163] Kevin A. Masser, Daniel B. Knorr Jr., Jian H. Yu, Mark D. Hindenlang, and Joseph L. Lenhart. Dynamic heterogeneity in epoxy networks for protection applications. *Journal of Applied Polymer Science*, 133(45), December 2016. ISSN 0021-8995. doi: 10.1002/app.43566.

[164] Kevin A. Masser, Daniel B. Knorr, Mark D. Hindenlang, Jian H. Yu, Adam D. Richardson, Kenneth E. Strawhecker, Frederick L. Beyer, and Joseph L. Lenhart. Relating structure and chain dynamics to ballistic performance in transparent epoxy networks exhibiting nanometer scale heterogeneity. *Polymer*, 58:96–106, February 2015. ISSN 0032-3861. doi: 10.1016/j.polymer.2014.12.027.

[165] Kevin A Masser, Tyler R Long, Jian H Yu, Daniel B Knorr, Mark D Hindenlang, Terrence Taylor, Doug Harris, and Joseph L Lenhart. The temperature-dependent ballistic performance and the ductile-to-brittle transition in polymer networks. *Journal of Polymer Science Part B: Polymer Physics*, 57(9): 511–523, 2019. ISSN 0887-6266. doi: 10.1002/polb.24807.

[166] Daniel B. Knorr, Jian H. Yu, Adam D. Richardson, Mark D. Hindenlang, Ian M. McAninch, John J. La Scala, and Joseph L. Lenhart. Glass transition dependence of ultrahigh strain rate response in

amine cured epoxy resins. *Polymer*, 53(25):5917–5923, November 2012. ISSN 0032-3861. doi: 10.1016/j.polymer.2012.09.058.

[167] ASTM D5045-14: Standard Test Methods for Plane-Strain Fracture Toughness and Strain Energy Release Rate of Plastic Materials. 2014. doi: 10.1520/D5045-14.

[168] R. J. C. Carbas, E. A. S. Marques, L. F. M. da Silva, and A. M. Lopes. Effect of Cure Temperature on the Glass Transition Temperature and Mechanical Properties of Epoxy Adhesives. *The Journal of Adhesion*, 90(1):104–119, January 2014. ISSN 0021-8464. doi: 10.1080/00218464.2013.779559.

[169] Lawrence E Nielsen. Cross-linking–effect on physical properties of polymers. *Journal of Macromolecular Science, Part C*, 3(1):69–103, 1969. ISSN 1532-1797.

[170] A Leyland and A Matthews. On the significance of the H/E ratio in wear control: A nanocomposite coating approach to optimised tribological behaviour. *Wear*, 246(1):1–11, November 2000. ISSN 0043-1648. doi: 10.1016/S0043-1648(00)00488-9.

[171] J Malzbender, G De With, and JMJ Den Toonder. Elastic modulus, indentation pressure and fracture toughness of hybrid coatings on glass. *Thin Solid Films*, 366(1-2):139–149, 2000. ISSN 0040-6090.

[172] David Labonte, Anne-Kristin Lenz, and Michelle L. Oyen. On the relationship between indentation hardness and modulus, and the damage resistance of biological materials. *Acta Biomaterialia*, 57:373–383, July 2017. ISSN 1742-7061. doi: 10.1016/j.actbio.2017.05.034.

[173] Ella Amitay-Sadovsky and H. Daniel Wagner. Evaluation of Young's modulus of polymers from Knoop microindentation tests. *Polymer*, 39(11):2387–2390, January 1998. ISSN 0032-3861. doi: 10.1016/S0032-3861(97)00550-8.

[174] Mahmoud M Reda Taha. *International Congress on Polymers in Concrete (ICPIC 2018): Polymers for Resilient and Sustainable Concrete Infrastructure*. Springer, 2018. ISBN 3-319-78175-8.

[175] M. Sakai. The Meyer hardness: A measure for plasticity? *Journal of Materials Research*, 14(9):3630–3639, 1999. ISSN 0884-2914. doi: 10.1557/JMR.1999.0490.

[176] József Karger-Kocsis and Sándor Kéki. Review of progress in shape memory epoxies and their composites. *Polymers*, 10(1):34, 2018.

[177] K.S. Santhosh Kumar, R. Biju, and C.P. Reghunadhan Nair. Progress in shape memory epoxy resins. *Reactive and Functional Polymers*, 73(2):421–430, February 2013. ISSN 1381-5148. doi: 10.1016/j.reactfunctpolym.2012.06.009.

[178] J.T. Fulcher, Y.C. Lu, G.P. Tandon, and D.C. Foster. Thermomechanical characterization of shape memory polymers using high temperature nanoindentation. *Polymer Testing*, 29(5):544–552, August

2010. ISSN 0142-9418. doi: 10.1016/j.polymertesting.2010.02.001.

[179] Adonias Ribeiro Franco Jr, Giuseppe Pintaúde, Amilton Sinatora, Carlos Eduardo Pinedo, and André Paulo Tschiptschin. The use of a Vickers indenter in depth sensing indentation for measuring elastic modulus and Vickers hardness. *Materials Research*, 7(3):483–491, 2004. ISSN 1516-1439.

[180] T. Koch and S. Seidler. Correlations Between Indentation Hardness and Yield Stress in Thermoplastic Polymers. *Strain*, 45(1):26–33, 2009. doi: 10.1111/j.1475-1305.2008.00468.x.

[181] Jessica A. Schroeder. Fracture toughness and molecular structure of unfilled epoxy adhesives. *Journal of Materials Science*, 23(9):3073–3082, September 1988. ISSN 1573-4803. doi: 10.1007/BF00551276.

[182] MD Hayes, DB Edwards, and AR Shah. Fractography Basics. *Fractography in Failure Analysis of Polymers*, pages 48–92, 2015.

[183] C. M. Roland. Interpenetrating Polymer Networks (IPN): Structure and Mechanical Behavior. In Shiro Kobayashi and Klaus Müllen, editors, *Encyclopedia of Polymeric Nanomaterials*, pages 1–9. Springer Berlin Heidelberg, Berlin, Heidelberg, 2013. ISBN 978-3-642-36199-9. doi: 10.1007/978-3-642-36199-9_91-1.

[184] B. Chen, D. Gui, and J. Liu. Improving the toughness and thermal properties of epoxy resin using for electronic packaging by interpenetrating polymer network. In *2009 International Conference on Electronic Packaging Technology & High Density Packaging*, pages 749–752, 10. doi: 10.1109/ICEPT.2009.5270650.

[185] Leslie H Sperling. Interpenetrating polymer networks: An overview. ACS Publications, 1994.

[186] Leslie Howard Sperling. *Interpenetrating Polymer Networks and Related Materials*. Springer Science & Business Media, 2012. ISBN 1-4684-3830-1.

[187] J. J. Fay, C. J. Murphy, D. A. Thomas, and L. H. Sperling. Effect of morphology, crosslink density, and miscibility on interpenetrating polymer network damping effectiveness. *Polymer Engineering & Science*, 31(24):1731–1741, December 1991. ISSN 0032-3888. doi: 10.1002/pen.760312407.

[188] Fábio L Barcia, Alex S Sirqueira, Caio M Paranhos, and Bluma G Soares. Rheological, mechanical, and morphological studies of epoxy/poly (methyl methacrylate) semi-interpenetrating polymer networks. *Journal of applied polymer science*, 106(6):3808–3815, 2007. ISSN 0021-8995.

[189] Jinrong Jia, Yan Qin, and Zhixiong Huang. Damping and mechanical properties of poly (methyl methacrylate)/epoxy interpenetrating polymer networks. *Journal of Chemical and Pharmaceutical Research*, 5(10):91–96, 2013.

[190] B Das, D Chakraborty, AK Hajra, and S Sinha. Epoxy/poly (methyl methacrylate) interpenetrat-

ing polymer networks—morphology, mechanical and thermal properties. *Journal of applied polymer science*, 53(11):1491–1496, 1994. ISSN 0021-8995.

[191] EM Woo and Min N Wu. Blends of a diglycidylether epoxy with bisphenol-A polycarbonate or poly (methyl methacrylate): Cases of miscibility with or without specific interactions. *Polymer*, 37(12): 2485–2492, 1996. ISSN 0032-3861.

[192] Matthew Jackson, Mukul Kaushik, Sergei Nazarenko, Steve Ward, Rob Maskell, and Jeffrey Wiggins. Effect of free volume hole-size on fluid ingress of glassy epoxy networks. *Polymer*, 52(20):4528–4535, September 2011. ISSN 0032-3861. doi: 10.1016/j.polymer.2011.07.042.

[193] Mitsukazu Ochi, Takashi Shiba, Hidenao Takeuchi, Makoto Yoshizumi, and Masaki Shimbo. Effect of the introduction of methoxy branches on low-temperature relaxations and fracture toughness of epoxide resins. *Polymer*, 30(6):1079–1084, June 1989. ISSN 0032-3861. doi: 10.1016/0032-3861(89)90084-0.

[194] Jung H. Han. Chapter 9 - Edible Films and Coatings: A Review. In Jung H. Han, editor, *Innovations in Food Packaging (Second Edition)*, pages 213–255. Academic Press, San Diego, January 2014. ISBN 978-0-12-394601-0. doi: 10.1016/B978-0-12-394601-0.00009-6.

[195] Karin Krogars, Osmo Antikainen, Jyrki Heinämäki, Niklas Laitinen, and Jouko Yliruusi. Tablet film-coating with amylose-rich maize starch. *European Journal of Pharmaceutical Sciences*, 17(1):23–30, October 2002. ISSN 0928-0987. doi: 10.1016/S0928-0987(02)00134-3.

[196] P. Mallikarjunan, M.S. Chinnan, V.M. Balasubramaniam, and R.D. Phillips. Edible Coatings for Deep-fat Frying of Starchy Products. *LWT - Food Science and Technology*, 30(7):709–714, November 1997. ISSN 0023-6438. doi: 10.1006/fstl.1997.0263.

[197] Olivia V. López, Carlos J. Lecot, Noemí E. Zaritzky, and María A. García. Biodegradable packages development from starch based heat sealable films. *Journal of Food Engineering*, 105(2):254–263, July 2011. ISSN 0260-8774. doi: 10.1016/j.jfoodeng.2011.02.029.

[198] Cláudia Leites Luchese, Tania Garrido, Jordana Corralo Spada, Isabel Cristina Tessaro, and Koro de la Caba. Development and characterization of cassava starch films incorporated with blueberry pomace. *International Journal of Biological Macromolecules*, 106:834–839, January 2018. ISSN 0141-8130. doi: 10.1016/j.ijbiomac.2017.08.083.

[199] A. Cano, E. Fortunati, M. Cháfer, J.M. Kenny, A. Chiralt, and C. González-Martínez. Properties and ageing behaviour of pea starch films as affected by blend with poly(vinyl alcohol). *Food Hydrocolloids*, 48:84–93, June 2015. ISSN 0268-005X. doi: 10.1016/j.foodhyd.2015.01.008.

[200] Daniel Domene-López, Juan Carlos García-Quesada, Ignacio Martin-Gullon, and Mercedes G Mon-

talbán. Influence of Starch Composition and Molecular Weight on Physicochemical Properties of Biodegradable Films. *Polymers*, 11(7):1084, 2019.

[201] Cláudia Leites Luchese, Patrícia Benelli, Jordana Corralo Spada, and Isabel Cristina Tessaro. Impact of the starch source on the physicochemical properties and biodegradability of different starch-based films. *Journal of Applied Polymer Science*, 135(33):46564, September 2018. ISSN 0021-8995. doi: 10.1002/app.46564.

[202] Mervyn J. Miles, Victor J. Morris, Paul D. Orford, and Stephen G. Ring. The roles of amylose and amylopectin in the gelation and retrogradation of starch. *Carbohydrate Research*, 135(2):271–281, January 1985. ISSN 0008-6215. doi: 10.1016/S0008-6215(00)90778-X.

[203] Mervyn J. Miles, Victor J. Morris, and Stephen G. Ring. Gelation of amylose. *Carbohydrate Research*, 135(2):257–269, January 1985. ISSN 0008-6215. doi: 10.1016/S0008-6215(00)90777-8.

[204] Riku A. Talja, Harry Helén, Yrjö H. Roos, and Kirsi Jouppila. Effect of various polyols and polyol contents on physical and mechanical properties of potato starch-based films. *Carbohydrate Polymers*, 67(3):288–295, February 2007. ISSN 0144-8617. doi: 10.1016/j.carbpol.2006.05.019.

[205] Eric Bertoft. Understanding starch structure: Recent progress. *Agronomy*, 7(3):56, 2017.

[206] Päivi Myllärinen, Riitta Partanen, Jukka Seppälä, and Pirkko Forssell. Effect of glycerol on behaviour of amylose and amylopectin films. *Carbohydrate Polymers*, 50(4):355–361, 2002. ISSN 0144-8617.

[207] Jeroen J.G. van Soest and Johannes F.G. Vliegenthart. Crystallinity in starch plastics: Consequences for material properties. *Trends in Biotechnology*, 15(6):208–213, June 1997. ISSN 0167-7799. doi: 10.1016/S0167-7799(97)01021-4.

[208] D Lourdin, L Coignard, H Bizot, and P Colonna. Influence of equilibrium relative humidity and plasticizer concentration on the water content and glass transition of starch materials. *Polymer*, 38 (21):5401–5406, 1997. ISSN 0032-3861.

[209] P. D. Orford, R. Parker, S. G. Ring, and A. C. Smith. Effect of water as a diluent on the glass transition behaviour of malto-oligosaccharides, amylose and amylopectin. *International Journal of Biological Macromolecules*, 11(2):91–96, April 1989. ISSN 0141-8130. doi: 10.1016/0141-8130(89)90048-2.

[210] G. Colomines, P. Decaen, D. Lourdin, and E. Leroy. Biofriendly ionic liquids for starch plasticization: A screening approach. *RSC Adv.*, 6(93):90331–90337, 2016. doi: 10.1039/C6RA16573G.

[211] D. Domene-López, M.M. Guillén, I. Martin-Gullon, J.C. García-Quesada, and M.G. Montalbán. Study of the behavior of biodegradable starch/polyvinyl alcohol/rosin blends. *Carbohydrate Polymers*, 202: 299–305, December 2018. ISSN 01448617. doi: 10.1016/j.carbpol.2018.08.137.

[212] Noé J. Morales, Roberto Candal, Lucía Famá, Silvia Goyanes, and Gerardo H. Rubiolo. Improving the physical properties of starch using a new kind of water dispersible nano-hybrid reinforcement. *Carbohydrate Polymers*, 127:291–299, August 2015. ISSN 0144-8617. doi: 10.1016/j.carbpol.2015.03.071.

[213] D. Domene-López, J.J. Delgado-Marín, J.C. García-Quesada, I. Martín-Gullón, and M.G. Montalbán. Electroconductive starch/multi-walled carbon nanotube films plasticized by 1-ethyl-3-methylimidazolium acetate. *Carbohydrate Polymers*, 229:115545, February 2020. ISSN 0144-8617. doi: 10.1016/j.carbpol.2019.115545.

[214] Shajaratuldur Ismail, Nurlidia Mansor, Zahid Majeed, and Zakaria Man. Effect of water and [Emim][OAc] as plasticizer on gelatinization of starch. *Procedia engineering*, 148:524–529, 2016. ISSN 1877-7058.

[215] Fengwei Xie, Bernadine M. Flanagan, Ming Li, Parveen Sangwan, Rowan W. Truss, Peter J. Halley, Ekaterina V. Strounina, Andrew K. Whittaker, Michael J. Gidley, Katherine M. Dean, Julia L. Shamshina, Robin D. Rogers, and Tony McNally. Characteristics of starch-based films plasticised by glycerol and by the ionic liquid 1-ethyl-3-methylimidazolium acetate: A comparative study. *Carbohydrate Polymers*, 111:841–848, October 2014. ISSN 0144-8617. doi: 10.1016/j.carbpol.2014.05.058.

[216] Binjia Zhang, Fengwei Xie, Julia L. Shamshina, Robin D. Rogers, Tony McNally, David K. Wang, Peter J. Halley, Rowan W. Truss, Siming Zhao, and Ling Chen. Facile Preparation of Starch-Based Electroconductive Films with Ionic Liquid. *ACS Sustainable Chem. Eng.*, 5(6):5457–5467, June 2017. doi: 10.1021/acssuschemeng.7b00788.

[217] Eric Leroy, Paul Decaen, Pierre Jacquet, Gildas Coativy, Bruno Pontoire, Anne-Laure Reguerre, and Denis Lourdin. Deep eutectic solvents as functional additives for starch based plastics. *Green Chem.*, 14(11):3063–3066, 2012. ISSN 1463-9262. doi: 10.1039/C2GC36107H.

[218] Magdalena Zdanowicz, Tadeusz Spychaj, and Honorata Mąka. Imidazole-based deep eutectic solvents for starch dissolution and plasticization. *Carbohydrate Polymers*, 140:416–423, April 2016. ISSN 0144-8617. doi: 10.1016/j.carbpol.2015.12.036.

[219] L. S. Sciarini, A. Rolland-Sabaté, S. Guilois, P. Decaen, E. Leroy, and P. Le Bail. Understanding the destructuration of starch in water–ionic liquid mixtures. *Green Chem.*, 17(1):291–299, 2015. doi: 10.1039/C4GC01248H.

[220] E. Quijada-Maldonado, S. van der Boogaart, J.H. Lijbers, G.W. Meindersma, and A.B. de Haan. Experimental densities, dynamic viscosities and surface tensions of the ionic liquids series 1-ethyl-3-

methylimidazolium acetate and dicyanamide and their binary and ternary mixtures with water and ethanol at T=(298.15 to 343.15K). *The Journal of Chemical Thermodynamics*, 51:51–58, August 2012. ISSN 0021-9614. doi: 10.1016/j.jct.2012.02.027.

[221] Kaihua Guo, Yin Bi, Li Sun, Hang Su, and Lixia Hungpu. Experiment and Correlation of Vapor–Liquid Equilibrium of Aqueous Solutions of Hydrophilic Ionic Liquids: 1-Ethyl-3-methylimidazolium Acetate and 1-Hexyl-3-methylimidazolium Chloride. *J. Chem. Eng. Data*, 57(8):2243–2251, August 2012. ISSN 0021-9568. doi: 10.1021/je3001987.

[222] D. T. Bowron, C. D'Agostino, L. F. Gladden, C. Hardacre, J. D. Holbrey, M. C. Lagunas, J. McGregor, M. D. Mantle, C. L. Mullan, and T. G. A. Youngs. Structure and Dynamics of 1-Ethyl-3-methylimidazolium Acetate via Molecular Dynamics and Neutron Diffraction. *J. Phys. Chem. B*, 114 (23):7760–7768, June 2010. ISSN 1520-6106. doi: 10.1021/jp102180q.

[223] Martin Brehm, Henry Weber, Alfonso S. Pensado, Annegret Stark, and Barbara Kirchner. Proton transfer and polarity changes in ionic liquid–water mixtures: A perspective on hydrogen bonds from ab initio molecular dynamics at the example of 1-ethyl-3-methylimidazolium acetate–water mixtures—Part 1. *Phys. Chem. Chem. Phys.*, 14(15):5030–5044, 2012. ISSN 1463-9076. doi: 10.1039/C2CP23983C.

[224] Stephan H.D. Hulleman, Frank H.P. Janssen, and Herman Feil. The role of water during plasticization of native starches. *Polymer*, 39(10):2043–2048, May 1998. ISSN 0032-3861. doi: 10.1016/S0032-3861(97)00301-7.

[225] Suzana Mali, Laura Beatriz Karam, Luiz Pereira Ramos, and Maria Victória E. Grossmann. Relationships among the Composition and Physicochemical Properties of Starches with the Characteristics of Their Films. *J. Agric. Food Chem.*, 52(25):7720–7725, December 2004. ISSN 0021-8561. doi: 10.1021/jf049225+.

[226] Daniel Domene-López, José Javier Delgado-Marín, Ignacio Martin-Gullon, Juan Carlos García-Quesada, and Mercedes G Montalbán. Comparative study on properties of starch films obtained from potato, corn and wheat using 1-ethyl-3-methylimidazolium acetate as plasticizer. *International journal of biological macromolecules*, 135:845–854, 2019. ISSN 0141-8130.

[227] Susana Mali, Lyssasetsuko S Sakanaka, Fabio Yamashita, and MVE Grossmann. Water sorption and mechanical properties of cassava starch films and their relation to plasticizing effect. *Carbohydrate polymers*, 60(3):283–289, 2005. ISSN 0144-8617.

[228] Aji P Mathew and Alain Dufresne. Plasticized waxy maize starch: Effect of polyols and relative

humidity on material properties. *Biomacromolecules*, 3(5):1101–1108, 2002. ISSN 1525-7797.

[229] Jeannine Bonilla Lagos, Nívea M Vicentini, Rodolfo MC Dos Santos, Ana Mônica QB Bittante, and Paulo JA Sobral. Mechanical properties of cassava starch films as affected by different plasticizers and different relative humidity conditions. *Embrapa Gado de Leite-Artigo em periódico indexado (ALICE)*, 2015.

[230] D.R. Tapia-Blácido, P.J. do Amaral Sobral, and F.C. Menegalli. Effect of drying conditions and plasticizer type on some physical and mechanical properties of amaranth flour films. *LWT - Food Science and Technology*, 50(2):392–400, March 2013. ISSN 0023-6438. doi: 10.1016/j.lwt.2012.09.008.

[231] Javier Osés, Idoya Fernández-Pan, Mauricio Mendoza, and Juan I. Maté. Stability of the mechanical properties of edible films based on whey protein isolate during storage at different relative humidity. *Food Hydrocolloids*, 23(1):125–131, January 2009. ISSN 0268-005X. doi: 10.1016/j.foodhyd.2007.12.003.

[232] T Habig McHugh, R Avena-Bustillos, and JM Krochta. Hydrophilic edible films: Modified procedure for water vapor permeability and explanation of thickness effects. *Journal of food science*, 58(4):899–903, 1993. ISSN 0022-1147.

[233] P. Forssell, J. Mikkilä, T. Suortti, J. Seppälä, and K. Poutanen. Plasticization of Barley Starch with Glycerol and Water. *Journal of Macromolecular Science, Part A*, 33(5):703–715, May 1996. ISSN 1060-1325. doi: 10.1080/10601329608010888.

[234] CE Chinma, CC Ariahu, and JS Alakali. Effect of temperature and relative humidity on the water vapour permeability and mechanical properties of cassava starch and soy protein concentrate based edible films. *Journal of food science and technology*, 52(4):2380–2386, 2015. ISSN 0022-1155.

[235] Huafeng Tian, Jiaan Yan, A. Varada Rajulu, Aimin Xiang, and Xiaogang Luo. Fabrication and properties of polyvinyl alcohol/starch blend films: Effect of composition and humidity. *International Journal of Biological Macromolecules*, 96:518–523, March 2017. ISSN 0141-8130. doi: 10.1016/j.ijbiomac.2016.12.067.

[236] Jong-Yea Kim, Yoon-Gyoung Choi, Sae Ron Byul Kim, and Seung-Taik Lim. Humidity stability of tapioca starch–pullulan composite films. *Food Hydrocolloids*, 41:140–145, December 2014. ISSN 0268-005X. doi: 10.1016/j.foodhyd.2014.04.008.

[237] D. Lourdin, H. Bizot, and P. Colonna. "Antiplasticization" in starch-glycerol films? *Journal of Applied Polymer Science*, 63(8):1047–1053, February 1997. ISSN 0021-8995. doi: 10.1002/(SICI)1097-4628(19970222)63:8<1047::AID-APP11>3.0.CO;2-3.

[238] Yachuan Zhang. Retrogradation and Antiplasticization of Thermoplastic Starch. In Curtis Rempel ED1 - Adel Zaki El-Sonbati, editor, *Thermoplastic Elastomers*, page Ch. 7. IntechOpen, Rijeka, March 2012. doi: 10.5772/35848.

[239] Y.P. Chang, A. Abd Karim, and C.C. Seow. Interactive plasticizing–antiplasticizing effects of water and glycerol on the tensile properties of tapioca starch films. *Food Hydrocolloids*, 20(1):1–8, January 2006. ISSN 0268-005X. doi: 10.1016/j.foodhyd.2005.02.004.

[240] Asgar Farahnaky, Bahareh Saberi, and Mahsa Majzoobi. Effect of glycerol on physical and mechanical properties of wheat starch edible films. *Journal of Texture Studies*, 44(3):176–186, 2013.

[241] Siti H. Othman, Nurul R. A. Kechik, Ruzanna A. Shapi'i, Rosnita A. Talib, and Intan S. M. A. Tawakkal. Water Sorption and Mechanical Properties of Starch/Chitosan Nanoparticle Films. *Journal of Nanomaterials*, 2019:3843949, March 2019. ISSN 1687-4110. doi: 10.1155/2019/3843949.

[242] Kenneth A. Marx. Quartz Crystal Microbalance: A Useful Tool for Studying Thin Polymer Films and Complex Biomolecular Systems at the Solution-Surface Interface. *Biomacromolecules*, 4(5):1099–1120, September 2003. ISSN 1525-7797. doi: 10.1021/bm020116i.

[243] Diethelm Johannsmann. Viscoelastic analysis of organic thin films on quartz resonators. *Macromolecular Chemistry and Physics*, 200(3):501–516, March 1999. ISSN 1022-1352. doi: 10.1002/(SICI)1521-3935(19990301)200:3<501::AID-MACP501>3.0.CO;2-W.

[244] Diethelm Johannsmann. The quartz crystal microbalance in soft matter research. *Fundamentals and modeling. Switzerland: Springer International Publishing*, 2015.

[245] Garret C. DeNolf, Lauren F. Sturdy, and Kenneth R. Shull. High-Frequency Rheological Characterization of Homogeneous Polymer Films with the Quartz Crystal Microbalance. *Langmuir*, 30(32):9731–9740, August 2014. ISSN 0743-7463. doi: 10.1021/la502090a.

[246] Kenneth R. Shull, Meredith Taghon, and Qifeng Wang. Investigations of the high-frequency dynamic properties of polymeric systems with quartz crystal resonators. *Biointerphases*, QCM2020(1):021012, March 2020. ISSN 1934-8630. doi: 10.1116/1.5142762@bip.2020.QCM2020.issue-1.

[247] Akira Baba, Futao Kaneko, and Rigoberto C Advincula. Polyelectrolyte adsorption processes characterized in situ using the quartz crystal microbalance technique: Alternate adsorption properties in ultrathin polymer films. *Colloids and Surfaces A: physicochemical and engineering aspects*, 173(1-3):39–49, 2000. ISSN 0927-7757.

[248] Masaru Tanaka, Akira Mochizuki, Tadahiro Motomura, Kenichi Shimura, Makoto Onishi, and Yoshio Okahata. In situ studies on protein adsorption onto a poly(2-methoxyethylacrylate) surface by a

quartz crystal microbalance. *Colloids and Surfaces A: Physicochemical and Engineering Aspects*, 193 (1):145–152, December 2001. ISSN 0927-7757. doi: 10.1016/S0927-7757(01)00682-3.

[249] Jonas Carlstedt, Joanna Wojtasz, Peter Fyhr, and Vitaly Kocherbitov. Hydration and the phase diagram of acid hydrolyzed potato starch. *Carbohydrate Polymers*, 112:569–577, November 2014. ISSN 0144-8617. doi: 10.1016/j.carbpol.2014.06.037.

[250] Gwen E. AU - dePolo, Emily AU - Schafer, Kazi AU - Sadman, Jonathan AU - Rivnay, and Kenneth R. AU - Shull. Sample Preparation in Quartz Crystal Microbalance Measurements of Protein Adsorption and Polymer Mechanics. *JoVE*, (155):e60584, January 2020. ISSN 1940-087X. doi: 10.3791/60584.

[251] C. Joshua Yeh, Michael Hu, and Kenneth R. Shull. Oxygen Inhibition of Radical Polymerizations Investigated with the Rheometric Quartz Crystal Microbalance. *Macromolecules*, 51(15):5511–5518, August 2018. ISSN 0024-9297. doi: 10.1021/acs.macromol.8b00720.

[252] Robert D. Deegan, Olgica Bakajin, Todd F. Dupont, Greb Huber, Sidney R. Nagel, and Thomas A. Witten. Capillary flow as the cause of ring stains from dried liquid drops. *Nature*, 389(6653):827–829, October 1997. ISSN 1476-4687. doi: 10.1038/39827.

[253] Kazi Sadman, Clinton G. Wiener, R. A. Weiss, Christopher C. White, Kenneth R. Shull, and Bryan D. Vogt. Quantitative Rheometry of Thin Soft Materials Using the Quartz Crystal Microbalance with Dissipation. *Anal. Chem.*, 90(6):4079–4088, March 2018. ISSN 0003-2700. doi: 10.1021/acs.analchem.7b05423.

[254] Connor R. Bilchak, Yucheng Huang, Brian C. Benicewicz, Christopher J Durning, and Sanat K. Kumar. High-Frequency Mechanical Behavior of Pure Polymer-Grafted Nanoparticle Constructs. *ACS Macro Lett.*, 8(3):294–298, March 2019. doi: 10.1021/acsmacrolett.8b00981.

[255] R Jowitt and PJ Wagstaffe. *The Certification of the Water Content of Microcrystalline Cellulose (MCC) at 10 Water Activities*. EC, 1989.

[256] Paul Sotta, Pierre-Antoine Albouy, Mohammad Abou Taha, Didier R. Long, Pauline Grau, Caroline Fayolle, and Aurélie Papon. Nonentropic Reinforcement in Elastomer Nanocomposites. *Macromolecules*, 50(16):6314–6322, August 2017. ISSN 0024-9297. doi: 10.1021/acs.macromol.7b00698.

[257] C. G. Robertson, C. J. Lin, M. Rackaitis, and C. M. Roland. Influence of Particle Size and Polymer-Filler Coupling on Viscoelastic Glass Transition of Particle-Reinforced Polymers. *Macromolecules*, 41 (7):2727–2731, April 2008. ISSN 0024-9297. doi: 10.1021/ma7022364.

[258] A. Mujtaba, M. Keller, S. Ilisch, H.-J. Radusch, T. Thurn-Albrecht, K. Saalwächter, and M. Beiner. Mechanical Properties and Cross-Link Density of Styrene–Butadiene Model Composites Containing

Fillers with Bimodal Particle Size Distribution. *Macromolecules*, 45(16):6504–6515, August 2012. ISSN 0024-9297. doi: 10.1021/ma300925p.

[259] Fei Zhao, Weina Bi, and Shugao Zhao. Influence of Crosslink Density on Mechanical Properties of Natural Rubber Vulcanizates. *Journal of Macromolecular Science, Part B*, 50(7):1460–1469, July 2011. ISSN 0022-2348. doi: 10.1080/00222348.2010.507453.

[260] TY Lee, CA Guymon, E Sonny Jönsson, and Charles E Hoyle. The effect of monomer structure on oxygen inhibition of (meth) acrylates photopolymerization. *Polymer*, 45(18):6155–6162, 2004. ISSN 0032-3861.

[261] I Mondragon, PM Remiro, MD Martin, A Valea, M Franco, and V Bellenguer. Viscoelastic behaviour of epoxy resins modified with poly (methyl methacrylate). *Polymer international*, 47(2):152–158, 1998. ISSN 0959-8103.

[262] Joseph M. Antonucci, Diana N. Zeiger, Kathy Tang, Sheng Lin-Gibson, Bruce O. Fowler, and Nancy J. Lin. Synthesis and characterization of dimethacrylates containing quaternary ammonium functionalities for dental applications. *Dental Materials*, 28(2):219–228, February 2012. ISSN 0109-5641. doi: 10.1016/j.dental.2011.10.004.

[263] Jeremiah W. Woodcock, Richard J. Sheridan, Ryan Beams, Stephan J. Stranick, William F. Mitchell, L. Catherine Brinson, Vamshi Gudapati, David Hartman, Amol Vaidya, Jeffrey W. Gilman, and Gale A. Holmes. Damage sensing using a mechanophore crosslinked epoxy resin in single-fiber composites. *Composites Science and Technology*, 192:108074, May 2020. ISSN 0266-3538. doi: 10.1016/j.compscitech.2020.108074.

[264] Sha Wang, Xinwen Peng, Linxin Zhong, Shuangshuang Jing, Xuefei Cao, Fachuang Lu, and Runcang Sun. Choline chloride/urea as an effective plasticizer for production of cellulose films. *Carbohydrate Polymers*, 117:133–139, March 2015. ISSN 0144-8617. doi: 10.1016/j.carbpol.2014.08.113.

[265] Min Zhang. *Local Mechanical Properties Characterization of Soft Polymeric Material via Atomic Force Microscopy Nanoindentation and Finite Element Simulations.* Doctoral, Northwestern University, Evanston, Illinois, USA, September 2018.

[266] Bruker Corporation. Tip Qualification, 2011.

[267] Alicia Salazar and Yatish Patel. Influence of crack sharpness on the fracture toughness of epoxy resins. In *ICF13*, 2013.

Appendix A

Appendix

A.1 Tip Radius Estimation

Scanning electron microscopy (SEM) of the AFM tips, like the one shown in figure 2.5b, are typically the best method for estimating the AFM tip radius. From the image, a parabola or circle can be superimposed over the the tip radius in an image analysis software, like ImageJ, and a radius can be estimated from that. However, conducting an SEM of every single AFM tip is rather tedious, so a quicker way to estimate the tip radius can be done using a by performing a tapping mode scan on the surface of a Bruker Titanium standard roughness sample, or a "TipCheck" sample. This sample is very rough, and so has very fine features. The quality of the AFM tapping mode image and the sharpness of the features can be used to recreate the geometric profile of the AFM tip [39]. This has been shown to agree well with SEM images of the tip [265], but the procedure will be breifly discussed here.

Figure A.1a shows the AFM TappingMode topology map of the Bruker Titanium Roughness Sample for an AFM RTESPA tip with a small tip radius, where the rough features of the roughness sample are very sharp. On the other hand, use of the AFM tip can cause it to wear, chip, or break, resulting in an increase of the tip radius. This will cause the features of the roughness sample to be less sharp and less defined, as seen by the tapping image of the roughness sample using a worn tip in A.1b.

Using the height image, the Bruker Nanoscope Analysis software can provide a recreation of the tip profile from the sharpness of the features, because a tip cannot resolve the linear and angular aspects of any sample feature sharper than the tip itselfas described in the online NanoScope Software User Guide from Bruker [266]. In the "Tip Qualification" window of the Nanoscope Analysis software, the estimated tip diameter,

or ETD, can be estimated by inputting a specific height from the tip apex, or h, as shown in figure A.1c. Mulitple heights from apex and correspondong ETD's must be collected for tip re-creation, up until a height that accounts for maximum depth of penetration on the sample performed in the experiment. Figure A.1d plots theheight from apex inputs to the corresponding radius, r, of the cross section at that height (half the ETD). A parabolic function can then be fit to the data, as eq. A.1 to find the radius of curvature of the tip, R. In this example the tip is $R \sim 9.33$nm. Note it is not perfect, especially at smaller depths, but overall provides a pretty good estimate in the height range analyzed.

$$h = \frac{1}{2R} r^2 \tag{A.1}$$

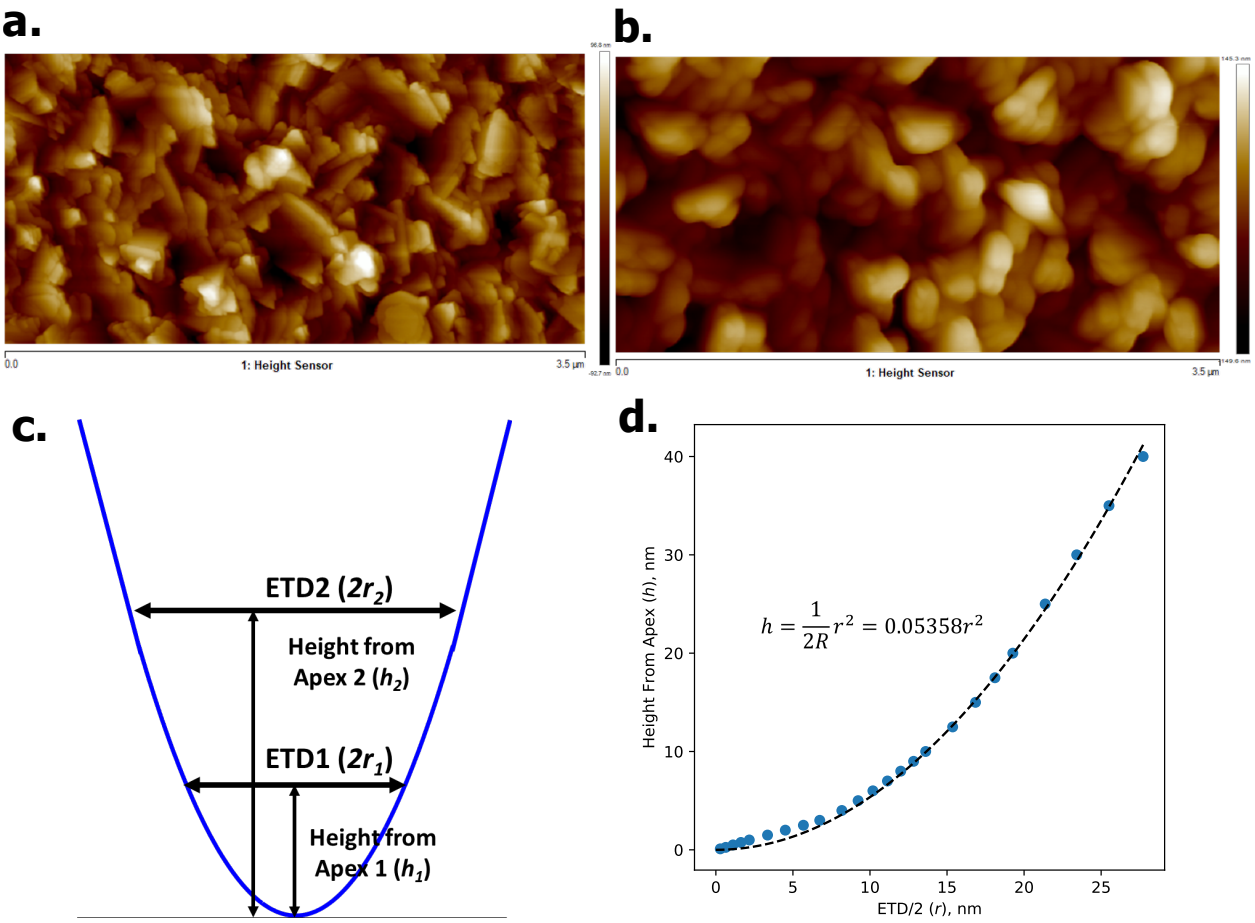

Figure A.1: AFM Tapping mode height sensor topography images of the Bruker Titanium roughness sample using a (**a**). sharp, new tip, and (**b**). worn, large tip. (**c**) Schematic of the tip qualification parameters needed for tip reconstruction using the Bruker Nanoscope Analysis software. (**d**) Tip reconstruction data from tip used in image (**a**) fit to parabolic function. Shows a tip radius, $R \sim 9.33$nm

A.2 More In-Depth Look at Fractography

A.2.1 Fractography in Homogeneous DGEBA/PACM/D400 Samples

Section 3.3.2 in the main text highlights some of the most important features of the fracture surfaces of the SENB toughness samples. Here is a more in depth look at all the images for each system. The fracture surfaces at each temperature for the DGEBA/PACM/D400 epoxy systems are shown in figure A.2. As explored in the main text, for DGEBA/PACM/D400 at low temperature, there were distinct morphology differences between the low D400 and high D400 content epoxies. Namely, for the low D400 epoxies (PACM,

D400-25, and D400-50), arrest lines, caused by the introduction of cracks into the matrix by hammering a razor blade into the notch are evident. The initial crack front for these samples are magnified and shown in figure A.3. It's apparent from these images that the arrest line consists of a rough, striated "hackled" region. This is due to the localized plastic deformation in front of the crack tip that results in the slowing of the crack growth, and has been shown to be on the order of magnitude of the Dugdale zone [157]. In front of this hackled region, the striations coalesce into longer lines known as "river markings" that corresponds to the increased crack velocity as critical, brittle fracture results in a smooth, featureless region far ahead of the initial crack front. These fracture features are well documented in the literature for brittle epoxy resins [146, 147, 150, 157, 181]. However, these features are not seen for the higher D400 systems (D400-75 & D400-100). Particularly, the precrack region, which due to more compliant nature of the epoxies, the razor blade more easily slides through the epoxy instead of generating a crack in front of the blade. At higher temperatures, starting at room temperature for PACM, and 40 °C for D400-25, the region immediately in front of the hackled region becomes very rough. Although this region is very relatively small for PACM, it becomes quite large for D400-25 and may be related to the relatively low fracture toughness measured for these systems even near the T_g. PACM at 60 °C shows a couple more arrest lines far above the initial crack front. These are likely evidence of "stick-slip" propagation, where the crack stops or "sticks" before initiating and moving "slip" again. At room temperature and 40 °C, the hackled region for the D400-50 becomes noticeably larger compared to the lower D400 samples at any temperature. This corresponds to the large increase in fracture toughness with increasing temperature for this formulation that the samples with the lower D400 content formulations lack.

These arrest lines and hackled regions are not seen for the higher D400 systems (D400-75 & D400-100). Particularly, the precrack region, which due to more compliant nature of the epoxies, the razor blade more easily slides through the epoxy instead of generating a crack in front of the blade. This has been shown to lead to larger, more blunt, crack tip radius, which likely results in the larger measured K_{IC} [267]. For the D400-75 sample, the region above the precrack region is mostly smooth, with some river markings extending outwards towards the edges of the sample. Zooming in on the initial crack front for some of these low temperature samples of D400-75, show very small "plastic arches" at some of the crack initiation sites that seem very similar in morphology to the arches seen in the D2000 samples but much smaller, suggesting it is of a similar mechanism. In the PACM sample, however, zooming in on the region above the precrack region, shown in figureA.3, show a very rough region of various markings parallel to the crack front, suggesting it may be akin to slow initial crack growth regime for the stiffer epoxies, but the longer amine chains result in

a different morphology that leads to a higher fracture toughness. Even though the fracture toughness was noticeably higher at 0 °C for both D400-100 and D400-75 than at lower temperatures, there is no noticeable change in the fracture surface morphology until room temperature, where it seems the failure is dominated by large scale yield behavior.

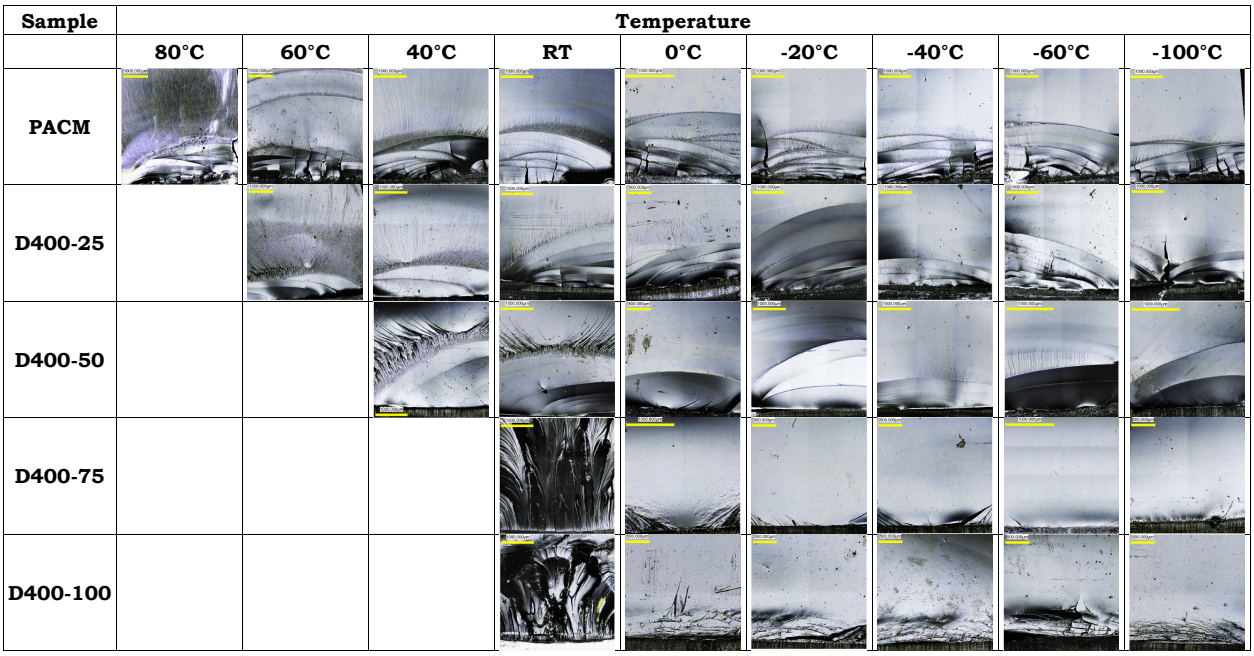

Figure A.2: Optical Microscope images of the SENB toughness sample fracture surfaces for the DGEBA/PACM/D400 epoxy systems at each temperature between 60°C and -100 °C. Initial notch is at the bottom of each image, and crack propagates in towards the top of each image.

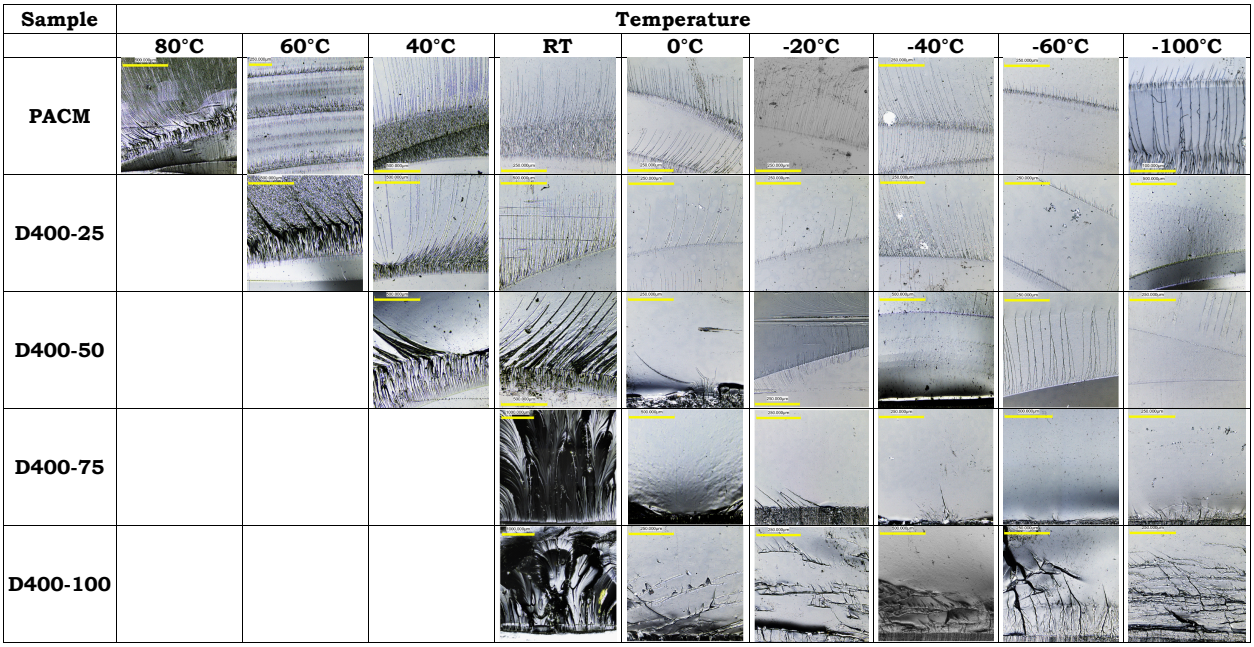

Figure A.3: Magnified in regions from the optical Microscope images fracture surfaces for the DGEBA/PACM/D400 epoxy system shown in figure A.2.

A.2.2 Fractography in Dynamically Heterogeneous DGEBA/PACM/D2000 Samples

The fracture surfaces for the DGEBA/PACM/D2000 epoxy systems at each temperature are shown in A.4, with zoomed in regions shown in figure A.5. As mentioned in the main text, the characteristic feature of the fracture surfaces in these samples is the plastic zone arch seen in the low temperature fracture surface, that seems to increase in roughness with D2000 content, which corresponds to increasing K_{IC}. Even the case of D2000-100, where there was no nanoscale heterogeneity, there was a plastic arch, but this arch is noticeably rougher, seems to be broken up into sections, and the surface didn't seem to have the same striations that appeared in the other D2000 formulations. At higher temperatures, as the T_g was approached for the D2000-100 sample, the entire surface seemed to have similar morphology to the plastic zone arch at -100 °C, showing bulk yield behavior.

The transition to bulk yield behavior for the mixed amine PACM/D2000 systems showed much different morphology. As described in the main text, for the mixed amine PACM/D2000 systems, as the temperature increased from the low temperature K_{IC} plateau, the K_{IC}decreased until bulk yield behavior occurred, which is the opposite trend of the DGEBA/PACM/D400 systems. The temperature at which the K_{IC}

began to decrease, which was -40 °C for D2000-20, D2000-30, and D2000-40, the roughness in the arch began disappeared, although the outline of the edge of the arch was still visible initially (it fully disappeared at -20 °C for D2000-30). Suggesting this plastic zone is very important for slowing down crack growth. Bulk yield behavior is seen at 0 °C and -20 °C for D2000-30 and D2000-40 respectively, corresponding to a low K_{IC} measurement of $\sim 0.65MPa\sqrt{m}$ but its worth noting this bulk yield behavior is distinct from that seen at room temperature for D400-100 and D400-75, where the K_{IC} values were very high, suggesting very distinct plastic flow properties.

D2000-20, which is the sample that was shown to have the best ballistic properties in previous literature studies [163], and different morphology in the fracture surface as the temperature increased. As the arch faded, river lines from the initial crack front became more apparent, starting at -20 °C, with some arches at -20 °C and 0 °C that are somewhat similar to arrest lines. These arches eventually go away as the temperature is further increased, but the toughness remains about the same ($\sim 0.65MPa\sqrt{m}$) from 0 to 40 °C, relatively low value similar to PACM. This suggests that room temperature K_{IC} can not be the mechanism behind the increased ballistic properties, and it would make more sense that the higher K_{IC} at low temperature (via principle of time-temperature superpositon) be related to the ballistic behavior. However, given the even higher low temperature toughness for the higher D2000 content epoxies, it is not the full picture.

The morphology of the D2000-10 is actually the most consistent among all temperatures for the D2000 formulations, which makes sense given that it provided the most modest increase in toughness with decreasing temperature. This sample also has arrest lines that grow infront of the inserted razorblade, however, unlike the low D400 systems described earlier, the regions between the arrest lines are not smooth, but all have characteristic striations in the initial crack arch. These striations are noticeable thinner and more uniform that in the higher D2000 content epoxies, likely due to the higher crosslink density/PACM content. At higher temperatures, where the K_{IC} starts to decrease, the region in front of the initial crack is much more rough, and actually seem like a continuation of the same roughness patter in the precrack region. So in this case, the roughness actually corresponds to a decrease in K_{IC}.

Finally, given the very low T_g of the D2000-100 sample (-27°C), only 3 data points (-100 °C, -80 °C, -60 °C) could be taken. Despite being homogeneous (single T_g, no PACM, ergo no phase separation), a rough, plastically deformed region similar to the other PACM/D2000 systems at low temperature above the initial crack is still seen for the lowest temperatures. At -100 °C, the arch is more rough macroscopically, breaking into several large chunks, but this region seems to lack the thinner striations that appear in the

mixed PACM/D2000. It is unclear if this morphological difference is due to the much lower crosslinking density of this system or lack of nanoscale heterogeneity. Regardless, this sample does have the highest fracture toughness. This region remains at -80 °C, but, at -60 °C, the surface has similar morphology to the plastic zone in its -100 °C counterpart in over the whole fracture surface. Unlike the other PACM/D2000 formulations, there is no decrease in toughness before the material yields too much for proper measurement, suggesting that the nanoscale phase separation is the principal reason for the decrease in toughness with increasing temperature and the differences in morphology in the fracture surface.

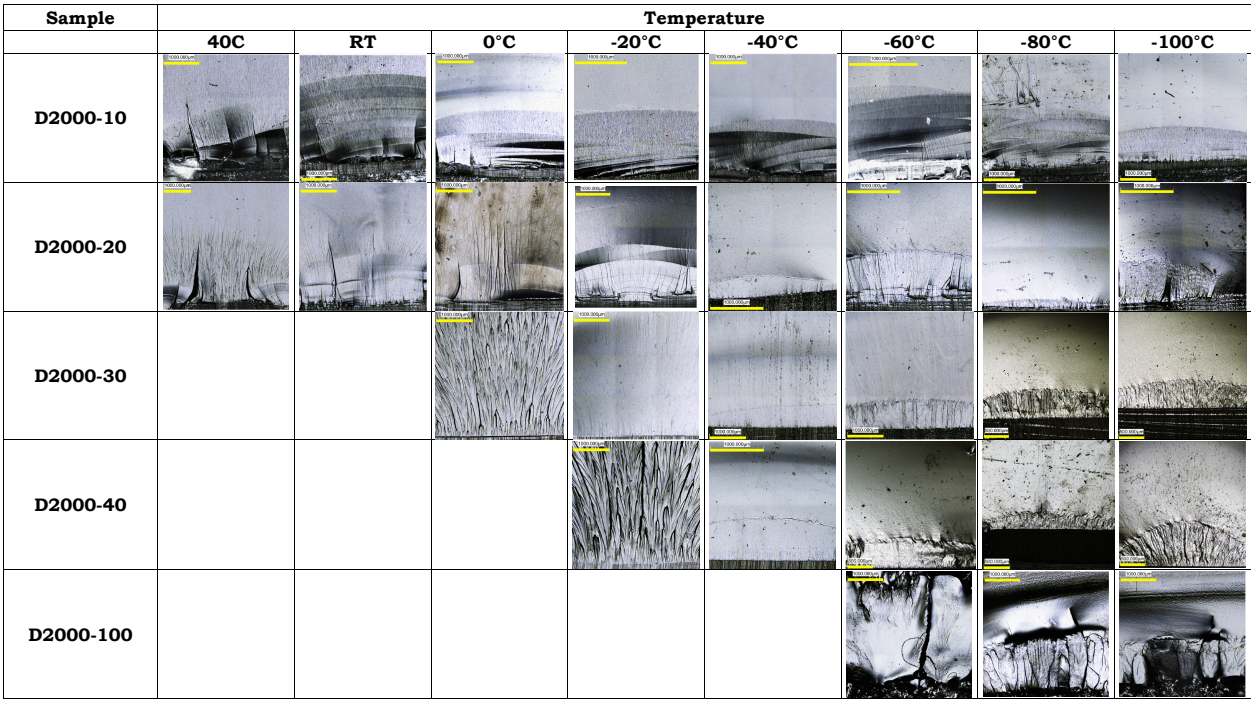

Figure A.4: Optical Microscope images of the SENB toughness sample fracture surfaces for the DGEBA/PACM/D2000 epoxy systems at each temperature between 60ºC and -100 ºC.

Sample	Temperature							
	40C	RT	0°C	-20°C	-40°C	-60°C	-80°C	-100°C
D2000-10	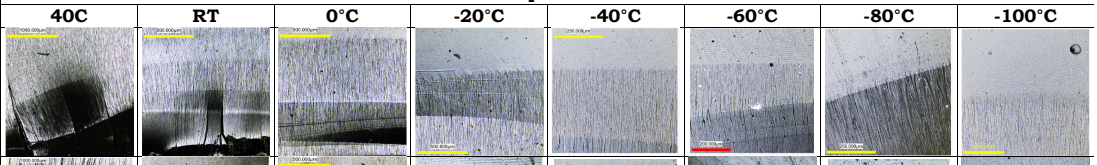							
D2000-20	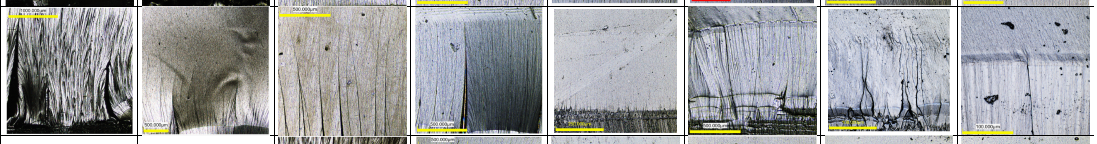							
D2000-30	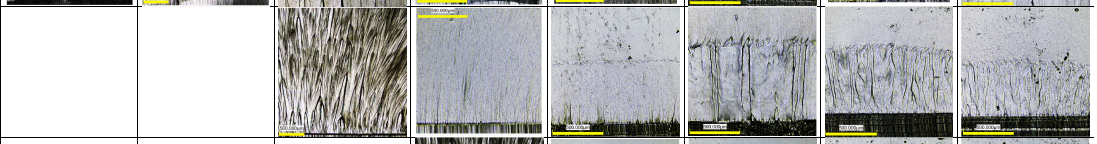							
D2000-40	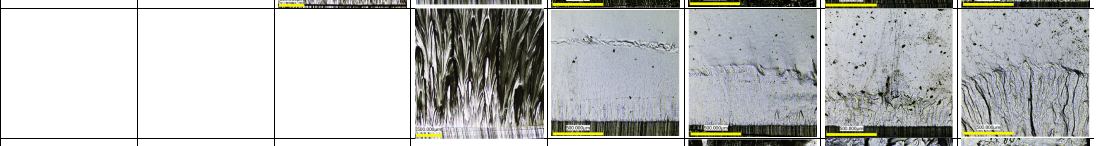							
D2000-100								

Figure A.5: Magnified regions from the optical Microscope images fracture surfaces for the DGEBA/PACM/D400 epoxy system shown in figure A.4.